

**HZDR-083**

# **DIODE-PUMPED HIGH-ENERGY LASER AMPLIFIERS FOR ULTRASHORT LASER PULSES**

## **THE PENELOPE LASER SYSTEM**

Markus Löser

Wissenschaftlich-Technische Berichte  
HZDR-083 · ISSN 2191-8708

**WISSENSCHAFTLICH-  
TECHNISCHE BERICHTE**

**hZDR**



**HELMHOLTZ  
ZENTRUM DRESDEN  
ROSSENDORF**



Wissenschaftlich-Technische Berichte  
HZDR-083

Markus Löser

**DIODE-PUMPED HIGH-ENERGY LASER AMPLIFIERS  
FOR ULTRASHORT LASER PULSES  
THE PE<sub>N</sub>ELOPE LASER SYSTEM**

**HZDR**

 **HELMHOLTZ**  
| ZENTRUM DRESDEN  
| ROSSENDORF

Druckausgabe: ISSN 2191-8708

Elektronische Ausgabe: ISSN 2191-8716

Die elektronische Ausgabe erscheint unter Creative Commons License (CC BY 4.0):

<https://www.hzdr.de/publications/Publ-26578>

<urn:nbn:de:bsz:d120-qucosa-232322>

Die vorliegende Arbeit wurde sowohl als Dissertation an der Fakultät Mathematik und Naturwissenschaften der Technischen Universität Dresden sowie als Wissenschaftlich-Technischer Bericht des Helmholtz-Zentrum Dresden – Rossendorf mit der Berichtsnummer **HZDR-083** veröffentlicht.

2018

Herausgegeben vom

Helmholtz-Zentrum Dresden - Rossendorf

Bautzner Landstraße 400

01328 Dresden

Germany





**TECHNISCHE  
UNIVERSITÄT  
DRESDEN**

**HZDR**

 **HELMHOLTZ  
ZENTRUM DRESDEN  
ROSSENDORF**

---

Fakultät Mathematik und Naturwissenschaften

Institut für Strahlenphysik

---

# **Diode-Pumped High-Energy Laser Amplifiers for Ultrashort Laser Pulses**

## **The PE<sub>N</sub>ELOPE Laser System**

**D I S S E R T A T I O N**

zur Erlangung des wissenschaftlichen Grades

Doctor rerum naturalium

(Dr. rer. nat.)

vorgelegt der

**Fakultät Mathematik und Naturwissenschaften  
der Technischen Universität Dresden**

von

**Markus Löser**

geboren am 08.01.1983 in Pirna

Die Dissertation wurde in der Zeit von 5/2010 bis 8/2017 am Helmholtz-Zentrum Dresden-Rossendorf im Institut für Strahlenphysik angefertigt.

Eingereicht am 09.08.2017  
Verteidigt am 16.11.2017

1. Gutachter: Prof. Dr. Dr. h.c. Roland Sauerbrey
2. Gutachter: Prof. Dr. Ulrich Schramm
3. Gutachter: Prof. Dr. Peter Hartmann

## Abstract

The ultrashort chirped pulse amplification (CPA) laser technology opens the path to high intensities of  $10^{21}$  W/cm<sup>2</sup> and above in the laser focus. Such intensities allow laser-matter interaction in the relativistic intensity regime. Direct diode-pumped ultrashort solid-state lasers combine high-energy, high-power and efficient amplification together, which are the main advantages compared to flashlamp-pumped high-energy laser systems based on titanium-doped sapphire. Development within recent years in the field of laser diodes makes them more and more attractive in terms of total costs, compactness and lifetime.

This work is dedicated to the Petawatt, Energy-Efficient Laser for Optical Plasma Experiments (PENELOPE) project, a fully and directly diode-pumped laser system under development at the Helmholtz-Zentrum Dresden-Rossendorf (HZDR), aiming at 150 fs long pulses with energies of up to 150 J at repetition rates of up to 1 Hz. The focus of this thesis lies on the spectral bandwidth manipulation of the front-end amplifiers, trivalent ytterbium-doped calcium fluoride (Yb<sup>3+</sup>:CaF<sub>2</sub>) as gain material as well as the pump source for the final two main amplifiers of the PENELOPE laser system. Here, all crucial design parameters were investigated and a further successful scaling of the laser system to its target values was shown.

Gain narrowing is the dominant process for spectral bandwidth reduction during the amplification at the high-gain front-end amplifiers. Active or passive spectral gain control filter can be used to counteract this effect. A pulse duration of 121 fs was achieved by using a passive spectral attenuation inside a regenerative amplifier, which corresponds to an improvement by a factor of almost 2 compared to the start of this work. A proof-of-concept experiment showed the capability of the pre-shaping approach. A spectral bandwidth of 20 nm was transferred through the first multipass amplifier at a total gain of 300. Finally, the predicted output spectrum calculated by a numerical model of the final amplifier stages was in a good agreement with the experimental results.

The spectroscopic properties of Yb<sup>3+</sup>:CaF<sub>2</sub> matches the constraints for ultrashort laser pulse amplification and direct diode pumping. Pumping close to the zero phonon line at 976 nm is preferable compared to 940 nm as the pump intensity saturation is significantly lower. A broad gain cross section of up to 50 nm is achievable for typical inversion levels. Furthermore, moderate cryogenic temperatures (above 200 K) can be used to improve the amplification performance of Yb<sup>3+</sup>:CaF<sub>2</sub>. The optical quality of the doped crystals currently available on the market is sufficient to build amplifiers in the hundred joule range.

The designed pump source for the last two amplifiers is based on two side pumping in a double pass configuration. However, this concept requires the necessity of brightness conservation for the installed laser diodes. Therefore, a fully relay imaging setup (*4f optical system*) along the optical path from the stacks to the gain material including the global beam homogenization was developed in a novel approach.

Beside these major parts the amplifier architecture and relay imaging telescopes as well as temporal intensity contrast (TIC) was investigated. An all reflective concept for the relay imaging amplifiers and telescopes was selected, which results in several advantages especially an achromatic behavior and low B-Integral. The TIC of the front-end was improved, as the pre- and postpulses due to the plane-parallel active-mirror was eliminated by wedging the gain medium.

## Kurzfassung

Die CPA-Technik (chirped pulse amplification<sup>1</sup>) ermöglicht Intensitäten im Laserfokus von mehr als  $10^{21}$  W/cm<sup>2</sup>. Solch extreme Intensitäten führen zu Laser-Materie-Wechselwirkungen im relativistischen Intensitätsregime. Direkt diodengepumpte Ultrakurzpuls-Festkörperlaser kombinieren zugleich hohe Energie, eine hohe Spitzenleistung, sowie eine effiziente Verstärkung. Dies stellt einen der zentralen Vorteile gegenüber blitzlampengepumpter hochenergetischer Lasersysteme auf Basis von Titan dotiertem Saphir dar. Die stetige Entwicklung im Bereich der Laserdioden macht diodengepumpte Systeme immer attraktiver in Bezug auf Gesamtkosten, Kompaktheit und Lebensdauer.

Diese Arbeit ist im Rahmen des PENELOPE-Projekt (Petawatt, Energy-Efficient Laser for Optical Plasma Experiments) eingeordnet, einem vollständig und direkt diodengepumpten Lasersystem, welches zum Zeitpunkt dieser Arbeit am HZDR in Entwicklung ist. Dieses System zielt auf 150 fs lange Laserpulse mit Energien von bis zu 150 J bei Wiederholraten von bis zu 1 Hz ab. Der Schwerpunkt dieser Doktorarbeit liegt dabei auf der spektralen Bandbreitenmanipulation der ersten Verstärkerstufen, der Qualifizierung des verwendeten Lasermaterials (trivalent Ytterbium-dotierten Kalziumfluorid – Yb<sup>3+</sup>:CaF<sub>2</sub>), sowie der Realisierung der Pumpquellen der beiden letzten Verstärkerstufen des PENELOPE-Lasersystems. Alle wesentlichen Designparameter wurden hierbei untersucht und eine Skalierung des Lasersystems auf seine Zielwerte gezeigt.

Die Spektrale Einschnürung (*gain narrowing*) ist einer der dominierenden Effekte zur ungewünschten Reduzierung der verfügbaren spektralen Bandbreite während der Verstärkung in den ersten Verstärkerstufen mit besonders hohem Verstärkungsfaktor. Um diesem Effekt entgegenzuwirken können aktive und passive spektrale Verstärkungsregelungsfilter genutzt werden. Verglichen mit der Situation vor dieser Arbeit konnte mit Hilfe von passiven spektralen Abschwächern eine Verbesserung der Pulsdauer von fast einem Faktor 2, auf nun 121 fs, erreicht werden. Die Tragfähigkeit der spektralen Vorformung wurde in einem Experiment gezeigt. Dabei konnte eine Erhaltung von 20 nm Bandbreite bei einer gleichzeitigen Verstärkung von mehr als 300 in einem Yb<sup>3+</sup>:CaF<sub>2</sub> Multipass-Verstärker gezeigt werden. Abschließend wurde das zu erwartende Ausgangsspektrum der finalen Verstärkerstufen mit Hilfe einer numerischen Simulation berechnet, welche eine gute Übereinstimmung mit dem Experiment zeigte.

Die spektroskopischen Eigenschaften von Yb<sup>3+</sup>:CaF<sub>2</sub> machen dieses Material zu einem attraktiven Kandidaten für direkt diodengepumpte Verstärker ultrakurzer Pulse. Ein Arbeitspunkt der optischen Pumpe nahe des Null-Phononen-Übergangs bei 976 nm ist gegenüber der weit verbreiteten Wellenlänge von 940 nm zu bevorzugen, da die Pumpsättigungsintensität bei dieser Wellenlänge deutlich geringer ausfällt. Für typische Inversionsniveaus ist eine Verstärkungsbandbreite von bis zu 50 nm erreichbar. Im Temperaturbereich zwischen Raumtemperatur und kryogenen Temperaturen (über 200 K) kann die Funktion des Verstärkers deutlich verbessert werden. Die optische Qualität der derzeit auf dem Markt erhältlichen dotierten Kristalle reicht für eine Verstärkung im 100 J-Bereich aus.

---

1 Vor der Verstärkung werden die Laserpulse zeitlich gestreckt und nach der Verstärkung wieder komprimiert.

Die entworfenen Pumpquellen für die letzten beiden Verstärkerstufen nutzt eine beidseitige optische Pumpe auf dem in Transmission genutzten Verstärkermaterial. Der jeweils transmittierte Pumpanteil wird anschließend ein weiteres Mal auf den Verstärkerkopf abgebildet um die Gesamtabsorption zu erhöhen. Dieses Konzept erfordert jedoch die Notwendigkeit der Erhaltung des Lichtleitwertes (engl. brightness) für die eingesetzten Laserdioden. Daher wurde der Ansatz der vollständigen Abbildung (*4f-Aufbau*) des optischen Weges vom Stack bis zum Lasermaterial, einschließlich der globalen Strahlhomogenisierung, gewählt.

Neben diesen Hauptteilen wurde auch der Verstärkeraufbau und die abbildenden Teleskope, sowie der zeitliche Intensitätskontrast (TIC<sup>1</sup>) untersucht. Ein achromatisches Verhalten sowie ein niedriges B-Integral sind die Hauptvorteile bei Verwendung von rein reflektiven Optiken in den abbildenden Verstärkern und Teleskopen. Ein besonderes Augenmerk wurde auf die Vermeidung von Nach- und Vorpulsen aufgrund von planparallelen Bauteilen gelegt.

---

1 temporal intensity contrast (TIC)



---

# Contents

---

<b>1</b>	<b>Introduction</b>	<b>1</b>
<b>2</b>	<b>Theoretical Principles for Laser Development</b>	<b>5</b>
2.1	Chirped Pulse Amplification CPA . . . . .	5
2.1.1	Laser pulse generation . . . . .	6
2.1.2	Description of Ultrashort Laser Pulses . . . . .	7
2.1.2.1	Dispersion Management . . . . .	11
2.1.2.2	Nonlinear Effects . . . . .	15
2.2	Amplification of Ultrashort Laser Pulses . . . . .	17
2.2.1	Pump Energy Storage . . . . .	18
2.2.2	Energy Extraction . . . . .	21
2.2.3	Amplified Spontaneous Emission . . . . .	21
2.2.4	Efficiency Considerations . . . . .	22
2.3	Diagnostics for Ultrashort Laser Pulses . . . . .	25
2.3.1	Optical Autocorrelation . . . . .	25
2.3.2	<i>SPIDER</i> - Spectral Phase Interferometry for Direct Electric-field Re- construction . . . . .	27
2.3.3	<i>WIZZLER</i> - Self-Referenced Spectral Interferometry . . . . .	28
<b>3</b>	<b>The PENELOPE Laser System</b>	<b>31</b>
3.1	Overview of High-Energy Laser Systems . . . . .	31
3.2	System Overview and Description . . . . .	34
3.2.1	Amplifier Architecture . . . . .	37
3.2.2	Beam Shaping, Relay Imaging Telescopes and Amplifiers . . . . .	39
3.2.3	Stretcher and Compressor of the PENELOPE System . . . . .	51
3.3	Laser Diodes as a Pump Sources for High-Energy Lasers . . . . .	54
3.3.1	Structure and Performance . . . . .	55
3.3.2	Beam Combination, Shaping and Transport . . . . .	60
3.3.3	Experimental Benchmark of the 10 J Amplifier Pump Source . . . . .	68
3.4	Conclusion . . . . .	74
<b>4</b>	<b>Gain Material Choice for DPSSL</b>	<b>77</b>
4.1	General Properties for High-Energy Gain Materials . . . . .	77
4.2	Optical Quality . . . . .	80

4.3	Spectroscopic Properties of Trivalent Ytterbium-doped Gain Materials . . .	84
4.3.1	Yb <sup>3+</sup> :CaF <sub>2</sub> the Gain Medium for the PENELOPE System . . . . .	85
4.3.2	Divalent Ytterbium (Yb <sup>2+</sup> ) Formation in Calcium Fluoride . . . . .	91
4.4	Alternative Gain Materials . . . . .	92
4.5	Conclusion . . . . .	92
<b>5</b>	<b>Amplifier Experiments</b>	<b>95</b>
5.1	The Active-Mirror Concept . . . . .	95
5.2	Yb <sup>3+</sup> -CaF <sub>2</sub> Amplifiers . . . . .	98
5.2.1	Continuous Wave Laser Operation . . . . .	98
5.2.2	Regenerative Amplifier . . . . .	99
5.2.3	Spectral Manipulation . . . . .	105
5.2.3.1	Spectral Response of the Regenerative Amplifier . . . . .	107
5.2.3.2	Passive Gain Control . . . . .	113
5.2.3.3	Active Gain Control . . . . .	117
5.2.4	Bandwidth Scaling of the Large Amplifiers . . . . .	118
5.3	Temporal Intensity Contrast . . . . .	125
5.4	Conclusion . . . . .	129
<b>6</b>	<b>Conclusion and Outlook</b>	<b>131</b>
	<b>Bibliography</b>	<b>137</b>
	<b>List of Figures</b>	<b>153</b>
	<b>List of Tables</b>	<b>157</b>
	<b>Acronyms</b>	<b>159</b>
<b>A</b>	<b>Appendix</b>	<b>163</b>
A.1	The Term Schema of the Quasi-Three-Level System Yb <sup>3+</sup> :CaF <sub>2</sub> . . . . .	163
A.2	Single Lens Imaging versus Relay Imaging . . . . .	164
A.3	Influence of Yb <sup>2+</sup> -ions on the Laser Performance . . . . .	167
A.4	Alternative Yb <sup>3+</sup> -doped Gain Materials . . . . .	168
A.4.1	Spectroscopic Properties . . . . .	168
A.4.1.1	Laser Glasses . . . . .	168
A.4.1.2	CALGO and CALYO . . . . .	170
A.4.2	Amplifier Experiments with Alternative Gain Materials . . . . .	171
A.4.2.1	Laser Glasses . . . . .	171
A.4.2.2	CALGO . . . . .	175
	<b>Publications</b>	<b>177</b>
	<b>Danksagung</b>	<b>183</b>
	<b>Eidesstattliche Erklärung</b>	<b>185</b>



## CHAPTER 1

---

# Introduction

---

The first experimental realization of the laser (*light amplification by stimulated emission of radiation*) by T. Maiman in 1960 laid the cornerstone for the industrial and scientific development for bright and coherent light sources as we know it today. Nowadays, lasers affect almost every aspect of our daily life, be it in material processing, telecommunication, health care, etc. In basic science, whole recent fields as quantum optics or ultrafast science have evolved and lasers have pushed the frontiers of high field science. An important milestone was the development of the chirped pulse amplification (CPA) technique by D. Strickland and G. Mourou in 1985 enabling the onset of an ongoing development to unprecedented peak intensities for ultrashort pulses.

Within the last decade the number of ultrashort high-intensity lasers systems reaching the TW ( $10^{12}$  W) and PW ( $10^{15}$  W) level around the world strongly increased. Nowadays, large laser facilities are constructed as international research centers, like the Extreme Light Infrastructure (ELI) project in Europe. By the end of 2017, the total peak power of all systems will reach more than 100 PW, which is ten times the total power of 2009 [1].

Ultrashort high-intensity lasers are a novel tool to reach intensities of  $10^{18}$  W/cm<sup>2</sup> to  $10^{23}$  W/cm<sup>2</sup> in the laboratory. These intensities are suitable for laser-matter interaction in the so-called relativistic intensity regime where electrons are accelerated nearly to the speed of light in single laser oscillations. The electric field strength can be in the order of TV/m, which opens entire new paths to very compact particle accelerators/sources.

These high electric fields can be rectified in plasmas and are of special interest for electron acceleration up to GeV energy range on a short length [2], known as laser wakefield acceleration. The generation of ultrashort x-ray pulses with unique properties is obtained in combination with an electron beam [3, 4].

Furthermore, one of the major goals of such a novel light source is to generate laser accelerated proton and ion beams with energies of 200 MeV and above, relevant for future cancer therapy applications. At the moment, energies up to 85 MeV were demonstrated with 500 fs to 800 fs long laser pulses based on neodymium-doped glass laser systems [5]. Proton energies up to 40 MeV were obtained with ultrashort laser pulses of 30 fs pulse duration at PW-level [6]. Different scaling laws are proposed for the maximum ion energy as a function of laser intensity and pulse duration. The relativistic electron energy scaling for ultrashort laser pulse was presented by T. Kluge et. al [7], which shows a good agreement with simulation and experimental data.

Typically, two types of laser sources are used to generate high-intensities: On the one hand there are neodymium-doped glasses which support high pulse energies up to several kJ and pulse durations in the sub-nanosecond to sub-picosecond range. On the other hand there are ultrashort pulse laser systems based on  $\text{Ti}^{3+}$ :sapphire that generate pulses up to several tens of joule in the femtosecond range (typically 20 fs to 30 fs). The pump source for high energy  $\text{Ti}^{3+}$ :sapphire laser amplifiers are typically frequency doubled neodymium-doped nanosecond lasers, producing output energies of up to several tens or hundred joule. These lasers rely on the well-established flashlamp technology, which limits the repetition rate (i.e. several shots per hour for kJ-class lasers) as well as the wall plug efficiency of these laser systems.

In addition to these well-established laser sources, a third type is becoming increasingly important in these energy- and intensity-levels. Diode-pumped high-energy laser systems using trivalent ytterbium ( $\text{Yb}^{3+}$ ) are still rising, as their high efficiency, compactness and low thermal load is very attractive to build high-energy as well as high repetition rate laser systems. Additionally, the price trend for the laser diodes makes them more and more attractive in terms of the total system cost. The market of diode-pumped laser systems is dominated by industrial applications in the nanosecond down to picosecond range and high-average powers (i.e low output energy but high repetition rate). Of scientific interest are high energy ultrashort laser system based on  $\text{Yb}^{3+}$ -doped gain materials and only a very few selected laser development teams engage this issue. A well-known laser system is the Polaris laser developed at the IOQ at Jena [8].

In order to engage the scientific questions about laser-matter interaction, two different PW-class laser projects are situated at the Helmholtz-Zentrum Dresden-Rossendorf (HZDR). The first is a commercial system based on  $\text{Ti}^{3+}$ :sapphire, the Dresden laser acceleration source (Draco). It provides 30 fs long pulses with energies up to 30 J. The second PW-class system is the Petawatt, Energy-Efficient Laser for Optical Plasma Experiments (PENVELOPE) laser system, which is a fully, direct diode-pumped solid state laser. This system is dedicated to generate 150 fs long pulses with energies of up to 150 J at repetition rates of up to 1 Hz.

The PENVELOPE laser system is an in-house development of the HZDR and currently under construction. The main goal for both laser systems lies centrally in particle acceleration, especially protons. Figure 1.1 shows the relativistic electron energy scaling for the PENVELOPE and Draco laser. The prediction of the scaling law is that laser pulses close to 170 fs at the PW-level produce ion energies in the clinical relevant range (i.e. above 200 MeV). The PENVELOPE laser system matches to the foreseen parameters to aim for this specific proton energy range.

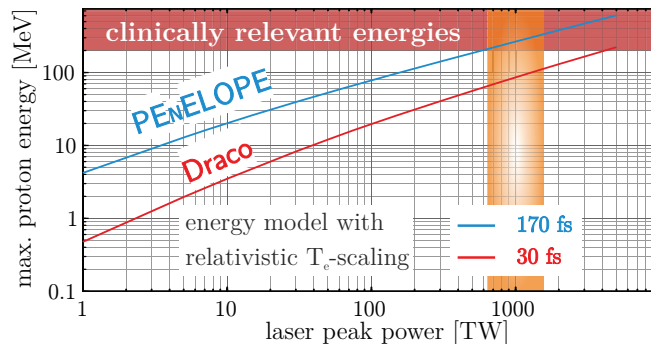


**Figure 1.1:** The maximum proton energy as a function of the laser peak power. The laser power scaling is based on the model by T. Kluge et al. [7].

---

Ultrashort, high-energy, diode-pumped solid state laser systems contain different components - three essential ones are of central importance - the gain material, the pump source and a broadband front-end to support ultrashort pulses out of the high-energy amplifier chain.

The gain medium has to fulfill various constraints (e.g. broad emission bandwidth, high optical quality and good thermal properties). In order to keep the necessary bandwidth, the choice for  $\text{Yb}^{3+}$ -doped materials is limited to a few host materials. Additionally, thermal properties and the optical quality are important as well. The optical quality of large doped gain materials has to be investigated and thus an appropriate method to characterize them needs to be defined.

Laser diodes are taken as a pump source due to the fact that they offer a high electrical-to-optical efficiency, which reduces the running cost of the laser system. Furthermore, the long lifetime of the laser diodes shows an improvement in terms of maintenance as well. Additionally, the narrow emission bandwidth and the pump center wavelength close to the laser wavelength reduce the thermal load, strongly affecting the achievable repetition rate of the laser system. High-energy, flashlamp-pumped laser systems are typically limited to several shots per hour. In contrast to this, diode-pumped lasers operate at up to several shots per second.

A large number of laser diodes is required to deliver the needed pump energy. Therefore, new pump geometries have to be designed to reshape the beam output of the large number of laser diodes. Especially, the beam profile has to be homogenized to pump a large gain medium. At the beginning of the PENELOPE project such a kind of pump source was not available on the market.

The limiting factor for the laser pulse duration during the amplification is gain narrowing, which reduces the spectral bandwidth. This leads to a longer pulse duration at the end of the CPA chain compared to the input pulse duration. One of the main goals is to overcome this limitation directly at the amplifier level. As the gain narrowing depends on the amplification factor, the crucial part is the front-end of a laser system (so-called High-Gain Broadband Amplifier (HGBA)), where most of the gain is generated. The HGBAs consist of regenerative amplifiers, as well as subsequent multipass amplifiers and they have to be optimized to counteract the gain narrowing effect.

In addition to these major components of a high-energy laser system there are several difficult tasks to solve, which are needed to perform laser-plasma experiments. One challenge is the architecture of the main amplifiers (so-called High-Energy Power Amplifiers (HEPAs)) boosting the energy to the desired level while preserving the quality of the laser pulse. This is directly linked to the quality of the laser gain medium and the design of the amplifier stages, respectively.

After the entire amplification stages and final compression, the laser output pulses requires a low temporal intensity contrast (TIC). This is of utmost importance to perform laser-plasma experiments, as the contrast of the laser pulses has an essential impact on the experimental results. Prepulses on nanosecond (ns) and picosecond (ps) timescales as well as the background level generated by amplified spontaneous emission in the laser amplifiers can dramatically affect the target properties due to ionization and preplasma [9, 10].

This thesis is set within the framework of the **PENELOPE** project and is dedicated to demonstrate a proof-of-principle experiment of diode-pumped  $\text{Yb}^{3+}$ -doped  $\text{CaF}_2$  amplifiers with a high-gain ( $>1000$ ) in combination with a large spectral bandwidth ( $>20$  nm). Such an experimental proof would assess the suitability of a rather new laser medium  $\text{Yb}^{3+}:\text{CaF}_2$  for a high-energy laser system such as **PENELOPE**. Additionally, the thesis includes also the pump source for the last two multipass amplifiers of the **PENELOPE** laser system. The gain material is pumped close to the zero phonon line, which leads to constraints for the optical setup and the performance of the laser diodes. An experimental proof of the concept based on two side pumping with single beams will open the path to direct diode-pumped ultrashort, high-energy laser system at the PW-level.

Following the introductory chapter, the theoretical principles for laser development are presented in the second chapter. In the main part chirped pulse amplification is described, including the mathematical description of the pulse stretching and compression. Typical measurement techniques for ultrashort laser pulses are explained in detail. Additionally, the fundamental rate equations for laser pulse amplification are discussed.

The third chapter gives an overview of high-energy laser systems and especially with a detailed introduction of the **PENELOPE** system. Furthermore, laser diode stacks as a pump source are described and investigated. The designed pump source for the second to last amplifier stage is benchmarked with its experimental setup.

In the fourth chapter, the  $\text{Yb}^{3+}$ -doped  $\text{CaF}_2$  as gain medium is discussed in terms of optical quality and general properties. Especially, the spectroscopic characteristics are analyzed. A special emphasis lies on the optimization of pump wavelength and operation temperature.

The fifth chapter concentrates on experimental results obtained with  $\text{Yb}^{3+}:\text{CaF}_2$  used in HGBAs (e.g. regenerative and multipass amplifiers). The main interest is the bandwidth preservation during amplification in order to support ultrashort pulses in the 150 fs range. The necessity to manipulate the amplifier gain spectrum itself as well as to pre-shape the HEPAs (final amplifiers) input spectra is studied. The impact of additional optical elements on the available bandwidth during transport in the laser chain is discussed. Special dedication is given on the temporal intensity contrast out of the regenerative amplifier and first optimizations are performed.

Finally, the thesis is summarized and an outlook for further development is presented. Furthermore, the activation of the second to last amplifier has started and the first experimental campaign was performed. The current performance is presented up to the 10 J level.

## CHAPTER 2

---

# Theoretical Principles for Laser Development

---

In this chapter theoretical principles for laser development are discussed. In the first section, the main focus of the discussion is on chirped pulse amplification (CPA) technology. The mathematical description of ultrashort laser pulses, dispersion and selected nonlinear effects are presented. Furthermore, the diagnostic concepts for femtosecond pulses are highlighted. The amplification is treated in terms of laser rate equations and efficiency considerations, as well as parasitic effects like amplified spontaneous emission (ASE).

## 2.1 Chirped Pulse Amplification CPA

In 1985, Donna Strickland and Gérard Mourou demonstrated CPA as a novel amplification technique for ultrashort laser pulses, opening the way to unprecedented intensity levels [11]. Up to this point, the laser intensity was limited by damage of the gain material and optics.

The basic concept relies on stretching the laser pulse at the beginning by adding a frequency depending delay (so-called chirp). This results in a significant reduction of the intensity during amplification. Typical stretching factors are in the range of 4 to 5 orders of magnitude to achieve nanosecond pulse duration from the original 10 fs to 100 fs range of mode-locked oscillators. The amplification is achieved in a set of subsequent amplifiers, each operating well below the damage threshold. Afterwards, the frequency depending delay of the pulse is reversed by a compressor. A schematic sketch of the CPA scheme is shown in Figure 2.1.

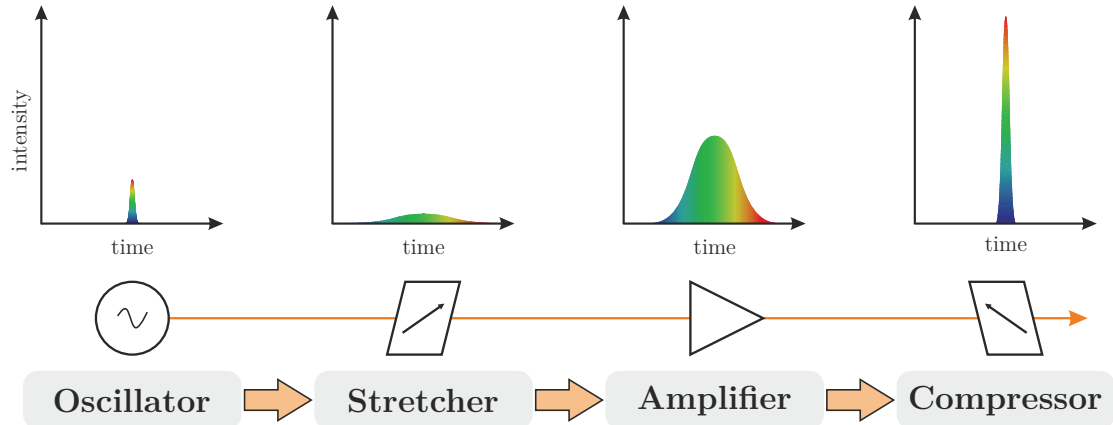


**Figure 2.1:** Schematic drawing of the CPA scheme. The oscillator generates ultrashort laser pulses, by propagating through the stretcher a frequency depending delay is added. At the end of the amplification the delay is reversed via the compressor.

## 2.1.1 Laser pulse generation

Ultrashort laser pulses are generated by a laser oscillator using the mode-locking principle briefly described here after. The longitudinal modes (so-called axial modes) of a laser resonator are defined by its eigenfrequencies. The frequency of stable axial modes is

$$\nu_q = q \frac{c_0}{2L \cdot n} \quad , \quad (2.1)$$

with  $L$  the resonator length,  $q$  the number of the mode,  $c_0$  the speed of light in vacuum,  $n$  the refractive index of the material. The spacing between two modes is given by

$$\Delta\nu_{q,q+1} = \frac{c_0}{2L \cdot n} \quad . \quad (2.2)$$

This corresponds to the repetition rate and the inverse of the round trip time of a laser pulse, respectively.

The electric field of a pulse is a superposition of many axial modes and can be derived by using the angular frequency  $\omega_q = 2\pi\nu_q$  to [12]

$$\mathcal{E}(t) = \sum_{q=1}^o \mathcal{E}_q(t) \cdot \exp[\tilde{\varphi}_q + \omega_q t] \quad , \quad (2.3)$$

with  $o$  the number of oscillating modes,  $\mathcal{E}_q(t)$  the amplitude of the electric field and  $\tilde{\varphi}_q$  the phase offset of the  $q$ -th mode. In general, longitudinal modes have a random phase relationship (a non-constant phase offset).

In order to achieve the so-called mode-locking, they have to fulfill two conditions: On the one hand the axial modes have to be phase-locked ( $\tilde{\varphi}_q = \text{const.} \forall q$ ) and on the other hand the gain for each axial mode in the laser resonator has to be larger than 1. If the phase difference is constant, a constructive interference of the longitudinal modes will occur and this results in short pulses.

There are active and passive mode-locking techniques. Several are described in [13]. State of the art commercially available titanium-sapphire femtosecond laser oscillators produce pulse durations below 10 fs [14] by using a passive technique called Kerr-lens mode-locking.

The impact of the number of phase locked modes on the peak laser intensity is shown in Figure 2.2 (a) and (b). Additionally, the laser intensity for a random phase of 50 modes is presented in Figure 2.2 (c). For ultrashort pulses in the femtosecond range, a large number<sup>a</sup> of longitudinal modes is necessary. Therefore a large gain bandwidth of the laser material is essential. As a result, bandwidth is the central issue for every ultrashort pulse laser system.

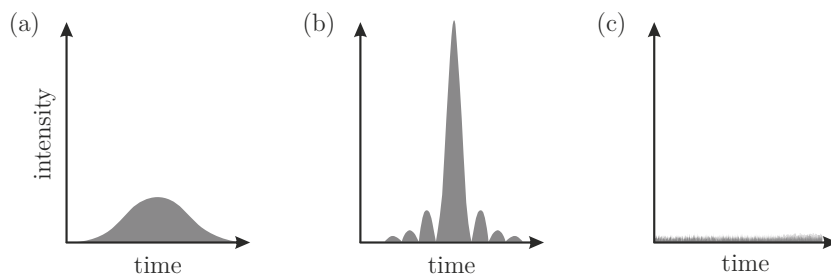


**Figure 2.2:** The laser intensity as a function of time  $I(t) \propto |\mathcal{E}(t)|^2$  for the superposition of (a) 10 and (b) 50 modes with a constant phase ( $\tilde{\varphi}_q = \text{const. } \forall q$ ) and (c) 50 modes with a random phase.

## 2.1.2 Description of Ultrashort Laser Pulses

In general the electric field strength of an electromagnetic wave is a function of space and time. This can be derived from the Maxwell equations [15]. For a fixed point in space the electric field strength does depend on time only. As mentioned before in Equation (2.3), the electric field of a laser pulse  $\mathcal{E}(t)$  is a superposition of monochromatic waves.

A more accurate mathematical explanation of a laser pulse is given by its Fourier decomposition [16]:

$$\mathcal{E}(t) = \frac{1}{2\pi} \int_{-\infty}^{\infty} \tilde{\mathcal{E}}(\omega) e^{i\omega t} d\omega \quad . \quad (2.4)$$

The complex spectrum  $\tilde{\mathcal{E}}(\omega)$  is derived using the Fourier transformation

$$\tilde{\mathcal{E}}(\omega) = \mathcal{F}\{\mathcal{E}(t)\} = \int_{-\infty}^{\infty} \mathcal{E}(t) e^{-i\omega t} dt \quad . \quad (2.5)$$

Due to the fact that  $\mathcal{E}(t)$  is a real function, it holds true, that

$$\tilde{\mathcal{E}}(\omega) = \tilde{\mathcal{E}}^*(-\omega) \quad , \quad (2.6)$$

<sup>a</sup> A typical value is  $\sim 3.8 \times 10^4$  with  $\lambda_c = 1 \mu\text{m}$ ,  $\Delta\lambda = 10 \text{ nm}$  and  $f_{rep} = 80 \text{ MHz}$ .

where  $\tilde{\mathcal{E}}^*(-\omega)$  is the complex conjugate of  $\tilde{\mathcal{E}}(\omega)$ . Hence, the knowledge of the spectrum for positive frequencies is enough for the full characterization of the pulse and we can define for the positive part  $\tilde{\mathcal{E}}^+(\omega)$  as well as for the negative part  $\tilde{\mathcal{E}}^-(\omega)$

$$\tilde{\mathcal{E}}^+(\omega) = \begin{cases} \tilde{\mathcal{E}}(\omega) & \text{for } \omega \geq 0 \\ 0 & \text{for } \omega < 0 \end{cases} \quad (2.7)$$

$$\tilde{\mathcal{E}}^-(\omega) = \begin{cases} 0 & \text{for } \omega \geq 0 \\ \tilde{\mathcal{E}}(\omega) & \text{for } \omega < 0 \end{cases} . \quad (2.8)$$

The complex electric field can be derived by the inverse Fourier integrals

$$\mathcal{E}^+(t) = \mathcal{F}^{-1}\{\tilde{\mathcal{E}}^+(\omega)\} = \frac{1}{2\pi} \int_{-\infty}^{\infty} \tilde{\mathcal{E}}^+(\omega) e^{i\omega t} d\omega \quad (2.9)$$

and

$$\mathcal{E}^-(t) = \mathcal{F}^{-1}\{\tilde{\mathcal{E}}^-(\omega)\} = \frac{1}{2\pi} \int_{-\infty}^{\infty} \tilde{\mathcal{E}}^-(\omega) e^{i\omega t} d\omega . \quad (2.10)$$

These equations relate to an electric field

$$\mathcal{E}(t) = \mathcal{E}^+(t) + \mathcal{E}^-(t) \quad (2.11)$$

and its complex Fourier transform

$$\tilde{\mathcal{E}}(\omega) = \tilde{\mathcal{E}}^+(\omega) + \tilde{\mathcal{E}}^-(\omega) . \quad (2.12)$$

The positive complex electric field can be presented as a product of an amplitude function  $\mathcal{A}(t)$  and an additional phase term

$$\mathcal{E}^+(t) = \frac{1}{2} \mathcal{A}(t) e^{i[\omega_0 t + \tilde{\varphi}(t)]} , \quad (2.13)$$

with  $\tilde{\varphi}(t)$  the temporal phase and  $\omega_0$  the central angular frequency. The same can be derived for  $\mathcal{E}^-(t)$  due to the slowly varying envelope approximation [16]. The amplitude function is combined with the temporal phase and is called the complex field envelope:

$$\mathcal{E}_c(t) = \mathcal{A}(t) e^{i\tilde{\varphi}(t)} . \quad (2.14)$$



The instantaneous angular frequency  $\omega(t)$ :

$$\omega(t) = \frac{d\tilde{\varphi}(t)}{dt} + \omega_0 \quad (2.15)$$

is interpreted as the first derivative of the temporal phase of the laser pulse. If the angular frequency increases over time ( $d^2\tilde{\varphi}/dt^2 > 0$ ), then this is called up-chirp. The intensity of a laser pulse is given by:

$$I(t) = \varepsilon_0 c_0 n \frac{1}{T} \int_{t-T^*/2}^{t+T^*/2} \mathcal{E}^2(t') dt'$$

$$I(t) = 2\varepsilon_0 c_0 n |\mathcal{E}(t)|^2 = \frac{1}{2} \varepsilon_0 c_0 n |\mathcal{E}_c(t)|^2 = \frac{1}{2} \varepsilon_0 c_0 n \mathcal{E}_c(t) \mathcal{E}_c^*(t) \quad , \quad (2.16)$$

where  $\varepsilon_0$  is the dielectric constant in vacuum and  $c_0$  is the speed of light in vacuum. The (instantaneous) laser power in any material can be derived from the Poynting theorem of electrodynamics and is given by:

$$P(t) = \varepsilon_0 c_0 n \int_A d\mathcal{S} \frac{1}{T} \int_{t-T^*/2}^{t+T^*/2} \mathcal{E}^2(t') dt'$$

$$P(t) = \int_A d\mathcal{S} I(t) \quad , \quad (2.17)$$

where  $\int_A d\mathcal{S}$  is the integration over the laser beam cross section (area). The averaging is done over one optical period  $T^* = 2\pi/\omega_0$ . It is to be noted that in a realistic case the averaging time is much longer due to the response time of a detector. This is the fundamental reason why it is not possible to measure the instantaneous laser power of femtosecond pulses directly. The laser peak power  $P_{peak}$  is calculated as

$$P_{peak} = K_P \frac{E_p}{\tau_p} \quad , \quad (2.18)$$

from a measured laser energy  $E_p$

$$E_p = \int_{-\infty}^{\infty} P(t') dt' \quad , \quad (2.19)$$

with a pulse duration  $\tau_p$  at full width at half maximum (FWHM) and a scaling factor  $K_P$  by assuming a temporal and spatial shape, such as Gaussian for both ( $K_P = 2\sqrt{\ln 2/\pi} \approx 0.939$ ). The laser fluence  $F$  is defined as:

$$F = \int_{-\infty}^{\infty} I(t') dt' \quad . \quad (2.20)$$

Often parameters are used, which are dependent on the photon number, such as the photon density  $\phi(t)$ :

$$\phi(t) = \frac{I(t)}{h\nu_0 c_0} \quad , \quad (2.21)$$

where  $h\nu_0$  is the photon energy and  $\nu_0$  is the laser frequency, which can be given by the laser wavelength  $\lambda_0 = c_0/\nu_0$ .

By analogy, the complex electric field in the frequency domain can be presented as

$$\tilde{\mathcal{E}}^+(\omega) = |\tilde{\mathcal{E}}^+(\omega)| e^{-i\varphi(\omega)} \quad , \quad (2.22)$$

where  $|\tilde{\mathcal{E}}(\omega)|$  is the spectral amplitude and  $\varphi(\omega)$  the spectral phase.

The spectrum  $\tilde{I}(\omega)$  of a laser pulse can be measured with spectrometer. We can derive it from the energy conservation and Parseval's theorem to be [16]:

$$\tilde{I}(\omega) = \frac{\varepsilon_0 c_0 n}{4\pi} |\tilde{\mathcal{E}}(\omega)|^2 \quad . \quad (2.23)$$

Both representations in the temporal  $I(t)$  and spectral domain  $\tilde{I}(\omega)$  are equivalent.

Table 2.1 summarizes the temporal amplitude and intensity as well as the corresponding spectral amplitude and intensity for different pulse shapes (Gaussian, squared Hyperbolic Secant ( $\text{Sech}^2$ ) and rectangle). The pulse duration is given at FWHM. It is also possible to define the pulse duration at other intensity levels like  $1/e$  ( $\tau_{1/e}$ ) or  $1/e^2$  ( $\tau_{1/e^2}$ ). In the event of a rectangular pulse, all these representations yield in the same value and the duration  $\tau_p$  is identical at the different intensity levels. In the case of a Gaussian and  $\text{Sech}^2$  pulse shape, these durations are given as:

$$\text{Gaussian: } \tau_p = \sqrt{\ln 2} \cdot \tau_{1/e} = \sqrt{\frac{\ln 2}{2}} \cdot \tau_{1/e^2} \quad , \quad (2.24)$$

$$\text{Sech}^2: \tau_p = 0.812 \cdot \tau_{1/e} = 0.532 \cdot \tau_{1/e^2} \quad . \quad (2.25)$$

The dependence between the temporal and spectral intensity is given by the Fourier transform. In this case the relationship between pulse duration and spectral bandwidth  $\Delta\nu$  is given by the time bandwidth product (TBP):

$$\tau_p \cdot \Delta\nu \geq K_{TBP} \quad , \quad (2.26)$$

where  $K_{TBP}$  is a constant and depends on the given pulse shape, such as Gaussian ( $K_{TBP} \geq 2 \ln 2/\pi \approx 0.441$ ),  $\text{Sech}^2$  ( $K_{TBP} \geq 0.315$ ) or rectangle ( $K_{TBP} \geq 0.886$ ).

Important consequences are expressed in Equation (2.26) for the temporal properties of ultrashort laser pulses:

- To achieve ultrashort pulses, a broad spectrum is needed.
- The TBP for a pulse has a minimum (“Fourier transform-limited”), if the instantaneous angular frequency does not depend on time ( $\omega(t) = \text{const.}$ ). Therefore, the spectral phase has to be linear or constant. This is described in the next section.

Shape	Temporal amplitude	Temporal intensity
Gaussian	$\exp \left[ -2 \ln 2 \left( \frac{t}{\tau_p} \right)^2 \right]$	$\exp \left[ -4 \ln 2 \left( \frac{t}{\tau_p} \right)^2 \right]$
Sech <sup>2</sup>	$\operatorname{sech} \left[ 2 \ln (1 + \sqrt{2}) \frac{t}{\tau_p} \right]$	$\operatorname{sech}^2 \left[ 2 \ln (1 + \sqrt{2}) \frac{t}{\tau_p} \right]$
Rectangle	1 for $\left  \frac{t}{\tau_p} \right  \leq \frac{1}{2}$ , 0 else	1 for $\left  \frac{t}{\tau_p} \right  \leq \frac{1}{2}$ , 0 else
Spectral amplitude		Spectral intensity
Gaussian	$\sqrt{\frac{\pi}{2 \ln 2}} \tau_p \exp \left[ -\frac{\tau_p^2 (\omega - \omega_0)^2}{8 \ln 2} \right]$	$\frac{\pi}{2 \ln 2} \tau_p^2 \exp \left[ -\frac{\tau_p^2 (\omega - \omega_0)^2}{4 \ln 2} \right]$
Sech <sup>2</sup>	$\frac{\pi}{2 \ln(1+\sqrt{2})} \tau_p \operatorname{sech} \left[ \frac{\pi \tau_p (\omega - \omega_0)}{4 \ln(1+\sqrt{2})} \right]$	$\left( \frac{\pi}{2 \ln(1+\sqrt{2})} \tau_p \right)^2 \operatorname{sech}^2 \left[ \frac{\pi \tau_p (\omega - \omega_0)}{4 \ln(1+\sqrt{2})} \right]$
Rectangle	$\tau_p \operatorname{sinc} \left[ \frac{\tau_p (\omega - \omega_0)}{2} \right]$	$\tau_p^2 \operatorname{sinc}^2 \left[ \frac{\tau_p (\omega - \omega_0)}{2} \right]$

**Table 2.1:** The mathematical description of some pulse shapes in the time and frequency domain, according to [16].  $\tau_p$  and  $\omega_o$  are the pulse duration at FWHM and the center angular frequency, respectively.

### 2.1.2.1 Dispersion Management

The impact of optics on the spectral and temporal properties of ultrashort pulses is described by dispersion [17]. Dispersion directly impacts the spectral phase  $\varphi(\omega)$ . Consequently, in the following,  $\varphi(\omega)$  it is used to explain this influence.

For a slow variation of  $\varphi(\omega)$ , a Taylor expansion at the central angular frequency  $\omega_0$  can be performed.

$$\varphi(\omega) = \sum_{a=0}^{\infty} \frac{\varphi^{(a)}(\omega_0)}{a!} (\omega - \omega_0)^a \quad \text{with} \quad \varphi^{(a)}(\omega_0) = \left. \frac{d^a \varphi(\omega)}{d\omega^a} \right|_{\omega_0} \quad (2.27)$$

$$\varphi(\omega) = \varphi|_{\omega_0} + \varphi'|_{\omega_0} (\omega - \omega_0) + \frac{1}{2} \varphi''|_{\omega_0} (\omega - \omega_0)^2 + \frac{1}{6} \varphi'''|_{\omega_0} (\omega - \omega_0)^3 + \dots \quad (2.28)$$

Special attention should be given, that periodic functions with more than one period, cannot be described with Equation (2.28), if the order  $a$  is low. In this case phase modulation has to be solved analytically.

The first term of Equation (2.28) corresponds to the offset between the carrier angular frequency and the envelope of the electric field and is called carrier-envelope phase (CEO). The first derivation of  $\varphi(\omega)$  is the group delay (GD) and describes a time shift of the pulse in the temporal domain. The second derivation is the group delay dispersion (GDD). The third-order dispersion (TOD) and fourth-order dispersion (FOD) are  $\varphi'''|_{\omega_0}$  and  $\varphi''''|_{\omega_0}$ , respectively. If higher order phase terms are present, an influence on the temporal electric field structure is visible.

By analogy, the temporal phase  $\tilde{\varphi}(t)$  can also be expanded as a Taylor series at  $t = 0$ . GDD leads to a quadratic temporal phase and a linear chirp ( $\tilde{\varphi}''(t) = \text{const.}$ ). This is a

symmetric broadening of the laser pulse. For a Gaussian distribution, the resulting pulse duration  $\tau_{p,out}$  is given by [18]:

$$\tau_{p,out} = \sqrt{\tau_p^2 + \left(4 \ln 2 \frac{\varphi''}{\tau_p}\right)^2} . \quad (2.29)$$

A spectral phase term of TOD or higher results in an asymmetric temporal pulse shape [18] leading to pre- and post-pulses.

## Sources of Dispersion

CPA is based upon on the principle idea of manipulating the spectral phase in order to change the temporal behavior (i.e. stretcher, compressor). Subsequently, a device introducing a spectral dispersion ( $n(\omega)$ ), spatial delay ( $z(\omega)$ ) or a combination of both is needed to stretch the laser pulse before amplification. At the end an inverse dispersion is used to compress the pulse again. Typical sources for dispersion are optical transparent media, gratings, prism, GRISM<sup>a</sup> or chirped mirrors [19].

In a laser system the phase term can be assigned to the material (gain medium, windows, coatings, etc.)  $\varphi_m(\omega)$ , the stretcher  $\varphi_s(\omega)$  and the compressor  $\varphi_k(\omega)$ . At the end of the laser chain all spectral phases ideally cancel each other:

$$\varphi_m(\omega) + \varphi_s(\omega) + \varphi_k(\omega) = 0 . \quad (2.30)$$

## Material dispersion

For transparent, linear and absorption free materials with a length  $L$  and a refractive index  $n(\omega)$ , the spectral phase introduced by the material  $\varphi_m(\omega)$  can be described using the dispersion relation:

$$\varphi_m(\omega) = k(\omega) \cdot z = \frac{\omega}{c_0} \cdot n(\omega) \cdot z , \quad (2.31)$$

where  $n(\omega)$  is the angular frequency dependent refractive index of a material. This leads to a change of the spectral phase and thus potentially the pulse duration. Consequently, optical setups have a frequency depending optical path length  $z(\omega)$ . Now, Equation (2.22) can be rewritten by inserting Equation (2.31) to

$$\tilde{\mathcal{E}}^+(z_0 + L, \omega) = \tilde{\mathcal{E}}^+(z_0, \omega) \cdot e^{-i\varphi_m(\omega)} . \quad (2.32)$$

---

<sup>a</sup> GRISM is a combination of a GRating and a prISM.

Higher order phase terms, such as GDD and TOD, can be derived by using Equation (2.28):

$$GDD = \varphi_m'' = \frac{L}{c_0} \left( 2 \frac{dn}{d\omega} + \omega \frac{d^2n}{d\omega^2} \right) = \frac{\lambda^3 L}{2\pi c_0^2} \frac{d^2n}{d\lambda^2} \Big|_{\lambda_0} \quad (2.33)$$

$$TOD = \varphi_m''' = \frac{L}{c_0} \left( 3 \frac{d^2n}{d\omega^2} + \omega \frac{d^3n}{d\omega^3} \right) = -\frac{\lambda^4 L}{4\pi^2 c_0^3} \left( 3 \frac{d^2n}{d\lambda^2} + \lambda \frac{d^3n}{d\lambda^3} \right) \Big|_{\lambda_0} . \quad (2.34)$$

The dispersion parameters  $n(\lambda)$ ,  $dn/d\lambda$ ,  $d^2n/d\lambda^2$  and  $d^3n/d\lambda^3$  can be estimated using the Sellmeier equation. Commonly used materials such as most of the glasses (e.g. fused silica) and crystals (e.g. YAG, CaF<sub>2</sub>) in the visible and near-infrared show a positive GDD.

### Stretcher and Compressor Dispersion

In high-energy laser systems, reflective gratings are mostly used to stretch and compress the laser pulses.

The generation of dispersion relies on angular splitting and is given by the grating equation

$$\sin(\alpha_{in}) + \sin(\alpha_{out}) = \Lambda m \lambda \quad , \quad (2.35)$$

where  $\alpha_{in}$  and  $\alpha_{out}$  are the input and the output angle,  $m$  is the diffraction order and  $\Lambda$  the line density of the grating. A grating setup introduces a negative GDD [16]. For a pair of gratings, the first provides an angular dispersion and the second collimates the spectral components. This leads to a lateral displacement of the spectral components and can be removed in a double-pass configuration. This was presented by Treacy in 1969 [20] and is called ‘‘compressor’’. The principle optical setup is shown in Figure 2.3.

Here, the gratings  $G_1$  and  $G_2$  have a grating separation  $L_G$  perpendicular to the surface, the input angle  $\alpha_{in}$  and diffraction angle  $\alpha_{out}$  are given for the angular center frequency  $\omega_0$  and for slightly higher frequencies ( $\omega_0 + \Delta\omega$ , blue-shift) and lower values ( $\omega_0 - \Delta\omega$ , red-shift). The end mirror M is placed after the second grating for a double-pass configuration

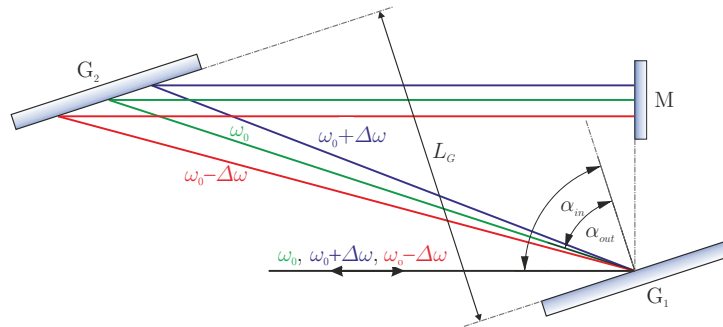


**Figure 2.3:** Principle optical setup of a Treacy compressor in a double-pass configuration by using a retro mirror M. The gratings  $G_1$  and  $G_2$  have a grating separation of  $L_G$ . The green line represent the diffracted center angular frequency and the red such as the blue illustrate the red and blue component of the laser pulse. The input angle  $\alpha_{in}$  is constant for all frequencies and the diffraction angle  $\alpha_{out}$  depends on the wavelength.

through the device. The angular frequency dependency of the spectral phase  $\varphi_k(\omega)$  after a double-pass through the compressor is

$$\varphi_k(\omega) = 2 \left( \frac{\omega}{c_0} L_G \frac{1 + \cos(\alpha_{in} - \alpha_{out}(\omega))}{\cos(\alpha_{out}(\omega))} - 2\pi m L_G \Lambda \tan(\alpha_{out}(\omega)) \right) . \quad (2.36)$$

In the first CPA system, by Strickland and Mourou, a fiber stretcher was used to introduce positive dispersion [11]. As this comprises of higher order phase terms, which could not be removed by the compressor, a non-transform-limited pulse was obtained. To overcome this limitation, an arrangement with a telescope between the two gratings was proposed by Martinez [21] and realized by Pessot [22].

In this configuration it is possible to produce zero, negative and positive dispersion. Figure 2.4 (a) shows a zero dispersion stretcher/compressor. The gratings  $G_1$  and  $G_2$  are in the focal plane of the lenses  $L$ . The distance between them is two times the focal length  $f$ . The Fourier plane FP is located in between, where the spectrum of the pulse can be measured directly. The end mirror  $M$  is placed for a double-pass through the system. In this case the optical path length is the same for all frequencies, if aberrations of the optical elements are neglected. For a stretcher with positive dispersion, as shown in Figure 2.4 (b), the gratings are shifted by  $\Delta x$  towards the lenses. A compressor can be realized by shifting the gratings away from the focal plane of the lenses, as shown in Figure 2.4 (c).

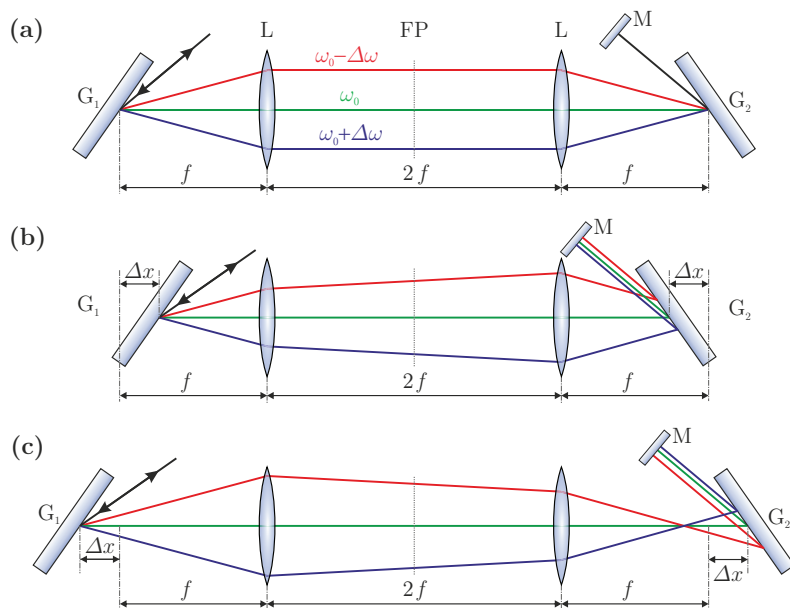


**Figure 2.4:** Illustration of a relay imaging setup for temporal laser pulse manipulation. The red and blue lines represent the red and blue spectral parts of the laser pulse. A double-pass configuration is realized with a retro mirror  $M$ . (a) zero dispersion stretcher/compressor, the gratings  $G_1$  and  $G_2$  are in the focal plane of the lenses  $L$  and the Fourier plane is located in between the lenses. (b) Stretcher with positive dispersion, the gratings  $G_1$  and  $G_2$  are shifted by  $\Delta x$  towards the lenses. (c) Compressor with negative dispersion, the gratings  $G_1$  and  $G_2$  are shifted by  $\Delta x$  away from focal plane of the lenses.

The spectral phase  $\varphi_s(\omega)$  for a double-pass configuration is given by

$$\begin{aligned} \varphi_s(\omega) = & 2 \frac{\omega}{c_0} \left[ r + 4f + 2 \Delta x \cos(\alpha_{in} - \alpha_{out}(\omega_0)) \right. \\ & \left. + \cos(\alpha_{out}(\omega_0)) \frac{1 + \cos(\alpha_{in} - \alpha_{out}(\omega))}{\cos(\alpha_{out}(\omega))} \right] \\ & - 8 \pi l m \Delta x \cos(\alpha_{out}(\omega_0)) \tan(\alpha_{out}(\omega)) \quad , \end{aligned} \quad (2.37)$$

where  $r$  is the optical path length of the center angular frequency from the second grating to the end mirror. With this setup it was possible to match the compressor phase to the stretcher phase. Higher order derivations of the phase can be determined by inserting Equations (2.36) and (2.37) into Equation (2.28). Due to the phase-conjugate behavior of the stretcher to the compressor, it is possible to implement an equivalent length  $L^*$ , which is:

$$L^* = \begin{cases} \frac{L_G}{\cos(\alpha_{out}(\omega))} & \text{for the compressor} \\ -2\Delta x(\omega) & \text{for the stretcher} \end{cases} . \quad (2.38)$$

With this the GDD and TOD can be derived as:

$$GDD = \varphi_{k,s}'' = -L^*(\omega) \frac{\lambda^3 l^2}{\pi c_0^2 \cos^2(\alpha_{out}(\omega))} \Big|_{\lambda_0} \quad (2.39)$$

$$TOD = \varphi_{k,s}''' = L^*(\omega) \frac{3 \lambda^4 l^2}{2 \pi^2 c_0^3 \cos^2(\alpha_{out}(\omega))} \left( 1 + \lambda l \frac{\sin(\alpha_{out}(\omega))}{\cos^2(\alpha_{out}(\omega))} \right) \Big|_{\lambda_0} , \quad (2.40)$$

with  $\lambda_0$  the center wavelength and  $\alpha_{out}(\omega_0)$  the diffraction angle at the frequency  $\omega_0$ .

In a realistic CPA system, it is mandatory to remove residual higher order spectral phase terms due to a non-compensated phase by using dispersion control devices like a *DAZZLER*<sup>™</sup> (by FASTLITE) [23] or a GRISM compressor [24, 25].

### 2.1.2.2 Nonlinear Effects

High-energy lasers are used to generate high optical intensity. This gives rise to a number of potential nonlinear optical effects. Nonlinear effects occur when the laser is propagating through a material (the components of the susceptibility tensor  $\chi$  are non-zero). The most important effects are:

- Frequency conversion (e.g. sum, difference, etc.) and parametric amplification occur from the second order susceptibility  $\chi^{(2)}$ .
- The optical Kerr effect increases the refractive index due to the third order susceptibility  $\chi^{(3)}$ . This directly relates to B-integral, self-focusing, small ripple growth, critical power, etc.
- Spontaneous and stimulated Raman and Brillouin scattering are the interaction of photons with phonons.

In the following, only the optical Kerr effect and related nonlinear effects are of main interest.

The refractive index can be expanded as a Taylor series at high electric fields

$$n(r,t) = n_0 + \gamma \langle \mathcal{E}^2 \rangle = n_0 + n_2 I(r,t) \quad , \quad (2.41)$$

where  $n_0$  is the linear refractive index, the intensity  $I(r,t)$  average over one period of the electric field  $\langle \mathcal{E}^2 \rangle$  in electrostatic units (esu),  $n_2$  and  $\gamma$  the nonlinear refractive index in SI units as well as esu units. The dependency between  $\gamma$  and  $n_2$  can be described with:

$$n_2 = \frac{4\pi}{c_0} \frac{\gamma [\text{esu}]}{[\text{m/s}]} \cdot 10^5 \text{ [cm}^2/\text{W}] \quad . \quad (2.42)$$

The Kerr effect appears in all optical materials and typically has a positive value. The phase difference between light transmitted through a material compared to vacuum is derived from Equation (2.31) in a general form to be:

$$\hat{\varphi}(r,t) = \frac{2\pi}{\lambda_0} \int_0^L n(r,t) dz \quad . \quad (2.43)$$

Here,  $\lambda_0$  is the wavelength in vacuum and  $L$  the length of the material. This can be rewritten with Equation (2.41) to be

$$\hat{\varphi}(r,t) = \frac{2\pi}{\lambda_0} n_0 L + \frac{2\pi}{\lambda_0} \int_0^L n_2 I(r,t) dz \quad . \quad (2.44)$$

The phase consists of a constant term and an intensity dependent term, which is referred to as the so-called B-integral [26, 27]

$$\mathcal{B}(r,t) = \frac{2\pi}{\lambda_0} \int_0^L n_2 I(r,t) dz \quad . \quad (2.45)$$

In analogy to the self phase modulation in the time domain a critical power can be approximated for a flat-top beam to [28]:

$$P_c \simeq \frac{\pi(0.61)^2 \lambda_0^2}{8 n_0 n_2} \quad . \quad (2.46)$$

If the laser power is considerably greater than the critical power, beam self-focusing after a certain distance takes place [29]. The corresponding nonlinear lens is called Kerr-lens [30]. One of the most prominent application is the mode-locking mechanism to build femtosecond laser oscillators [31, 32].

If the power is substantially larger than the critical power, small amplitude modulations in the beam profile grow faster than the average intensity of the whole beam. Hot spots in the laser beam profile are visible and can lead to damage of the optical elements (e.g lenses,



mirrors, gain material, etc.). The gain of spatial frequency  $\hat{f}$  with the highest growth rate is derived to [33]

$$G(\hat{f}) = \exp(\mathcal{B}) \quad . \quad (2.47)$$

In CPA laser systems the B-integral tends to result in the generation of additional prepulses by postpulses [34, 35] even when no spatial effects occur. Therefore the B-integral has to be checked carefully and has to be taken into account during the design phase.

## 2.2 Amplification of Ultrashort Laser Pulses

As the PENELOPE system is an  $\text{Yb}^{3+}$ -based diode-pumped solid state laser, the fundamental laser rate equations for a quasi-three-level lasers are developed in this section. Three- and four-level lasers can be described in a similar fashion. The laser emission wavelength of the  $\text{Yb}^{3+}$ -ions is close to  $1 \mu\text{m}$  and the lifetime of the upper state laser level is in the millisecond range. However, the given equations are only valid for a one-dimensional approach. For a three-dimensional case, this set of equations has to be adapted to describe a proper numerical model.

Several theoretical treatments of energy storage and extraction using quasi-three-level lasers have been published [36–39]. In a quasi-three-level laser, the transitions are between the lower  ${}^2\text{F}_{7/2}$  manifold and the upper  ${}^2\text{F}_{5/2}$  manifold. The term schema and typical energy levels for trivalent ytterbium-doped calcium fluoride ( $\text{Yb}^{3+}:\text{CaF}_2$ ) is given in Appendix A.1. The lower laser and pump levels are thermally close, which means they are considerably thermally populated (Boltzmann-distribution).

The doping density  $N_{dop}$  either in the lower or upper state of the  $\text{Yb}^{3+}$ -ions is given using

$$N_{dop} = N_{low} + N_{up} \quad , \quad (2.48)$$

where  $N_{low}$  and  $N_{up}$  are the population densities of the lower and upper manifold. The fraction of excited  $\text{Yb}^{3+}$ -ions is given by  $\beta = N_{up}/N_{dop}$ . The Boltzmann occupation factors are  $f_{low_p}$  and  $f_{up_p}$  for the pump and  $f_{low_l}$  and  $f_{up_l}$  laser level, respectively. The laser rate equation for the upper and lower population density and the photon transport equation can be described using

$$\begin{aligned} \frac{dN_{up}}{dt} = -\frac{dN_{low}}{dt} &= \sigma_p c \phi_p (f_{low_p} N_{low} - f_{up_p} N_{up}) - \frac{N_{up}}{\tau_f} \\ &\quad - \sigma_l c \phi_l (f_{up_l} N_{up} - f_{low_l} N_{low}) \\ &= \sigma_p c \phi_p \Delta N_p - \frac{N_{up}}{\tau_f} - \sigma_l c \phi_l \Delta N_l \end{aligned} \quad (2.49)$$

$$\frac{d\phi_k}{dz} + \frac{1}{c} \frac{d\phi_k}{dt} = \sigma_k \phi_k \Delta N_k \quad \text{with} \quad k = p, l \quad , \quad (2.50)$$

where  $\phi_k$  is the photon density (Equation (2.21)) for the pump and the laser,  $\sigma_k$  is the absorption ( $k = p$ ) and the emission ( $k = l$ ) cross section,  $c = c_0/n$  is the speed of light in

the medium,  $\tau_f$  the fluorescence lifetime,  $h$  Planck's constant and  $\nu$  the frequency of the photon.

The Equations (2.49) and (2.50) can be rewritten to

$$\frac{d\beta}{dt} = -g_0 \frac{I_p(z)}{h \nu N_{dop}} - \frac{\beta}{\tau_f} - g_0 \frac{I_l(z)}{h \nu N_{dop}} \quad (2.51)$$

$$\frac{dI_k}{dz} + \frac{1}{c} \frac{dI_k}{dt} = g_0 \cdot I_k(z) \quad \text{with } k = p, l \quad (2.52)$$

with

$$N_{up} = N \quad (2.53)$$

$$g_0(\lambda_k) = N_{dop} [\beta (\sigma_{em}(\lambda_k) + \sigma_{abs}(\lambda_k)) - \sigma_{abs}(\lambda_k)] = N_{dop} \sigma_g(\lambda_k) \quad (2.54)$$

$$\sigma_g(\lambda_k) = \beta \sigma_{em}(\lambda_k) - (1 - \beta) \sigma_{abs}(\lambda_k) \quad \text{with } k = p, l \quad , \quad (2.55)$$

where  $g_0(\lambda_k)$  is the small-signal gain (SSG) for the pump and laser and  $\sigma_a(\lambda_k)$  is the effective gain cross section.

Due to the quasi-three-level nature of ytterbium-doped materials, an equilibrium fraction of excited ions for pumping and extraction

$$\beta_k = \frac{\sigma_{abs}(\lambda_k)}{\sigma_{em}(\lambda_k) + \sigma_{abs}(\lambda_k)} \quad (2.56)$$

with  $k = p, l$  and  $\beta_p = \beta_{max}$   $\beta_l = \beta_{min}$

is required. A minimum inversion  $\beta_{min}$  is necessary to overcome the reabsorption. At an infinite pump power, a maximum inversion  $\beta_{max}$  is reached. Those are the limits for the excited state ions and depend on the pump and laser wavelength. In addition, a saturation intensity can be given by

$$I_{sat_k} = \frac{h \nu_k}{(\sigma_{em}(\lambda_k) + \sigma_{abs}(\lambda_k)) \tau_f} \quad \text{with } k = p, l \quad . \quad (2.57)$$

As a limit of Equation (2.49) no influence of amplified spontaneous emission (ASE) is taken into consideration, but a short overview of its principle effect is given in Section 2.2.3.

## 2.2.1 Pump Energy Storage

In a pulsed pumped nanosecond laser amplifier with a pump duration in the millisecond range, as it is normally done in ytterbium-doped lasers, the energy storage is decoupled from the laser amplification. This means, that during the pump process no energy extraction occurs ( $\phi_l = 0$ ). Thereby Equation (2.49) can be rewritten to

$$\frac{d\beta}{dt} = \frac{I_p(z)}{I_{sat_p} \tau_f} (\beta_{max} - \beta) - \frac{\beta}{\tau_f} \quad . \quad (2.58)$$

Here, it can be clearly seen that the fraction of excited ions are limited to  $\beta_{max}$ . In this case, the pump intensity has to be considerably larger than the saturation pump intensity. Therefore a low  $I_{sat_p}$  results in a high cross section at the pump wavelength.

The efficiency of an amplifier is an important characteristic and depends on the lifetime of the upper laser state. This is given in Chapter 4. The fluorescence efficiency can be derived from Equation (2.58) under the favorable assumption of non-saturated absorption ( $\beta \ll \beta_{max}$ ) and the normalized result to [27]

$$\eta_F = \frac{\tau_f}{\tau_p} \left[ 1 - \exp\left(-\frac{\tau_p}{\tau_f}\right) \right] . \quad (2.59)$$

On the other hand, the stored energy is proportional to  $\left[ 1 - \exp\left(-\frac{\tau_p}{\tau_f}\right) \right]$ . Equation (2.59) indicates, that the efficiency drops with increasing pump duration, but the stored energy is growing with  $\tau_p$ . Consequently, a short pump duration results in high efficiency, but therefore the stored energy is limited and can be only improved by increasing the pump intensity. If  $\tau_p$  equals to  $\tau_f$ , then  $\eta_F$  is 63 %. In this case 37 % for the absorbed pump energy is lost due to spontaneous emissions alone.

In Equation (2.50) the part  $\frac{1}{c} \frac{dI_k}{dt}$  is neglected as the pump pulse duration  $\tau_p$  is typically longer than the traveling time of a photon within the gain medium (i.e picosecond to nanosecond range) The absorption coefficient with saturation is

$$\alpha = -g_0 = \underbrace{\sigma_{abs}(\lambda_p)}_{\alpha_0} N_{dop} \underbrace{\left( 1 - \frac{\beta}{\beta_{max}} \right)}_{\text{saturation}} , \quad (2.60)$$

where  $\alpha_0$  is the linear absorption coefficient. Equation (2.50) can now be rewritten as

$$\frac{dI_p}{dz} = -\sigma_{abs}(\lambda_p) N_{dop} \left( 1 - \frac{\beta}{\beta_{max}} \right) I_p(z) . \quad (2.61)$$

The density of  $\text{Yb}^{3+}$ -ions is  $N_{dop} = N_0 \cdot c'_{dop}$ , where  $c'_{dop}$  is the doping concentration, typically given in [mol %], [wt %] or [at %], and  $N_0$  is the density of the replaced ions in the crystal lattice or the density of ions in the glass.

As shown in Section 3.3, laser diodes have a considerably broader emission spectrum compared to the absorption peak. For this reason, it is necessary to consider the pump spectrum. All equations before are given for the monochromatic case. Now we derive the laser rate equations and the photon transport equation for a polychromatic approach. The pump intensity is defined by

$$I_p(z) = \int_0^{\infty} \tilde{I}_p(\lambda, z) d\lambda , \quad (2.62)$$

where  $\tilde{I}_p(\lambda, z)$  is the spectral intensity distribution of the laser diode. The spatial-temporal differential Equations (2.58) and (2.61) modify to

$$\frac{d\beta(t, z)}{dt} = \int_0^{\infty} \left[ \sigma_{abs}(\lambda) - (\sigma_{abs}(\lambda) + \sigma_{em}(\lambda))\beta(t, z) \right] \frac{\tilde{I}_p(\lambda, z, t) \lambda}{h c} d\lambda - \frac{\beta(t, z)}{\tau_f} \quad (2.63)$$

$$\frac{d\tilde{I}_p(\lambda, z, t)}{dz} = N_{dop} \left[ (\sigma_{abs}(\lambda) + \sigma_{em}(\lambda))\beta(t, z) - \sigma_{abs}(\lambda) \right] \tilde{I}_p(\lambda, z, t) \quad . \quad (2.64)$$

After the determination of the fraction of the ions in the excited state the following equations need to be considered. The non-saturated total gain is defined as  $G = \exp(g_0 L)$ , where  $L$  is the gain material length. The average inversion, SSG and total gain  $\bar{G}$  of the gain material is given by

$$\bar{\beta}(\tau_p) = \frac{1}{L} \int_0^L \beta(\tau_p, z) dz \quad , \quad (2.65)$$

$$\bar{g}_0(\tau_p) = N_{dop} \bar{\sigma}_g(\lambda_l) = N_{dop} [\sigma_{em}(\lambda_l) \bar{\beta}(\tau_p) - (1 - \bar{\beta}(\tau_p))\sigma_{abs}(\lambda_l)] \quad , \quad (2.66)$$

$$\bar{G}(\tau_p) = \exp(\bar{g}_0(\tau_p) L) \quad . \quad (2.67)$$

For optimization of the pump storage efficiency two different options are available. First of all, the extractable energy

$$F_{Extr} = \frac{h c N_{dop}}{\lambda_l} \int_0^L (\beta(\tau_p, z) - \beta_{min}) dz \quad (2.68)$$

can be optimized via variation of the doping concentration times the length of the gain material ( $c'_{dop} \times L$ ) for a given pump duration  $\tau_p$ . On the other hand  $\bar{G}$  from Equation (2.67) can be maximized. Both cases result in the same optimum doping length. The extraction efficiency is given by

$$\eta_{Extr} = \frac{F_{Extr}}{I_p \tau_p} \quad . \quad (2.69)$$

## 2.2.2 Energy Extraction

This subsection covers the complementary case to the energy storage. During the energy extraction no pump radiation is present ( $\phi_p = 0$ ). Equations (2.49) and (2.50) lead to

$$\frac{d\beta}{dt} = -g_0 \frac{I_l(z)}{h \nu N_{dop}} - \frac{\beta}{\tau_f} \quad (2.70)$$

$$\frac{dI_l}{dz} + \frac{1}{c} \frac{dI_l}{dt} = g_0 \cdot I_l(z) \quad . \quad (2.71)$$

For nanosecond pulses  $\frac{1}{c} \frac{dI_l}{dt}$  can be neglected similar to the previous section and are only taken into account, if the pulse length is shorter than the traveling time of the pulse through the laser material (pico- to femtosecond pulse duration range). Furthermore, the fluorescence losses  $\frac{\beta}{\tau_f}$  can also be neglected as the amplification process timescale is in the nanosecond to sub-microsecond range, while the lifetime of the upper state is in the millisecond scale.

Using these simplifications and using Equations (2.54), (2.55) and (2.57), Equations (2.70) and (2.71) can be written as

$$\frac{d\beta}{dt} = -(\beta - \beta_{min}) \frac{I_l(z)}{I_{sat_l} \cdot \tau_f} \quad (2.72)$$

$$\frac{dI_l}{dz} = N_{dop} (\sigma_{em} + \sigma_{abs}) (\beta - \beta_{min}) \cdot I_l(z) \quad . \quad (2.73)$$

The laser rate equation and the photon transport equation can be solved numerically for the laser pulse amplification. For different starting conditions the numerical model has to be adapted. If chirped laser pulses are taken for the simulation, the laser pulse spectrum is stretched over the pulse in the temporal domain. Therefore, each spectral component arises at a different time step.

## 2.2.3 Amplified Spontaneous Emission

During the pumping process, spontaneously emitted photons travel through the gain medium and get amplified due to stimulated emission. This process is called ASE and is an inevitable effect of every laser. In the case of an ASE gain larger than the lasing threshold, parasitic oscillations occur. While parasitic oscillations can be avoided by proper laser engineering, ASE cannot. ASE can only be minimized.

ASE is a loss mechanism that reduces the stored energy. This can be taken into account in the laser rate equation by extending Equation (2.63) to [40]:

$$\frac{d\beta}{dt} = \left. \frac{d\beta}{dt} \right|_P - \left. \frac{d\beta}{dt} \right|_{SE} - \left. \frac{d\beta}{dt} \right|_{ASE} \quad , \quad (2.74)$$

where the first term  $d\beta/dt|_P$  is the increasing inversion caused by the pump light, the second  $d\beta/dt|_{SE}$  is the depopulation due to the spontaneous emissions and the third part  $d\beta/dt|_{ASE}$  is the impact as a consequence of ASE.

The first two parts in Equation (2.74) are described in Section 2.2.1. The ASE part can be written in a similar fashion as the pump term [40]:

$$\left. \frac{d\beta}{dt} \right|_{ASE} = \frac{1}{N_{dop}} \int_{\lambda} g_0 \phi_{ASE}(\lambda, \vec{r}_0) d\lambda \quad (2.75)$$

with  $\phi_{ASE}(\lambda, \vec{r}_0)$  the ASE photon density and  $\vec{r}_0$  the position in the gain material. The ASE photon density depends on pump conditions like gain material size, pumped volume, pump duration etc. A detail derivation of the  $\phi_{ASE}(\lambda, \vec{r}_0)$  can be found in [40, 41].

Additionally, ASE can be interpreted as an equivalent reduction of the upper state laser lifetime. SE is amplified and depopulates the upper state laser level. For this reason the lifetime modifier  $M_{ASE}$  can be introduced [40, 41] and Equation (2.74) can be written as

$$\frac{d\beta}{dt} = \left. \frac{d\beta}{dt} \right|_P - \left. \frac{d\beta}{dt} \right|_{SE} \cdot M_{ASE} \quad . \quad (2.76)$$

However, it is important to note, that this is not a parameter for calculations. It can be an indicator, if ASE needs to be investigated in more detail or not. A more general behavior can also be found in [41], where  $\phi_{ASE}$  is proportional to the energetic gain of the ASE  $\phi_{ASE} \propto \exp(g_0 L_{Char})$ .  $L_{Char}$  is the characteristic length in the pumped volume and in the simplest case the largest dimension. If total internal reflection and reflections from the gain media boundaries are taken into account, this length can be dramatically increased. In principle, it can be seen that the losses due to ASE grow exponentially with  $L_{Char}$  or  $\beta$ . For laser amplifier scaling it is necessary to keep  $g_0 L_{Char}$  constant to preserve similar energy storage performance.

## 2.2.4 Efficiency Considerations

The most important parameter for high-energy or high-average-power laser systems is the electrical-to-optical efficiency  $\eta_{e-o}$ . It is a product of several efficiencies  $\eta_i$

$$\eta_{e-o} = \prod_i \eta_i \quad . \quad (2.77)$$

More common is the optical-to-optical efficiency  $\eta_{o-o}$  of a laser amplifier, which does not include the generation and transportation of the pump energy.

The optical-to-optical efficiency is defined by

$$\eta_{o-o} = \frac{E_{out} - E_{in}}{E_{pump}} \quad , \quad (2.78)$$

where  $E_{out}$ ,  $E_{in}$  and  $E_{pump}$  is the output, input and pump energy of the laser amplifier. These parameters can be measured directly with an appropriate sensor (e.g. pyroelectric).

The energy flow is shown in Figure 2.5. The starting point is the pump source efficiency  $\eta_{PS}$  and contains the driver and the laser diode efficiency. Typically, laser diode drivers have an efficiency of about 80 % and diodes of about 60 %, respectively. The light has to

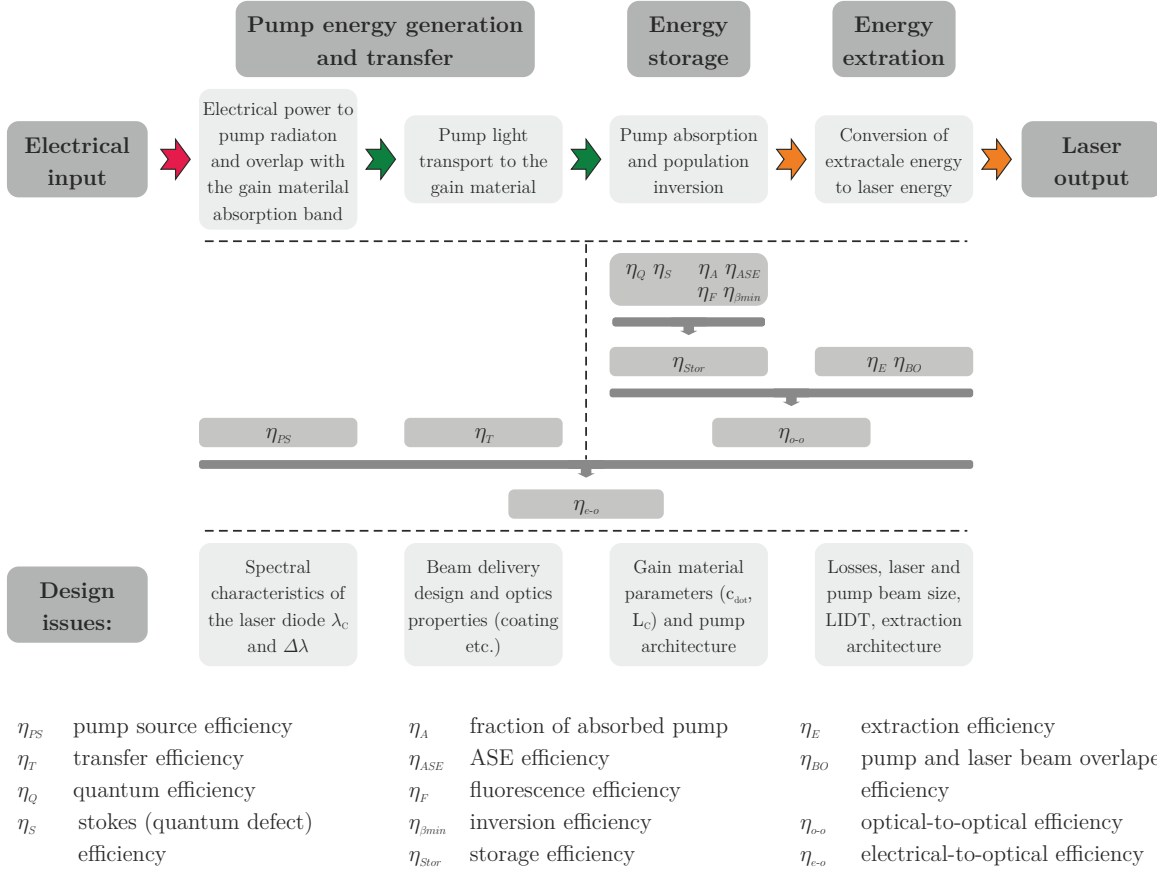


**Figure 2.5:** Energy flow in a solid state laser amplifier, the efficiency parameters and the corresponding design issues.

be transported to the gain material and is represented by the transfer efficiency  $\eta_T$ . This should be as high as possible to preserve the high energy generation efficiency.

The optical efficiency includes a lot of different parameters and can be split into two contributions. The first is the energy storage and the second is the energy extraction. Some of the parameters can be optimized due to design issues while others are fixed. For example, the stokes efficiency  $\eta_S$ , which describes the quantum defect with  $\eta_S = \lambda_p/\lambda_l$  and the quantum efficiency  $\eta_Q$ , which comprises of losses due to non-radiative and parasitic transitions are invariable.

To increase the efficiency of a laser amplifier, the following parameters have to be optimized to get the best conversion from pump to laser energy. The fraction of absorbed pump radiation  $\eta_A$  has to be optimized using a numerical model based on the laser rate equations described in the previous section. The fluorescence efficiency  $\eta_F$  is a result of the fluorescence lifetime and the pump duration.

In a quasi-three-level laser a minimum inversion is needed to overcome the reabsorption and therefore the inversion efficiency  $\eta_{\beta_{min}}$  stand for the non-extractable energy.

The last loss term is ASE, which reduces the absorbed energy and is represented by the ASE efficiency  $\eta_{ASE}$ . All parameters for energy extraction together stands for storage efficiency  $\eta_{Stor}$ . A typical  $\eta_{Stor}$  value for a  $\text{Yb}^{3+}:\text{YAG}$  thick disk amplifier like the Lucia system is in the order of 30% [40].

Finally, the extraction of energy is represented by the pump and laser beam overlap efficiency  $\eta_{BO}$  as well as the extraction efficiency  $\eta_E$ , which includes the number of extraction passes as well as the damage fluence etc. The energy storage and extraction is combined to the optical-to-optical efficiency  $\eta_{o-o}$ .

When high-power lasers are operated at cryogenic or low temperatures, the cooling power becomes relevant. For system efficiency  $\eta_{sys}$  the cooling has to be taken into account (not shown in Figure 2.5) and is determined as

$$\frac{1}{\eta_{Sys}} = \frac{1}{\eta_{e-o}} + \frac{1}{\eta_{Cool}} \quad , \quad (2.79)$$

where  $\eta_{Cool}$  is the cooling system efficiency with  $E_{out}/E_{cool}$ . Here,  $E_{out}$  is the laser output energy.

As a lower bound for the required cooling power (or energy) a Carnot process with a Carnot efficiency  $\eta_c$  is taken into consideration

$$\eta_c = \frac{E_{cool}}{E_{heat}} \quad , \quad (2.80)$$

where  $E_{heat}$  is the generated heat. We then have to find a dependence of the Carnot efficiency  $\eta_c$  in Equation (2.79). Next, the expression of  $E_{out}$  is a fraction of stored energy  $E_{sto}$  which is extracted

$$E_{out} = \eta_{extr} E_{sto} \quad . \quad (2.81)$$

The specific thermal load  $\eta_h$  can be determined by

$$\eta_h = \frac{E_{heat}}{E_{sto}} \quad (2.82)$$

and is a constant as well as independent from pumping power and laser material temperature. Now, we can rewrite  $\eta_{cool}$  by using Equations (2.80) to (2.82) to

$$\eta_{cool} = \frac{\eta_{Extr}}{\eta_h \eta_c} \quad . \quad (2.83)$$

This is used to derive system efficiency as

$$\eta_{Sys} = \frac{\eta_{e-o}}{1 + \frac{\eta_h \eta_{e-o}}{\eta_{Extr}} \cdot \eta_c} \quad . \quad (2.84)$$

We now need the temperature dependence of the Carnot cycle. As per the Second Law of Thermodynamics, a minimum required energy  $E_{cool}$  is needed to get an amount of energy  $E_{heat}$  from the cold body at a cold temperature  $T_c$  to a higher temperature  $T_a$ . This is the ideal Carnot cycle and the ratio of energies is given by

$$\left. \frac{E_{cool}}{E_{heat}} \right|_{min} = \frac{T_a - T_c}{T_c} \quad . \quad (2.85)$$

Indeed, the ideal case cannot be achieved in practice.



## 2.3 Diagnostics for Ultrashort Laser Pulses

In order to use ultrashort high-intensity laser pulses in experiments it is essential to determine sophisticated the pulse duration, spectral behavior and its TIC. Pulse diagnostics are consequently needed for construction and operation of a CPA laser system.

Knowledge of the spectral intensity and the spectral phase is sufficient to retrieve the complete temporal information of a laser pulse. A series of methods have been developed over recent decades. The most common techniques for the pulse duration estimation are the second harmonic autocorrelation as well as spectral interferometry.

Additionally, the repetition rate of a high-energy laser system is in the range of several hertz. Preferentially, the method should be based on a single shot mode. However, in order to access information of the TIC over a large dynamic range ( $>10$  dB) multiple shots are necessary. This holds especially true for scanning methods, measuring online characteristics is particularly difficult.

The following list is an overview of typically used pulse characterization methods for the PENELOPE system:

- Optical autocorrelation
  - Second-order autocorrelation
  - Third-order autocorrelation
- Spectral Phase Interferometry for Direct Electric-field Reconstruction (*SPIDER*) and
- Self-Referenced Spectral Interferometry (SRSI), especially the *WIZZLER*<sup>™</sup> by FASTLITE.

Electronic devices for example a photodiode are limited to the nanosecond or picosecond range (important for prepulse contrast measurement).

### 2.3.1 Optical Autocorrelation

#### Second-order autocorrelation

The schematic experimental setups for collinear and non-collinear autocorrelation are shown in Figure 2.6 (a) and (b). As in the collinear case both beams overlap, the measured signal cannot be easily distinguished from the background.

For autocorrelations, the result is a function of the time delay  $\Delta\tau$  between two replicas. One of the most important collinear methods is the so-called interferometric autocorrelation (iAC), shown in Figure 2.6 (a). The intensity of the interferometric autocorrelation function  $I_{iAC}(\Delta\tau)$  is derived to [13, 16, 42]

$$I_{iAC}(\Delta\tau) = \int_{-\infty}^{+\infty} |\{\mathcal{E}(t) + \mathcal{E}(t - \Delta\tau)\}|^2 dt \quad , \quad (2.86)$$

where  $\mathcal{E}(t)$  is the electric field from Equation (2.11). The iAC has an oscillating term resulting in a fringed signal.

M	plane mirror AoI = 0°/45°	L	lens	$\Delta\tau$	delay	$\Delta x$	distance on the CCD
BS	beam splitter	NLC	non-linear crystal	$\varpi$	overlapping angle		

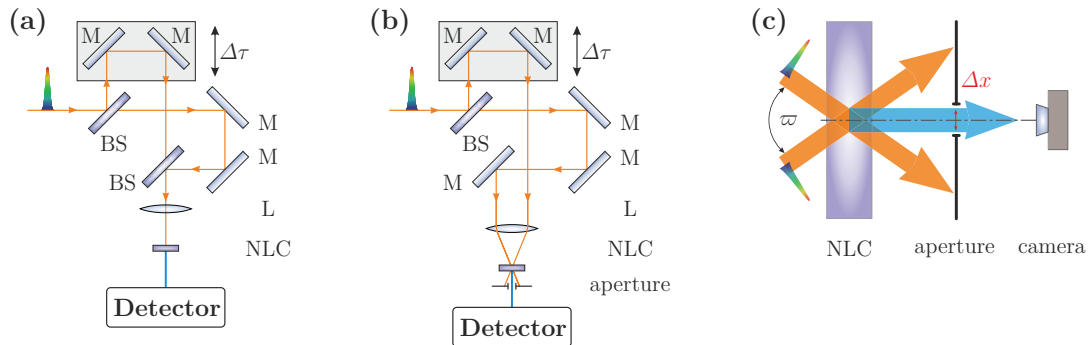


**Figure 2.6:** The schematic experimental setup for (a) collinear, (b) non-collinear time-delayed second-order autocorrelation and (c) non-collinear single-shot second-order autocorrelation.

In the non-collinear case the measured signal is background free and the principle configuration is shown in Figure 2.6 (b). The intensity of the autocorrelation function  $I_{AC}(\Delta\tau)$  depends on the pulse overlap and is derived to

$$I_{AC}(\Delta\tau) \propto \int I(t) \cdot I(t - \Delta\tau) dt \quad , \quad (2.87)$$

where  $I(t)$  is the intensity of the laser pulse and  $\Delta\tau$  is the delay of both pulses to each other.

For a low repetition rate amplifier the incremented delay has to be transformed into a geometrical arrangement. Therefore a spatial intensity distribution is measured with a CCD camera. The schematic setup is presented in Figure 2.6 (c). The overlapping angle  $\varpi$  and the distance  $\Delta x$  on the CCD is transformed into a delay. The delay  $\Delta\tau$  is given by [42]

$$\Delta\tau = \frac{n \Delta x \sin(\varpi / 2)}{c_0} \quad , \quad (2.88)$$

where  $c_0$  is the speed of light in vacuum.

Due to correlation of the laser pulse the reconstruction of the duration depends on the temporal shape. The correlation factor  $K_{AC}$  of a Gaussian laser pulse is  $K_{AC} = \tau_p / \tau_{AC} = 0.707$  and  $0.643$  for a Sech<sup>2</sup> [13, 16, 42].

Any phase information about the laser pulse is lost in the measurement. Thus the pulse duration is assumed to be Fourier transform-limited. This has to be verified with the measured spectrum and the time bandwidth product of the expected pulse distribution (see Equation (2.26) on page 10).

Note, that the intensity and interferometric autocorrelation are symmetric. For this reason, one cannot distinguish between pre- and post-pulses in the second order case.

### Third-order autocorrelation

The third-order autocorrelation gives an indication of the time-depending intensity of an ultrashort laser pulse. The measured signal is not symmetric and thus the pre- and post-pulses can be distinguished.

The principle experimental idea is shown in Figure 2.7. The input pulse is split into two replicas. The first is used to generate a second-harmonic signal. The second replica is time-delayed to the other and non-collinear overlapped in a non-linear crystal to generate the third-harmonic of the fundamental wavelength. This signal is analyzed with a detector. The third-harmonic generation is realized in a non-collinear case as the background free measurement is essential to get satisfying results.

The intensity signal is given by [43, 44]

$$I_{TAC}(\Delta\tau) \propto \int I^2(t) \cdot I(t - \Delta\tau) dt \quad . \quad (2.89)$$

The type of detector is important to achieve a high-dynamic range. Typically, a photomultiplier tube is used in combination with a set of neutral density filters. A dynamic range of more than 10 orders of magnitude is available. In our case, the device is a so-called “*SEQUOIA*” by Amplitude Technologies.

M	plane mirror	SHG	second-harmonic generation	$\Delta\tau$	delay
BS	beam splitter	THG	third-harmonic generation		

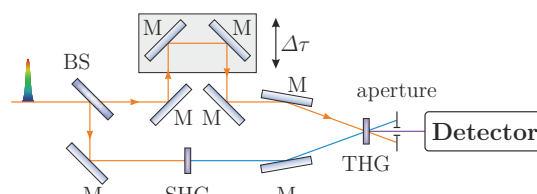


**Figure 2.7:** Schematic setup of a third-order autocorrelation.

### 2.3.2 SPIDER - Spectral Phase Interferometry for Direct Electric-field Reconstruction

The basis for this instrument is the spectral interferometry technique. An interferogram is produced by two delayed pulses. This approach has a limited range of confidence as a reference pulse is needed [42].

This technique has been improved and the acronym *SPIDER* describes the setup given in Figure 2.8. The laser pulse is split into two replicas. The first replica is split again into two time-delayed pulses either by a thin plate (eg. etalon) or a Michelson interferometer with a time-delay  $\Delta\tau$ . The second one is temporally stretched using a grating based stretcher or a glass block. The two time-delayed pulses are mixed with different parts of the stretched

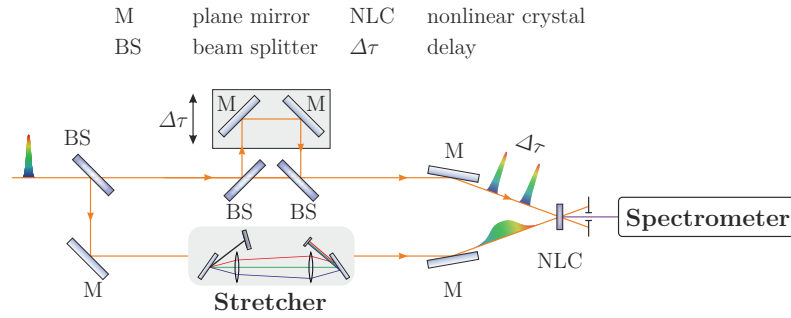


**Figure 2.8:** Schematic of the *SPIDER* apparatus.

pulse. The spectral shear is identical for both pulses. The signal is measured with a spectrometer and the intensity of the *SPIDER* signal  $\tilde{I}_{SPIDER}(\omega)$  is given by [13, 16, 42]

$$\begin{aligned} \tilde{I}_{SPIDER}(\omega) = & \tilde{I}(\omega) + \tilde{I}(\omega + \Omega) \\ & + 2\sqrt{\tilde{I}(\omega)\tilde{I}(\omega + \Omega)} \times \cos[\varphi(\omega + \Omega) - \varphi(\omega) + \omega \Delta\tau] \quad , \end{aligned} \quad (2.90)$$

where  $\Omega$  is the spectral shear. The interference fringes are analyzed with a standard Fourier analysis and provide the spectral amplitude and phase of the laser pulse. This method is a single-shot measurement and enables one to optimize the spectral phase of an amplified laser pulse [45, 46].

The measurement range of the *SPIDER* device depends on three parameters: delay, spectral shear and the group-delay dispersion  $GDD_{up}$  of the linearly stretched pulse. The relation is derived to

$$\Omega = \frac{\Delta\tau}{GDD_{up}} \quad . \quad (2.91)$$

A detailed description can be found in [47].

### 2.3.3 WIZZLER - Self-Referenced Spectral Interferometry

This method was invented by FASTLITE. The Self-Referenced Spectral Interferometry (SRSI) was published by T. Oksenhendler et. al in 2010 [48].

The principle setup is given in Figure 2.9. A weak replica pulse is created with a perpendicular polarization and a time-delay  $\Delta\tau$  to the main pulse using a calcite plate. The reference pulse is generated via cross polarized wave generation (XPW) and has a perpendicular polarization to the main pulse [49, 50]. This pulse has a flat spectral phase and a broad spectrum, being broader than the original. Both generated pulses are separated and sent to a spectrometer. The spectrometer measures the spectral interferogram  $\tilde{I}_{SRSI}(\omega)$ , which can be described using

$$\tilde{I}_{SRSI}(\omega) = |\tilde{\mathcal{E}}_{ref}(\omega) + \tilde{\mathcal{E}}(\omega) \exp[i\omega \Delta\tau]|^2 \quad , \quad (2.92)$$

where  $\tilde{\mathcal{E}}_{ref}$  is the electric field of the reference pulse. The spectral amplitude and phase is calculated using the Fourier-Transform Spectral Interferometry (FTSI) [51].

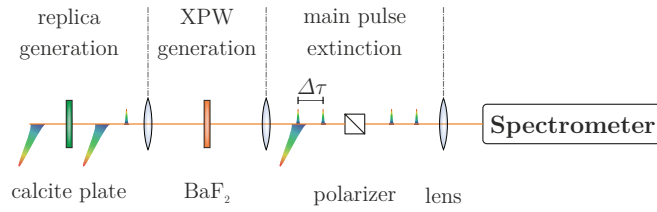


**Figure 2.9:** Schematic of the *WIZZLER* apparatus.

The collinear setup is easy to align and to operate. It is a calibration free method, which leads to reproducible and user-independent results. Additionally, SRSI provides the highest temporal dynamic range of a standard pulse duration measurement device with up to 8 orders of magnitude [52, 53].



## CHAPTER 3

---

# The PENELOPE Laser System

---

In this chapter, the Petawatt, Energy-Efficient Laser for Optical Plasma Experiments (PENELOPE) laser system is discussed. At the beginning an overview of ultrashort high-energy laser systems around the world is presented.

A short description of the laser system is given including all its important sections. Furthermore the amplifier architecture is discussed. The beam shaping and relay imaging setups for the telescopes and amplifiers are analyzed, respectively. Experimental settings are illustrated and the performance is optimized with a ray tracing software. The stretcher and compressor setups are shown in more detail and the estimated performance is discussed.

An overview of laser diodes as a pump source for high-energy amplifiers is given, which includes the design criteria for beam delivery and homogenization. The pump modules for the final amplifier stage are characterized and an experimental benchmark of a beam delivery system for the final multipass amplifier is presented.

### 3.1 Overview of High-Energy Laser Systems

The fundamental laser technology of femtosecond optical pulse amplification in broadband solid state laser materials and (or) nonlinear crystals is chirped pulse amplification (CPA). The starting point was the experimental proof in 1985 by D. Strickland et al. [11]. The first Petawatt laser system based on this concept was realized at the Lawrence Livermore National Laboratory in 1996 [54]. Numerous high-peak-power high energy laser systems have been designed and built consecutively, like Vulcan at the STFC or the PHELIX (Petawatt High-Energy Laser for Heavy Ion EXperiments) laser at the GSI Darmstadt.

The number of TW and PW laser systems around the world are strongly increased, which is culminating in large laser facilities like the ELI. In this context, it is illustrative to concentrate on the global distribution of high-power laser systems beyond 10 TW peak power, as well its evolution over the last several years.

Figure 3.1 shows the International Committee on Ultrahigh Intensity Lasers (ICUIL) world map of 2009 from C. P. J. Barty [1, 55]. Labels represent the establishments for the high-power laser systems or facilities. The upper part shows, that high power lasers are predominantly located in three global regions: North America, Europe and Asia.

The current status is illustrated in the lower part of Figure 3.1 and was taken from [1, 56]. All operating and proposed facilities are given. The increase of density of facilities

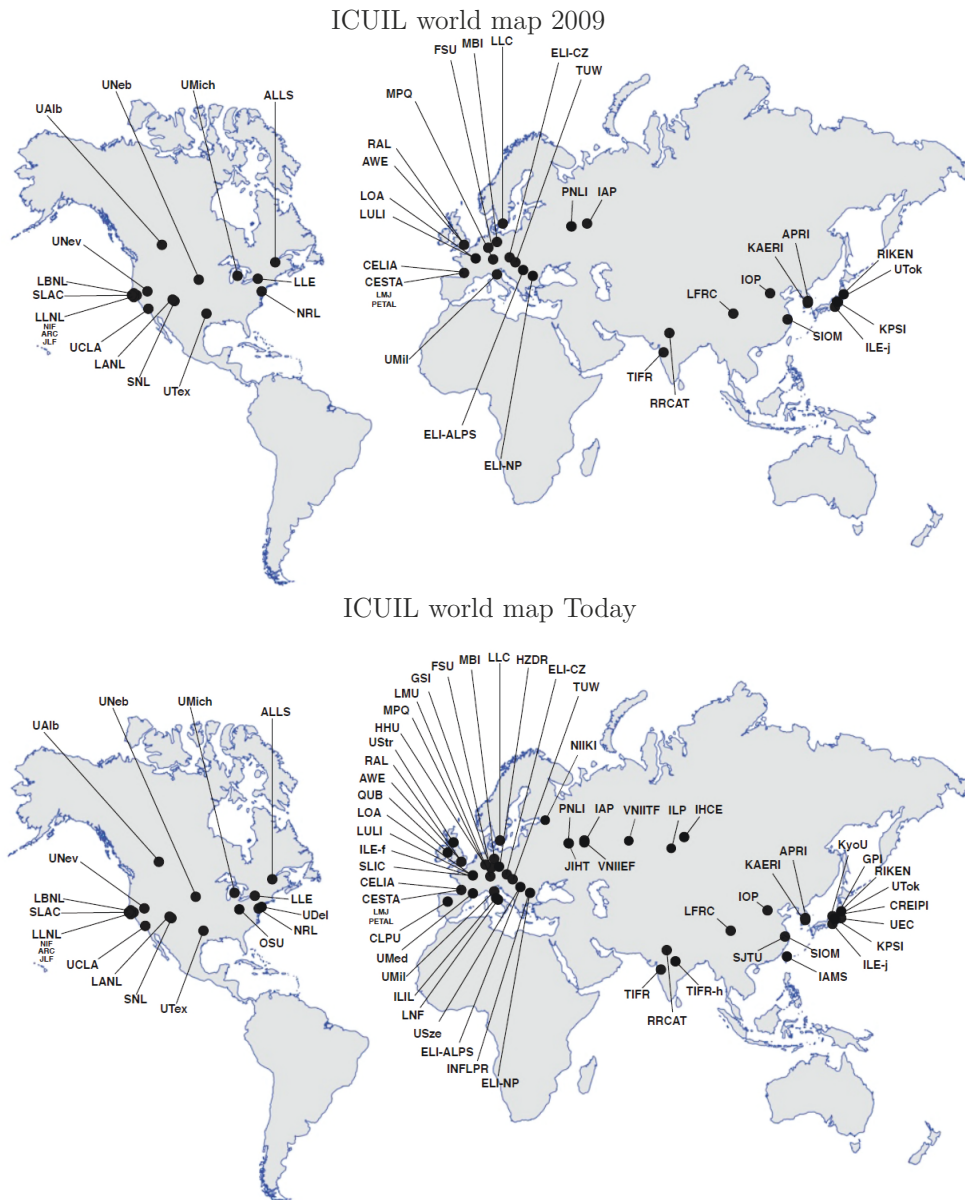


**Figure 3.1:** ICUIL world map of ultrahigh intensity laser capabilities of 2009 (upper) and today (lower). The map was established by C. P. J. Barty from the Lawrence Livermore Laboratory and can be found on the ICUIL website (<http://www.icuil.org/events-a-activities/laser-labs.html>).

located in Europe is obvious. The total power of all systems in 2009 was above 10 PW [1]. By the end of 2017 the total power will be more than 100 PW [1]. This does not include the planned Exawatt facilities. Most of the ultrashort pulse laser systems are based on  $\text{Ti}^{3+}$ :sapphire or  $\text{Nd}^{3+}$ :glass. Those systems are typically directly or indirectly pumped by flashlamps. Only a very small part of the facilities are direct diode-pumped lasers.

Around the world a limited number of High-Energy-Class Diode-Pumped Solid-State Lasers (HEC-DPSSL) are currently under construction or have been built. Most of them are located in the USA, Europe and Japan. They can be split into two groups related to their application and pulse duration. The first group consists of nanosecond laser systems



mainly dedicated to inertial fusion energy (IFE) or acts as a pump for CPA laser amplifiers, while the second group are direct CPA lasers on their own.

In the following the most important systems are listed, which are operating around 1  $\mu\text{m}$  of wavelength.

**Mercury, US** The first 100 J-class DPSSL system, partially completed in 2007 demonstrated an output energy of 62 J at 10 Hz for ns-pulses [57, 58]. This is the record energy for a HEC-DPSSL at the moment. The system was based on a relay imaging four pass extraction setup. The amplifier consisted of two heads with seven thin slabs and was cooled by using a He-gas flow. The gain medium was  $\text{Yb}^{3+}$ :S-FAP.

This system was also planned to be used for pumping a titanium sapphire laser [59]. Currently a follow-up project, HAPLS (High Average Power Laser System) [60], is under construction based on Mercury technology. A 1 PW  $\text{Ti}^{3+}$ :Sa laser is pumped by a He-gas cooled, diode-pumped a  $\text{Nd}^{3+}$ -glass laser. The aim of the pump source is 200 J at 10 Hz at fundamental wavelength. The laser is planned to be installed at the ELI facility at Prague in 2017.

**Polaris, GER** Petawatt Optical Laser Amplifier for Radiation Intensive experiments The gain material is  $\text{Yb}^{3+}$ :FP-glass as well as  $\text{Yb}^{3+}$ : $\text{CaF}_2$  for the amplification of 150 fs long pulses aiming at energies up to 150 J. Due to the rod type amplifier architecture, the repetition rate of 0.025 Hz is low compared to the other projects, typically operating from 1 Hz to 10 Hz. At the present time, pulse energies up to 54.2 J without compression as well as 16.7 J with a pulse duration of 98 fs have been demonstrated [61]. This leads to a peak power of 170 TW.

**PFS, GER** The Petawatt Field Synthesizer (PFS) is an OPCPA laser system with target parameters of 3 J with few-cycle laser pulses ( $\sim 5$  fs) at a repetition rate of 10 Hz. The pump source is a CPA based  $\text{Yb}^{3+}$ :YAG laser with a foreseen energy up to 12 J with a total number of four pump beams [62]. The pulse duration is close to 1 ps. The synchronization is achieved by using a pickup of oscillator at 1030 nm. Currently 1 TW (1 ps, 1 J) has been shown on the pump laser part with an active-mirror architecture [63]. The last amplifier stage is currently under development.

**DiPOLE, UK** The Diode Pumped Optical Laser for Experiments (DiPOLE) project aims to develop a scalable, efficient nanosecond high pulse energy diode pumped laser amplifier system based on cryogenic gas cooled, multi-slab, ceramic  $\text{Yb}^{3+}$ :YAG technology [64]. This system is based on the Mercury laser technology. The main differences cover the gain material and the operation temperature. Currently, an energy of 105 J at 10 Hz repetition rate has been shown with an optical-to-optical efficiency of 22.5% [65]. A design study for a 1 kJ laser was presented in [66].

**HiLASE, CZ** The main goal of the Czech R&D project HiLASE (High average power pulsed laser) is to bring new laser technologies to industrial applications [67]. The project is focused on diode-pumped solid-state laser systems and two technological concepts for DPSSLs are explored within HiLASE. One is thin-disk technology, trying to scale the pulse energies up to 1 J and an average power in the  $\sim$  kW level [67]. The other is a 100 J-class multi-slab amplifier, based on the DiPOLE technology. At the moment theoretical studies

of the cryogenic cooled multi-slab lasers are the main focus [68, 69].

**Lucia, FR** The Lucia laser project aimed at 1 kW average power with 10 ns long pulses with an energy of 100 J at 10 Hz repetition. It is based on an  $\text{Yb}^{3+}$ :YAG active-mirror architecture. So far, an 8 ns pulse is amplified in three stages to an energy of 14 J at 2 Hz [70].

**GENBU, JP** The Generation of ENergetic Beam Ultimate (GENBU) laser is a CPA laser system with two optically synchronized laser beams [71]. One laser beam will be assigned to operate at cryogenic temperatures using  $\text{Yb}^{3+}$ :YAG. The target parameters are 1 kJ pulse energy, 10 ps to 100 ps pulse duration and a repetition rate of up to 100 Hz. A portion of this beam will be used as a pump laser for an OPCPA laser line. The current development rests at the first amplifier stage of the laser system demonstrating 1 J with a repetition rate of 10 Hz [72].

## 3.2 System Overview and Description

Figure 3.2 illustrates the schematic overview of the PENELOPE laser. It is configured as a fully diode-pumped solid state CPA laser system. Ultrashort laser pulses are generated in a commercial  $\text{Yb}^{3+}$ :KGW oscillator giving a pulse energy of 20 nJ and a pulse duration of 60 fs at a center wavelength of 1035 nm. The repetition rate is 78 MHz, being a multiple of the Electron Linac for beams with high Brilliance and low Emittance (ELBE) accelerator. Consequently both can be synchronized in order to perform coupled experiments.

The laser pulses are stretched before amplification using a stretcher to about 3 ns (FWHM) with a spectral hard clip of 50 nm in order to achieve a good pulse contrast. The compressor is using highly efficient multilayer dielectric reflection gratings to compress the pulses at the end of the amplification chain. The throughput is estimated to be more than 80%. The stretcher-compressor setup is explained in Section 3.2.3 in more detail.

Furthermore, an acousto-optic programmable dispersive filter (AOPDF or *DAZZLER*<sup>TM</sup> by FASTLITE) is placed after the stretcher to compensate for higher order dispersion due to uncompensated material dispersion, wavefront aberrations of the stretcher/compressor or stretcher compressor mismatch.

The amplifier-chain starts with two regenerative amplifiers with active or passive spectral gain control in order to preserve a bandwidth of more than 20 nm after amplification. An acousto-optic programmable gain control filter (AOPGCF) is placed into the cavity of the first regenerative amplifier to optimize for spectral losses (i.e. to flatten the spectral gain curve). It consists of a Brewster-cut crystal with a damage threshold of about 30 mJ/cm<sup>2</sup> at 1 ns pulses. The available output energy is limited to be less than 1 mJ. The passive gain control is performed using a birefringent quartz implemented in the cavity as well as before the multipass amplifiers (MPA). This topic is investigated in more detail in Chapter 5.

The multipass amplifier chain is based on a hybrid active-mirror/multi-slab architecture. The regenerative and the first multipass amplifiers are based on a single active-mirror, which is usable for high-repetition rates up to 10 Hz and energies of several hundred mJ. Therefore for energies above 1 J, a multi-slab amplifier is required. The hybrid architecture is discussed in more detail in Section 3.2.1.

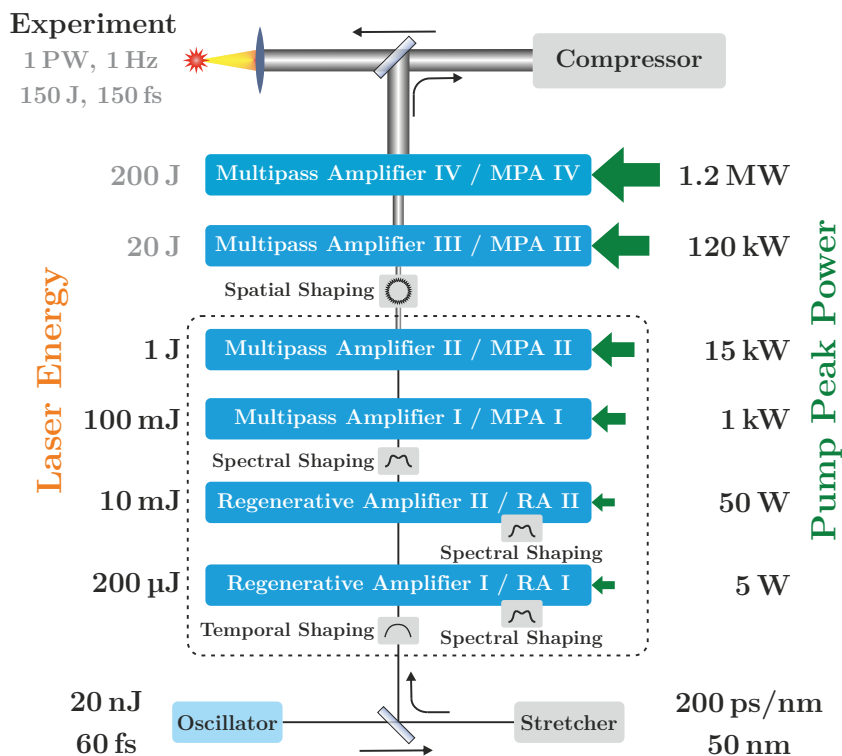


**Figure 3.2:** The conceptual layout of the PENELOPE laser system.

Before further amplification, (i.e. for more the 1 J pulse energy) transverse laser beam shaping is performed. The final amplifier stages and the beam magnification telescopes are based on relay imaging. A detailed explanation is given in Section 3.2.2.

The laser system is built inside the ELBE building. In 2010 to 2011 it was extended to host the PENELOPE and the Draco laser. A class 7 cleanroom with more than 300 m<sup>2</sup> is dedicated for the PENELOPE laser alone. The planned lab infrastructure is shown in Figure 3.3. The layout of the different laser parts and the approximate location/dimension of each are given.

The front-end consists of two branches, each located on two separate optical tables. One is the conventional front-end sketched in Figure 3.2. The other optical table offers the opportunity to implement contrast improvement approaches in the future. As an option for such future upgrades, several possibilities were implemented and tested in other high-energy laser systems like PHELIX [73] or POLARIS [74].

Typically, the energy level of the oscillator pulses is increased from the nJ to the  $\mu$ J range with an improved contrast. One option is a double CPA system with a XPW filter between the two amplification stages. The laser pulse of the first stage is cleaned using a XPW filter and is sent as a high contrast laser pulse to the second CPA stage. This technique was implemented in different laser systems and a TIC improvement of several orders of magnitude are reported [74, 75]. The drawbacks are the high costs for an additional stretcher-compressor system as well as the energy degradation of the output due to the high intensity on the crystal [74].

A second viable option is a parametric amplification of the oscillator pulse with a pump pulse in the ps range. This is called ultrafast optical parametric amplifier (uOPA) [76].

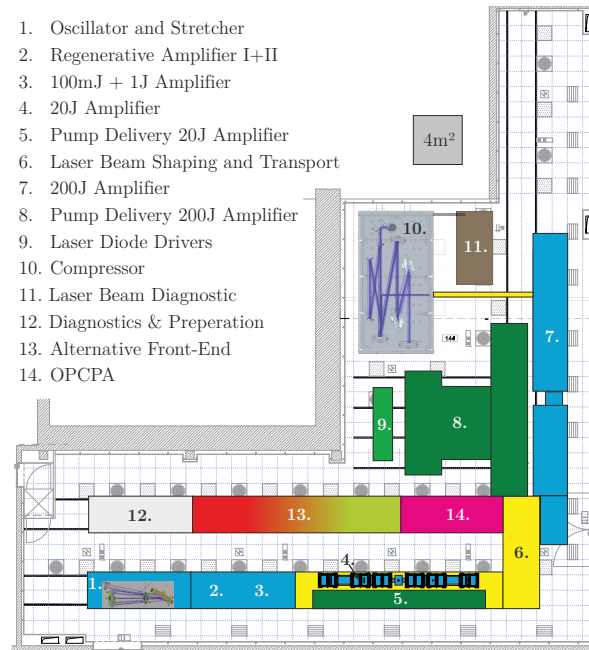


**Figure 3.3:** Projected lab infrastructure of the PENELOPE laser system.

Therefore no additional CPA system is needed and it can be implemented between the oscillator and the stretcher. This technique was successfully demonstrated by Dorrer [76] and also implemented in the PHELIX laser system at the GSI Darmstadt [73]. The difficulty is to generate the pump pulse and synchronize it to the laser pulse. The jitter between the pump and seed signal has to be in the femtosecond range.

Both approaches are attractive options. In both cases, clean laser pulses are sent to the stretcher, as it is shown in Figure 3.4. Furthermore the first multipass amplifier stages can be replaced by an optical parametric chirp pulse amplification (OPCPA) stage. This is due to the fact, that the active-mirror approach cannot be easily scaled to high energies with large bandwidth, as well as high repetition rate.

For a future upgrade the most attractive option for the PENELOPE system with more than 1 Hz is an OPCPA approach, also a bandwidth broader than 30 nm can be scaled up to the joule level [77, 78]. Figure 3.4 illustrates the implementation of the different options.

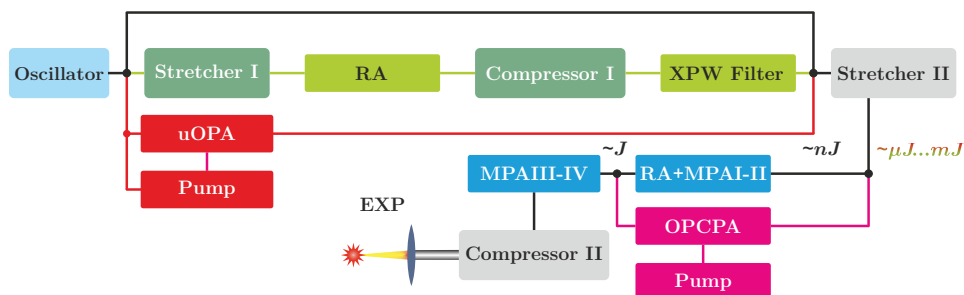


**Figure 3.4:** RA regenerative amplifier; MPA multipass amplifier; EXP experiment. Comparison of the existing concept (black line) and the alternative front-end concepts XPW filtering (green line) and uOPA (red line) as well as the high-energy OPCPA stage (magenta line). The XPW and uOPA increase the energy before the stretcher to the  $\mu\text{J}$  range and inject the CPA/OPCPA system.

### 3.2.1 Amplifier Architecture

For high-energy laser amplifiers, three different laser gain medium geometries are commonly used. Figure 3.5 shows the rod, active-mirror and slab concept. In the past, the most employed geometry is the rod-type amplifier, which is limited by thermally induced effects [30].

The cooling is in the transversal direction, whereas the laser and pump beam are in the longitudinal direction of the rod. This results in a radial temperature gradient and generates a radial refractive index gradient, which leads to focusing/defocussing. Additionally, the thermal stress inside the rod has to be kept low to avoid fracture of the gain medium. Accordingly, this approach is limited in average power leading to a low repetition rate (typically of several shots per minute).

However, the gain material can be used as a plate/slab (thickness small compared to width of the plate), where the cooling is applied in the same direction as the pump and laser beam (see Figure 3.5). This approach can be realized in two geometries, i.e. the active-mirror and slab. The thermal gradient (axial) is in the same direction as the laser beam, leading to reduced thermally induced effects on the beam.

The PENELOPE laser amplifiers are based on a hybrid concept, where both geometries are used. In the following both are compared.

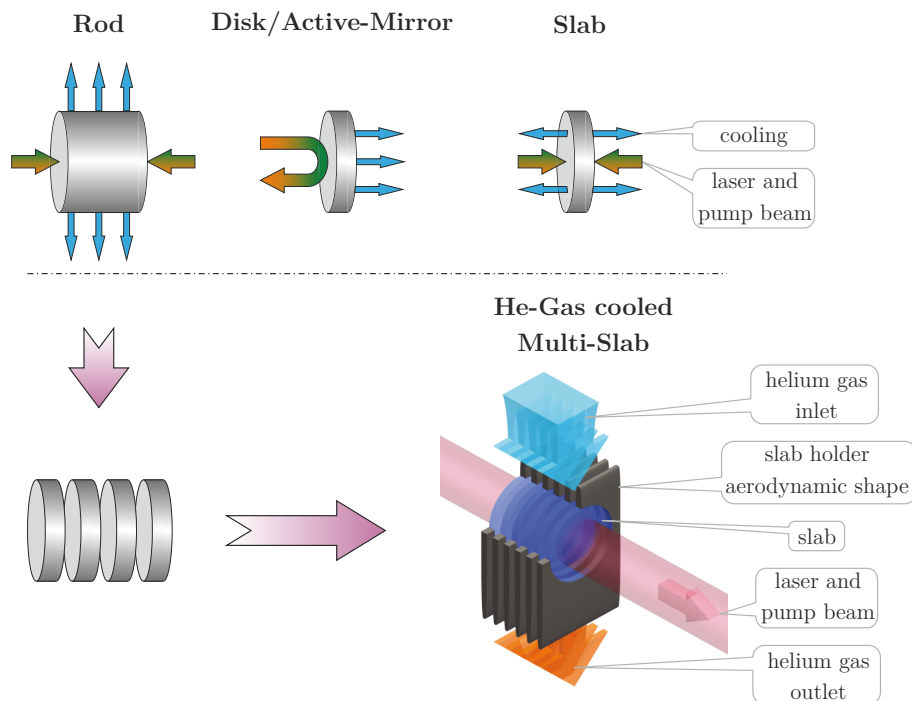


**Figure 3.5:** Top from left to right: Transversely cooled laser rod, longitudinally cooled active-mirror as well as slab laser. Bottom left: Laser rod sliced in several slabs (multi-slab). Bottom right: He-gas cooled multi-slab laser head.

#### The Active-Mirror Concept

The active-mirror concept has an inherent double pass of the pump and extraction beam through the active area, as shown in Figure 3.5. While this configuration is suitable for many applications, it carries several drawbacks at the same time:

- vibrations are translated directly into the far field (beam pointing),
- interferences due to overlapping of the input and output beam inside the gain material,
- ASE limitations and
- the bonding quality for indirectly cooled active-mirrors.

Due to these limiting effects the active-mirror concept can only be used in regenerative amplifiers and first multipass amplifier stages. A detailed overview is presented in Section 5.1.

The diameter has to be increased to get a higher output energy. A shear increase in lateral size of the disk while keeping the doping concentration constant is limited by ASE, as its impact on the stored energy grows exponentially with the characteristic length (lateral size) multiplied with the doping concentration. To keep ASE on a reasonable level, the thickness of the disk has to be increased and the doping concentration decreased at the same time. The absorption stays constant. In the active-mirror scheme this however would ultimately result in increased thermally induced effects.

The volume can be split into several disks, as shown in Figure 3.5. Therefore, the thermal load per disk is low and allows a high-repetition rate operation. This leads to a multiple slab concept in transmission.

#### The Slab Concept

The slab geometry reduces the problems that limit high-power operation. There are generally four issues to be addressed:

- heat accumulation in the material,
- thermally induced wavefront distortions,
- thermally induced depolarization losses and
- beam profile changes due to gain variation.

The general idea of the slab concept is to distribute the heat load equally over several slabs. In the case of volumetric scaling, it is essential to split the gain volume in several slabs to achieve a high repetition rate of a few Hz. This is the so-called multi-slab laser, as shown in Figure 3.5. The basic thermal analysis of a slab can be found in [79, 80].

In order to avoid thermally induced buckling, it is of high importance to symmetrically distribute the heat load and cooling for each slab. Ideally, every slab carries the same overall heat load. For this purpose, an adapted doping level for each slab or a gradient doping is needed [66, 68]. First numerical studies about the PENELOPE laser head can be found in [81].

The cooling can be realized with a high velocity gas stream (see Figure 3.5). In the past, He-gas cooled multi-slab lasers have been successfully demonstrated [82, 83]. The design of the He-gas cooled multi-slab can be found in [64]. The complexity of the laser head and the



required infrastructure (helium transport, cooling system, etc.) makes this design only a viable solution for operation above the 1 J-level.

Helium was chosen as coolant due to the fact that it offers a low index of refraction and low scattering losses. The gas stream in the flow channels is turbulent with Reynolds number of several thousands. The scattered fraction  $I_{scat}/I_0$  is almost 600 times smaller for helium than for nitrogen [84]. A detailed explanation of the problem can be found in [84, 85].

### 3.2.2 Beam Shaping, Relay Imaging Telescopes and Amplifiers

In high-energy laser systems the beam waist has to be matched to each of the amplifier stages. This can be done by a single lens or telescope. An imaging system consisting of a single lens cannot preserve the beam parameter product and results in an increased beam divergence. A derivation using the matrix formalism can be found in Appendix A.2.

Telescopes in contrast, collimate the beam and the parameter product is constant, when aberrations of the optical system are neglected. There are two different kinds of telescopes: Galilean and Keplerian. The principle setup of both types is shown in Figure 3.6. In general, a Galilean type telescope shows a smaller footprint. The main difference is that for the Keplerian type a real image is formed, which is schematically represented in Figure 3.7.

This advantage can be used in amplifiers to image the output onto the input image plane (IP) of the next stage. Furthermore, free propagation of the laser beam can be prevented and the intensity distribution is conserved in the IP. The focal spot of the two convex lenses in a Keplerian style telescope coincide in the same plane. A low pass (for spatial frequencies) can be generated by inserting an aperture/pinhole in the Fourier/focal plane (FP), which is called spatial filtering, as shown in Figure 3.7. Close to the FP the intensity is so high, that it would cause an air breakdown. This is circumvented by evacuating the whole affected volume and it is called vacuum spatial filter (VSF).

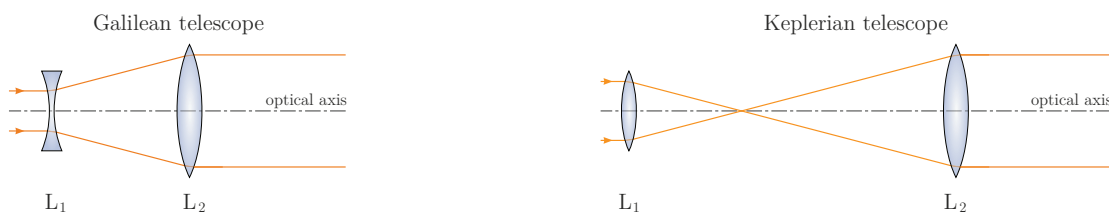


**Figure 3.6:** The principle setup of Galilean and Keplerian telescope.

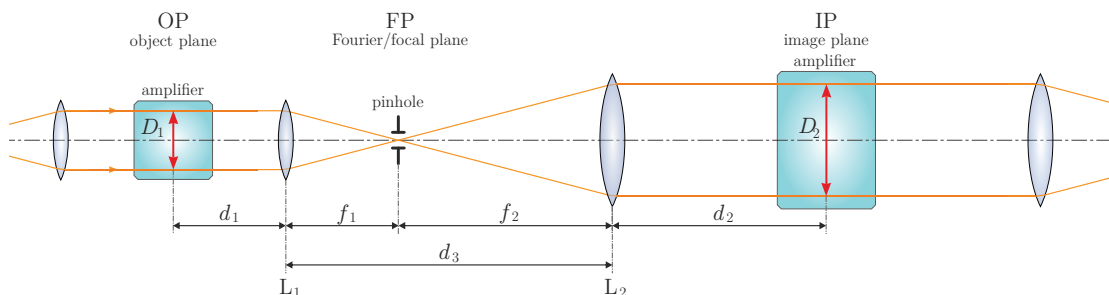


**Figure 3.7:** The relay imaging setup including a pinhole, which is needed for a spatial filter. The amplifier is located in the OP as well as in the IP of the telescope.

The beam diameter between two stages is adapted by using two different focal lengths  $f_1$  and  $f_2$ . In the case of magnification it follows  $f_1 < f_2$ . For a telescope with two lenses  $f_1$  and  $f_2$  the object distance  $d_1$  and image distance  $d_2$  have the following relationship

$$d_2 = (f_1 + f_2) m - d_1 m^2 \quad (3.1)$$

$$m = \frac{f_2}{f_1} = \frac{D_2}{D_1} \quad , \quad (3.2)$$

where  $m$  is the magnification factor,  $D_1$  is the object (input beam diameter) and  $D_2$  the image (output beam diameter) height. If the object distance equals to  $f_1$ , the image distance equals to  $f_2$ . This configuration is called *4f optical system* - the distance between the object and the image plane is  $2 f_1 + 2 f_2$ . The correlation between a change of object distance to the image distance is given by

$$\Delta d_2 = -\Delta d_1 m^2 \quad (3.3)$$

and for a large  $m$ , a small  $\Delta d_1$  leads to a large  $\Delta d_2$  in the reversed direction. This can be used to shift the image of the laser beam to the best position.

Furthermore, the relationship between the beam diameter and the focal length is given by the F-number  $F^\#$ :

$$F^\# = \frac{f}{D} \quad . \quad (3.4)$$

In the case of high F-numbers the aberrations of spherical lenses are low. A large F-number implies a large focal spot size. In the case of a tight focus spherical aberrations are the limiting factor. Therefore, off-axis parabolas or similar focusing elements are used to achieve diffraction limited spot sizes [86].

The spatial beam profile of the first amplifier stages is Gaussian (near and far field). The propagation properties of a Gaussian beam are self-preserving. To get the same output fluence on the optics for each amplifier, the beam size has to be magnified due to the increasing laser pulse energy. For energies above 1 J the optic size must be very large to transport the beam without clipping. A typical value is at least two times the beam diameter at  $1/e^2$ . This is due to the fact that the edge of a Gaussian beam goes to infinity. The beam diameter at  $1/e^2$ , which is 13.5% of the peak intensity, contains 95% of the energy. Furthermore, the space for the extraction beam inside the amplifier is limited and therefore a Gaussian beam would generate diffraction ripples due to clipping on mechanical or optical components. Also the beam overlap plays an important role in terms of efficiency, as shown in Figure 2.5 on page 23. In general, the dimension of the pump and extraction beam has to be matched as best as possible. To fulfill all these requirements a beam shaping has to be implemented ideally before the 10 J amplifier stage (MPA III).

The task is to generate a defined slope at the edge of the beam, with a smooth transition to zero intensity. The slope has to have low spatial frequencies to avoid diffraction patterns that appear at the beam cut with hard edges, like diaphragms. This is done with a serrated aperture in combination with a spatial filter [87]. This technique was introduced by J. Trenholme et al. on the NOVA laser system in 1978 [88]. The experimental setup is shown in Figure 3.7. A serrated aperture with a fine tooth pattern is introduced in the OP of



the telescope. The high frequencies are filtered by means of a pinhole in the FP and the apodized beam appears in the IP. The serrated aperture has 250 teeth, which have a height of 0.98 mm and a width of 0.28 mm. This leads to higher angular as opposed to radial spatial frequency components. Thus, both components can be separately filtered. The outer diameter is 22 mm. The triangular teeth are structured on a chromium mask with an anti-reflection coated glass substrate. A segment of the serrated aperture is shown in Figure 3.8 (a). A detailed explanation of the design can be found in [40, 87]. The pinhole size depends on the focal length of the first lens and the tooth height. The beam after the apodizer with and without filtering is shown in Figure 3.8 (b). The tooth structure is visible in the beam profile after the telescope, when no pinhole is inserted in the FP it vanishes out, if the high frequencies are filtered.

After apodization, the beam has to be relay imaged to avoid diffraction patterns that arise after a certain propagation distance. A free propagation test of the apodized beam in an experimental case was performed in order to get a perception which distance is acceptable for propagation. Therefore, a helium-neon laser was used and apodized with the serrated aperture. To fit the beam on a CCD camera, a subsequent reduction telescope with  $m = 1/5$  was built. A measurement in the image plane, as well as after 3 cm, 10 cm and 30 cm propagation distance was done, which leads to a free propagation of 0.75 m, 2.5 m and 7.5 m for the original beam size by using Equation (3.3). The beam diameter is slightly increased and first ripples occur at 2.5 m, which is shown with a profile line of the beam in Figure 3.9 (a). This propagation length is acceptable in e.g. the 10 J amplifier stage (MPA III), when the beam is out of the image plane. This is especially important for the imaging optics and steering mirrors. Furthermore, it corresponds to a propagation distance of more than 74 m for a beam diameter of 120 mm. This is the output beam diameter of the final amplifier stage. In addition, a hard aperture was inserted instead of the serrated aperture, to illustrate the propagation difference at the same distance. The ripples are clearly visible and much stronger in Figure 3.9 (b) on the left side.

Due to the fact that the gain cross section for  $\text{Yb}^{3+}:\text{CaF}_2$  is small, a large number of amplification passes are needed to achieve a certain output energy. This leads to a relay imaging amplifier setup following the beam shaping unit. Therefore, the beam size at every extraction pass is the same. A solution has to be found that fits all constrains for space

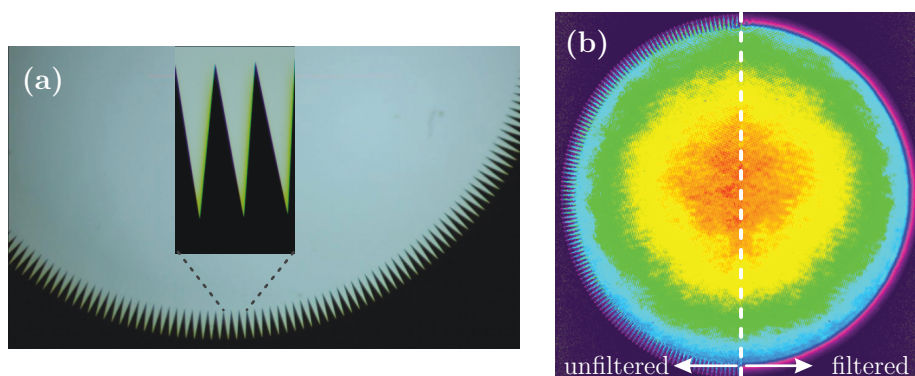


**Figure 3.8:** (a) the serrated aperture with 250 teeth, which have a height of 0.98 mm and a width of 0.28 mm. The outer diameter is 22 mm. In (b) the beam profile in the IP with (right) and without (left) the pinhole in the FP.

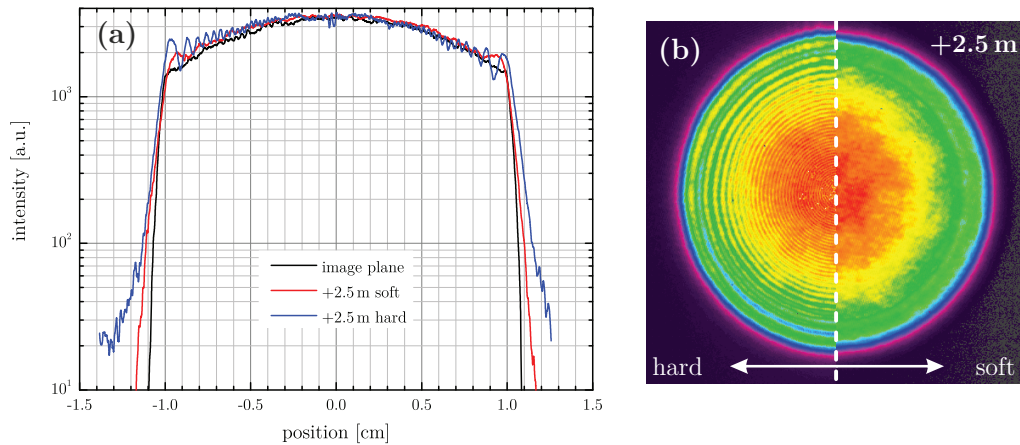


**Figure 3.9:** Comparison of a hard and soft apodized beam after a 2.5 m propagation with a diameter of 22 mm; (a) profile lines of the apodized beam in the image plane and after the propagation as well as the hard apodized beam after the same distance. (b) image of both beams with a hard on the left and a soft apodized beam on the right.

and desired beam quality. The same is true for the telescopes between the amplifiers having a long distance (see Figure 3.2). There are two solutions in building a telescope: one is a refractive (lens based) and the other is a reflective (mirror based) telescope. A comparison of their pros and cons are given in the following list. Reflective telescopes are distinguished by spherical or parabolic shaped surfaces.

### Lens

- + simplicity of the setup
- Ghost<sup>a</sup>foci
- more material
  - higher B-integral
  - more dispersion
  - material absorption
- lower transmission
  - AR coating typically  $\mathcal{T} > 99.8\%$
  - more surfaces
- radial group delay<sup>b</sup>[89, 90]
- tilted lens to avoid Ghost images  $\rightarrow$  wavefront aberrations

### Mirror

- spherical mirror
  - astigmatism due to  $\text{AoI} > 0^\circ$
  - more required space due to the perpendicular folding planes
  - + standard optic (lower costs)
  - + alignment insensitive
- off-axis parabolas (OAP)
  - alignment sensitive
  - expensive optics
  - + no astigmatism or coma
- + less material
  - lower B-integral
  - less dispersion
- complexity of the setup
- + higher transmission
  - HR coating typically  $R > 99.9\%$
  - less surfaces
- + no radial group delay

The best solution in the case of the PENELOPE system is the spherical mirror based telescope. The main disadvantage is the resulting wavefront aberration due to the angle of incidence on the spherical mirrors. This leads to an astigmatism, as well as higher order aberrations, especially coma. Consequently the beam quality is reduced.

Astigmatism leads to different focal lengths in the sagittal and tangential plane of the beam. Additionally, unobscured two-mirror afocal systems can be constructed also with off-axis parabolas (OAPs). These telescopes have a perfect on-axis imaging property and ideally no astigmatism or coma. But OAP are expensive optics and the wavefront quality is very sensitive to alignment errors.

The definition of the beam quality for a non-Gaussian profile can be given with the point spread function (PSF) or the Strehl ratio, which includes the effects of aberrations and diffraction. The Strehl ratio is defined as the ratio of the peak intensity at the focal point (the point of maximum intensity in the observation plane) in the presence of aberration  $\Phi$ , divided by the intensity that would be obtained if no aberration  $\Phi = 0$  were present [91]

$$S = \frac{I(0)_\Phi}{I(0)_{\Phi=0}} . \quad (3.5)$$

This can be measured and calculated by wave front sensors or interferometers. But for a practical solution, a simple analytic expression can be found by Mahajan in [92] and is determined to be

$$S = \exp \left( - \left( \frac{2 \pi \Phi_{rms}}{\lambda} \right)^2 \right) , \quad (3.6)$$

where  $\Phi_{rms}$  is the root mean square (rms) wavefront error in wavelength units and  $\lambda$  is the wavelength of the laser beam. This means, a  $\Phi_{rms} = \lambda/20$  results in a Strehl ratio of 0.9, which is a good value for an optical system.

The Marèchal criterion is “the golden rule of optical design” and is defined as an rms wavefront error of 14 times less than its wavelength. This is equivalent to a Strehl ratio of 0.82 [93]. This wavefront can be considered as diffraction limited in terms of the Marèchal approximation. Nowadays, the diffraction limit, for example of focusing optics used in high-energy lasers, is defined by the Airy disc diameter, which equals 83.8% of the distributed energy within the PSF. The diameter with 83.8% encircled energy is calculated with the wavefront from the optics or laser beam and then compared with the diffraction limited case [86].

Now the optical quality of an imaging system or optical component can be verified with Equation (3.6). An easy way to compensate for astigmatic aberration in a spherical mirror telescope is the folding of the input perpendicular to the output plane. This is always assumed in every telescope.

- 
- a Ghosts are a form of stray light from an unwanted reflection, which occur on imperfect anti-reflection coating. For a quantitative ghost analysis a non-sequential ray tracing is required.
  - b The laser pulse traveling through the center of a lens is delayed with respect to the laser pulse traveling through edge. Therefore, the peak intensity in the focus is reduced, when the delay is comparable with the pulse duration. This delay is called radial group delay (RGD) or longitudinal chromatism.

For a large Strehl ratio there are several parameters like the angle of incidence (AoI) on the mirror and the  $F^\#$ . These can be optimized for a given magnification factor  $m$  and input/output beam diameter  $D_1$  and  $D_2$ . The design of the telescope is done with ray tracing software. In our case, Zemax<sup>TM</sup> in the sequential mode is used to construct and optimize such telescopes. What has to be kept in mind is, that due to the high pulse energy, the focal spot has to be in vacuum. Therefore between the two mirrors a vacuum pipe with windows has to be installed. The windows are tilted a few degrees to avoid direct reflections. This tilt leads to a slight astigmatism that can be compensated with an appropriated AoI on the telescope mirrors.

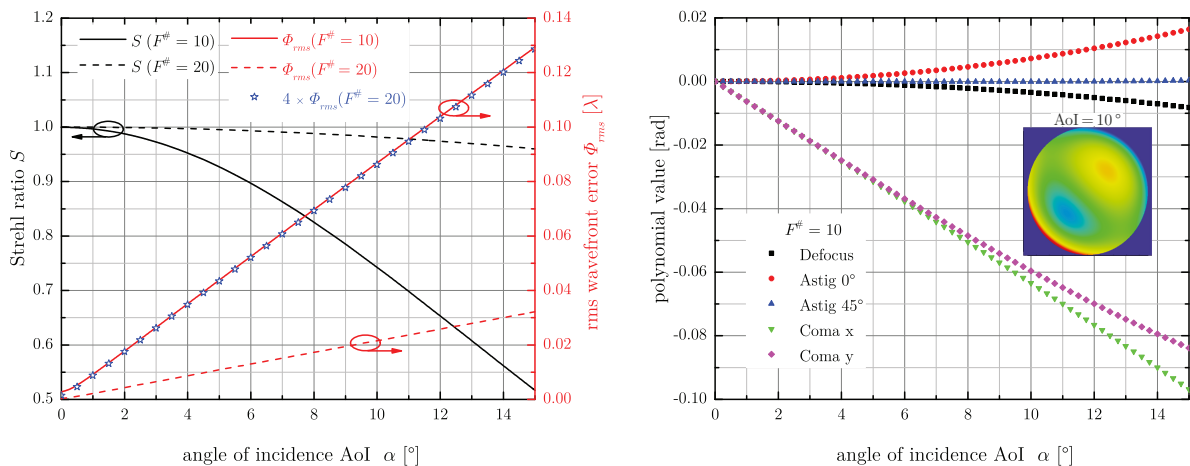
A short overview of the optimization of a telescope is described. A rule of thumb is presented for the design. All simulations are done with a magnification factor equal to or larger than one and at a wavelength of 1035 nm.

At first the AoI is varied from  $0^\circ$  to  $15^\circ$  for an 1:1 telescope with a  $F^\#$  of 10 and 20. The Strehl ratio and the  $\Phi_{rms}$  are given in Figure 3.10(a). For an F-number of 10,  $S$  drops from 1 to 0.5. This is due to the fact that the rms wavefront error increases linearly with larger AoI. To compensate for this, the  $F^\#$  has to be increased, whereas the reduction of the rms wavefront error has a square dependence of the F-number:

$$\Phi_{rms}(F^\#_2) / \Phi_{rms}(F^\#_1) = (F^\#_1 / F^\#_2)^2 \quad . \quad (3.7)$$

This can also be seen in Figure 3.10(a). Therefore the F-number was doubled and  $\Phi_{rms}$  is four times less than before. For a better presentation, the values were quadrupled. They fit very well to the values for the case of half the F-number.

To find out which type of wavefront error dominates, Zernike polynomials for defocus, astigmatism  $0^\circ / 45^\circ$  and coma x / y are shown in Figure 3.10(b). As the astigmatism is



(a) Analysis of the influence of the AoI on the Strehl ratio as well as the rms wavefront error in an 1:1 telescope. The Strehl ratio is plotted for a F-number of 10 and  $F^\# = 20$ . The beam diameter is 10 mm. The  $\Phi_{rms}$  is given for both cases.

(b) Analysis of the influence of the AoI on the Zernike polynomial in an 1:1 telescope. Here, the defocus, astigmatism  $0^\circ/45^\circ$  and the coma x/y are selected. The wavefront map for an AoI of  $10^\circ$  is inserted.

**Figure 3.10:** Influence of the AoI on the spherical mirror to the optical quality of a reflective telescope.

compensated, the coma terms are the main remaining wavefront errors. Both, x and y, are present, as the resulting coma-like wavefront error is rotated by  $45^\circ$ . This can also be seen on the inserted wavefront for an AoI of  $10^\circ$ . For higher angles, the astigmatism increases as well and the beam becomes slightly elliptical.

Moving on, the ratio of the AoI on the first mirror  $\alpha_1$  (variable) and second mirror  $\alpha_2$  (fixed) is traced for a fixed  $D_1$  and F-number as a function of the magnification factor. The general trend is given in Figure 3.11. The input angle is larger for  $m > 1$ . The relationship between  $\alpha_1$ ,  $\alpha_2$  and  $m$  is determined to be

$$\frac{\alpha_1}{\alpha_2} = \sqrt{m} \quad . \quad (3.8)$$

This fits the optimized  $\alpha_1$  values very well. The beam size on the output is increasing, which leads to a longer distance to separate them. In addition, the rms wavefront error is plotted and for larger  $m$  the  $\Phi_{rms}$  is obviously enhanced. There are two different reasons for the increase. One is the increasing  $\alpha_2$  and thus  $\Phi_{rms}$  rises as well (see Figure 3.10(a)). The other is the larger output beam diameter for the same F-number. This is investigated in more detail in the following paragraph.

Now the dependence of the F-number from the beam diameter  $D$  is investigated to get the same Strehl ratio. Therefore, the diameter  $D'$  changes from 10 mm to 120 mm for  $m = 2$  and  $F^\# = 20$ . The  $F^\#(D')$  was optimized for the beam diameter  $D'$ . The starting telescope is for  $D = 10$  mm. The trend is shown in Figure 3.12. Thus it can be decided which F-number is required when the beam size is changed for a given telescope. The question is how to scale  $F^\#$  with an increasing beam diameter to have the same Strehl ratio. This is

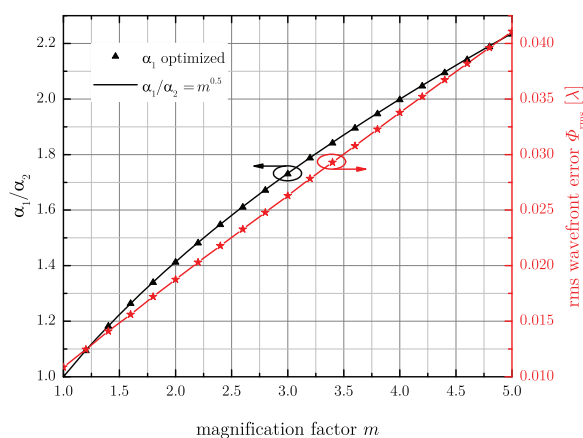


**Figure 3.11:** Influence of the magnification factor on the ratio of the AoI on the first mirror  $\alpha_1$  and second mirror  $\alpha_2$  as well as the rms wavefront error  $\Phi_{rms}$  is shown. Here,  $\alpha_2$  is fixed to  $5^\circ$  and the F-number equals 20.

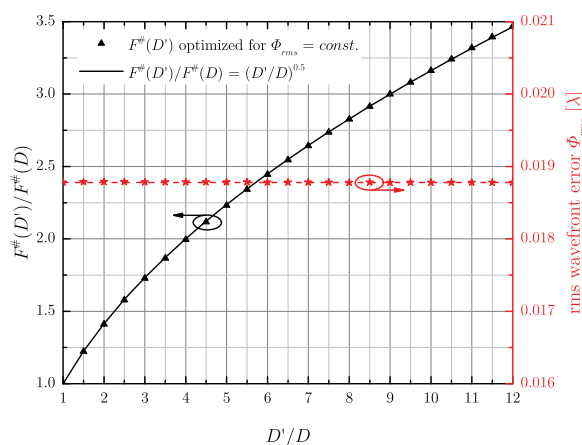


**Figure 3.12:** Scaling of the F-number  $F^\#$  by changing the beam diameter  $D$  to have a constant rms wavefront error.  $D$  is the initial values and  $D'$  the target diameter.  $F^\#$  is the starting F-number and  $F^\#'$  is the F-number for the target beam diameter to have the same wavefront aberrations as before.

illustrated in Figure 3.12. An empirical formula is determined to be

$$\frac{F^\#(D')}{F^\#(D)} = \sqrt{\frac{D'}{D}} \quad (3.9)$$

This relationship fits the computed values very well, which can be seen in Figure 3.12. If the F-number of the telescope gets larger, then the estimated Strehl ratio improves. This value is a lower limit. In summary, it is better to split a large magnification ( $m > 2$ ) into several telescopes to get a good beam quality. Furthermore, it is easier to optimize the footprint.

All results shown are taken at a wavelength of 1035 nm. For shorter wavelengths the  $F^\#$  has to increase to get the same rms wavefront error. A root dependency of the F-number can be found by using:

$$\frac{F^\#(\lambda_2)}{F^\#(\lambda_1)} = \sqrt{\frac{\lambda_1}{\lambda_2}} \quad (3.10)$$

This is due to the fact that  $\Phi_{rms}$  has a linear dependence on the wavelength. Based on these given design criteria, a rough estimation for a given telescope can be found, which has to be checked using a ray tracing software for instance.

In Table 3.1 the five telescopes planned behind the front-end are shown with their optimized parameters. The wavefront error of the optical components, as well as the vacuum windows, are ignored for these calculations. The  $F^\#$  of VT4 and VT5 are the smallest leading to the worst Strehl ratio. Nevertheless, the telescopes provide a good optical quality. So far, all optical components are placed in their ideal position. In a real scenario, misalignment is always present and the question arises as to how sensitive the telescopes are against it.

As the distance can be finely adjusted using translation stages, all critical impact on the Strehl ratio falls on the adjustment of the AoI. The change in the Strehl ratio was investigated by detuning the AoI by  $\pm 0.25^\circ$ . However, the variation of the Strehl ratio depends on the initial condition. This can be seen in Figure 3.10(a). At an AoI of  $6^\circ$

	$f_1$	$f_2$	$F^\#$	$\alpha_1$	$\alpha_2$	$D_1$	$m$	$S$	comment	
	[mm]	[mm]		[ $^\circ$ ]	[ $^\circ$ ]	[mm]				
VT1	2400	4800	240	7.0	5.0	10.0	2.00	1	MPA II	→ SA
VT2	3100	4800	141	5.0	4.0	22.0	1.55	1	SA	→ MPA III
VT3	3700	4800	109	5.0	4.4	34.1	1.30	1	MPA III	→ II
VT4	1800	2400	41	6.9	6.0	44.2	1.33	0.98	II	→ PC
VT5	3300	6600	56	9.0	6.4	58.9	2.00	0.98	PC	→ MPA IV

**Table 3.1:** List of the planned vacuum telescopes (VT) behind the front-end. SA serrated aperture; MPA multipass amplifier; II intermediate image plane; PC Pockels cell;  $D_1$  input beam diameter;  $f_{1/2}$  input and output focal lengths of the imaging mirrors;  $F^\#$  F-number;  $\alpha_{1/2}$  AoI on the input and output mirror;  $m$  magnification factor of the telescope;  $S$  Strehl ratio.



the slope is steeper for  $F^\# = 10$  than for  $F^\# = 20$ . If the Strehl ratio is above 0.95, the misalignment sensitivity is very low. Thus with the given precision of the AoI adjustment it is feasible to set up the telescope in principle with a good optical quality. Additionally, a tolerancing could be performed to determine the worst case for a given set of optical and mechanical print values.

All multipass amplifiers are based on relay imaging. Due to the thermal load at the gain material, either a positive or negative thermally induced lens  $f_{TL}$  occurs in general. The gain material is placed in the object plane of the telescope. Therefore, the near field beam profile for each pass on the material is not affected, but the lens is added to the wavefront for each pass. For this reason, the beam divergence increases per pass and leads to a reduced beam size out of the image plane, where the imaging optics are located. The peak fluence on those transport optics rises and can lead to catastrophic damage. Therefore the thermally induced lens has to be compensated. This can be realized by using a phase plate or by adjusting the distance between the imaging optics (see Figure 3.7). The equivalent distance  $d_3$  is appointed to be

$$d_3 = f_1 + f_2 - \frac{f_1 f_2}{f_{TL}} \quad . \quad (3.11)$$

If  $f_{TL}$  goes to infinity, the common solution appears where  $d_3$  is the sum of  $f_1$  and  $f_2$  (see Figure 3.7).

There are two different types of relay imaging multipass setups used on the PENELOPE system. The first multipass amplifiers are based on a two mirror setup, which is shown in Figure 3.13 and was proposed by M. Kumkar et al. [94]. The passes are arranged in a horizontal line on the curved mirrors  $M_3$  and  $M_4$  (see top view in Figure 3.13). The number of possible passes depends on the RoC, the beam diameter and the gap between the input beam and the curved mirror  $M_3$  (see top view Figure 3.13). The separation of the input and output is performed using a vertical displacement, leading to two beam spot lines on the curved mirror (see side view Figure 3.13). The output beam passes above  $M_1$ . The gain material is placed at the position of  $M_2$ . This can be a rod or an active-mirror as well.  $M_5$  is the second image plane of the telescope. In order to compensate for the thermally induced lens or even higher order aberrations, a phase plate or a deformable mirror can be inserted at this position. The AoI  $\alpha$  on  $M_3$  and  $M_4$  of the 1:1 telescope are the same in two perpendicular planes to compensate for astigmatism (see top and side view Figure 3.13). A typical number of possible passes in MPA I is 6 to 12.

This number can be doubled by reflecting the beam back with mirror  $M_6$  into itself. A consequence of this is a free propagation of the beam from  $M_2$  to  $M_6$  and backwards. This can be solved by an additional imaging telescope, imaging the beam profile back to  $M_2$ . The separation between the in- and output is achieved by polarization coupling. A quarter-wave plate (QWP) is placed in front of mirror  $M_6$ , which is operating as a half-wave plate after a double pass. The polarizer (thin film polarizer (TFP)) separates the input from the output beam, as it is shown in Figure 3.14. The input beam is transmitted through the TFP, whereas the output is reflected.

One of the issues of polarization coupling is the potential damage or disturbance of the previous amplifier stages as the beam travels its initial way back. Optical isolation with a Faraday isolator or a Pockels cell as well as an optimized position of the QWP is very

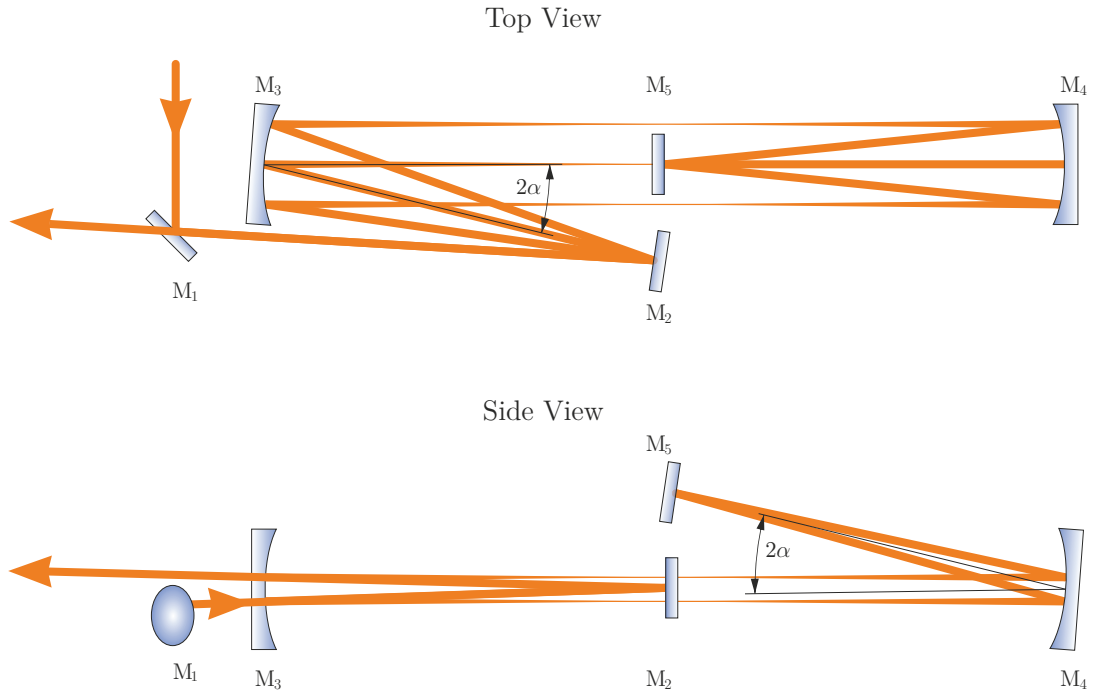


**Figure 3.13:** Top and side view of the two mirror based relay imaging amplifier setup. The beam is folded in two perpendicular planes to compensate the astigmatism. Mirror  $M_3$  and  $M_4$  have the same radius of curvature (RoC). The multipass is spanned a horizontal line on the mirrors and is illustrated in the top view. The input and output beam is separated in a vertical displacement and the output passes above  $M_1$ , which is shown in the side view. The image planes of the telescope are on plane mirrors  $M_2$  and  $M_4$ .

important. Nevertheless, a depolarization of the laser beam as a consequence of thermally induced stress inside the gain material will lead to a leakage backwards into the pre-amplifier and has to be taken into account. A typical setup is given in [95, 96], where the RoC is 750 mm. In this case, no vacuum in between the imaging optics is needed as the intensity is below the air breakdown threshold.

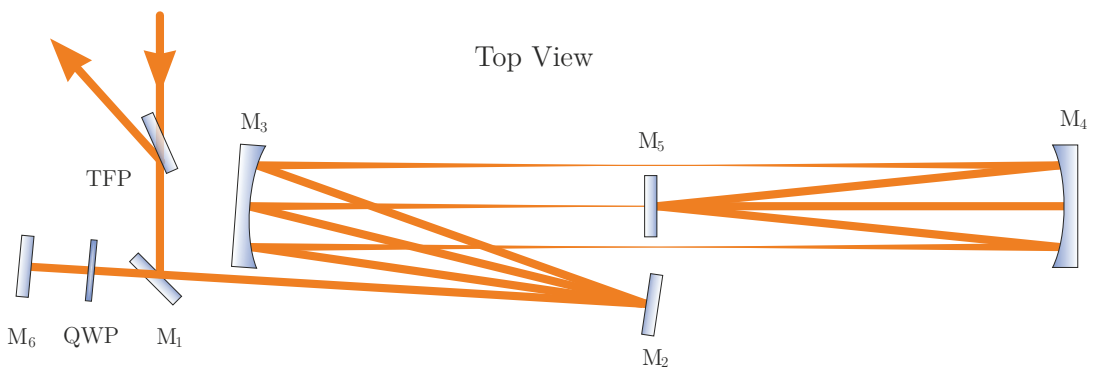


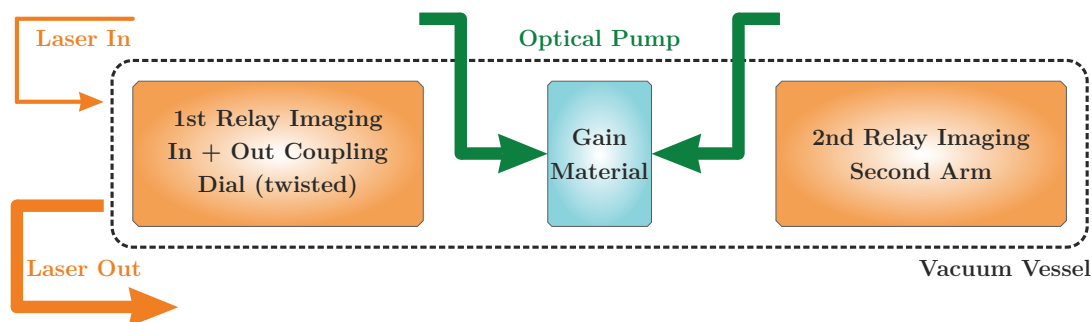
**Figure 3.14:** Top view of the two mirror based relay imaging amplifier setup with doubled pass configuration via polarization coupling. Therefore the beam is back reflected with  $M_6$  and the polarization is rotated about  $90^\circ$  with a QWP that act as a half-wave plate in a double pass. The in- and output beam is separated using a polarizer (TFP).



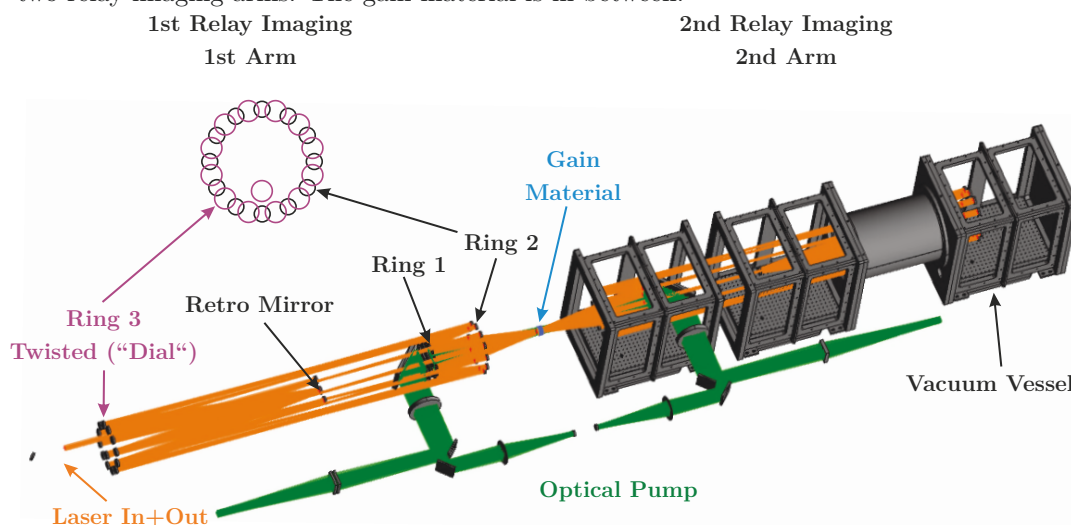
The limit of this approach is reached below the Joule-level. The imaging mirrors would be very large, which makes the setup very difficult and expensive. One solution to this problem is the separation of each pass into individual telescopes. Thus, the mirror size is matched to the beam diameter again.

The telescopes are arranged on a circle. This results in a radial symmetry, whereby the astigmatism is ideally compensated. In this circular extraction arrangement, the necessary optical pump is guided in the center of the multipass ring structure. As the pump laser has a low beam quality compared to the extraction beam, it is better to operate it in an on-axis pump geometry. This is described in more detail in Section 3.3.

The multiple mirror setup was introduced in [97] and adapted for high-energy lasers in [63]. The difference of the structure used in the PENELOPE system is that the laser material is a multi-slab amplifier instead of an active-mirror. This results in a two arm structure and



(a) Simplified layout of MPA III. The laser in- and out-coupling is shown as well as the two relay imaging arms. The gain material is in between.



(b) Experimental arrangement of MPA III. The first arm is shown in more detail with the three rings, the retro mirror and the in- and out-coupling mirrors. The ring 3 is twisted (“Dial”) compared to ring 2 of the first arm. The pump beam and the optical setup is illustrated. The gain material is located between the two arms.

**Figure 3.15:** Simplified (a) and experimental setup (b) of MPA III.

is shown in its principle scheme in Figure 3.15(a). The first arm is for in- and out-coupling of the laser beam as well as the rotation of the beam (called “Dial”, see Figure 3.15(a)). The gain material is in between. The optical pump coming from each side is only shown in principle.

The other arm provides only a pure relay imaging the beam profile, thus the distance in between can be adapted to compensate for thermal lens effects without changing the beam position on the respective optics. Furthermore, the beam is magnified on the imaging plane on both sides. The magnification factor is 1.35, reducing the fluence by about a factor of 1.8.

The experimental setup used is shown in Figure 3.15(b). The vacuum vessel is shown in black, the optical pump in red and the laser beam in orange. There are three rings on each arm. Ring 2 and 3 contain the spherical mirrors for the telescopes and ring 1 steers the beam inside the laser amplifier head. The retro mirrors are at the position of the image plane, which is located in between the telescope mirrors.

Ring 3 of the first arm is twisted compared to ring 2 (see Figure 3.15(b)) by half a dial. This is necessary to change (“Dial”) the telescopes from pass to pass. The second arm is not rotated. The number of passes depends on the geometric dimensions. The selected values in this case is a compromise of brightness of the pump, angle of incidence on the laser material and total length of the amplifier. 12 passes are realized in a 6 m long vacuum vessel. Nevertheless, it is possible to double the number of passes by implementing polarization coupling.

The balanced astigmatism due to the rotational symmetry creates a defocus, which can be compensated by adapting the distance between the imaging mirrors of the second arm. In any case, a deformable mirror can be placed in the image plane (replacing one of the retro mirrors) to act against any aberration.

The amplifier has been tested with Zemax<sup>TM</sup> on its optical function. The resulting wavefront is shown in Figure 3.16 and the data are provided with kind permission of D. Albach [98]. A Strehl ratio of about 0.98 is possible, while the optical quality of the amplifier material, as well as for the used imaging optics, were not considered. An rms wavefront error of smaller than  $\lambda/50$  is feasible. Currently, the optical function of MPA III is experimentally verified and can be found Chapter 6 on Page 131.

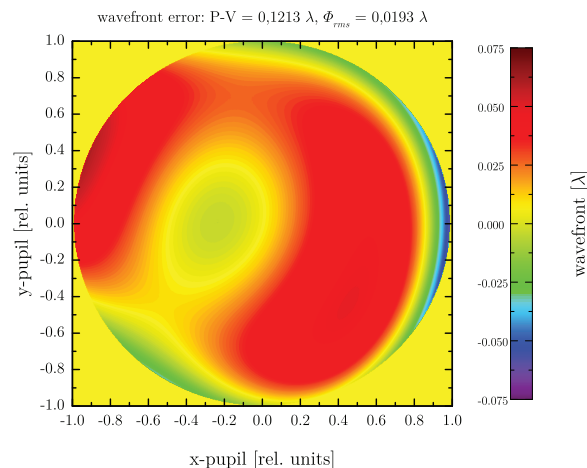


**Figure 3.16:** Wavefront analysis with Zemax<sup>TM</sup> of the relay imaging amplifier MPA III after 12 amplification passes. The maximum aberration is less than  $\lambda/8$ , the rms wavefront error less than  $\lambda/50$  and the Strehl ratio is better than 0.98. The data are provided with kind permission of D. Albach [98].

The transmission through the amplifier is larger than 80% by estimating a reflectivity and a transmission of 99.9%. In total 76 mirrors, 4 laser material slabs and two high pressure windows are taken into account.

### 3.2.3 Stretcher and Compressor of the PENELOPE System

The laser pulse stretcher and compressor of the PENELOPE laser system are carefully designed to match the target parameters of 150 J/120 fs. A large number of parameters have to be considered and the three main targets are as follows:

1. high transmission efficiency,
2. broad transmission bandwidth and
3. high stretching factor.

The first is needed to achieve a high pulse energy yield and to reduce the output requirements for the final amplifier stage. In addition, it is economically necessary to make good use of the installed laser diode power. The large bandwidth is needed for a high pulse contrast as well as for the support of pulse duration down to about 100 fs. The pulse contrast is an important parameter for experiments. Furthermore, the large stretching factor reduces the B integral during amplification.

The compressor parameters are summarized in Table 3.2. Multilayer dielectric (MLD) gratings are the best choice for a compressor of a high-energy laser system at a wavelength close to 1  $\mu\text{m}$ . This is for several reasons.

First of all, they have a high diffraction efficiency over the target bandwidth of 50 nm. The absorption is very low compared to standard gold gratings. This makes them resistant against the thermal load of high average powers, which is essential for a repetition rate upgrade above 1 Hz. The laser induced damage threshold is higher for MLD gratings compared to gold gratings, which reduces the beam diameter in the compressor. Due to the high groove density, a compact design that saves space as well as hardware cost for the vacuum chamber can be realized.

The compressor is a standard Treacy-compressor [20], which has been discussed in Section 2.1.2.1 and illustrated in Figure 3.17. It consists of two  $940 \times 420 \text{ mm}^2$  MLD gratings arranged in a double pass configuration. The overall transmission efficiency is estimated to 84%. Here, the spectral and spatial constraints of the beam as well as the

MLD gratings		Compressor design	
groove density	17601/mm	angle of incidence	72°
diffraction efficiency	>97%	grating separation	2200 mm
grating size	940 × 420 mm <sup>2</sup>	group delay dispersion	195 ps/nm
design wavelength	1035 nm	beam diameter	250 mm
damage threshold	>1 J/cm <sup>2</sup>	design fluence	0.41 J/cm <sup>2</sup>

**Table 3.2:** Compressor design parameters according to [81].

## Ray Trace and Mechanical Layout

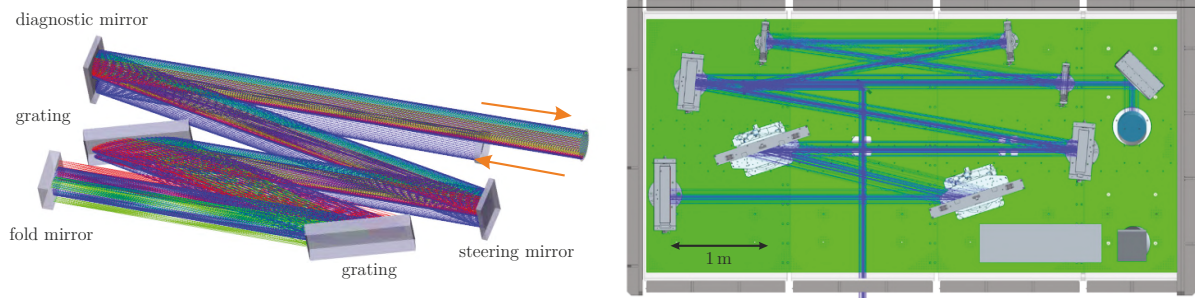


**Figure 3.17:** Ray tracing plot according to [81] as well as the mechanical layout of the compressor [99].

diffraction efficiency of the gratings are taken into account. The shift of central wavelength due to the amplifiers can be adapted within the existing design.

The separation between the input and output is done by a vertical tilt of the folding mirror. This tilt in the beam path results in a small vertical chirp of  $\sim 0.5$  mm/nm [81]. The diagnostic beam is generated by a leakage through the following folding, the diagnostic mirror (Figure 3.17). The beam size is reduced by a telescope and sent to an optical table, where all important parameters (e.g. wavefront, pulse duration, TIC, etc.) are measured and analyzed. Additionally, Figure 3.17 shows the compressor chamber with the optical and mechanical layout on the right side.

The corresponding stretcher is designed to match the compressor parameters as well as the additional dispersion due to the transmitted material like the gain medium. The optical setup of the Öffner type stretcher [100] is given in Figure 3.18.

It incorporates an Öffner triplet, meaning an aberration free telescope setup [101]. Two spherical concentric mirrors are used, the first one is concave and the second is convex. The RoC of the convex mirror is two times less compared to the concave one. The stretching factor of 195 ps/nm is realized in an eight-pass configuration reducing the required optics size. The beam path is folded two times with a horizontal and a vertical roof. The grating has the same groove density as the ones used in the compressor, i.e. 17601/mm. An angle of incidence of  $72^\circ$  is used to get a hard clip bandwidth of 50 nm at a center wavelength of

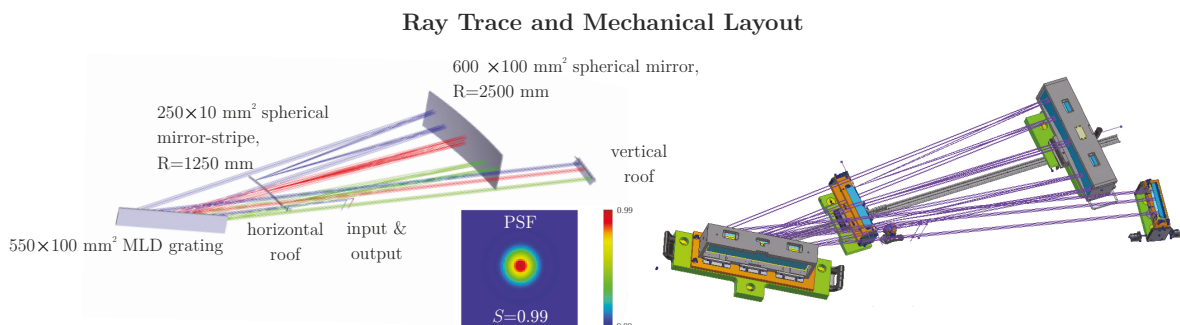


**Figure 3.18:** Ray tracing plot according to [81] as well as the mechanical layout of the stretcher. The insert picture represent the resulting PSF with a calculated Strehl ratio of 0.99 according to [81].

1035 nm. The good beam quality is tested with a Zemax<sup>TM</sup> ray tracing model and provides a Strehl ratio of 0.99 (see inset of Figure 3.18). The transmission throughput of a 15 nm Gaussian pulse is estimated to be 74 %.

The spectral performance of the stretcher and the compressor has an impact on the temporal intensity contrast. Therefore, the temporal performance is shown in Figure 3.19 (logarithmic scale). The contrast degradation is observable and the stretcher has the strongest influence. This is due to the spectral clip, which is smoothed out in the case of the compressor. Here, the hard clip is a compromise between optic size and pulse contrast. However, the numerous quantities of impact factors on the temporal intensity contrast were not taken into account.

A typical contrast curve is given in Figure 3.20. The low spectral frequency modulations lead to pre- and postpulses in the vicinity of the main pulse. The higher spectral frequency modulations, for example on the stretcher optics (surface imperfection) lead to the steepness of the falling edge to the baseline. The baseline is generated by the ASE level of the amplifier stages and was characterized for an Yb<sup>3+</sup>-doped amplifier system by S. Keppler et al. [102]. Discrete prepulses occur for example by plane parallel transmission elements (Pockels cells, waveplates etc.) or not perfectly suppressed oscillator pulses.

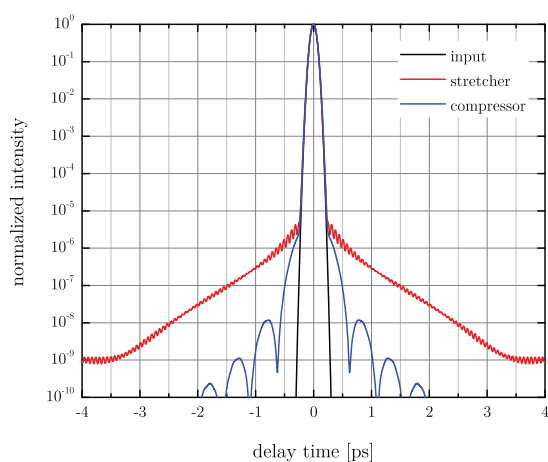


**Figure 3.19:** Temporal performance of the stretcher and compressor for a 100 fs Gaussian pulse (FWHM) in logarithmic scale, according to [81].

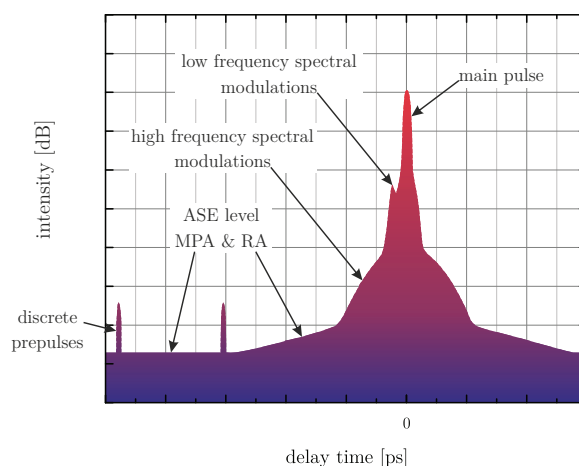


**Figure 3.20:** Schematic representation of the temporal intensity contrast of an ultra-short high-energy laser; MPA multipass amplifier, RA regenerative amplifier. The intensity is represented in logarithmic scale.

### 3.3 Laser Diodes as a Pump Sources for High-Energy Lasers

Currently laser diodes are the light source with the highest electrical to optical efficiency and show a high brightness at the same time. The first laser diodes operated at cryogenic temperatures and in pulse mode with low duty cycles only. The theoretical description of the double heterostructure in 1963 by Kroemer [103, 104] and the first successful demonstration of continuous wave (CW) operation at room temperature of an AlGaAs/GaAs semiconductor was shown in 1970 [105, 106]. With the invention of the quantum wells [107], the threshold current density was reduced and efficient room temperature operation of the laser diode was possible. Continuous improvements have been shown over recent decades to optimize output power, efficiency and brightness of the laser diode.

High-power laser diodes are interesting candidates for efficient pumping of solid state lasers, especially using rare earth doped laser materials. The thermal load of the laser material, which is pumped using laser diodes, is less compared to flashlamp-pumped one. This is due to the narrow spectral emission bandwidth. Additionally, an efficient absorption leads to a high wall-plug efficiency. Long lifetime and low running costs due to less invasive laser maintenance combined with the steadily decreasing investment costs over recent decades make laser diodes an interesting candidate to replace flashlamps as a pump source in the future.

At the moment, the starting cost of a high-energy diode-pumped laser is higher compared to flashlamp-pumped lasers. The GaAs technology for high power laser diodes from 730 nm to 980 nm are the most common ones for pumping ytterbium doped laser materials. Other wavelength ranges are possible with other semiconductor material combinations, for example GaInP.

One major advantage of the laser diode over flashlamps is their considerably better directional characteristics. The beam quality of a laser beam can be described with the beam parameter product  $BPP$

$$BPP = \frac{D_0 \theta}{2 \cdot 2} \quad , \quad (3.12)$$

where  $D_0$  is the beam waist diameter and  $\theta$  is the full divergence angle at a power content of 95%. As fast and slow axis of laser diodes have different  $BPP$ , one can define the brightness  $B$  instead as:

$$B = \frac{P}{A \Omega} \quad , \quad (3.13)$$

with  $P$  the optical power of the laser diode,  $A$  the emitting area and  $\Omega$  the solid angle in which the light is emitted. This parameter combines all important values and is useful for especially asymmetric beams. However, the difficulty lies in the definition of solid angle. The common definition is a segment area of a sphere  $A$  divided by the square of the radius  $r$ :

$$\Omega = \frac{A}{r^2} \quad . \quad (3.14)$$



The full solid angle of a sphere is  $4\pi$  sr. Figure 3.21 shows the solid angle in terms of angles  $d\theta$  and  $d\vartheta$ , where  $dA$  is a infinite area on a surface of a sphere. Equation (3.14) can be rewritten with the surface integral

$$\Omega = \iint_A \sin \theta \, d\theta \, d\vartheta \quad , \quad (3.15)$$

where  $\theta$  is the colatitude (angle from the North pole) and  $\vartheta$  is the longitude. The solution of a cone (a circular area) and pyramid (rectangular area) is given in Table 3.3. An analytic solution of an elliptical beam cannot be found. For an asymmetric angular distribution the best assumption is the pyramid and it is taken for all calculations from now on.

The angles for the x and y direction are given with a power content of  $\sim 95\%$ . A rectangular aperture in the far field has a transmission of 90% for the optical power consequently. Due to the sharp edges in the near field, almost the whole power lies in the emitting area. One should note for values given in the literature, whether the definition includes power transmission in the far field or not.

angular shape	solid angle
cone	$\Omega = 2\pi (1 - \cos \frac{\theta}{2}) = 4\pi \sin^2 \frac{\theta}{2}$
pyramid	$\Omega = 4 \arcsin \left( \sin \frac{\theta_x}{2} \sin \frac{\theta_y}{2} \right)$

**Table 3.3:** Definition for cone and pyramid shaped solid angle  $\Omega$ .

### 3.3.1 Structure and Performance

In the case of single laser diode emitters a  $TEM_{00}$  laser mode has an output power of up to several hundred milliwatts - operation at higher order modes yields in several watts of optical power per emitter. As this is sufficient for most industrial applications, high-power lasers demand more power, however. Typically, around 40 broad area emitters are combined in a so-called laser diode bar. The layout is shown in Figure 3.22 (a). The emitter has a width and a pitch, being the distance in between them. The ratio of both is called fill factor.

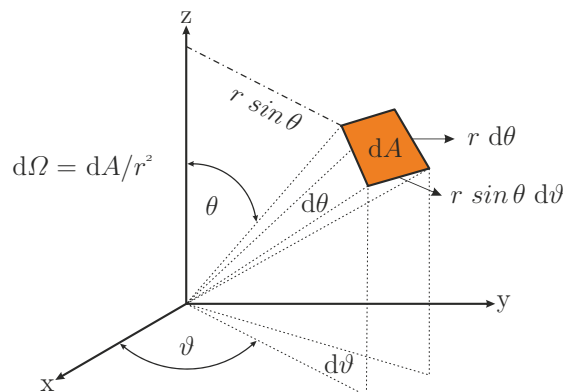


**Figure 3.21:** Solid angle in terms of angles  $d\theta$  and  $d\vartheta$ , where  $dA$  is a infinite area on a surface of a sphere.

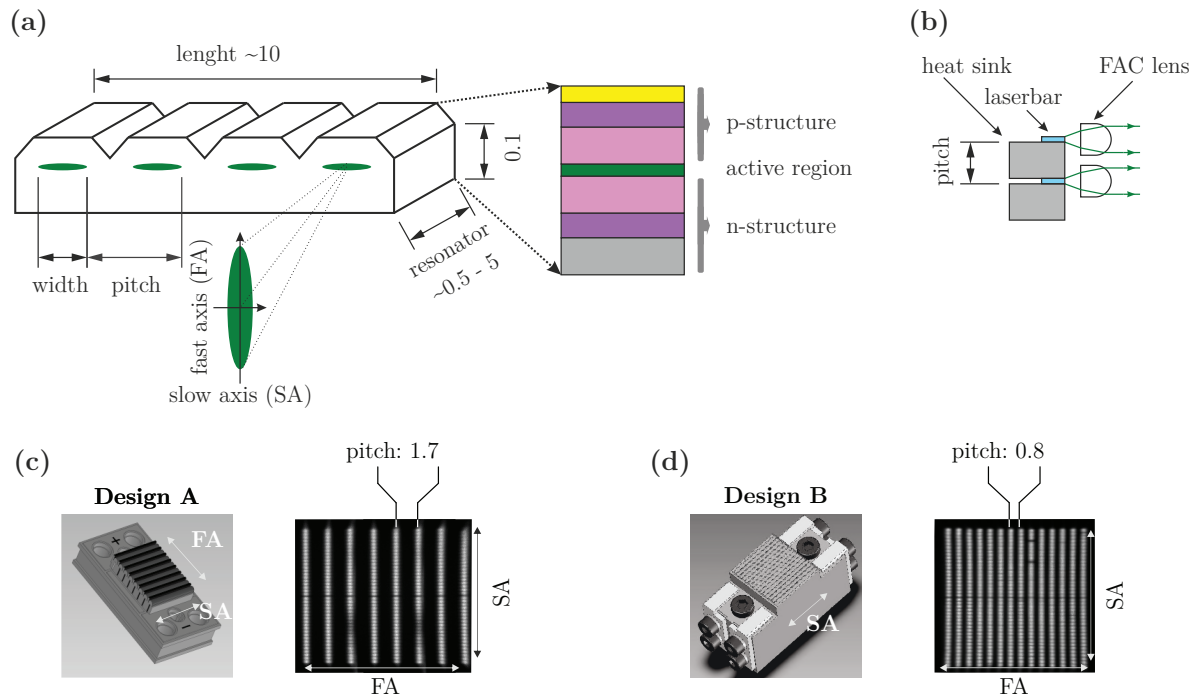


**Figure 3.22:** Overview of laser diode bars/stacks; (a) structure of a laser diode bar, typically several broad area emitters are arranged to a bar, the fill factor is the emitter width to pitch ratio of the laser diode bar; (b) stacking of several laser diode bars including fast axis collimation, the heat sink is needed to passively cool the bar; (c) a laser diode stack with a pitch of 1.7 mm, the electrical connection are in the fast axis direction, which is called design A; (d) a laser diode stack with a pitch of 0.8 mm, the electrical connection are in the slow axis direction, which is called design B. In (c) and (d) real images of the stacks are shown, which make it possible to identify the numbers of bars and emitters of the stack. All dimension are given in mm.

This factor is typically up to 50% for CW operation and up to 80% for quasi continuous wave (QCW) operation.

In QCW, mode currents up to 500 A are used to achieve optical powers of currently up to 500 W per bar. In the PENELOPE project the driving current of the laser diode stacks is limited to  $\sim 330$  A leading to an optical power of about 300 W per bar (2.4 kW for an eight bar stack). Typically, 8 to 16 bars are combined to 1 stack. Figure 3.22 (c) and (d) shows two different designs called A and B from now on.

The distance between the laser bars, the pitch, varies from 0.4 mm to 1.7 mm. The electrical connections should be in the slow axis (SA) direction for an easier assembly of the stacks. This is discussed in the next section.

The beam characteristics depends on the lateral axis of the waveguide structure, as shown schematically in Figure 3.22 (a). The fast axis (FA) is perpendicular to the active area with a nearly fundamental mode. The divergence angle  $\Theta_{FA}$  is large (around  $45^\circ$ ). The SA is parallel to the waveguide with a non-diffraction limited beam quality. This is due to the large dimension of several hundreds of micrometer. The slow axis divergence angle  $\Theta_{SA}$  is small (around  $10^\circ$ ). The fast axis collimation (FAC) can be done by using an aspheric



cylindrical lens with a high numerical aperture ( $NA > 0.7$ ). This is schematically shown in Figure 3.22 (b). The conservation of the  $BPP$  depends on several parameters:

- The smile<sup>a</sup> of the laser diode bar,
- Alignment precision of the FAC lens and
- Mounting stress in the stack.

In the case of no aberrations, the brightness is the same as for the uncollimated bar. This is the brightness theorem [91]. But in real application the  $BPP$  increases after the FAC and typically doubles at least. This depends on the given faults and varies for each stack. Therefore, the overall brightness is reduced.

While the SA divergence scales proportionally with the laser diode driving current, FA divergence is to the first order independent of it. This results in larger  $\Theta_{SA}$  for increasing output power. In recent years the development of laser diode bars with more than 500 W is also linked to new cavity designs with optimized resonator length, emitter width and pitch in order to keep the slow axis divergence as low as possible [108, 109]. What also has to be kept in mind is the wall-plug efficiency, which has to be optimized for the maximum driving current and depends on the same parameters. The efficiency can be increased by going to lower temperatures down to  $-70^\circ\text{C}$  [109].

Table 3.4 gives an overview of the different laser diode bar parameters and the stacks being tested in the PENELOPE project (marked as “old”) and the next generation of high-power laser diode bars (marked as “new”).

The new bars should show almost the same divergence as the old ones [109]. That leads to a higher brightness, which helps reduce the optic size (lower costs and complexity) of the beam transport system.

supplier	No. of emitters	width [ $\mu\text{m}$ ]	pitch [ $\mu\text{m}$ ]	No. of bars	stack pitch [ $\mu\text{m}$ ]	P/bar [W]
1 old	40	200	250	8	1.7	300
new	40	200	250	8	1.7	500
2 old	37	186	250	8	1.7	300
new	37	186	250	8	1.7	500
3 old	40	200	250	16	0.8	300
new	40	200	250	16	0.8	500

**Table 3.4:** Comparison of three different stacks from three suppliers with the old (300 W/bar) and new (500 W/bar) bars. The stack characteristics are given: the number of emitters per bar, emitter width, emitter pitch, number of bars per stack, stack pitch, optical output power  $P$  per bar.

<sup>a</sup> The smile effect, caused by thermal expansion mismatch during solder bonding, prevents the FAC lens from being correctly positioned for all points along the bar, resulting in beams with variable pointing direction.

The performance of two stack designs A and B (see Figure 3.22 (c) and (d)) were tested in terms of power, efficiency, spectrum and beam characteristics. Here, the “old” design was used and therefore the operating current was limited to 330 A. The laser diode stack has a lifetime<sup>a</sup> of more than 1 GShot, which corresponds to an operation time of more than 30 years (24/7) at a repetition rate of 1 Hz. The stacks are designed for 10 Hz operation, which yields in a 10 year long operation time with 8 h per day during the whole year. Figure 3.23 (a)-(c) show in principle the experimental measurement setups. These setups were used to characterize the brightness of the pump modules and beam transport, as well as the homogenized beam. The energy/power measurement (Figure 3.23 (a)) is based on imaging the source onto the detector. The spectral measurement setup is similar to the energy/power setup, where the detector is replaced by a scatter plate and the spectrometer fiber is placed behind it. Measuring the far field distribution is done by using a single (cylindrical) lens as a Fourier transformation element. This is illustrated in Figure 3.23 (b). The far field arises at the focal plane (FP) of the lens and the divergence  $\theta$  is calculated as

$$\theta = 2 \arctan \frac{\Delta_{95}}{2f} \quad , \quad (3.16)$$

where  $f$  is the focal length of the lens and  $\Delta_{95}$  is the smallest dimension that contains 95 % of the power. This method is used for the FA divergence of the stacks, the homogenized pump spot as well as the pump modules. Secondly, for larger divergence angles it is also possible to measure the propagation of the near field dimension  $D_{95}'/D_{95}''$  with 95 % power content at two different positions ( $d'' > d'$ ), as shown in Figure 3.23 (c). The divergence angle is determined as

$$\theta = 2 \arctan \frac{D_{95}'' - D_{95}'}{2(d'' - d')} \quad . \quad (3.17)$$

This method is of particular interest for the slow axis, as it shows angles in the order of 10°.

In the FP a screen is placed, which is imaged onto a camera. In our case, a camera from Ophir Photonics with its patented Ultracal<sup>TMb</sup> background subtraction was used.

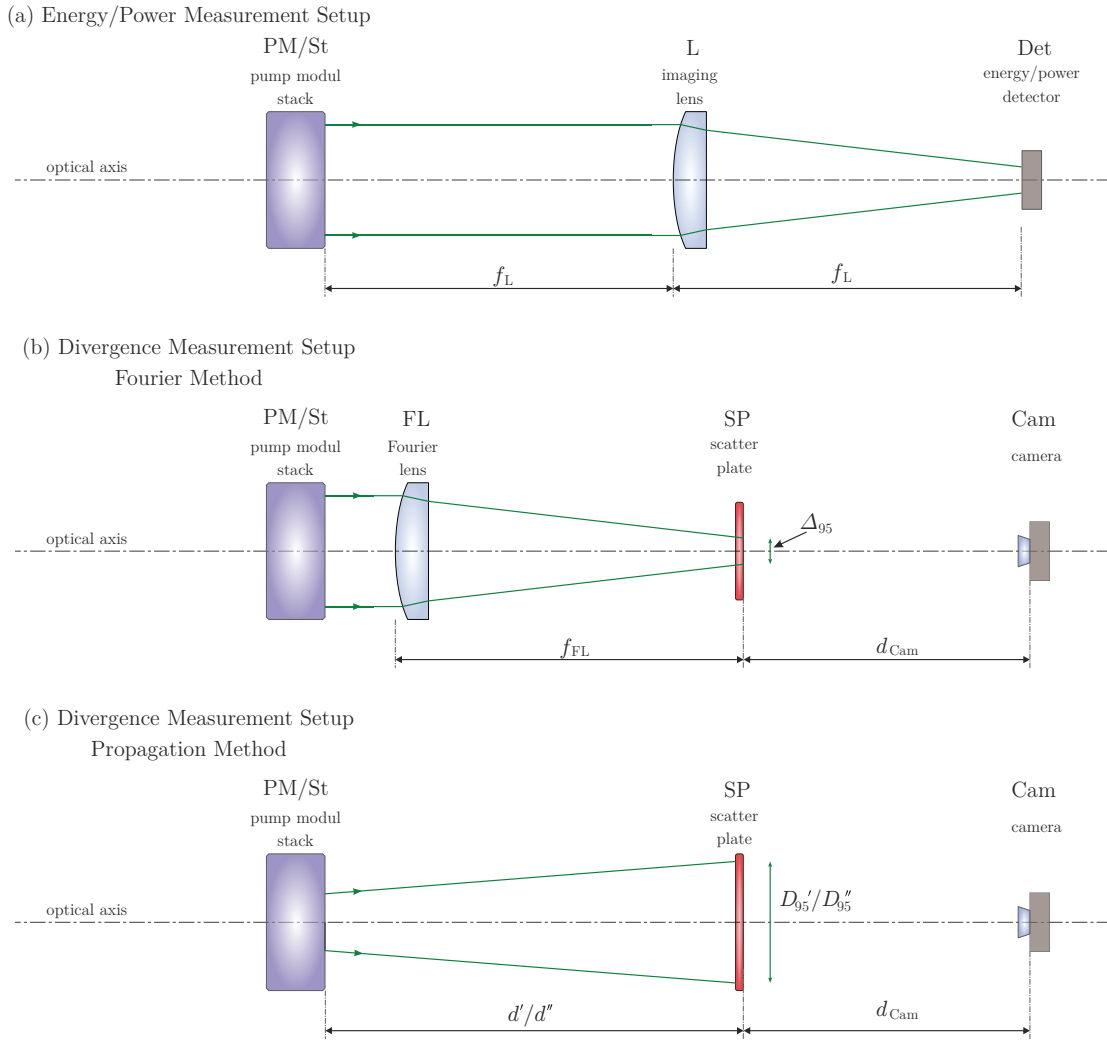
Figure 3.24 shows the spectral (a) and lasing parameters (b) of both stack designs. For a better comparison the power per bar is plotted as a function of the laser diode driving current  $\mathcal{I}_{LD}$ . Both stacks perform with only a negligible difference. The electrical-to-optical efficiency is more than 60 % in both cases. The bandwidth  $\Delta\lambda_{95}$  at 95 % power content of stack A is 6.7 nm. The spectral power is higher in design B, which is due to a smaller bandwidth of 5.9 nm, as shown in Figure 3.24 (a). The center wavelength  $\lambda_c$  was 976 nm and can be adjusted by either the cooling water temperature (0.3 nm K<sup>-1</sup>) and/or increased by applying a bias current.

Table 3.5 shows a performance summary of 32 stack for design A and 16 for B. This represents the combined number of stacks in a pump module, as described in more detail in the next section.

---

a The lifetime is defined, when the optical power is dropped more than 10 %

b Ultracal<sup>TM</sup> is a method to calibrate the zero level of the camera system. It is a more effective background compensation than other techniques.



**Figure 3.23:** Principle measurement setup of the laser diode parameters; (a) energy/power measurement of a pump module (PM) or a stack (St), L imaging lens, Det detector; (c) Fourier method to determined the divergence angle, FL Fourier lens, SP scatter plate, Cam CCD camera; (c) propagation method to measure the divergence angle.

The average FA divergence is better than  $0.5^\circ$  (8.7 mrad) in both cases, which is the specification given by the manufacturer. Divergence results are 20 % smaller for A compared to B. The spectral emission is narrower and with less variation for design B. The optical power per bar at 300 A is a few percent higher for design A. Please note, that the optical power is given before being installed into a pump module. The SA divergence (not shown in Table 3.5) was measured with the propagation method and the calculated values are between  $8^\circ$  and  $9^\circ$ , better than the guaranteed  $10^\circ$  at the maximum driving current.

Overall, the performance of the stacks is better than the guaranteed values for most of the parameters. The average brightness for design A is  $2.15 \text{ MW}/(\text{cm}^2 \text{ sr})$  and  $3.35 \text{ MW}/(\text{cm}^2 \text{ sr})$  for B, when  $\Theta_{SA}$  equals to  $9^\circ$ . The value in case A can be doubled up by interleaving two stacks.

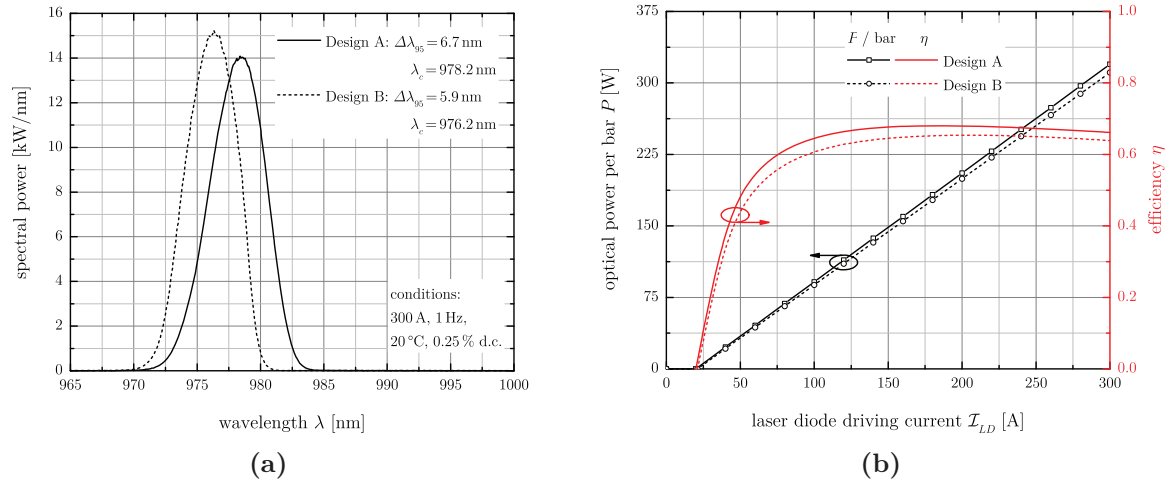


**Figure 3.24:** Laser diode stack performance; (a) emission spectrum of the laser diode stacks, the characteristic parameters bandwidth  $\Delta\lambda_{95}$  at 95 % power content, as well as the center wavelength  $\lambda_c$  and the measurement conditions are inserted; (b) output power per bar and optical-to-electrical efficiency as a function of the laser diode driving current  $I_{LD}$ .

	divergence				spectral emission						optical power			$B$
	[mrad]				[nm]						[kW]			$[\frac{\text{MW}}{\text{cm}^2 \text{sr}}]$
	$\Theta_{FA}$				$\Delta\lambda_{95}$				$\lambda_c$				$P$	
	N	av	min	max	av	min	max	av	min	max	av	min	max	av
A	32	5.63	4.55	7.44	7.7	6.8	9.1	978.1	977.5	979.1	2.58	2.52	2.66	2.15
B	16	6.88	6.38	7.69	6.5	6.3	6.7	976.1	975.8	976.5	4.83	4.81	4.87	3.35

**Table 3.5:** Statistical analysis of the performance of the two stack designs, such as FA divergence  $\Theta_{FA}$ , spectral bandwidth  $\Delta\lambda_{95}$  at 95 % power content, center wavelength  $\lambda_c$ , optical power  $P$  and the brightness  $B$ ; N number of stacks, av average value, min minimal value, max maximal value.

### 3.3.2 Beam Combination, Shaping and Transport

Incoherent beam combination of individual laser diode stacks is common in pump sources for high-energy laser systems. In the state of the art high-energy amplifiers, high brightness laser diodes are needed to get a compact and cost efficient pump source. The goal is to conserve the brightness of a stack  $B_{St}$  or to increase it for the pump module assembly  $B_{PM}$ . There are several ways to archive this [110]:

- spatial multiplexing,
- increasing the filling factor with interleaving or enlarged focal length of the FAC lens,
- polarization coupling or
- wavelength coupling.

The basic principle is spatial multiplexing, where the stacks are simply set side by side in a one- or a two-dimensional array. The maximum  $B_{PM}$  can be linked to the  $B_{St}$ , on which the system is built. The overall relationship is given as [110]:

$$\begin{aligned}
 B_{PM} &= \eta_{PL} \cdot \eta_{StQ} \cdot \eta_{FF} \cdot \kappa_{FF} \cdot \kappa_P \cdot \kappa_W \cdot B_{St} & (3.18) \\
 \text{with } \eta &\leq 1 \text{ and } \kappa \geq 1 \\
 \eta_{PL} &= \frac{P_{PM}}{N} \\
 &\quad \sum_{i=1} P_{St_i} \\
 \eta_{StQ} &= \frac{\arcsin\left(\sin \frac{\theta_{FA,St}}{2} \sin \frac{\theta_{SA,St}}{2}\right)}{\arcsin\left(\sin \frac{\theta_{FA,PM}}{2} \sin \frac{\theta_{SA,PM}}{2}\right)} \\
 \eta_{FF} &= FF_{FA} \cdot FF_{SA} \\
 \kappa_{FF} &= 2 \\
 \kappa_P &= 2 \\
 \kappa_W &= j \quad ,
 \end{aligned}$$

where  $\eta_{PL}$  is the power loss due to the optical components (including polarization losses),  $\eta_{StQ}$  is the angular tolerance in the FA direction (fast axis pointing) of the individual laser diode stacks,  $\eta_{FF}$  is filling factor quality (aperture underfilling) with the filling factor in FA  $FF_{FA}$  and SA direction  $FF_{SA}$ ,  $\kappa_{FF}$  filling factor increase by interleaving or other techniques,  $\kappa_P$  brightness increase by polarization coupling and  $\kappa_W$  brightness increase by wavelength multiplexing with  $j$  coupled wavelengths.

Wavelength multiplexing can be used, if the gain medium possesses a broad absorption peak compared to the spectral bandwidth of each individual laser diode. This is however often not the case and it turns out even more unlikely for high-power lasers, as usually one tries to minimize the difference between the pump and extraction wavelength in order to reduce the thermal impact.

In the case of the polarization multiplexing one has to consider whether the gain material to be pumped is susceptible to polarization or not and if the non-perfect state of polarization of the laser diode output (about 90%) leads to unacceptable losses during the polarization combination itself.

Interleaving and optimization of the FAC lens are typically more promising approaches. Taking as an example the stack design from Section 3.3.1, a viable option for both would be further optimization of the FAC lenses to decrease the FA divergence angle (i.e. longer FAC focal lengths). While stack design A shows a rather large pitch between each bar offering an option for interleaving, stack design B has a far too small pitch to accommodate a practical realization of it.

The most critical point is the stacking quality  $\eta_{StQ}$ , which is the ratio of the solid angle of each individual stack compared to the whole pump module. The FA pointing of the stacks increases the global divergence of the PM and therefore brightness is lost. The pointing of every individual stack has to be equal or it must be corrected. Typically machining precision is in the order of mrad, thus SA pointing due to the stack misalignment is negligible.

Beam combination and beam transport has to follow Equation (3.18) as well. Consequently, aberrations of the imaging system have to be kept considerably low. Furthermore the optical losses have to be taken into account, which means that the AR/HR coating of the optics has to be as good as possible.

The goal for the pump source in the PENELOPE project was to find a suitable vendor delivering the pump modules and, if possible the whole beam line with its homogenization stage.

First of all, the parameters for the pump modules were specified. Most important is that the brightness of the PM should be as close as possible to the doubled stack value via interleaving in the case of design A or nearly the same for design B. Therefore the stacking quality  $\eta_{StQ}$  and the power loss  $\eta_{PL}$  has to be larger than 0.95, yielding a  $B$  conservation of more than 90% in total. The spectral bandwidth with 95% power content should be smaller than 9 nm and the center wavelength has to be at  $976 \pm 1$  nm at the operation point (driving current of 300 A, pump duration of 2.4 ms). Fine tuning could be done with the cooling water temperature and a bias current.

Following on from this, the radiation pattern of the pump module has to be defined and shaped. The  $BPP$  has to be similar in both axes. This leads to a number  $N$  of  $2 \times 16 = 32$  (interleaving) in design A and 16 stacks for design B, which have to be arranged in an one-dimensional array along the FA direction. Here, the manufacturer guaranteed values are taken to calculate the  $BPP$ . For a compact pump module design with a high filling factor the interleaved stacks (design A) have to be arranged using turning mirrors. This is due to the fact that the electrical connections are in the FA direction.

In the other design they can be directly assembled as the electrical connections are in SA direction. The stacks are passively cooled by a water-cooled cooper heat sink. A hermetical package of the laser diodes is chosen to separate the cooling water from the active elements to avoid damage in the case of water leakage. The diode light emits through an anti-reflection (AR) coated window at the front panel. Due to the sealing of the laser diodes it is possible to purge them with dry air to prevent water condensation at cooling temperatures below 20°C. The electrical, interlock and water connections are on the backside of the pump modules. For safe machine operation, several interlock signals are measured, especially humidity and temperature at different positions within the PM. Figure 3.25 shows both pump modules and a typical near field profile.

The directional characteristics of the PMs are determined with the same setup as is shown in Figure 3.23. At first, a PM using stack design A was tested. For the  $\theta_{FA}$  a cylindrical lens with a focal length of 1442 mm was used to determine the FA divergence. The focal length was measured using an autocollimation setup. The image size of the focal plane on

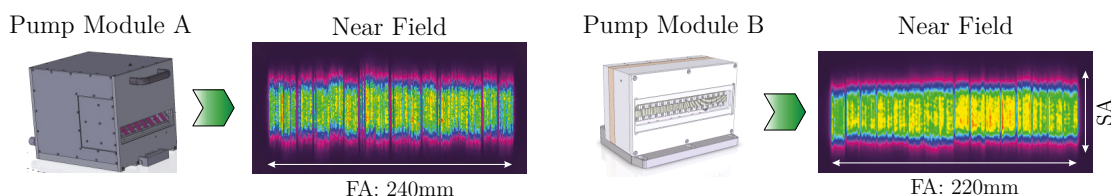


**Figure 3.25:** 76kW pump module consisting of 32 stack for design A and 16 for B and a typical near field profile after 300 mm propagation for both, according to [81]. The FA dimension is almost the same.

the CCD was chosen to have a good resolution and a measuring range being large enough to catch the stack pointing of a whole PM. The repeatability was specified to be better than  $\pm 0.05$  mrad by measuring the same module several times after removal from the setup.

At the beginning the pointing error of the stacks (PM A) was too high and had to be corrected. As a stop criterion, the pointing error of the individual stacks was set to no more than  $\pm 0.5$  mrad and the  $\theta_{FA,PM}$  has to be less than the average divergence of the stacks plus 0.3 mrad.

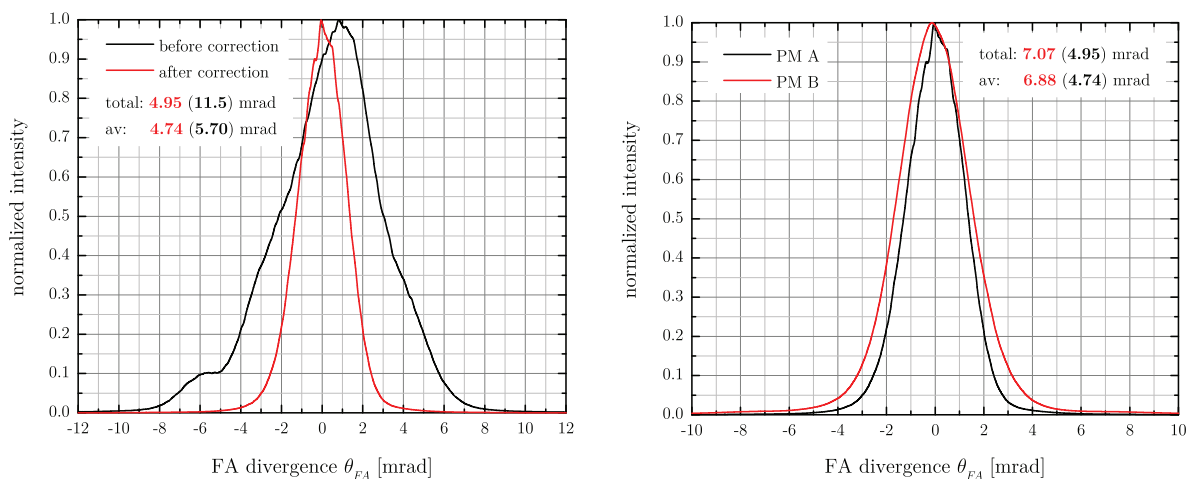
One module for design A and B is measured to compare both. Figure 3.26(a) shows the FA divergence of the pump module before and after the correction. The  $\theta_{FA}$  divergence of PM A was measured to about 11.5 mrad, but the average value of the installed stacks was only about 5.70 mrad. The total divergence of the FA could be reduced by correcting the stack pointing. That leads to a divergence of 4.95 mrad. At the same time, the average stack divergence decreased as well.

Due to mounting stress the mirrors were deformed leading to a substantial wavefront aberration. Thus, the mirrors add an additional divergence to the reflected stack output. This was corrected by the manufacturer at the same time the FA pointing was optimized.

For design B the error is not that large and therefore the stack pointing is constant for all the stacks. This leads to  $\theta_{FA,PM}$  of  $\sim 7.6$  mrad. The average divergence of the stack is larger for design B compared to stack design A.

A comparison of both PM is shown in Figure 3.26(b). In addition, the optical output power is measured for both designs. All parameters are compared in Table 3.6. Furthermore, the brightness of the whole pump module, as well as for the individual stacks is given.

It can be seen that PM A has reached the highest brightness, but suffers the worst brightness conservation at the same time. The largest deficit is the power loss and filling factor. However, the stacking quality is very good. The total installed power is reduced by about 7% for PM A and less than 1% for B. The gap between each stack is 2.25 mm in the



(a) Fast axis divergence of pump module A before and after the pointing correction.

(b) Comparison of the FA divergence of PM A and B.

**Figure 3.26:** Fast axis divergence is given for the pump modules. The results for the total and average are given at 95% power content. This corresponds to typical curves, but absolute values can differ.



PM	divergence		optical power		emitting area		filling factor	brightness	
	$\theta_{FA,St}$	$\theta_{FA,PM}$	$P_{out}$	$\eta_{PL}$	FA	SA	$FF_{FA}$	av $B_{St}$	$B_{PM}$
	[mrad]	[mrad]	[kW]	[%]	[mm]	[mm]	[%]	[ $\frac{MW}{cm^2 sr}$ ]	
A	4.74	4.95	76.9	93	238	10	86	2.15	3.75
B	6.88	7.07	77.3	99	216	10	88	3.35	2.90

**Table 3.6:** Comparison of both PM concepts in terms of brightness conservation.

case of PM A and 1.6 mm for B. This results in a filling factor of 86 % or 88 %, respectively. The filling factor has obviously the strongest impact on the decrease in brightness.

For the final amplifier stage of the PENELOPE laser, pump modules of design A were chosen as the pump source. Thereby, all optical beam lines are designed and optimized for these PMs (also called PM80). This is presumed in the following.

The large asymmetric near field pattern of the PM is symmetrically reshaped by a relay imaging cylindrical lens telescope for both axes. For designing such systems, an optical ray tracing software with the option of illumination calculation is necessary. In this case, Zemax<sup>TM</sup> in the non-sequential mode is used to design the beam shaping, combining, transport and homogenization system. Zemax<sup>TM</sup> has the capability of full three-dimensional sources, optical components, etc.

First of all, a laser diode source has to be generated for the pump modules. Zemax<sup>TM</sup> has an implemented source for laser diodes, called “Source Diode” [111]. The position and angular intensity distribution of a laser diode bar or stack can be modeled. The FAC is done with the LIMO FAC590 lens from the standard Zemax<sup>TM</sup> lens catalog.

The far field intensity distribution for the SA can be approximated with a super-Gaussian distribution, where the Super-gaussian factor is 2. The real  $\theta_{FA}$  is typically larger than in the ideal case. The main reason is the so-called smile. This can be adapted by changing the emitter size in the FA direction. The parameter for the source and the resulting values after the FAC are given in Table 3.7.

No.	Zemax <sup>TM</sup> Source Parameters									After FAC	
	Stack			Bar						$\theta_{FA}$	$\theta_{SA}$
	Delta x	$P_{St}$	Nx	Ny	sy	Delta y	alpha x	sx	alpha y	[mrad]	[°]
	[ $\mu m$ ]	[kW]			[ $\mu m$ ]	[ $\mu m$ ]	[°]	[ $\mu m$ ]	[°]		
1	850	2.4	16	40	200	250	21.5	1.677	4.55	6	8
2								2.007	5.12	7	9
3								2.211	5.50	7.7	10

**Table 3.7:** Example of the Zemax<sup>TM</sup> source parameters and the resulting angular distribution; The exact definition can be found in [111]; Delta x stack pitch;  $P_{St}$  optical power per stack; Nx number of bars per stack; Ny number of emitters per bar; Delta y emitter pitch; alpha x/y Gaussian width for the angular distribution; s x/y Gaussian width for the spatial distribution; Here, x stands for the fast axis and y for the slow axis direction.



The divergence of a modeled PM is matched with a stack that has the average divergence of the real pump module. A set of parameters is given in Table 3.7, which are linked to the measurements. Now, the PM can be modeled by arranging the stacks with a pitch of 15 mm. The interleaving can be realized with a doubled number of bar per stack and the pitch is two times less than before. The other way is to use a slotted turning mirror, where one beam is transmitted and one is reflected.

To analyze the optical quality of the imaging system in a worst case scenario, the “Two Angle Source” is used, providing a rectangular and flattop distribution for the spatial and angular space. Distortions are easier to catch using spatial and angular apertures. Thus, the power loss represents the aberrations of the imaging system. In the near field an area of  $240 \times 10 \text{ mm}^2$  and  $0.5^\circ \times 10^\circ$  in the far field are used for calculations. This simplified source was used to optimize all sections of the beam delivery system. At the end, the real source was taken to verify imaging system in a more realistic case.

The beam profile of the combined pump modules has to be transformed into a homogeneous and a flattop pump spot. For this purpose different techniques can be used like light pipes, segmented mirror, “Fly’s Eye Condensers” or similar. For more than 100 years “Fly’s Eye Condensers” (Köhler integrator) have been used to homogenize the illumination in a microscope [112]. Today microlens arrays (MLAs) are the most common solution for homogenizing a wide range of light sources, for example Excimer lasers, light emitting diodes (LED) or laser diodes [113]. A short overview of the optical properties of refractive beam homogenizers is given and detailed information can be found in [113].

There are two types of MLA based homogenizers, which are called “Non-Imaging” and “Imaging homogenizer”. Here, only the Imaging case is used as the brightness transfer, homogeneity and edge sharpness is better than in the Non-Imaging setup [113]. Both types consist of either cross-cylindrical, square or hexagonal micro-lens arrays. The principle setup of an Imaging homogenizer is shown in Figure 3.27. The first MLA divides the incident beam into several beams called “beamlets”. The second one, in combination with the Fourier lens (FL), superimposes the images of every beamlet in the first array onto the homogenization plane, which is the focal plane (FP) of the FL. The beam size  $D_{FT}$  of the homogenized beam is given by: [113]

$$D_{FT} = \frac{\mathcal{P}_{MLA1} f_{FL}}{f_{MLA1} f_{MLA2}} (f_{MLA1} + f_{MLA2} - a_{12}) \quad , \quad (3.19)$$

where  $\mathcal{P}_{MLA1}$  is the pitch of the lenses,  $f_{FL}$  is the focal length of the FL,  $f_{MLA1}$  and  $f_{MLA2}$  are the focal lengths of  $MLA_1$  and  $MLA_2$  and  $a_{12}$  is the separation of the MLAs. This is the

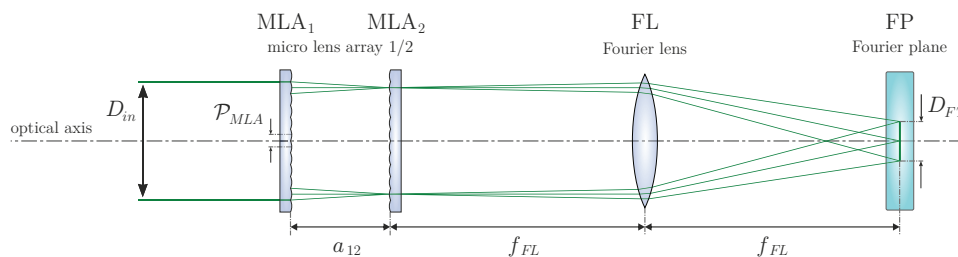


**Figure 3.27:** Imaging homogenizer consisting of two MLAs, a Fourier lens and the homogenized beam appears in the focal plane.

general equation and can be simplified by using the same MLA twice and the separation is equal to  $f_{MLA}$ . This leads to

$$D_{FT} = \frac{\mathcal{P}_{MLA} f_{FL}}{f_{MLA}} \quad . \quad (3.20)$$

The full acceptance angle  $\theta_{MLA}$  of the MLA is determined with

$$\frac{\theta_{MLA}}{2} = \arctan \left( \frac{\mathcal{P}_{MLA}}{2 f_{MLA}} \right) \quad , \quad (3.21)$$

where the pitch is equal for both dimensions of a rectangular lens array. In the case of a hexagonal shaped lens array the inner radius should be used. It equals to  $2/\sqrt{3}$  times the outer radius of the hexagon.

Normally the divergence of the laser diode beam has a nearly circular shape and Gaussian distribution. If the input divergence is larger than the acceptance angle, a cross talk of the beamlets occurs and in the FP ghosts around the central beam are visible. The complexity consists in aligning the two MLA parallel to each other and the center of the lenses have to be exactly in a line with the correct orientation at the same time. This can be avoided by using a monolithic MLA, having both surfaces structured on the same substrate. In this case it must be considered that the focal length in air  $f_{air}$  has to be multiplied with the refractive index  $n$  of the glass

$$f_{MLA}^{glass} = f_{MLA}^{air} \cdot n \quad . \quad (3.22)$$

One should note that the periodic structure acts as a grating, and a two dimensional diffraction pattern can be measured in the FP for a coherent source [114].

For the last two amplifier stages the schematic pump setup is shown in Figure 3.28. The multi-slab based amplifier is pumped from both sides in a double pass pumping configuration. The transmitted pump light is re-imaged using lens  $L_2$  and end-mirror M onto the gain material. The incoming and recovered beams are angularly multiplexed. For the final amplifier stage eight PMs have to be combined for one beam (see upper Figure 3.28). The near field of a single PM is transformed to an area of  $50 \times 50 \text{ mm}^2$  with a nearly symmetric far field and combined to an asymmetric  $2 \times 4$  pattern. A hexagonal MLA and a Fourier lens are used to generate a hexagonal flattop near field. The near field before the MLA is transformed into the far field of the homogenized beam. Therefore the angular multiplexing leads to a symmetric far field. The brightness of the pump source is high enough to separate the pump and the laser beam without the use of a dichroic mirror.

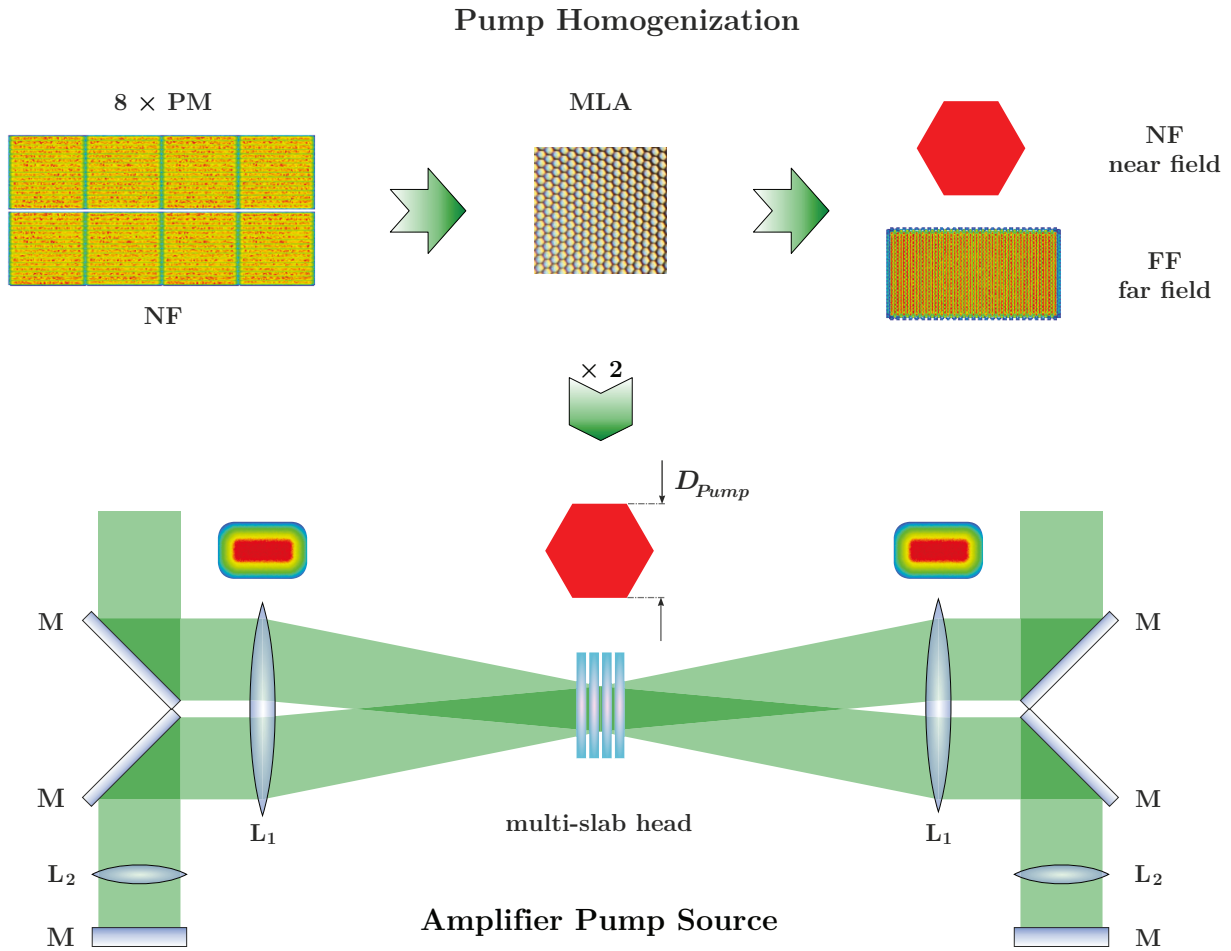


**Figure 3.28:** Top: Principle setup of the pump homogenization employing an MLA with hexagonal lens shape and resulting near and far field. Bottom: Schematic representation of the two side pump multi-slab amplifier with pump recovery, the beams are angularly multiplexed.

### 3.3.3 Experimental Benchmark of the 10 J Amplifier Pump Source

In order to test the pump module combination and beam homogenization concept on the 10 J level, pump module prototypes were used. As these pump modules are forerunners of the final amplifiers PM80s, the so-called PM48s are not FA corrected, nor do they show a symmetric *BPP*. They consist of  $2 \times 10$  stacks in the FA direction and five stacks are combined in one driving current channel, resulting in four channels per PM48 in total.

This stage is used to test all important sections for the final system and to benchmark the ray tracing simulations. The emitting near field area (FA  $\times$  SA) of  $150 \times 10 \text{ mm}^2$  is modified via two crossed cylindrical lens telescopes to  $8 \times 16 \text{ mm}^2$ . Two modules are combined in the FA direction to generate a symmetric near field. The used cylinder lenses with height, width, center thickness and RoC are given in Table 3.8 with the requested tolerances. Figure 3.29 shows the top and side view of the optical setup from the source until the combination. The lens distances from the source<sup>a</sup> were optimized to have both IP (FA & SA) on the same position and the lowest divergence angle at the same time. This was done by optimization of one beam line without the mirrors in a simple linear setup. A detector was used as an aperture in the spatial as well as in the angular domain. Its size in the image plane is corresponding to the source size scaled to the magnification factor of the imaging system. The encircled energy on the detector is more than 97%. This means that the brightness should be preserved due to the low aberrations of the optical system. The near field is given on every lens as well as in the IP in the optical system (see bottom pictures in Figure 3.29), traced with the real source.

The large asymmetric beam profile of the source is transformed into a symmetric one, when two PMs are combined. The evolution of the beam is shown in Figure 3.29 at the bottom. A highly reflective coated right angle mirror prism is used to combine the PMs. One beam gets reflected, while the other passes by. This method enables the positioning of the beams as close as possible and the best stacking quality.

It results in a high filling factor (see inserted picture on the lower left of Figure 3.29). The prism can be shifted in the plane of the optical table. The orientation of the pump module image is rotated by  $90^\circ$  using a periscope, resulting in a easier beam combination

component	RoC	length (pl)	width (cx)	center thickness
	[mm]	[mm]	[mm]	[mm]
FAL1	495.69	80	160	15
FAL2	26.44	30	20	6
SAL1	200.82	160	90	6
SAL2	321.30	100	90	6

**Table 3.8:** Component list of the crossed cylindrical lens system with the given dimensions and tolerances with  $\pm 0.1 \text{ mm}$  for all dimensions and  $\pm 0.5 \%$  for the RoC, respectively. The convex (cx) and plane (pl) side is indicated in brackets.

<sup>a</sup> In this case, the simplified source was used.

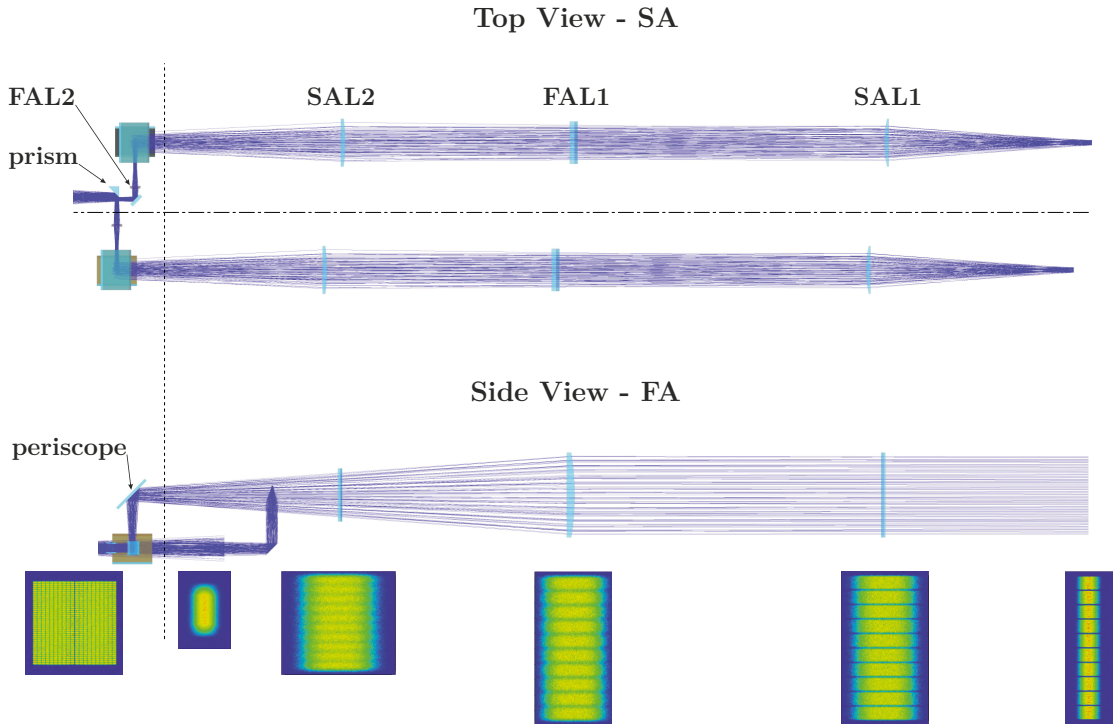


**Figure 3.29:** The top and side view of both cylindrical lens telescopes are given, where the SA is in the top and the FA in the side view. In the side view only one beam line is visible and the semicolon line in the top view represent the cutoff plane. The dashed line stands for the change of the axes due to the image rotation of the periscope. On the bottom the near field is shown in the IP, on the FAL2, SAL2, SAL1, SAL1 and 100 mm after the source by starting from the left.

alignment. This is represented by the dashed line in Figure 3.29, where in the top view the FA can be seen on the left side instead of the SA. The same applies to the side view with the axes reversed.

The opto-mechanical layout is given in Figure 3.30. The homogenization section and beam shaping is presented on the left side as well as the whole setup including the final imaging telescope (double pass pumping) and the gain material slabs in the picture on the right. In order to adjust the divergence angle of the pump modules to the numerical aperture of the MLA, a subsequent spherical lens telescope (red-purple rectangular) with a variable magnification is inserted. The homogenization section, including the Fourier lens, is illustrated with the blue rectangle. The IP of the homogenized beam as well as the beam shaping is marked by the green rectangle. The technical drawing of the used MLA is given in Figure 3.31. This document was provided with kind permission of *A $\mu$ S Advanced Microoptic Systems GmbH*, the manufacturer of the monolithic MLA. The full acceptance angle of the inner circle is  $3.1^\circ$  when using Equation (3.21). The Fourier lens is designed as a doublet (with a slightly variable focal length), consisting of two identical lenses, which can be separated to adjust the spot size  $D_{FT}$ . This gives the possibility to increase the pump spot size for higher output energies of MPA III with similar fluence on the optics.

Finally, the hexagonal beam is shaped circularly with a hard aperture. It is represented in the green rectangle in Figure 3.30. This beam is imaged onto the gain material using a

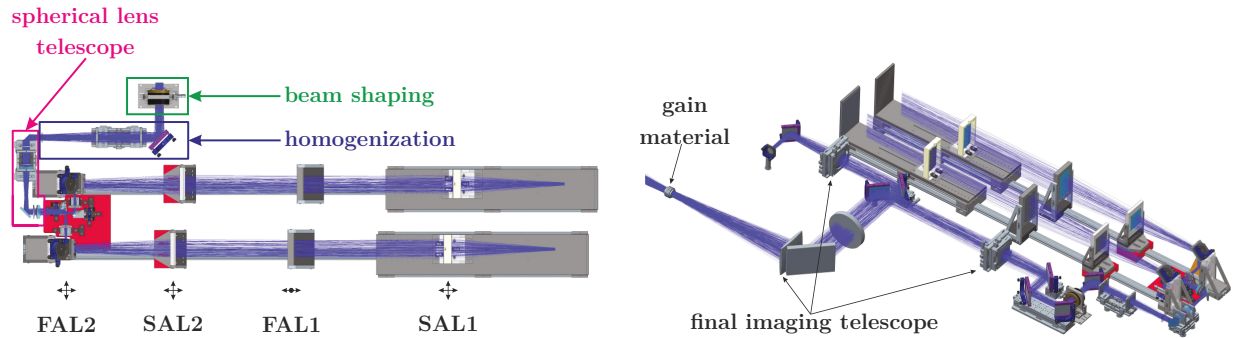
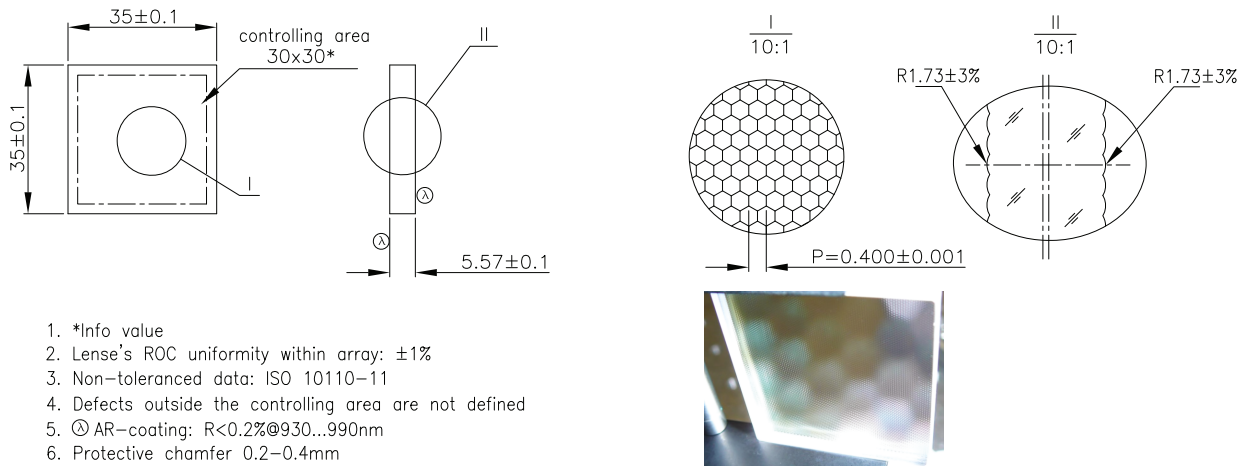


**Figure 3.30:** Opto-mechanical layout of the MPA III pump source. On the left side the top view is given with the marked sections after the combination. Red-purple is the spherical lens telescope, blue is the homogenization with the MLA as well as the Fourier lens and in green the beam shaping section, which is placed in Fourier plane of the FL. Furthermore, the possible adjustment of the lenses is shown in the lower left. On the right side the whole pump source is illustrated starting at the stacks until the gain material slabs. In addition, the final imaging telescope is given, which is shown in principle in the lower part of Figure 3.28.



1. \*Info value
2. Lense's ROC uniformity within array:  $\pm 1\%$
3. Non-toleranced data: ISO 10110-11
4. Defects outside the controlling area are not defined
5.  $\odot$  AR-coating:  $R < 0.2\%$  @ 930...990nm
6. Protective chamfer 0.2-0.4mm

**Figure 3.31:** Technical drawing of the used MLA with the given specifications and a picture of it on the lower right. The drawing were provided with kind permission of *AµS Advanced Microoptic Systems GmbH*.

relay imaging telescope, as shown in Figure 3.30 on the left side. The aperture is designed to catch all the reflected light and can be water cooled. The surfaces are black nickel coated for a very low reflectivity. The principle design and ray trace of the beam shaping is shown in Figure 3.32. The transmission is about 85 % including the losses of the MLA, as well as the beam shaping section.

The near and far field onto the MLA for all four driving current channels of one PM are shown in Figure 3.33 and can be compared with the ray tracing result, performed with a realistic source. So far it can be clearly seen that the pointing error for the FA has an important influence and has to be corrected. Furthermore, the SA divergence of these stacks shows a pedestal. The reason for this could be higher order modes in the emitters of the laser diode bar. This is not the case for the final amplifier pump module. In the near field, the structure of the stacks can be identified and no image distortion is present.



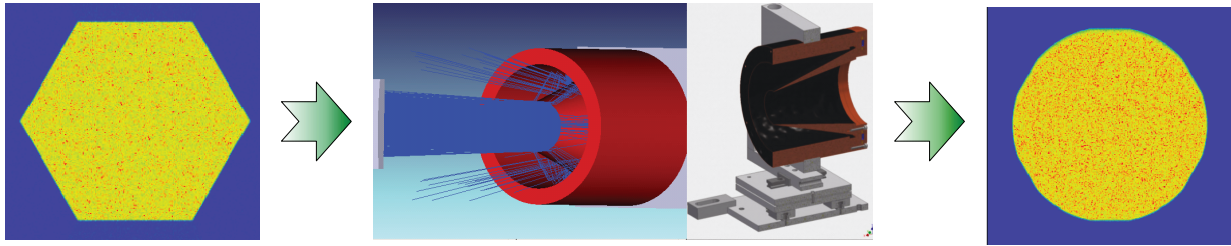


**Figure 3.32:** Beam shaping of the hexagonal flattop pump spot with a hard aperture, the input is on the left and the output on the right side. In between the aperture is shown as a cross section and the ray trace with 100% reflectivity on the surface to illustrate the ray catching capability.

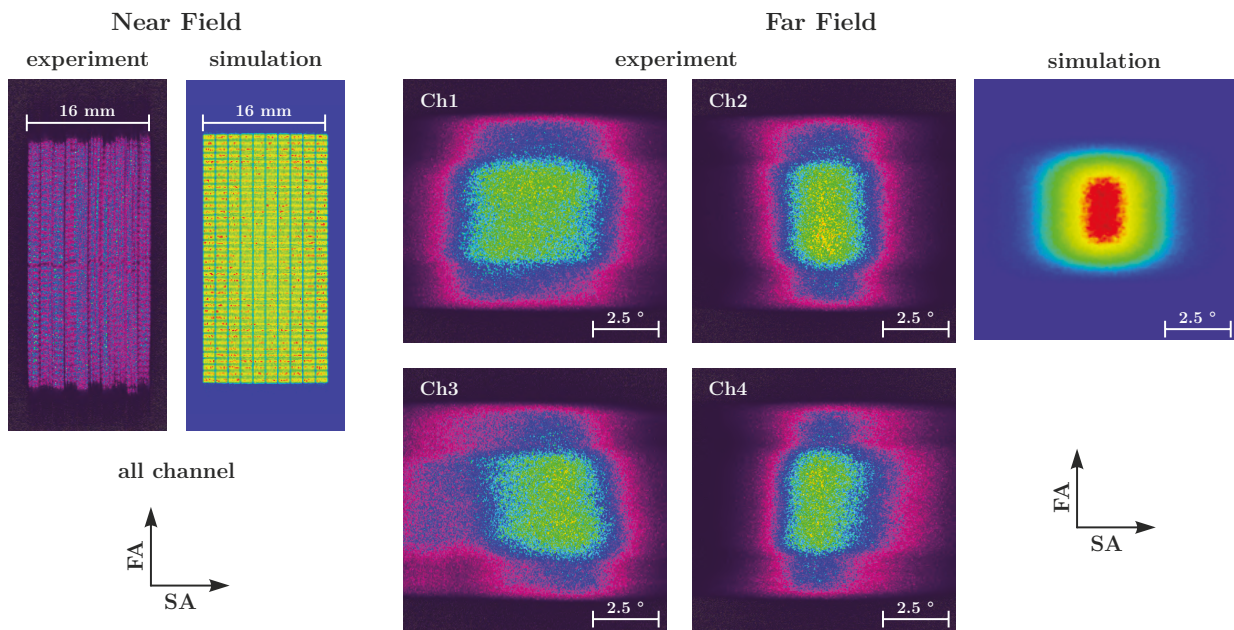


**Figure 3.33:** Experimental and simulated near and far field of one PM in the combination plane. The experimental far field is shown for every current channel separately. All images were measured at 300 A with a pulse duration of 1 ms.

The near field combination of the stacks in one PM has a small error in the SA direction, but that does not play an important role. For the measured near field a satisfactory match with the ray tracing result was found. The far field distribution of channel 2 (Ch2) and Ch4 looks similar to the simulation and the best performance of the pump module could be estimated. However, the pointing would have to be adjusted. To fit the required divergence onto the MLA (acceptance angle) the beam is manipulated by the spherical lens telescope after the combination. The experimentally measured and simulated homogenized beam (near and far field) are shown in Figure 3.34.

The hexagonal spot of one PM was achieved by using a test lens with a focal length of 200 mm.

Due to the not perfect far field distribution of the PM, ghosts around the central spot are observed. There is a satisfying correlation between the ray trace and the experiment. The plateau of the flattop beam has a peak-to-valley (P-V) of 7% and an rms of 2%. But what has to be kept in mind is the structure of the scatter plate, which is used to measure

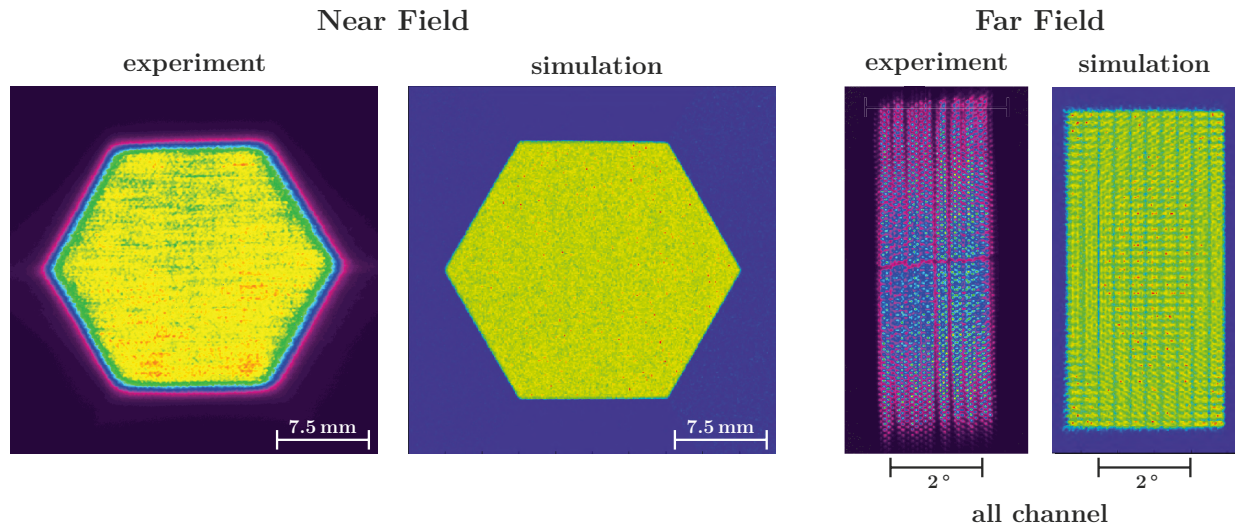


**Figure 3.34:** The homogenized beam profile and the associated far field distribution for both cases (experiment and simulation). Here, all driving current channel are running at 300 A with a pulse duration of 1 ms.

the beam profile, leading to a high frequency modulation. Thus, the P-V and rms values are deteriorated.

This can be reduced by moving the screen and averaging the image. The best way is to image the beam profile directly onto the camera chip. Thus, a large area CCD camera is needed due to the rather poor beam parameter product of the laser diodes.

The vertical profile lines of the near fields (see Figure 3.34) are given in Figure 3.35. The difference are the sharp edges, as well as the spot size being 12 % smaller in the experiment. The modulation in the plateau of the Zemax<sup>TM</sup> ray trace is due to the low ray number and can be in principle reduced by a long trace with more rays.

The edges of the measured spot have a smooth transition between the plateau and the baseline, whereas the simulation shows a steep transition. The reason for the difference is the intermediate zone between the lenses in the real manufactured MLA, as they are not

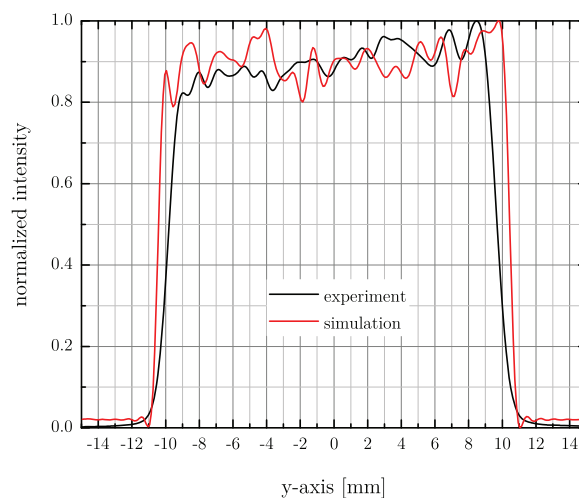


**Figure 3.35:** Vertical profile line of the measured and simulated beam spot.



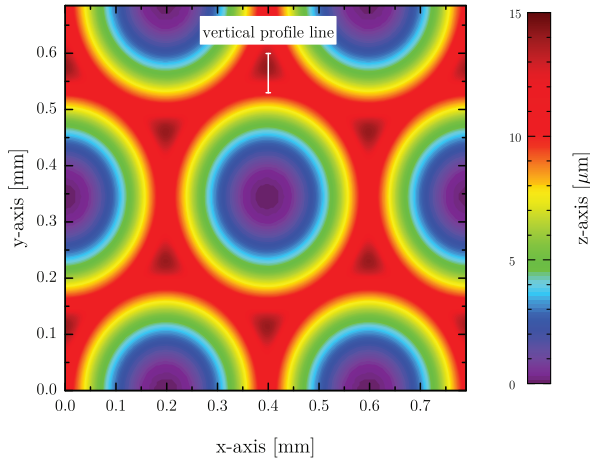


**Figure 3.36:** Contour plot of the height profile of a part of the real produced lens array with a whole lens in the middle and the neighboring lenses up to half. The vertical profile line of Figure 3.37 is marked in white. The data were provided with kind permission of *A $\mu$ S Advanced Microoptic Systems GmbH*.

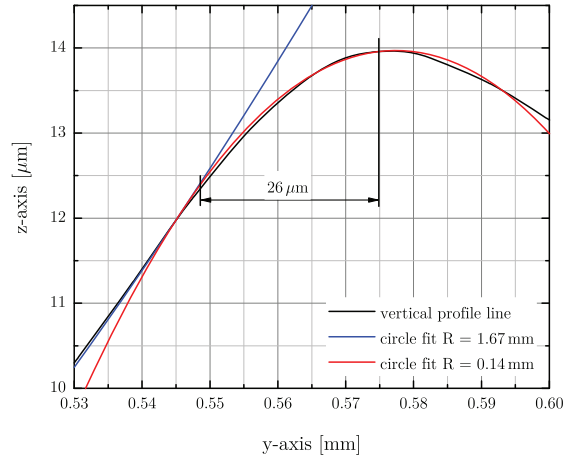


**Figure 3.37:** The vertical profile line in black of the transition zone with a dimension of about  $26\ \mu\text{m}$ . The circle fit of the lens is given in blue with a RoC of  $1.67\ \text{mm}$  and the concave transition zone in red has a RoC of  $0.14\ \text{mm}$ .

as perfect as it is assumed in the Zemax<sup>TM</sup> model. It has a soft concave transition with a dimension of around  $25\ \mu\text{m}$ , which is approximately 12% of the half pitch and has a RoC of  $140\ \mu\text{m}$ .

The surface data of one lens were supplied with kind permission of *A $\mu$ S Advanced Microoptic Systems GmbH*. Figure 3.36 shows the contour plot of a lens with its neighbors and in Figure 3.37 the vertical profile line is shown, which is marked in the two-dimensional plot. Two circles are fitted and the transition zone can be identified with a value of about  $26\ \mu\text{m}$ , which leads to approximately 13% of the half pitch. This is a satisfying agreement between the measured hexagonal spot size and the manufactured lens array because the typical uncertainty is a few percent. The falling edge of the measured hexagonal beam contains roughly 5% of the power. The transition zone has to be taken into account for the size of the homogenized beam and leads to a Fourier lens with a 12% larger focal length by using an effective pitch in Equation (3.20). Furthermore, the full acceptance angle is smaller, which is also due to the effective pitch by using Equation (3.21). In the future more detailed investigations of the MLA have to be done with a reduced transition area. That has to be optimized by the manufacturer.

## 3.4 Conclusion

The principle design of the PENELOPE laser system consists of 6 amplification stages between a stretcher and a compressor arrangement. The overall goal is 1 PW peak power (150 J, 150 fs, 1 Hz).

The amplifier chain is based on a hybrid active-mirror/multi-slab architecture. Both are used to achieve higher repetition rates as compared to the rod-type amplifier. The active-mirror concept is used up to MPA II to obtain output energies up to 1 J.

As ASE losses and thermal issues are the major limitations for power scaling of the active-mirror, a He-gas cooled multi-slab architecture is used for the two final amplification stages. Helium is preferred due to the dramatically lower scatter losses compared to other potential gases. The heat load in the head can be equally split over all slabs, using a stepwise gradient doping and a two sided pumping scheme. The large cooling surface (4 slabs) enables good heat removal.

Ideally before the 10 J stage the spatial distribution has to be shaped using a serrated aperture to reduce the required optic size and to fulfill the space requirement. The apodized beam at a diameter of 22 mm can propagate over a distance of 2.5 m without any major changes, which is a typical free propagation distance in MPA III.

All amplifiers and telescopes are based on relay imaging. For the PENELOPE laser system an imaging system consisting of spherical mirrors was conceived. Some main advantages of this choice are the achromatic behavior, less dispersion, lower B-integral, as well as the absence of the radial group delay. The inherent astigmatism of this setup is compensated by folding the beam into two perpendicular planes. In combination with large F-numbers this provides satisfactory results.

The multipass amplifier setups are realized in two different arrangements. One is the two mirror setup, which is employed up to MPA II. Typically, a number of 12 to 16 passes are obtained using polarization multiplexing. The scaling limitation of that approach is solved by using an individual telescope for each extraction pass as realized at MPA III and IV. The thermally induced lens can be compensated in both cases by adjusting the distance between the imaging optics.

Laser diodes are the optical pump source of the PENELOPE laser system. The present state of two different laser diode stack designs are shown with a maximum optical power of 300 W per bar at a driving current of 330 A. An average stack brightness of about  $2.15 \text{ MW}/(\text{sr cm}^2)$  is achieved and doubled via interleaving. Additionally, the latest laser diode stack development is shown with optical output powers up to 500 W.

The stacks are assembled in a pump module (PM). The major goal is to conserve the brightness of the stacks in the PM. This is accomplished with a total brightness transfer factor of almost 87%. The final pump source of MPA IV consists of 16 PM80s and the amplifier head is pumped from both sides.

A bench test on the 10 J amplifier stage is used to characterize and verify the simulation results of the PM combination, as well as the homogenization concept using a microlens array with hexagonal shaped lenses. Both are satisfactory solutions and fulfill the necessary requirements. Furthermore, they will be implemented on the final pump source. The realized tophat pump spot has a peak-to-valley variation of less than 10%, which is the specification. The falling edge of the spot is not as steep as estimated, which is due to the

natural behavior of the transition between the individual lenses on the array. The realized beam delivery system including all sections matches all needed constraints and allows the operation of MPA III.

Such a system, where the laser diodes are combined and finally homogenized, was not available on the market at the beginning of the PENELOPE project.



## CHAPTER 4

---

# Gain Material Choice for DPSSL

---

The gain material is a crucial component of a high-energy amplifier and many requirements are linked to it. First of all the absorption  $\sigma_{abs}(\lambda)$  and emission cross section  $\sigma_{em}(\lambda)$ , as well as the upper-state lifetime  $\tau_f$ , are the most important parameters. The fluorescence lifetime indicates the possibility to store enough energy. For high-energy, large aperture laser amplifiers the availability of large volumes of the gain material is crucial as well. The optical quality of such large crystals or glass blocks is difficult to achieve. For high-repetition rate (0.1 Hz to 10 Hz) or high-average power lasers, thermal properties are very important.

To achieve laser pulses in the picosecond (ps) to femtosecond (fs) range, a broad emission cross section from few to several tens of nanometers is required. The relationship between minimum pulse duration (so-called transform limited) and bandwidth is given by the time-bandwidth-product  $K_{TBP}$  (see Section 2.1.2 on Page 10).

If we assume a Gaussian pulse with  $K_{TBP} = 2 \ln 2 / \pi \approx 0.441$ , the duration of a Fourier transform limited pulse is derived by using Equation (2.26) to

$$\tau_{min} \geq \frac{\lambda_c^2 \cdot K_{TBP}}{c_0 \cdot \Delta\lambda} \quad , \quad (4.1)$$

where  $\lambda_c$  is the center wavelength,  $\Delta\lambda$  the bandwidth and  $c_0$  is the speed of light in vacuum. To achieve 150 fs long Gaussian pulses at 1030 nm a bandwidth of 10.4 nm at FWHM (17.7 nm full width at  $1/e^2$ ) is needed. For this reason, all properties have to be compared to find the best host material for a given application.

At this point, special focus lies on thermal and laser properties. The spectroscopic behavior and optical quality are shown for some materials, especially ytterbium-doped calcium fluoride ( $\text{Yb}^{3+}:\text{CaF}_2$ ). At the end, a summary and conclusions are given.

## 4.1 General Properties for High-Energy Gain Materials

Over the last two decades various lanthanide doped (especially  $\text{Nd}^{3+}$ ,  $\text{Er}^{3+}$  and  $\text{Yb}^{3+}$ ) host materials were investigated looking at their spectroscopic, thermal and optical properties. With the definition of a figure of merit (FOM), it is possible to compare different material parameters to some extent. As a result of FOM, a comparison and choice of the material for a specific application can be made.

A generalized parameter according to [115] describes the dependence of the saturation fluence  $F_{sat}$ , the lifetime  $\tau_f$  and the minimum pulse duration  $\tau_{min}$  of a laser material

$$\frac{\tau_f}{\tau_{min} \cdot F_{sat}} \approx \frac{\lambda_c^3}{8 \pi n^2 h c_0} \cdot \frac{\sqrt{\pi}}{\sqrt{\ln 2}} \quad , \quad (4.2)$$

where  $n$  is the refractive index of the laser material,  $\lambda_c$  the center wavelength of the pulse,  $h$  the Planck constant and  $c_0$  is the speed of light.

Equation (4.2) neglects reabsorption and a Gaussian shaped fluorescence spectrum is assumed. For ideal laser materials with  $n = 1.5$ ,  $\lambda_c = 1 \mu m$  and  $\tau_f = 1 ms$  we get  $\tau_{min} \cdot F_{sat} \approx 5.3 \times 10^{-13} J/cm^2$ . With a saturation fluence of  $10 J/cm^2$ , a perfect gain material supports a minimum pulse duration of about 53 fs. Of course, such a laser material is yet to be found.

The right side of Equation (4.2) is nearly constant for a given wavelength  $\lambda_c$  and the left side can be rewritten using Equation (2.57) to

$$\frac{\tau_f \cdot \sigma_{em}}{\tau_{min}} \approx const. \quad , \quad (4.3)$$

where  $\sigma_{em}$  is the emission cross section. In the case of ytterbium-doped gain materials, a drawback is clearly visible. If a short pulse duration is desired, the emission cross section has to be reduced for a constant upper-state lifetime, which leads to a low gain. Consequently, a large number of extraction passes are needed to obtain a reasonable output energy.

A detailed overview of the large number of laser materials and their comparative study is given in [40, 115]. According to [115], Figure 4.1 shows various gain materials doped with  $Yb^{3+}$ ,  $Nd^{3+}$  and transition metals. For diode pumped lasers a long fluorescence lifetime is beneficial. In the case of ultrashort pulse lasers a minimum bandwidth has to be available (see Equation (4.1)). For this reason, Figure 4.1 can also be plotted with the fluorescence lifetime instead of the bandwidth [40].

The saturation intensity has to be in the optimum range (dashed horizontal lines) to avoid amplified spontaneous emission (ASE) or laser induced damage. Most of the  $Yb^{3+}$ -doped materials have a relatively long fluorescence lifetime, but a high saturation fluence. This results in more complicated energy extraction, taking laser induced damaged threshold (LIDT) limitations into account.

The thermal properties play an important role for high-repetition rate lasers, especially for high-average power applications. Materials with high thermal conductivity  $\kappa$  and thermal shock resistance  $R_S$  are preferred. There is a linear dependence between both parameters  $R_S \sim \kappa$  [116]. Thus Figure 4.2 is used to compare some specific host materials.

It can clearly be seen that crystals have preferential properties compared to glasses. The best laser material in terms of thermal properties is  $Al_2O_3$  (sapphire), which can be doped with titanium. However, the thermal shock resistance can be enhanced, and this results in strengthened material for example in the case of yttrium aluminum garnet  $Y_3Al_5O_{12}$  (YAG) (see Figure 4.2) [117].

In a chirped pulse amplification (CPA) laser system, femtosecond pulses are stretched to the nanosecond range. After the amplification the pulses are compressed to the femtosecond range again. The damage mechanism strongly depends on the pulse duration. For femtosecond laser pulses the dielectric breakdown is the dominant effect [118]. However, from this

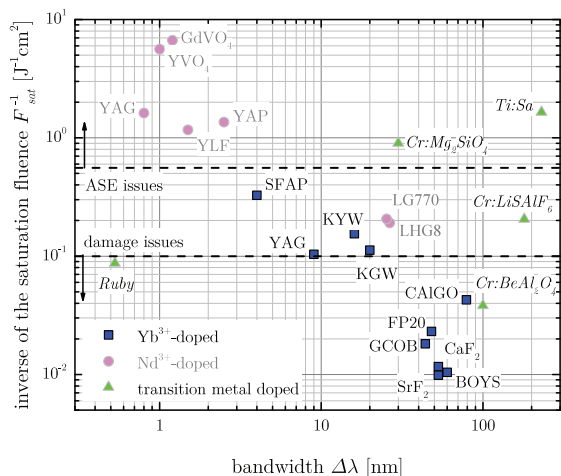


**Figure 4.1:** Bandwidth (x-axis) and saturation intensity (y-axis) for several host materials, doped with Nd, Yb or transition metals, according to [40, 115].

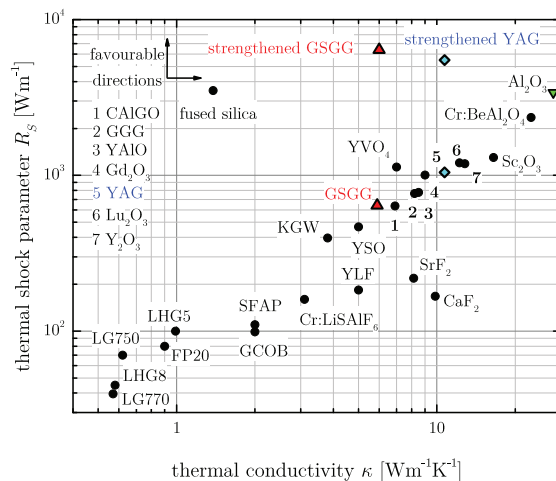


**Figure 4.2:** Thermal shock parameter  $R_S$  as a function of the thermal conductivity  $\kappa$ , according to [40].

point on nanosecond laser damage will be the point of focus, as during amplification the pulse duration is in this range.

A more practical parameter is the LIDT for high-energy laser amplifiers. Essential for extraction of stored energy, it is the damage resistance of the optical components in the amplifier chain. The empirical scaling law of the  $F_{LIDT}$  value is valid from 0.1 ns to 100 ns [119]

$$F_{LIDT} \sim \tau_p^a \quad \text{with} \quad a = [0.4 \cdots 0.5] \quad . \quad (4.4)$$

The dominant damage mechanism for pulse durations above 100 ps is a heating process in the dielectric coatings.

The measurement of LIDT is given in the international standard ISO 21254 [120]. Laser induced damage morphology is a good indicator of the kind of initial defect the damage originates. Typical morphologies are so-called “pin-points”, “delamination”, bulk damage, radial cracking etc. [121].

A typical damage threshold for highly reflecting mirrors is 10 J/cm<sup>2</sup> at 10 ns pulses. This is the fundamental behavior of the used optics to generate energies above 100 mJ. To achieve such a high LIDT fluence, a lot of parameters are important. First of all, the bulk material has to be resistant against damage. This has been shown for a number of materials, for example CaF<sub>2</sub>, YAG, fused silica.

Most critical are surface imperfections as well as the used coating material (e.g hafnia/hafnium(IV) oxide HfO<sub>2</sub> or tantala/tantalum(V) oxide Ta<sub>2</sub>O<sub>5</sub>) [122–124]. There is a strong dependence between LIDT and surface quality. The surface quality is specified in ISO 10110/5 [125] or the military standard MIL-PRF-13830B [126].

The ISO standard gives a quantitative number of defects. The MIL-PRF-13830B gives only the maximum size of defects only. For large optical pieces it is hard to get very good surface qualities and only a few suppliers can deliver such special optics. The typical

value for small standard optics (25.4 mm to 76.8 mm) is ISO 10110 5/2 x 0.040 L1x 0.001 (MIL-PRF-13830B scratch-dig 10-5).

The coating process has a minor effect on the LIDT. The handling before and after the coating process is crucial. The coating technique has an effect on reflectivity, hardness, stress, residual scattering, wavelength shift under non-air condition, etc.

Most favorable is a high reflectivity for mirrors and a low reflectivity for transmission optics such as gain material or lenses. Techniques for highly resistive coatings are ion assisted deposition (IAD), ion beam sputtering (IBS) and magnetron sputtering. These techniques deliver hard layers and good reflectivity. The spectral region for the PENELOPE optics is from 1000 nm to 1070 nm.

## 4.2 Optical Quality

As a result of several amplification passes through the gain material, a high optical quality is needed. In addition, a large size is crucial to obtain the necessary energy storage capability. The main challenge is to find a suitable gain material large in size and with high optical quality at the same time. Flashlamp-pumped ultrashort pulse high-energy laser systems, e.g Texas Petawatt Laser or OMEGA EP, and diode-pumped ultrashort high-energy laser systems like POLARIS often used phosphate, silicate or fluorophosphate glasses as host materials. A large volume can be produced via standard glass melting processes. This material has drawbacks like limited repetition rate (thermal properties) and glass defects i.e. bubbles, striae, etc.

Ten years ago, calcium fluoride  $\text{CaF}_2$  was introduced as a suitable host material by V. Petit et al. [127]. Calcium fluoride has several advantages, like the availability of large volumes (photo-lithographic lenses) up to 300 mm in diameter (120 kg crystals), a broad emission cross section and good thermal properties [128].

The current crystal quality is good enough to use large size  $\text{CaF}_2$  crystals in the final amplifier stages of the PENELOPE project. Several suppliers have been tested during recent years. Small scale test samples were delivered from laboratories, like CIMAP<sup>a</sup> or IKZ<sup>b</sup> (France) and large apertures were produced by crystal growth companies such as Korth Kristalle GmbH (Germany), Incrom (Russia) or Hellma Materials GmbH (Germany). All samples were measured by the means of shadowgraphy and interferometric imaging and white light depolarization loss visual inspection between crossed polarizers (qualitative analysis). Additionally, laser beam distortion was investigated using a multipass setup.

In Figure 4.3 (a) the experimental setup of the shadowgraphy technique is depicted. Figure 4.3 (b) - (d) show images of different  $\text{Yb}^{+3}:\text{CaF}_2$  samples. The crystal in Figure 4.3 (b) has small amount and in (c) large amount defects. Figure 4.3 (d) show a false color image for a thin sample, otherwise difficult to visualize. The most prominent source of the observed defects are small-angle grain boundaries (SAGB). These are clearly visible in Figure 4.3 (c) and (d). SAGB cannot be removed by annealing the crystal and lead to scatter loss for the laser light which acts as a precursor for laser induced damage.

---

a Centre de Recherche sur les Ions, les Matériaux et la Photonique

b Leibniz Institute for Crystal Growth



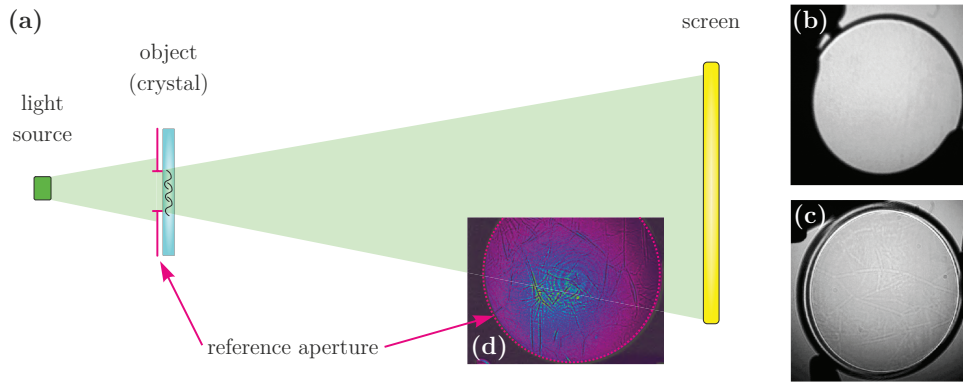


**Figure 4.3:** (a) experimental setup of the shadowgraph technique; (b) shadowgraph image of a sample with low defect density, (c) shadowgraph image of a sample with high defect density and (d) image with an improved defect contrast (false color scale).

Figure 4.4 illustrates bulk damage along a small-angle grain boundary in the case of an  $\text{Yb}^{3+}$ -doped  $\text{CaF}_2$  crystal with a length of 25 mm at different angles. The fluence was around  $2 \text{ J/cm}^2$ . The SAGB are clearly visible inside the sample.

The impact on the wavefront deformation (interferometric imaging) is not that easily visible. As a result, the best way to characterize this type of crystal defect is to measure the near field profile after several passes through the sample. The experimental setup uses a relay imaging multipass cavity, as it is shown in Figure 3.13 on Page 48. Here, the laser beam is imaged onto the gain material for each pass. Typically 6 to 12 passes are used to show the impact on the beam profile.

Figure 4.5 (c) and (d) shows the evolution of the beam profile after six passes for two different positions in the crystal with a high and low amount of SAGB. As a comparison, the input beam, as well as the output beam, with a plane mirror instead of the laser crystal is given in Figure 4.5 (a) and (b), respectively.

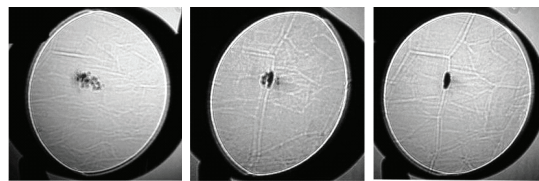


**Figure 4.4:** Volume damage in an  $\text{Yb}^{3+}$ -doped calcium fluoride crystal with a length of 25 mm long and an ytterbium concentration of 2.2 mol%. Images are taken at different angles and the damage arises along the SAGB. The picture on the right is taken along the SAGB.

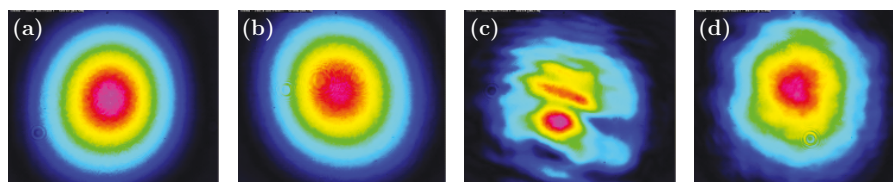


**Figure 4.5:** Near field beam profiles for an eight pass relay imaging multipass cavity, (a) is the input beam, (b) is with a plane mirror instead of the crystal, (c) transmitted beam in a bad and (d) in a good area of the crystal.

In the case of a low crystal quality, a clearly visible beam distortion can be seen after several passes through the gain medium. For high quality crystals, such distortions need a more sensitive observation method. Therefore, the near field images are analyzed with a rotationally symmetric Fast Fourier Transformation. The radially averaged power spectrum density is plotted over the spatial frequency in Figure 4.6 (b) for two different samples.

It can be clearly seen that the crystal quality of the "new sample" is dramatically better compared to the "old" sample. The difference between those two crystals is especially visible in the mid-spatial frequency range (Figure 4.6 (b)). No disturbance of the near field is visible (see Figure 4.6 (a)), in the case of the "new" one the power spectrum density is close to 1. The huge amount of SAGB in the "old sample" is indicated via the mid-spatial frequencies. The "new sample" does not have these significant defects. However, a difference to the reference beam is still visible and has to be investigated in more detail in the future.

In addition to the external stress (thermal or mechanical), every laser material has its own intrinsic stress inside the material. This can happen during crystal growth, for example. The stress causes birefringence and changes the state of polarization of the transmitted laser light. In Figure 4.7 (a) and (b) two examples are shown between crossed polarizers with different intrinsic stress levels. The samples are illuminated by white light (qualitative). Quantitative analysis has to be performed by the crystal manufacturer or at a certain wavelength to quantify the intrinsic stress birefringence. Typical values for laser materials have to be lower than 10 nm/cm peak-to-valley. The current available Yb<sup>3+</sup>-doped calcium fluoride quality is sufficient and promises to build high-energy laser amplifiers with output energies of more than 10 J.

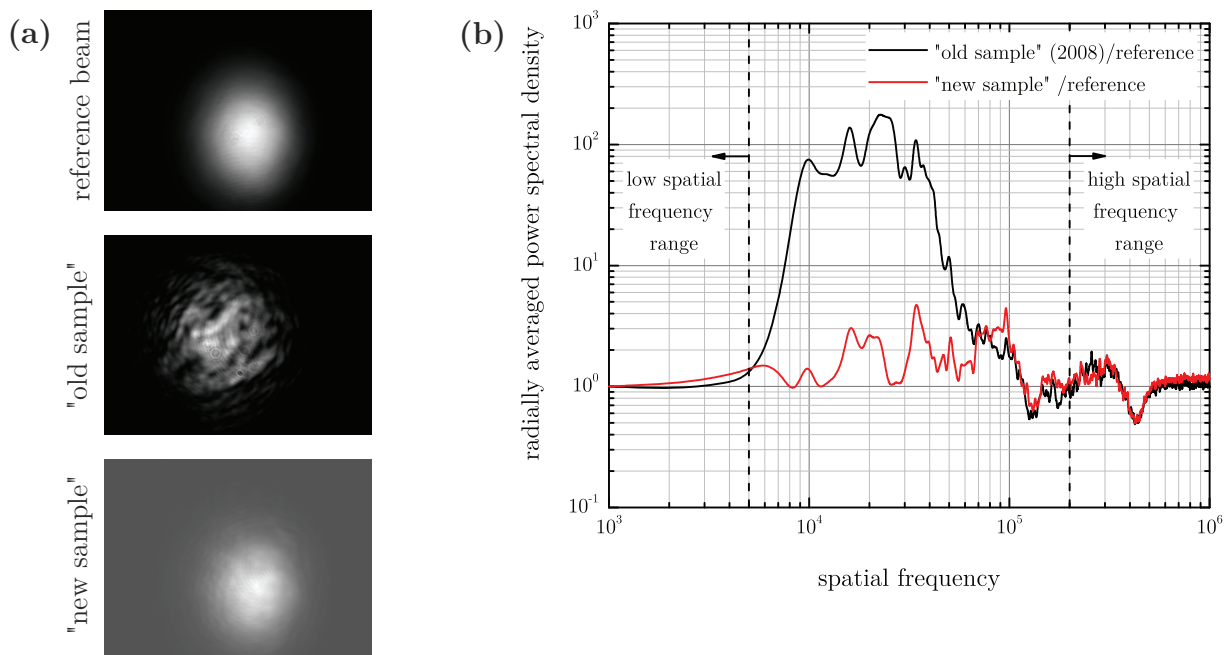


**Figure 4.6:** (a) near field profiles of the reference beam, an "old sample" and a "new sample" after several passes. (b) shows the rotationally symmetric FFT of the near field patterns and the normalized radially averaged power spectrum density to the reference beam for both crystals is plotted as a function of the spatial frequency.

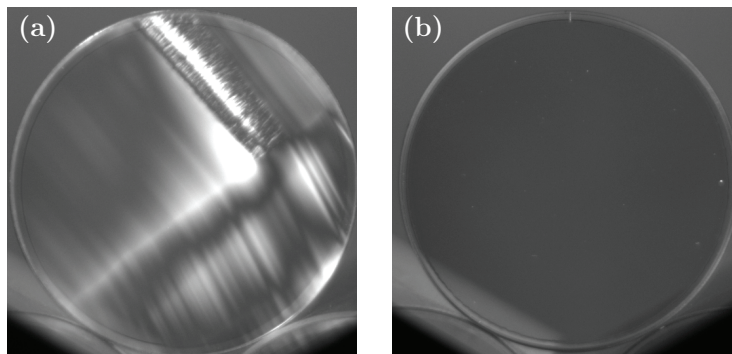


**Figure 4.7:** (a) and (b) transmission between crossed polarizers of 3 mm thick  $\text{Yb}^{3+}:\text{CaF}_2$  with 2.0 mol % doping concentration. The sample in (a) has a higher intrinsic stress compared to (b). The bright spots are dust on the samples.

Alternative gain media, like  $\text{Yb}^{3+}:\text{SiO}_2$  or multi component glasses have to fulfill these requirements as well. First auspicious experiments are done with such glasses [129, 130].

Nowadays, such glasses can be produced with apertures up to 50 mm. The homogeneity of the refractive index of the material is better than 15 ppm. However, typically a circular structure is visible due to agitation during the production process [130]. The glasses have to be annealed after the melting process to remove the stress remaining birefringence. But nevertheless, these laser gain materials are limited for high-average power lasers due to their thermal properties (see Figure 4.2).

To overcome the limitations of the available aperture and quality of crystals, ceramics are promising candidates. They can be produced in various shapes, large apertures and different doping concentrations [131–133]. Also it is possible to have materials with an attached absorber cladding for transverse ASE handling. Currently, the choice of ceramic materials are limited in the case of  $\text{Yb}^{3+}$ -doped to YAG or LuAG.  $\text{Yb}^{3+}:\text{CaF}_2$  test samples are only available with large insertion losses due to scattering [134, 135].

Several nanosecond high-energy laser systems above 10 J rely on ceramic  $\text{Yb}^{3+}:\text{YAG}$  such as DiPOLE [83], HiLASE [136] and Lucia [70]. A comprehensive experimental study of  $\text{Yb}^{3+}:\text{YAG}$  crystalline and co-sintered ceramic disks can be found in [137].

### 4.3 Spectroscopic Properties of Trivalent Ytterbium-doped Gain Materials

Particularly, laser gain materials doped with  $\text{Yb}^{3+}$ -ions are the main scope for the development of high-efficiency laser systems. The absorption cross section  $\sigma_{abs}(\lambda)$  of  $\text{Yb}^{3+}$ -doped host materials are in the range from 900 nm to 1000 nm. A strong absorption in that particular range is essential for direct laser diode pumping. Especially, lines close to 980 nm and 940 nm are preferred candidates as efficient operating laser diodes, based on GaAs are available.

In combination with an emission around 1030 nm, the quantum effect is low (less heat load). Therefore the possibility to generate efficient laser systems is given. The most important parameter for ultrashort pulse amplification is the emission cross section  $\sigma_{em}(\lambda)$  of the gain material. For ultrashort pulses a broad emission bandwidth is needed.

Due to the quasi-three level behavior of  $\text{Yb}^{3+}$  doped host materials, an overlap of emission and absorption cross sections exists. This is a major drawback of  $\text{Yb}^{3+}$  laser materials compared to four-level systems, for example when using  $\text{Nd}^{3+}$ .

The reason is the thermal population of the lower laser level at room temperature. The separation of the intra manifold energy levels (stark splitting) is in the order of the thermal energy  $kT$  at room temperature, and therefore the Boltzmann population of the lower laser level is non-negligible. The term schema and typical energy levels for  $\text{Yb}^{3+}$ -doped calcium fluoride ( $\text{Yb}^{3+}:\text{CaF}_2$ ) is given in Appendix A.1. If the material is cooled down to lower temperatures, the system changes its behavior similar to a four-level laser. This advantage can be used in high-energy laser amplifiers to increase the small signal gain and efficiency. However the bandwidth can get reduced or structured due to the thermal broadening mechanism in the case of crystals.

The absorption cross section  $\sigma_{abs}$  is calculated by using Beer-Lambert law [27, 30]

$$\sigma_{abs}(\lambda) = \ln \left( \frac{\tilde{I}_0(\lambda)}{\tilde{I}(\lambda)} \right) (N_{dop} L)^{-1} . \quad (4.5)$$

Here,  $N_{dop}$  is the density of the dopant and  $L$  is the length of the sample. The spectral intensity without the sample is  $\tilde{I}_0(\lambda)$  and  $\tilde{I}(\lambda)$  with the sample. This measurement can be performed by using a custom made absorption spectrometer, as presented in [138], to measure from room temperature down to cryogenic temperatures. The wavelength resolution of a high-performance UV-VIS-NIR spectrophotometer (for example Agilent Carry 7000) is down to 10 pm and it measures extinction levels down to  $10^{-8}$  [139]. With such high precision instruments, the absorption cross section can be determined with very high accuracy. This outstandingly high accuracy of the absorption cross section is also needed to calculate the emission cross section.

There are two different methods to determine the emission cross section. The first is the McCumber relation [140] where  $\sigma_{em}$  is calculated from  $\sigma_{abs}$  with the following formula

$$\frac{\sigma_{em}(\lambda)}{\sigma_{abs}(\lambda)} = \frac{Z_l}{Z_u} \exp \left[ E_{ZPL} - \frac{h c_0}{\lambda} \right] . \quad (4.6)$$

Here,  $E_{ZPL}$  is the zero phonon line (ZPL) energy,  $h$  is the Planck's constant and  $c_0$  is the speed of light in vacuum.  $Z_l$  and  $Z_u$  denote the partition function of the lower  ${}^2F_{5/2}$  and upper manifold  ${}^2F_{7/2}$ . An elaboration of this formula can be found in [138].

The drawback of this method lies in the exponential scaling factor centered at ZPL. Potentially large uncertainties for  $\sigma(\lambda)$  exists due to measurement noise, which arise from typically low absorption at the emission wavelength range plus a limited resolution of the spectrometer.

For comparison, a second method the so-called Füchtbauer-Ladenburg (F-L) is used [141]. The F-L equation is based on the fundamental aspects of the Einstein A and B coefficients [30]. The emission cross section is directly calculated from the fluorescence spectral intensity  $\tilde{I}_f(\lambda)$

$$\sigma_{em}(\lambda) = \frac{\lambda^2}{8 \pi n^2 \tau_r} \cdot g_\lambda(\lambda) \quad (4.7)$$

$$g_\lambda(\lambda) = \frac{\lambda^3 \cdot \tilde{I}_f(\lambda)}{c \cdot \int_{\lambda_{min}}^{\lambda_{max}} \lambda \cdot \tilde{I}_f(\lambda) d\lambda} \quad , \quad (4.8)$$

where  $n$  is the refractive index of the material,  $\tau_r$  the radiative lifetime and  $g_\lambda(\lambda)$  is the spectral line function. The precision of the method is limited to the exact knowledge of the radiative lifetime and reabsorption of the measured fluorescence.

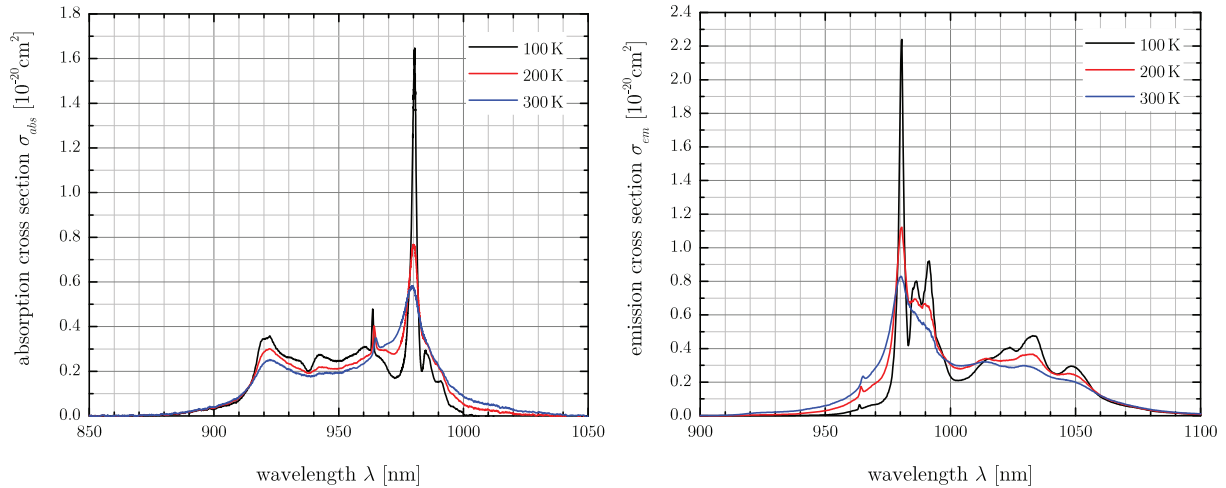
No influence of the reabsorption is assumed for the F-L equation. This becomes complicated for  $\text{Yb}^{3+}$ -doped laser materials where the emission and absorption cross sections overlap.

To eliminate the volumetric influence, very small samples, powders or fibers are necessary. An alternative approach is the pinhole method as described in [142], which corrects the reabsorption uncertainties of the measured fluorescence spectrum by extrapolating to zero volume. A good solution is to take the calculated values for  $\sigma_{em}$  from both methods and combine them.

### 4.3.1 $\text{Yb}^{3+}:\text{CaF}_2$ the Gain Medium for the PENELOPE System

Ytterbium-doped calcium fluoride is the material of choice for the PENELOPE laser system. As described in the previous sections, large apertures and high optical quality are available. The fluorescence lifetime is 2.4 ms [128].  $\text{Yb}^{3+}$ -doped calcium fluoride is a cubic and isotropic crystal. This is beneficial for high-energy laser amplifiers [128, 143]. Here, the spectroscopic properties are investigated in detail for different operation temperatures. All spectroscopic measurements were done by J. Körner et al. and published in [138, 144] and the data were kindly provided with his permission.

Figure 4.8 shows the absorption and emission cross sections for  $\text{Yb}^{3+}:\text{CaF}_2$  at 100 K, 200 K and 300 K. A major absorption peak located close to 980 nm is clearly visible. The peak is broad enough to support laser diodes without wavelength stabilization. Absorption at 200 K is about 1.3 times larger compared to room temperature values. At 100 K this factor increases by 2.8. It is also possible to pump with laser diodes from 920 nm to 950 nm. The reabsorption at the laser wavelength range from 1000 nm to 1070 nm is reduced at lower



(a) Absorption cross section of  $\text{Yb}^{3+}$ -doped  $\text{CaF}_2$  at 100 K, 200 K and 300 K.

(b) Emission cross section of  $\text{Yb}^{3+}$ -doped  $\text{CaF}_2$  at 100 K, 200 K and 300 K.

**Figure 4.8:** Absorption and emission cross section of ytterbium-doped  $\text{CaF}_2$  at different temperatures. Attention the horizontal and vertical axis are scaled differently. The data are provided with the kind permission of J. Körner and published in [138, 144].

temperatures. Thus the minimum inversion  $\beta_{min}$  (see Equation (2.56) with  $k = l$ ) is lower leading to higher gain  $G$  and extraction efficiency.

The peak emission is close to 1032 nm and very broad (about 50 nm), but a slight spectral modulation is visible. For temperatures considerably lower than room temperature, modulation of the emission cross section becomes visible. Temperature below 200 K will consequently lead to strongly modulated amplified spectra.

The broad and relatively smooth emission cross section arises due to the clustering effect of the  $\text{Yb}^{3+}$ -ions inside the  $\text{CaF}_2$  lattice. Therefore the doping concentration has to be larger than 0.5 mol % [145–147]. Below this value crystalline features in the cross sections occur (narrow lines). At lower temperatures the thermal broadening is reduced and a structured cross section is visible, which is not acceptable for the amplifier.

First of all, a comparison of diode pumping at 930 nm and 980 nm is made. The absorption without saturation can be derived from Equation (2.61) for  $\beta(z) = 0$  (Lambert Beer's law). If we take a spectral distribution of the laser diode into account, the integration leads to

$$I(z) = \int_0^L \tilde{I}_{LD}(\lambda) \cdot \exp[-\sigma_{abs} \cdot N_0 \cdot c'_{dop} \cdot z] d\lambda \quad , \quad (4.9)$$

where  $\tilde{I}_{LD}(\lambda)$  is the spectral intensity distribution of the laser diode,  $z$  is the propagation direction from 0 to the crystal length  $L$  and  $c'_{dop}$  doping concentration.

From this point on, a Gaussian shaped laser diode spectrum is taken, which can be assumed from Figure 3.24 (a) on page 60. We can calculate the necessary product of  $L \times c'_{dop}$  (so-called doping length) for a given absorption  $I(L)/I_0$ .

For the spectral intensity distribution we assume a Gaussian shape with  $\Delta\lambda$  the bandwidth at FWHM and  $\lambda_c$  the central wavelength of the laser diode. Figures 4.9(a) and 4.9(b) shows the doping length  $L \times c'_{dop}$  for 90 % pump intensity absorption at 300 K and 200 K as a



function of  $\Delta\lambda$  (vertical scale) from 1 nm to 10 nm and  $\lambda_c$  (horizontal scale) from 920 nm to 940 nm. Figures 4.10(a) and 4.10(b) represent the center wavelength range from 970 nm to 985 nm at 300 K and 200 K. The absorption close to 980 nm is stronger than pumping at 922 nm, which shows the highest absorption between 920 nm and 940 nm. The required doping length is reduced for lower temperatures. The modulation of the absorption cross section is visible and increases at lower temperatures. Therefore Figures 4.9 and 4.10 for 200 K and 300 K have to be compared. For large  $\Delta\lambda$  the doping length has to be increased. However, on the other hand the sensitivity for  $\lambda_c$  is reduced.

For large size  $\text{Yb}^{3+}:\text{CaF}_2$  crystals typical doping concentrations range from 2 mol % to 2.5 mol % maximum. The required crystal length for 979.5 nm is 2.3 times less compared to the 922.5 nm pump wavelength case.

However, this is only an indication of the strength of the absorption, but for high-energy lasers the feasible inversion is important. In Equation (2.58) on page 18 the relation between inversion and pump intensity is given. If we analyze a steady state (the left side is set to zero) and the lifetime modifier  $M_{ASE}$  (described in Section 2.2.3) can be implemented like in Equation (2.76), as a result an interesting relationship can be deduced. The inversion is derived to be

$$\beta = \frac{\beta_{max}}{1 + \frac{I_{sat_p} \cdot M_{ASE}}{I_p}} \quad , \quad (4.10)$$

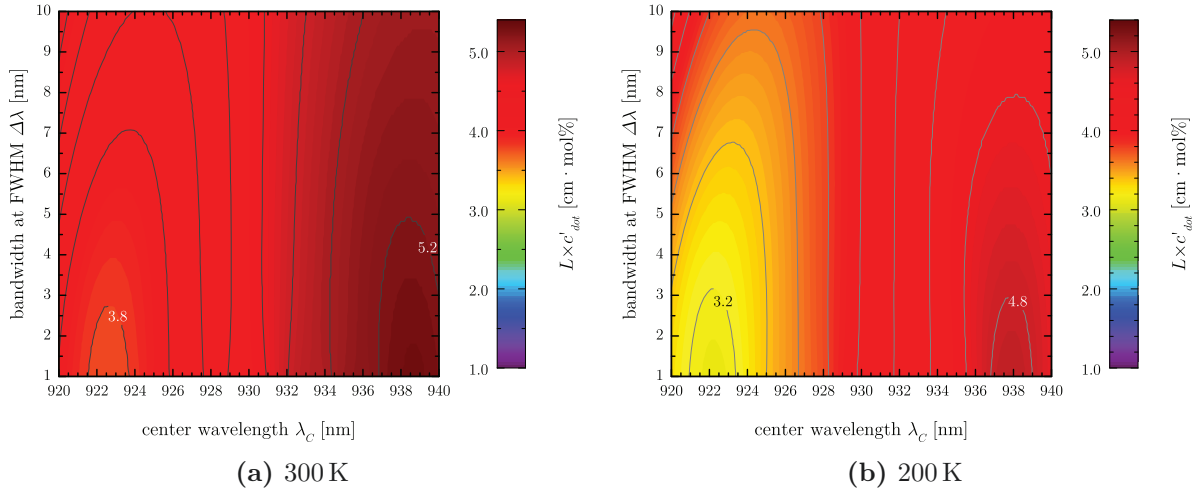
where  $I_{sat_p}$  is the pump saturation intensity (see Equation (2.57) with  $k = p$ ),  $I_p$  is the pump intensity and  $\beta_{max}$  the maximum inversion at a given pump wavelength (see Equation (2.56) with  $k = p$ ). Usually,  $I_{sat_p}$  and/or  $\beta_{max}$  is used to compare different pump wavelengths. But there is no relation from this two values to useful parameters like  $I_p$ . For this reason the steady state inversion from Equation (4.10) is used to compare different pump wavelengths. Additionally, the effect of the lifetime modifier  $M_{ASE}$  on  $\beta$  can be seen, as with increasing ASE the inversion is strongly reduced. For a simple estimation one can be safely assume  $M_{ASE} = 1$  (sufficiently small excited volume). Only  $\beta/\beta_{max} = 0.5$  is accessible in the case of  $I_p = I_{sat_p}$ . In the next discussion and figures the influence of  $M_{ASE}$  is neglected.

Figure 4.11(a) and Figure 4.11(b) show the steady state inversion as a function of pump intensities from 5 kW/cm<sup>2</sup> to 30 kW/cm<sup>2</sup> and in the wavelength range from 900 nm to 1000 nm for 300.200 K. Figure 4.11(c) represents the horizontal profile line at 5 kW/cm<sup>2</sup>, 15 kW/cm<sup>2</sup> and 25 kW/cm<sup>2</sup> in the case of 300 K and 200 K. In this ideal case a better comparison of the impact of different pump wavelengths is possible.

As a result of the low  $I_{sat_p}$  at 980 nm,  $\beta$  gets saturated at relatively low pump intensities. Pump saturation is preferred and results in a high inversion. Therefore, at 980 nm, a higher average inversion can be achieved in the same pump geometry as well as pump intensity compared to 922 nm. For more detailed information, a numerical investigation has to be done and can be found in [81].

Despite the fact that 940 nm pumping is found in the literature, it is obviously the worst choice. However, 940 nm pump sources can be used to pump other gain materials, especially  $\text{Yb}^{3+}:\text{YAG}$  and is readily available at the laboratory in many cases.

Nevertheless, this is usually a bad choice, as low pump intensities in the range from 5 kW/cm<sup>2</sup> to 15 kW/cm<sup>2</sup> are typically used for  $\text{Yb}^{3+}:\text{YAG}$  laser systems [70, 136], if they are operating at room or cryogenic temperatures. At these intensity values, for example



**Figure 4.9:** The doping length  $L \times c'_{dop}$  for 90 % pump intensity absorption at 300 K and 200 K as a function of  $\Delta\lambda$  (vertical scale) from 1 nm to 10 nm and  $\lambda_c$  (horizontal scale) from 920 nm to 940 nm.

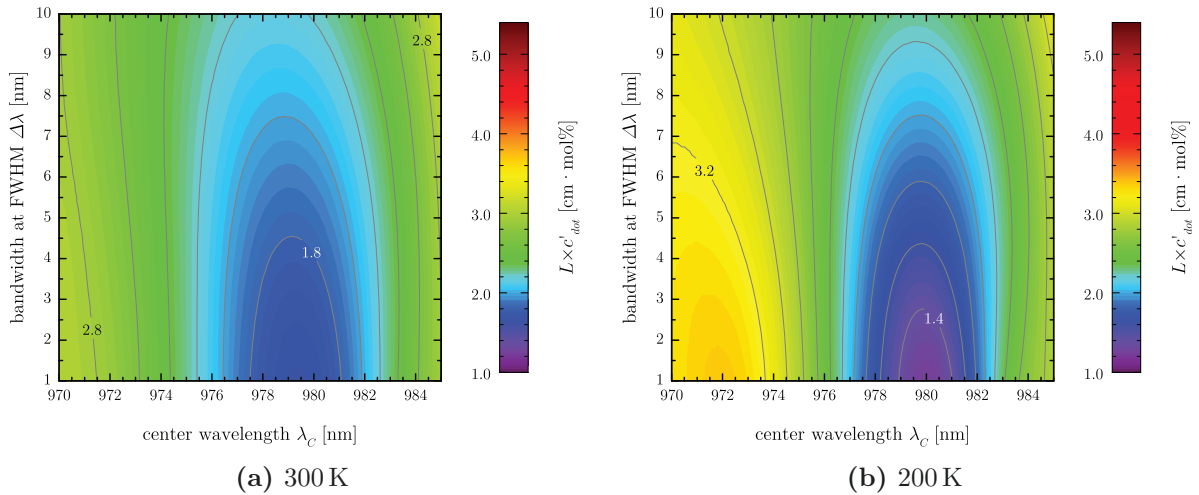


**Figure 4.10:** the doping length  $L \times c'_{dop}$  for 90 % pump intensity absorption at 300 K and 200 K as a function of  $\Delta\lambda$  (vertical scale) from 1 nm to 10 nm and  $\lambda_c$  (horizontal scale) from 970 nm to 985 nm.

15 kW/cm<sup>2</sup>, the steady state inversion is only 70 % of the one at 980 nm. The maximum achievable pump intensity depends on the laser diode beam parameter product, as it was described in Section 3.3. The design value for the PENELOPE lies between 15 kW/cm<sup>2</sup> and 20 kW/cm<sup>2</sup> using 980 nm laser diodes.

At lower temperatures the steady state inversion values for 922 nm and 980 nm are slightly increased, but the width of the peaks is narrowed. Finally, the quantum defect for 980 nm is only half compared to 920 nm, leading to half the heat load.

A similar observation is possible for the gain cross section  $\sigma_g(\lambda)$ , if we take Equation (2.55) into account. Here, it is a combination of emission and absorption cross section as a function of the inversion level  $\beta$ .

To get an idea of how the amplified spectrum is modulated by the gain cross section at a temperature of 300 K, Figure 4.12(a) shows the result for different inversion levels. The



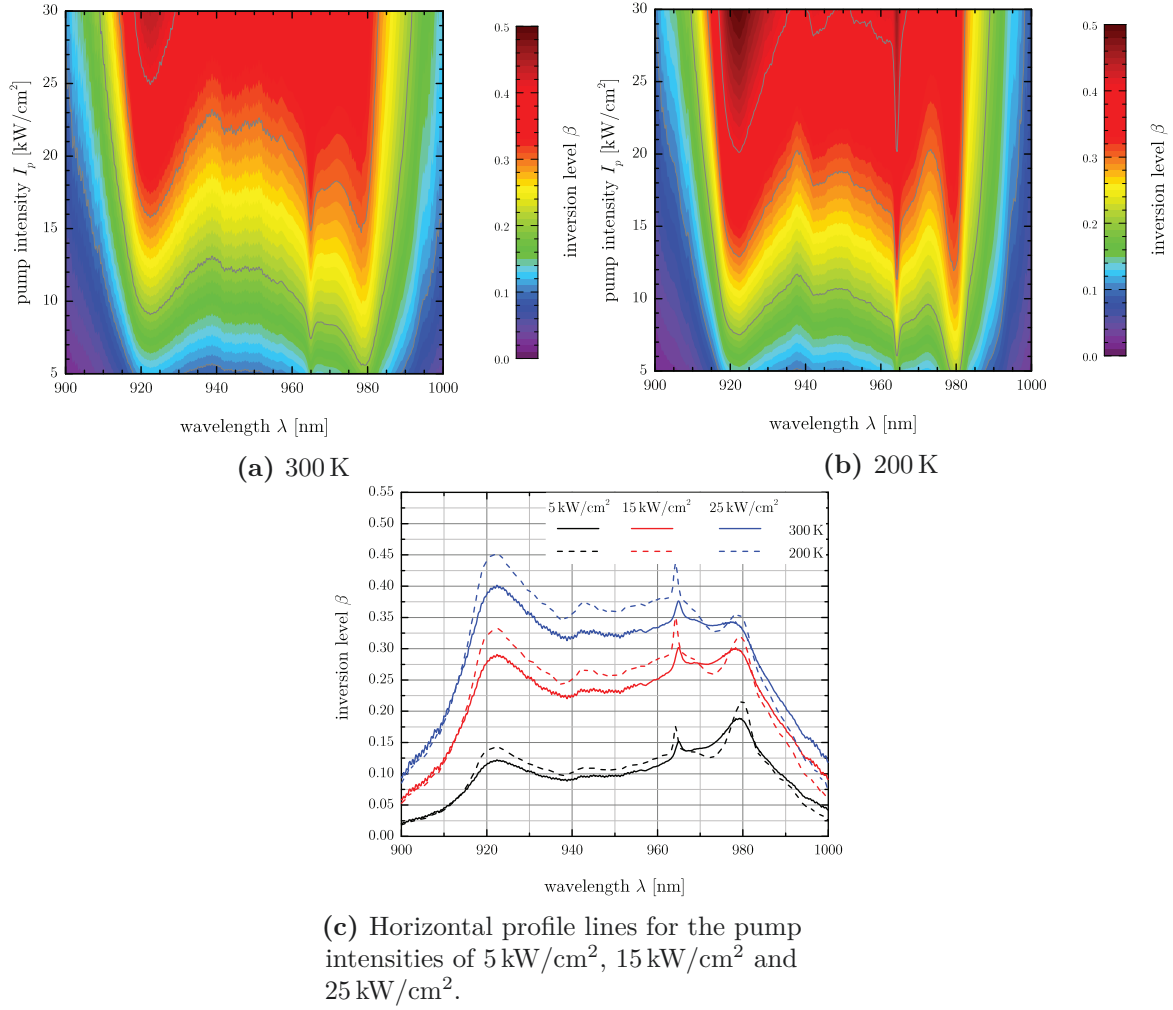
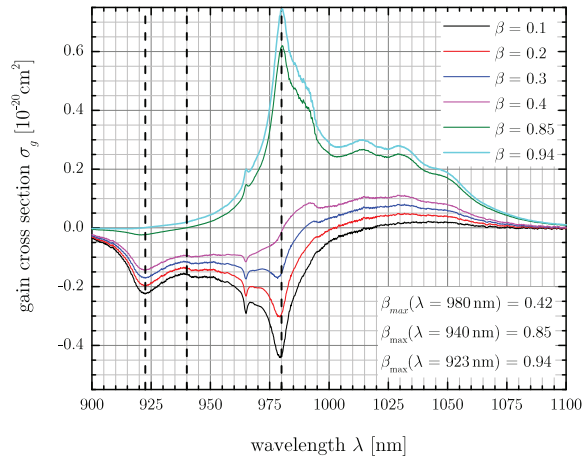


**Figure 4.11:** Steady state inversion at 200 K and 300 K as a function of the pump intensity and the wavelength.

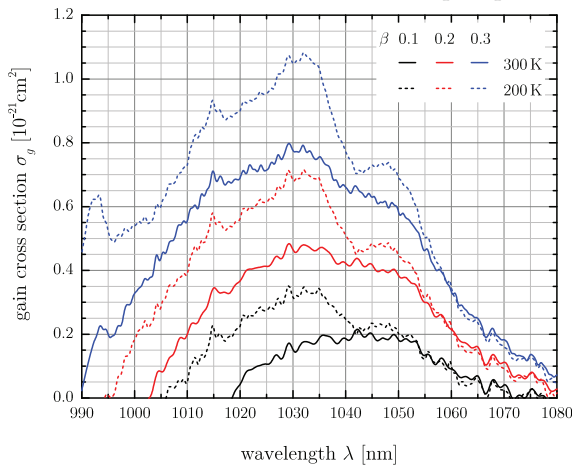
vertical dashed lines illustrate three different pump wavelengths at 922 nm, 940 nm and 980 nm. Gain cross sections at the maximum achievable inversion are shown. At these values  $\sigma_g(\lambda)$  equals zero at the pumping wavelength. The highest possible inversion can be accomplished at 922 nm. In Figure 4.11(c) it is obvious that the required pump intensity should be above 25 kW/cm<sup>2</sup>. This is not possible to achieve on a large scale amplifier. The large size pump sources are limited to the given laser diode stack beam parameter and result in pump intensities between 15 kW/cm<sup>2</sup> and 30 kW/cm<sup>2</sup>.

A typical average inversion level  $\beta$  of an amplifier is in the range of 0.1 to 0.3, which will be used for further calculations. A detailed illustrative visualization of the amplification range from 980 nm to 1080 nm is shown in Figure 4.12(b) for 300 K and 200 K and  $\beta$  of 0.1, 0.2 and 0.3. At 200 K the gain cross section is more modulated compared to room temperature. Thus, to remain above 200 K is preferred.

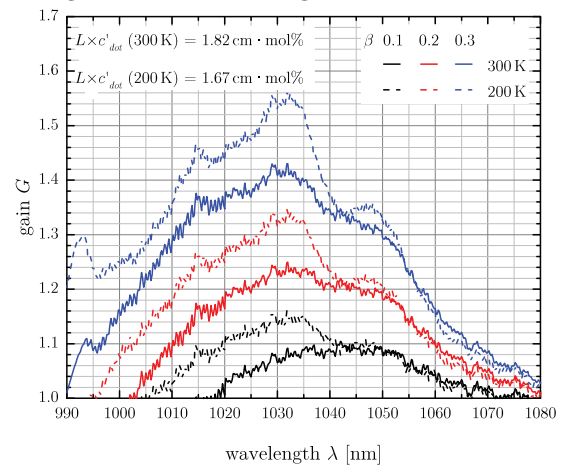
To compare two different temperatures, the gain  $G$  is calculated with Equation (2.67) and plotted in Figure 4.12(c). Here, the doping length for 90% absorption is taken by assuming a laser diode spectrum with a Gaussian shape and a bandwidth of 5 nm. For the amplifier performance a high gain per pass is requested. At lower temperatures the gain cross section



(a) Gain cross section at 300 K as a function of the wavelength for different inversion levels. The vertical dashed lines illustrate three different pump wavelengths at 922 nm, 940 nm and 980 nm. The maximum achievable inversion at the pump wavelength is given in the lower right.



(b) Zoom in the gain cross section for the amplification range and feasible excitation levels.



(c) The calculated gain at 200 K and 300 K for a pump light absorption of 90% with a spectral bandwidth of 5 nm for the laser diode.

**Figure 4.12:** (a) and (b) are the gain cross section and (c) is the gain as a function of the wavelength.

increases, resulting in a higher gain. Additionally, the absorption at the laser wavelength range is reduced due to the thermal depopulation of the lower laser level. However, the drawback is the stronger modulation of the spectrum at lower temperatures. At 200 K the difference between 1032 nm and 1045 nm is nearly a factor of 1.16 at an inversion level of 0.3 in a single pass.

If we take into account that the amplifier has 12 amplification passes, the difference is then a factor of 5.6. Such a strong modulation has to be addressed by spectral shaping to minimize the effect on the pulse duration (gain narrowing).

Finally, if all these different parameters are taken into account the optimum performance (i.e. minimum pulse duration, gain per pass, etc.) for the 10 J and 100 J amplifier stages are obtained with temperatures above 200 K. For this purpose, the cooling system is designed to be operated within this specific range.

### 4.3.2 Divalent Ytterbium ( $\text{Yb}^{2+}$ ) Formation in Calcium Fluoride

One source of unwanted energy transfer processes are contaminations, either due to impurities added during the growth process or due to problems of chemical separation. This is especially true for traces of other rare earth materials, particularly  $\text{Nd}^{3+}$ ,  $\text{Er}^{3+}$  or other Lanthanide. Another source is inherent to the growth process.

Besides  $\text{Yb}^{3+}$ ,  $\text{Yb}^{2+}$  can be formed during the growth process of  $\text{CaF}_2$ . The divalent ytterbium ions have strong absorption bands at 229.0 nm, 262.2 nm, 274.2 nm and 365.0 nm. Therefore it is easy to distinguish between crystals with and without  $\text{Yb}^{2+}$  content.

Figure 4.13 shows the absorption spectra of different samples. The absorption band in the UV is clearly visible. To avoid the  $\text{Yb}^{2+}$ -ions formation different solutions are found. First of all, co-doping with  $\text{Pb}^+$ ,  $\text{Li}^+$  or  $\text{Na}^+$  can be performed [148, 149]. The drawback of this technique has an influence on the emission and absorption cross section [150]. The bandwidth of the emission is reduced compared to non-co-doped  $\text{Yb}^{3+}:\text{CaF}_2$  samples.

Another solution is an additional heat treatment [143]. Absorption in the UV range for  $\text{Yb}^{2+}$  is 4 orders of magnitude stronger than that of the  $\text{Yb}^{3+}$  absorption in the near-infrared [151]. It can be found that the concentration of  $\text{Yb}^{2+}$  is two to three orders of magnitude lower than the  $\text{Yb}^{3+}$  concentration [152]. The effect on the laser performance is investigated in Appendix A.3.

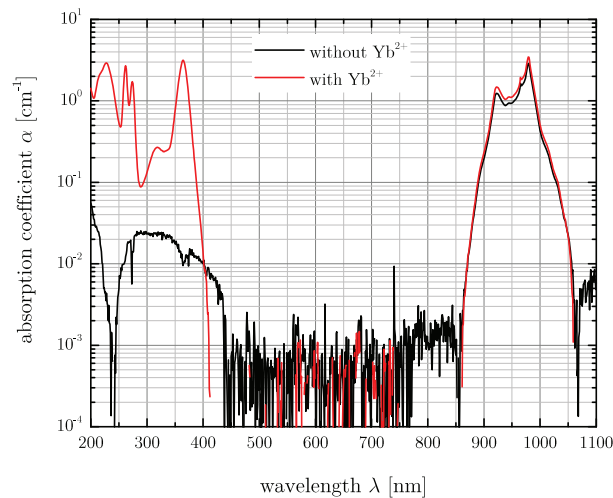


**Figure 4.13:** Absorption coefficient  $\alpha$  of calcium fluoride with and without divalent ytterbium.

## 4.4 Alternative Gain Materials

Many alternative  $\text{Yb}^{3+}$ -doped materials have been proposed and successfully used for high-power and/or high-energy sub-100 fs pulse generation [153]. These materials can be separated into two groups: crystals and glasses.

Glasses have smooth and large cross sections due to the inhomogeneous broadening mechanism, but on the other hand they have poor thermal properties as shown in Figure 4.2. Nevertheless with a reduced repetition rate and an aggressive cooling scheme these materials can be an alternative approach for  $\text{Yb}^{3+}:\text{CaF}_2$ .

For this purpose, new aluminosilicate glasses are under way, containing lithium oxide (LiAS) [154] or aluminum oxide (SAL) [129]. Pure fused silica can be an attractive candidate as well [130]. Besides these new materials, some other well-known glasses like pure phosphate glass (QX-glass) are available [155].

Furthermore, disordered crystal hosts with multisite structure, for example  $\text{Yb}^{3+}:\text{CaGdAlO}_4$  ( $\text{Yb}^{3+}:\text{CALGO}$ ) and  $\text{Yb}^{3+}:\text{CaYdAlO}_4$  ( $\text{Yb}^{3+}:\text{CALYO}$ ), one of the most exciting new materials that has been investigated over recent years. It owns a particularly attractive combination of thermo-mechanical and optical properties [156]. The drawbacks are the birefringent behavior, the relatively low fluorescence lifetime and the small aperture of the crystals. This renders them typically only usable in small scale amplifiers with several mJ of output energy.

The spectroscopic properties and laser experiments (e.g. cw laser performance, cavity-dumped regenerative amplifier and CPA experiments) of selected glasses and crystals are investigated in Appendix A.4, respectively.

## 4.5 Conclusion

Trivalent ytterbium-doped calcium fluoride ( $\text{CaF}_2$ ) is the best solution for the PENELOPE laser system. The good thermal properties are beneficial for a high repetition rate operation up to several Hz. Additionally, one of the main critical characteristics of a gain medium is the optical quality, especially for high-energy amplifiers as a result of the large number of amplification passes. The currently available quality for  $\text{CaF}_2$  is sufficient enough to support pulse energies up to several hundred joule. This was determined by a rotationally symmetric Fast Fourier Transformation of the near field after several passes through the material. The difference between the reference and the sample was negligible.

Furthermore, the spectroscopic properties match the requirements for ultrashort pulse amplification and direct diode pumping. The absorption band is in the region where high-power laser diodes are available. The best pump wavelength is close to 980 nm. First of all, the absorption is more than 2 times stronger compared to 940 nm. The achievable inversion level is higher close to 980 nm in comparison to 940 nm. The reason for this is the low saturation intensity at this specific range.

A broad gain cross section of up to 50 nm is possible at inversion levels of 10% to 20%. At low temperatures the gain cross section is increased leading to better amplification performance. The drawback is the modulation of the gain in this case and thus it is important to stay above 200 K. The structured gain is acceptable at this temperature level.

Other gain material is available only on a small scale, which make them usable in the low energy amplifier stages. In the near future, there is the possibility to test some of them on larger scales (e.g. at the 100 mJ level). Table 4.1 summarize the properties of the glasses SAL, LiAS and SiO<sub>2</sub> as well as for the crystals Yb<sup>3+</sup>:CaF<sub>2</sub>, Yb<sup>3+</sup>:CALGO and Yb<sup>3+</sup>:CALYO. Most promising candidate is SAL, which will be of interest for future investigations. Yb<sup>3+</sup>:CaF<sub>2</sub> is the main choice for PW-class high-energy diode pumped laser systems.

Material	$T_g$ [°C]	$n_0$	$\tau_f$ [ms]	$n_2$ [ $\times 10^{-16}$ cm <sup>2</sup> /W]	$\kappa$ [W/(m K)]	$\alpha_T$ [ $\times 10^{-6}$ K <sup>-1</sup> ]	Ref.
Yb <sup>3+</sup> -doped crystals							
CaF <sub>2</sub>	-	1.42	2.4	1.3	9.7	-18	[128]
CALGO	-	1.85	0.445	8	6.9	35	[156–158]
CALYO	-	1.85	0.445	-	3.3	8.99	[159]
Yb <sup>3+</sup> -doped glasses							
LiAS	693	1.531	1.07	-		6.6	[160]
SAL	870	1.6	0.69	5.8	1.25	4	[129, 161]
SiO <sub>2</sub>	1200	1.45	0.80	3.0	1.4	0.5	[161–163]
QX	450	1.52	2.0	7.7	0.85	8.3	[164]

**Table 4.1:** Properties of selected laser materials. The glass transition temperature  $T_g$  is only relevant for glasses.



## CHAPTER 5

---

# Amplifier Experiments

---

In this chapter amplification experiments are presented and discussed. The starting point is  $\text{Yb}^{3+}$ -doped  $\text{CaF}_2$  as the main gain material. It was selected for, especially its good thermal properties and broad emission spectrum.

A detailed overview of the spectral response of the laser resonator optics (e.g. waveplates, polarizers, etc.) and the possibility to counteract its impact is the central topic of this chapter. Furthermore, the options for spectral manipulation are given.

The temporal intensity contrast (TIC) of the regenerative amplifier is investigated and sources of pre- and postpulses are determined. Additionally, the influence of pulse picking contrast is discussed.

## 5.1 The Active-Mirror Concept

The thin-disk laser concept was introduced in the early 1990s within the group of A. Giesen at the university of Stuttgart, Germany [165, 166]. The capability of efficient cooling of the gain material (e.g.  $\text{Yb}^{3+}$ -doped YAG) was demonstrated for average powers up to several kilowatts in a multi-mode continuous-wave operation as well as up to 500 W with diffraction-limited beam quality [167]. As the basic idea relies on very thin gain media (e.g. sub mm), very high doping concentrations (up to 20 mol%) are necessary to ensure efficient pump light absorption. For large beam diameters, ASE and parasitic lasing thus are the limiting factors as was explained in Section 2.2.3.

In contrast to the thin-disk setup, an alternative idea is to use thicker disks with lower doping concentrations, the so-called "active-mirror" concept. This concept works typically in a pulsed operation mode with repetition rates from 0.1 Hz to 100 Hz instead of CW [95, 168, 169], hence a lower average power

The gain material has a highly reflective back side, while the front surface is anti-reflection coated. The HR coated side is cooled, as shown in Figure 5.1. The ratio of thickness to diameter is typically in the range of 0.1 to 0.2. In this case, longitudinal heat transfer is dominant, thus the thermally induced wavefront aberrations are ideally minimized. As a boundary condition, almost the whole surface of the disk has to be pumped.

For the first amplifier stages including MPA I, an active-mirror approach is used with disk thicknesses of several millimeters. Pump and laser radiation is incident from the

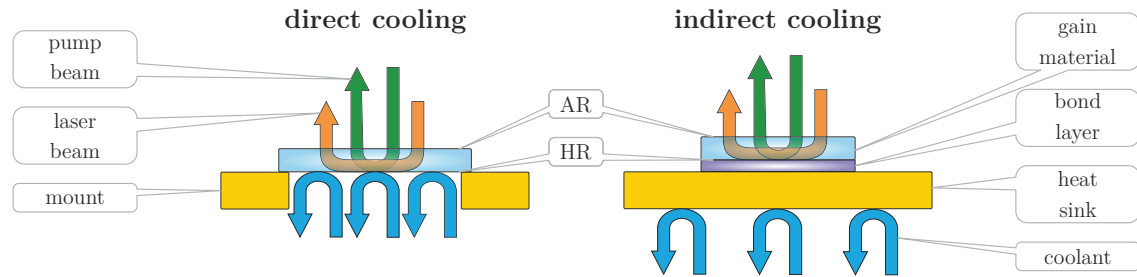


**Figure 5.1:** Direct and indirect cooling of an active-mirror.

same direction and the crystal is therefore intrinsically double pass pumped, as shown in Figure 5.1. As a result, the HR coating has to be specified for the pump wavelength as well.

In order to optimize heat extraction, two main possibilities for cooling exist. The first is a direct cooling approach, the second relies on indirect cooling using a heat sink, as shown in Figure 5.1. Direct cooling is typically limited by the available heat exchange rate per gain medium surface area. Cooling medium velocity and potential phase changes limit it to a few tens of  $\text{W}/\text{cm}^2$ . From this point on, we will concentrate on the indirect cooling approach.

The bonding has to be done on a heat sink with a thin bond layer for good heat transfer. There are numerous options for mounting the disk on a heat sink with every solution having its own pros and cons. The following list is a compilation of the most popular technologies:

- Chemical bonding (Chemically Activated Direct Bonding Process (CADB<sup>®</sup>)) [170]),
- Soldering and
- Epoxy or Adhesive.

Every layer has a specific coefficient of thermal expansion (CTE) and thermal conductivity. Usually, thin-disk laser heads are soldered onto a tungsten-copper alloy heat sink. This material is taken due to the matched CTE to the thermal expansion of the  $\text{Yb}^{3+}$ -YAG crystal.

All these constraints are very important for high-average-power laser operation and have to be taken into account for designing the interface connecting the gain material to the heat sink.

The epoxy or adhesive solution is a simple approach and can be carried out with standard high reflective coatings. The use of relatively low thermal conductivity material for the interface is acceptable, as long as the average power is kept low and the layer thickness is kept thin (several micrometers or wavelengths). Nevertheless, to find a suitable adhesive is the most critical part. Typical choices are silver-filled epoxies, with a good thermal conductivity. The drawback is their paste-like behavior, which makes it difficult to achieve a thin and homogeneous layer. An optical bond adhesive can be used with a low viscosity in order to get a thin contact layer of less than one micrometer. The optical adhesive cures under UV exposure.

A bonded laser material is shown in Figure 5.2 (a). The adhesive generates a rigid interface and the high thermal load in the gain material will lead to large stress. This is the reason for stress birefringence and in the worst case catastrophic damage, as shown in Figure 5.2 (c). For the heat sink material copper was chosen due to its good thermal



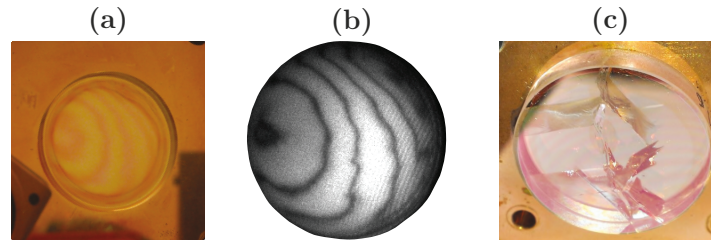


**Figure 5.2:** (a) glued crystal on a copper heat sink; (b) interference pattern of the bond layer observed at the illumination with green laser light; (c) fractured crystal at a high thermal load (pump spot at the center).

properties. The used copper heat sinks are standard IR ( $\text{CO}_2$ ) laser mirrors with excellent surface quality ( $\lambda/10$  at 633 nm), as shown in Figure 5.2 (a). This makes it possible to get a thin layer interface between the gain material and the copper mirror. A hard nickel coating protects the heat sink surface, as copper alone can easily be scratched.

The layer thickness was checked by white light interference between the back side of the crystal and the copper heat sink, as shown in Figure 5.2 (a). Additionally, Figure 5.2 (b) represents the interference pattern of a bond layer illuminated using a green laser. The goal is to have the number of fringes as low as possible. In the case of a non-optimal surface flatness of the copper mirror as well as the gain material, a large number of fringes are observed.

White light interference with day light has a maximum emission around 550 nm. Less than three fringes are preferred. The influence of the layer thickness on the laser beam profile has to be investigated. Therefore an experiment was performed with two different crystals. The active-mirror was placed into the image plane of a relay imaging multipass cavity (MPC). The setup is shown in Figure 3.13 on page 48. The resulting beam profiles after eight passes are given in Figure 5.3 and the input beam is presented on the left. One crystal was bonded with a relatively thick layer resulting in a significant beam profile modulation, which can be seen in the image. The other crystal was not glued and no modulations are found. This is also the case for a very thin layer with less than three interference fringes. This is one of the main reasons, why the scalability of the active-mirror concept with bonded gain material is limited.

The bonding technology can be used for amplifiers in the several hundred mJ range. The mounting difficulties are not present for other cooling options, such as multi-slab amplifiers. Additionally, the direct cooling concept can be scaled to the 10 J level [70].

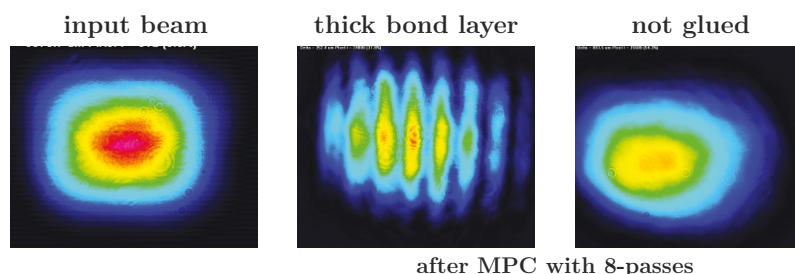


**Figure 5.3:** Resulting beam profiles after eight passes in a multipass cavity. The input beam is shown on the left side. In the middle is the output beam for an active-mirror with a thick bond layer and on the right a not glued example.

## 5.2 Yb<sup>3+</sup>-CaF<sub>2</sub> Amplifiers

### 5.2.1 Continuous Wave Laser Operation

The CW-operation mode is used to characterize the laser performance and to reach conclusions about the optical quality of the gain material. Furthermore, different materials can be compared in a standard setup. The experimental setup for the laser performance test is given in Figure 5.4.

A fiber-coupled laser diode is used as the pump source. An optical power of 9 W out of a multimode fiber with a 105  $\mu\text{m}$  core diameter and a numerical aperture (NA) of 0.15 is sent through a dichroic mirror onto the main material. The laser diode is not wavelength stabilized, leading to a spectral shift depending on the duty cycle of the pump pulse, as well as the driving current. The peak wavelength at the maximum current and in cw-operation mode is 976 nm at a heat sink temperature of 25 °C. The spectral bandwidth at FWHM is about 5 nm. The pump beam is imaged onto the laser material using a spherical lens telescope (L1 and L2) in a 4f configuration.

The magnification factor of the telescope depends on the used curved mirror. Typically, two configurations are carried out with a 200 mm and 300 mm convex mirror (M1), which results in a magnification of  $m = 4/3$  and  $m = 1$ , respectively. Pump and laser radiation is separated with the help of a dichroic mirror (DM), being highly reflective for the laser and anti-reflection coated for the pump wavelength, representing a so-called short wave pass filter (SPF).

A thin film polarizer (TFP) is inserted to polarize the laser radiation and to act as a variable output coupler in combination with a quarter-wave plate (QWP). The position of the QWP is optimized for each pump intensity to get the maximum output power. Mirrors M2 and M3 are plane and HR coated.

The two cavity branches have a length of 105 mm (165 mm for the 300 mm curved mirror) and 700 mm, respectively. This results in a stable confocal resonator with a beam diameter of 100  $\mu\text{m}$  as well as 125  $\mu\text{m}$  for a radius of curvature (RoC) of 300 mm on the active material and about 1.2 mm on the end mirror.

All values are checked using the ray transfer matrix formalism (also known as ABCD matrix formalism). A detailed overview can be found in [27].

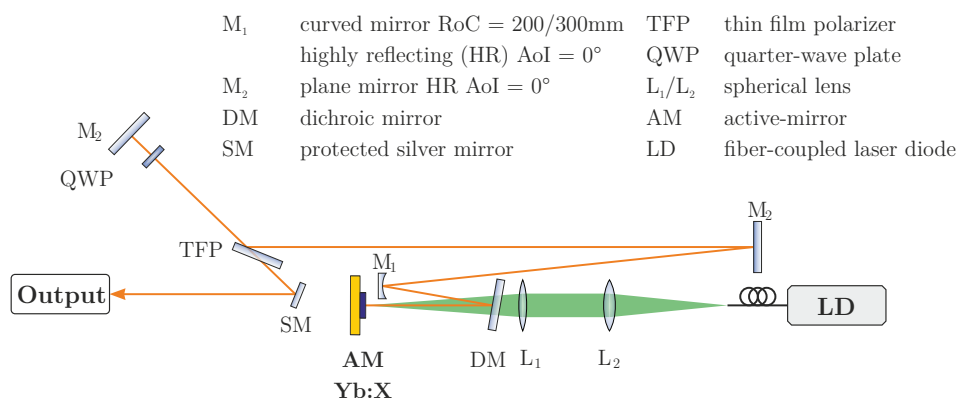


**Figure 5.4:** Experimental setup for continuous wave operation mode.

The investigated Yb<sup>3+</sup>-doped crystals were produced at CIMAP (Centre de Recherche sur les Ions, les Matériaux et la Photonique), France. The thickness of the sample is 3 mm with a doping concentration of 4.5 mol %. Due to the high doping concentration the optical quality limits the usable beam diameter to less than 1 mm. The polarization analysis is shown in Figure 5.5 (a). In the case of a small beam waist, no significant impact on the laser performance is found.

The continuous wave result is given in Figure 5.5. The heat sink was not water cooled. The output power is given as a function of the incident pump and the absorbed incident pump. The dashed line represents a spline curve between the measurement points to guide the eye. A linear regression is done for the absorption corrected values. A slope efficiency of 50 %, a laser threshold of 0.6 W pump power and a maximum optical-to-optical efficiency of 44 % is obtained. Better values could be achieved using a pulsed operation with a duty cycle of 20 %, which leads to a reduced thermal load of the crystal compared to the studied cw-operation case.

These are very promising results and further experiments in a regenerative amplifier setup have been carried out in the next section.

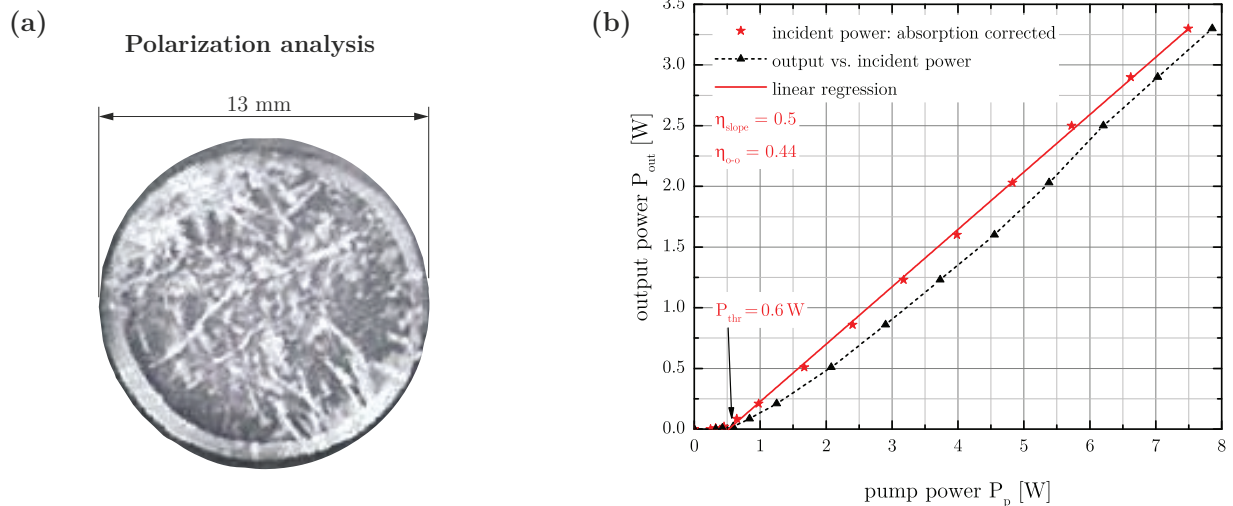


**Figure 5.5:** (a) polarization analysis of a 3 mm thick crystal; (b) the output power as a function of the incident pump and the absorbed incident pump. The dashed line represents a spline curve between the measurement points to guide the eye. The solid line is a linear regression of the measurement.

## 5.2.2 Regenerative Amplifier

The setup of the regenerative amplifier is tested in a cavity-dumped mode. This operation mode works as follows:

- At first, the quality of the resonator is kept low by using a QWP, where most of the spontaneously emitted light is coupled out and the intra-cavity photon build-up cannot occur. The absorbed pump energy is stored in the gain material and a large number of excited state ions are obtained.

- Secondly, a fast modulator is switched on to achieve a high resonator quality where the stored light is only reduced by very small parasitic losses. The intracavity power builds up very fast in a few tens of resonator round-trips.
- Finally, the modulator is switched off in a time which is shorter than the round-trip time. The light is coupled out within one round-trip time and the next cycle can be started. The pulse width is a convolution of the round-trip time and the response time of the quality-switch (dropping flank of the Pockels cell).

The experimental setup is illustrated in Figure 5.6. The difference in comparison to Figure 5.4 is the inserted Pockels cell (PC)<sup>a</sup>, which is the fast resonator loss modulator, between the TFP and the end mirror. Furthermore, the laser diode is operated in pulsed mode with a pump pulse duration of up to a maximum of three times the fluorescence lifetime and a repetition rate of 10 Hz to 100 Hz.

The build up of the intracavity power is observed by a photodiode behind the end mirror. The rising tail contains the information about the amplification factor. If the maximum pulse energy is accomplished, the circulating energy is reduced by the cavity losses. This leads to an exponential decay of the circulating energy. The decay time can be used to calculate the resonator losses. A typical photodiode signal is shown in Figure 5.7 as well as the coupled out pulse.

The output spectrum in the cavity-dumping mode nearly corresponds to the achievable spectrum for the amplification of stretched femtosecond pulses having much broader bandwidth (e.g. pulses shorter than 100 fs). The output spectrum of the cavity-dumped mode is presented in Figure 5.8 with a center wavelength at 1032 nm. The spectral bandwidth is about 6 nm (FWHM), which is much smaller than the gain cross section at a given inversion level between 0.1 and 0.3 (see Figure 4.12 on page 90).

The influence of the inversion was investigated by measuring the spectrum for different pump intensities (laser diode driving current variation) where the output energy is constant. This was done by adjusting the build-up time representing the number of round-trips in the resonator. The results are presented in Figure 5.8. The center wavelength exhibits a

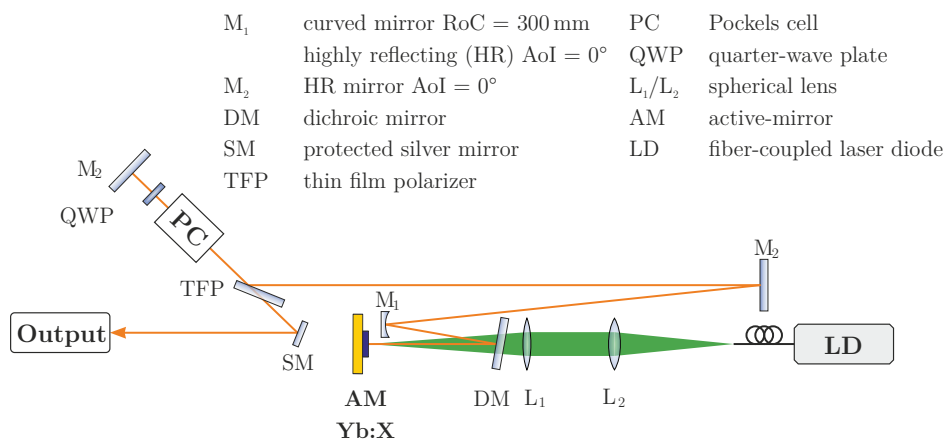


**Figure 5.6:** Schematic setup of a cavity-dumped laser resonator.

<sup>a</sup> A typical used material for PC is deuterated potassium dihydrogen phosphate (KD\*P).

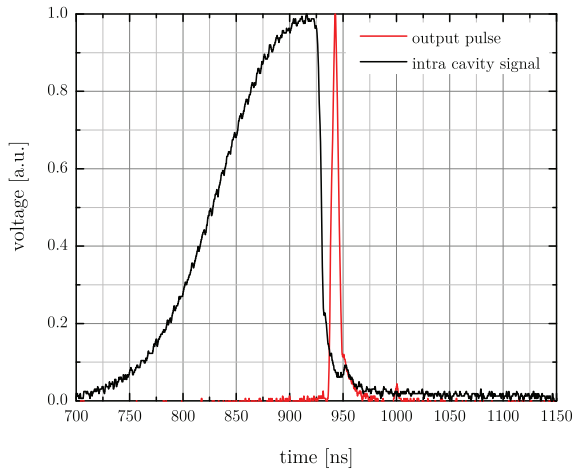


**Figure 5.7:** Cavity-dumping results; photodiode signal of the intracavity circulating energy and the output pulse with duration of about 8 ns.

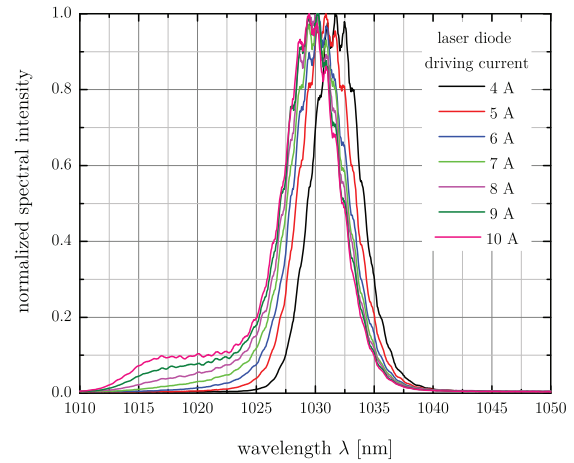


**Figure 5.8:** Cavity-dumped output spectrum at different laser diode driving currents for Yb<sup>3+</sup>:CaF<sub>2</sub>.

blue-shift at higher driving currents. This can be explained with the gain cross section. At higher inversion levels, the peak is shifted towards shorter wavelength (blue-shift), as shown in Figure 4.12 on page 90, leading to a shift of the amplified spectrum.

### Ultrashort laser pulse amplification

A test stretcher-compressor system was set up, which is comparable to the final PENELOPE setup, as described in Section 3.2.3 on page 51. In this way, the MLD grating can be tested and the required optic quality can be evaluated, on a smaller scale. Furthermore, the appropriate seed source was tested for the final CPA system.

The schematic setup is illustrated in Figure 5.9. The source of the initial laser pulses is a commercial Kerr-lens mode-locked Yb<sup>3+</sup>:KGW oscillator manufactured by Light Conversion Ltd. with pulse durations as short as 65 fs. A characteristic autocorrelation trace of the oscillator is shown in Figure 5.10. The pulse duration is 67.4 fs by assuming a Gaussian distribution or 60.2 fs for a Sech<sup>2</sup> distribution. A *SPIDER* measurement indicates an almost transform-limited pulse.

The oscillator is isolated against back reflections from the regenerative amplifier by a Faraday isolator. Additionally, the beam size is magnified before the stretcher with a spherical lens telescope LT<sub>1</sub>. The average power after the stretcher is around 200 mW at a repetition rate of 78 MHz. Thus the pulse energy is 2.5 nJ. The compression is performed in a grating compressor. The difference to the final stretcher-compressor system is the line density of the gratings, spectral hard-clip and the stretching factor/group delay dispersion. The groove density is 17401/mm and pulses are stretched to 2 ns. The spectral hard-clip is limited by the compressor to 30 nm, while the stretcher has a hard-clip of 40 nm. The system is compact due to the fact that the stretcher and compressor are using the same large grating with a size of 310 × 150 mm<sup>2</sup>. The maximum input energy for the compressor is close to 100 mJ.

The regenerative amplifier (see Figure 5.9) is placed in between the stretcher and compressor. A pulse picker, a combination of a Pockels cell and two polarizers, is used to reduce

## 5 Amplifier Experiments

$M_1$	curved mirror RoC = 300 mm highly reflecting (HR) AoI = $0^\circ$	FR	Faraday rotator	LT	spherical lens telescope
$M_2$	plane mirror HR AoI = $0^\circ$	FI	Faraday isolator	$L_1/L_2$	spherical lens
DM	dichroic mirror	TFP	thin film polarizer	AM	active-mirror
SM	protected silver mirror	HWP	half-wave plate	LD	fiber-coupled laser diode
TM	turning mirror (HR AoI = $45^\circ$ )	QWP	quarter-wave plate	Osc	femtosecond laser oscillator
		PC	Pockels cell		
		Pol	polarizer		

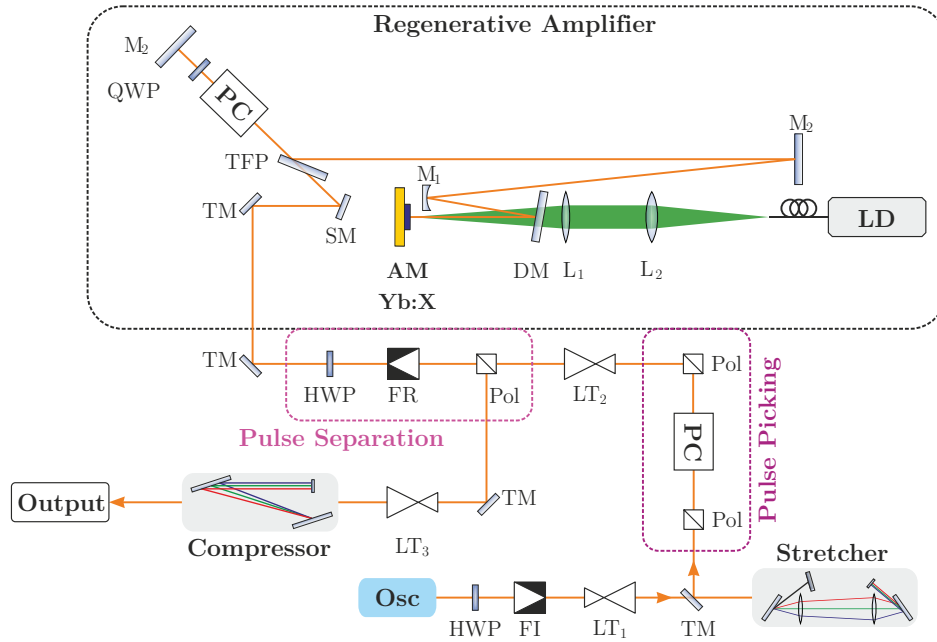


**Figure 5.9:** Experimental setup of the CPA laser system.

the repetition rate of the laser pulse train. The beam profile is matched to the resonator mode of the regenerative amplifier with a lens based telescope  $LT_2$ .

A global timing system is used to synchronize the amplifier chain to the oscillator pulses. Therefore the oscillator frequency is used to trigger the delay generator timing sequence ( $t_0$ ). A low jitter between the laser pulse and the PC switching is essential to realize a stable

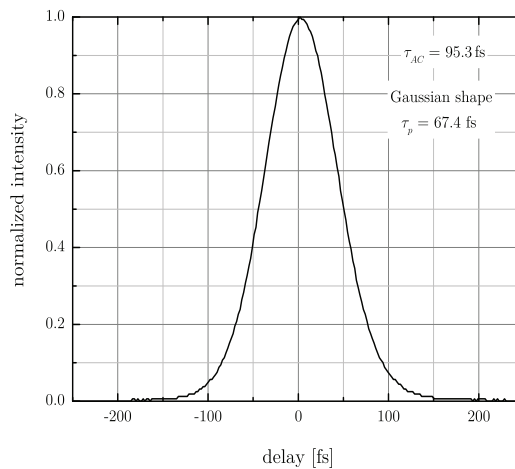


**Figure 5.10:** Intensity autocorrelation trace of the oscillator laser pulses.



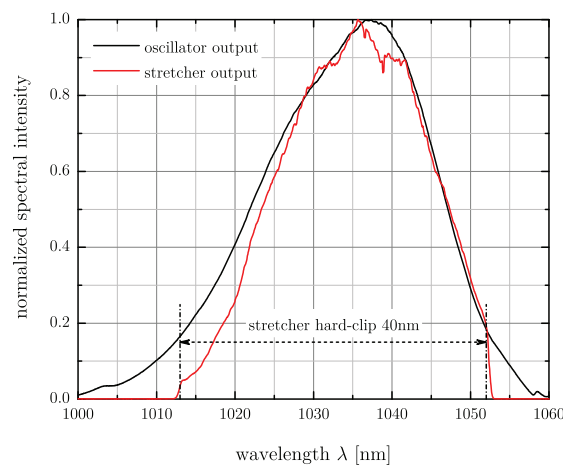
amplification. As the delay generator clock is independent from the femtosecond oscillator (i.e. not locked), jitter occurs and is increasing with the number of laser pulses after  $t_0$ . The pulse picking has to be very close to the trigger signal  $t_0$ , otherwise a large jitter is found in the nanosecond range.

The long pump pulse duration (several milliseconds) is insensitive against jitter and therefore the pump pulse is started at the end of the timing sequence. Thus the next amplification cycle is pumped by the cycle started before.

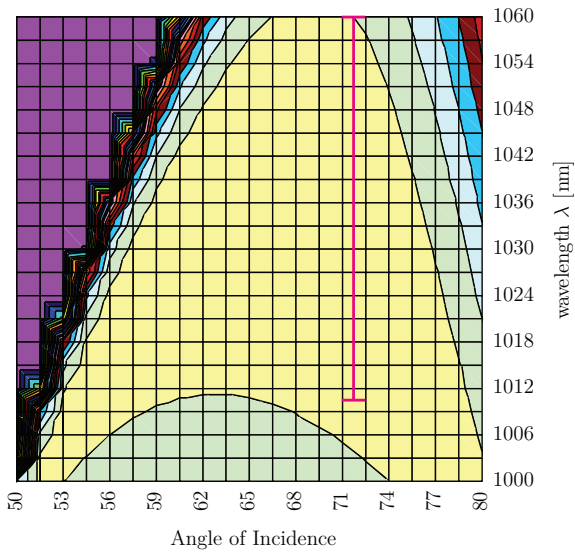
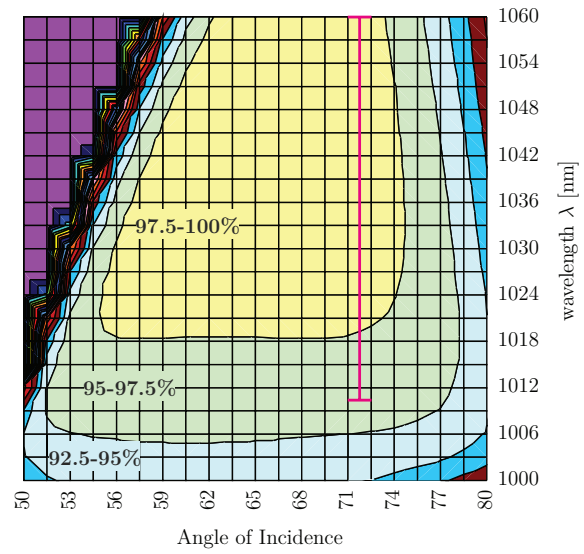
The separation between the input and output of the regenerative amplifier is realized with a Faraday rotator, a half-wave plate (HWP) and a polarizer (Pol). The position within the setup is shown in Figure 5.9. The input spectrum of the regenerative amplifier is presented in Figure 5.11 as well as the oscillator spectrum. The 40 nm hard-clip of the stretcher is clearly visible in the input spectrum. The blue part of the oscillator spectrum is attenuated in the stretcher compared to the red part. The reason for this lies in the transmission curve of the optical components and especially the grating. Figure 5.12 shows the theoretical diffraction efficiency of the gratings for both line densities. The data are provided with kind permission of *Plymouth Grating Laboratory, Inc.* The approximate stretcher/compressor range is represented by the vertical red line. The efficiency is low in the spectral range from 1010 nm to 1020 nm for 17401/mm compared to 17601/mm. This is the main reason why the 17601/mm are chosen in the final stretcher and compressor system.

The amplified signal is magnified with telescope LT<sub>3</sub> and sent to the compressor and finally diagnosed. The diagnostics consists of an energy meter, a spectrometer, a *SPIDER*, and a single-shot autocorrelator for the temporal pulse characterization.

The system was set up and seeded with the oscillator pulses and sent to the compressor after amplification. The compressor was optimized in order to compensate for collected material dispersion by adjusting the input angle on the first grating as well as the grating separation. Additionally, a *DAZZLER*<sup>TM</sup> was implemented following the stretcher. The *DAZZLER*<sup>TM</sup> gets a feedback from the *SPIDER* (spectral phase) to reach the desired flat spectral phase. The best result is shown in Figure 5.13 with a *SPIDER* measurement. The spectral bandwidth is reduced to  $\sim 7.9$  nm, which results in an almost Fourier limited pulse duration of 193.3 fs. The residual *GDD* of 68 fs<sup>2</sup> is negligible.



**Figure 5.11:** Normalized spectral intensity of the oscillator and stretcher output.

1760lns/mm MLD Grating, DC=0.35, Depth=480nm  
Diffraction Efficiency vs. Angle and Wavelength1740lns/mm MLD Grating, DC=0.33, Depth=450nm  
Diffraction Efficiency vs. Angle and Wavelength

**Figure 5.12:** Theoretical diffraction efficiency of gratings with a line density of 1760l/mm (on the left) and 1740l/mm (on the right). The approximate stretcher/compressor range is represented by the vertical red line. The data are provided with kind permission of *Plymouth Grating Laboratory, Inc.*

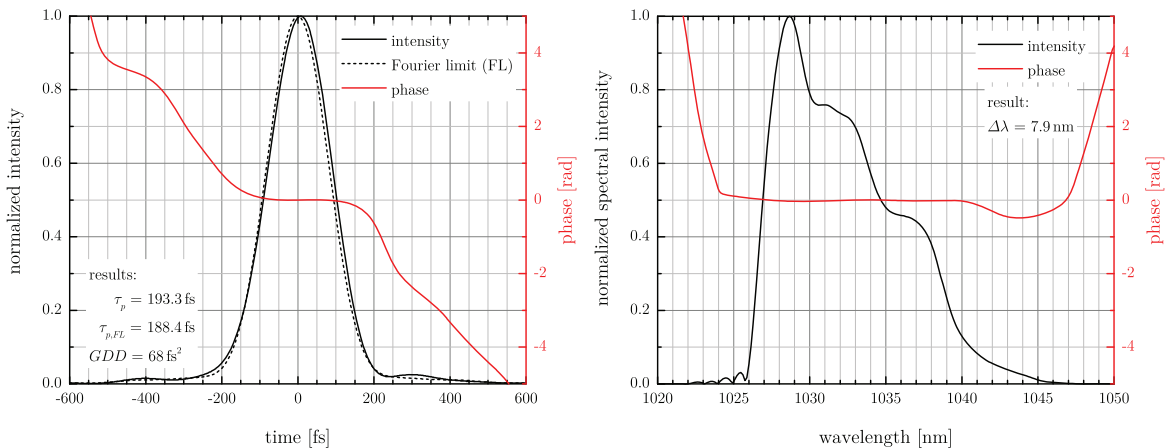


**Figure 5.13:** SPIDER measurement of the laser pulse.

At the edges of the spectrum the phase is not perfectly compensated. The measurement principle limits the compensation capacity. For a better compensation, a *WIZZLER*<sup>TM</sup> should be used instead, where the measurement principle has a higher dynamic range of up to 50 dB [52, 53] leading to a better phase measurement at the edges of the spectrum [171]. With only 7.9 nm bandwidth remaining, obviously the gain narrowing has to be overcome. In the next section the possibility of how a spectral manipulation can be performed will be elaborated. The spectral characteristics of the system are described in more detail.



### 5.2.3 Spectral Manipulation

As mentioned before, it is hard to get a Fourier limited pulse duration below 200 fs directly from a regenerative amplifier based on Yb<sup>3+</sup>:CaF<sub>2</sub> in a linear regime. The dominant effect is gain narrowing in our case. The influence on a Gaussian pulse can be approximated by [172]

$$\frac{1}{(\Delta\lambda_{out})^2} = \frac{1}{(\Delta\lambda_{in})^2} + \frac{\ln G}{(\Delta\lambda_{em})^2} \quad , \quad (5.1)$$

where  $G$  is the total gain,  $\Delta\lambda_{out}$  the spectral bandwidth of the output pulse,  $\Delta\lambda_{in}$  the spectral bandwidth of the input pulse and  $\Delta\lambda_{em}$  the emission bandwidth of the gain material by assuming a Gaussian distribution for all of them. If we assume a Fourier limited pulse duration, Equation (5.1) can be rewritten by using Equation (4.1) to

$$\tau_{out} = \tau_{in} \sqrt{1 + \frac{4(\ln 2)^2 \lambda_c^4}{c_0^2 \pi^2} \frac{\ln G}{\tau_{in}^2 (\Delta\lambda_{em})^2}} \quad , \quad (5.2)$$

where  $\tau_{out}$  is the Fourier limited pulse duration of the output pulse,  $\tau_{in}$  initial transform-limited pulse duration,  $\lambda_c$  is the center wavelength of the laser pulse and  $c_0$  is the speed of light in vacuum. Now the gain narrowing can also be interpreted as a pulse broadening in the temporal domain. The question is how to overcome this limitation.

If saturation effects are ignored, the output intensity spectrum  $\tilde{I}_{out}(\lambda)$  can be represented by

$$\tilde{I}_{out}(\lambda) = \tilde{I}_{in}(\lambda) \mathcal{T}_{str}(\lambda) \mathcal{T}_{comp}(\lambda) \mathcal{T}_{amp}(\lambda) G(\lambda) \quad , \quad (5.3)$$

where  $\tilde{I}_{in}(\lambda)$  is the input intensity spectrum,  $\mathcal{T}_{str}(\lambda)$  and  $\mathcal{T}_{comp}(\lambda)$  the spectral transmission of the stretcher and compressor,  $G(\lambda)$  the total spectral gain and  $\mathcal{T}_{amp}(\lambda)$  represents the passive spectral transmission of the amplifier and of the whole amplifier chain, respectively.

The goal is to extract energy from the amplifier with a high spectral bandwidth. The spectral transmission of the stretcher and compressor are close to 1 over the whole bandwidth, which was presented in Section 3.2.3, and can be ignored in further considerations.

Equation (5.3) indicates clearly the two ways to counteract gain narrowing. On the one hand, the gain spectra can be directly manipulated, by nonlinear gain broadening and gain material combination. On the other hand indirect spectral manipulation, especially by gain shaping, is a viable option as well.

One solution for direct manipulation is to use nonlinear effects, especially self-phase modulation (SPM), to generate a broader spectrum. It has been shown by J. Pouysegur et al. that in an Yb<sup>3+</sup>:CALGO nonlinear regenerative amplifier pulses below 100 fs with a pulse energy of 24  $\mu$ J are achievable [173, 174]. The main drawback of that technique is the limited energy range of the amplifier for which ultrashort pulses with a reasonable temporal quality can be generated. Additionally, the system is not CPA free (high complexity) and has to be designed very carefully in terms of its parameters (e.g. initial chirp, resonator round trips).

Another direct manipulation is the combination of gain materials with different peak emission wavelengths leading to a broader effective amplification bandwidth. This could be done in series in the same amplifier [175–178] or in parallel by recently demonstrated coherent beam combining [179].

For Nd<sup>3+</sup>-glass laser systems the mixed-glass approach is a standard technique to generate ultrashort laser pulses below 200 fs [78] on the Petawatt scale. The glass mixture is typically composed of both phosphate and silicate glass gain media. The advantage is the large number of investigated glass compounds for the Petawatt laser development at the Lawrence Livermore National Laboratory [180]. The limitation of this technique is that only a relatively small amount of Yb<sup>3+</sup>-doped gain media with a broad emission bandwidth are available, which can be produced in large size and good optical quality.

The direct manipulation is to shape the spectral gain distribution  $G(\lambda)$ . This can be performed by inserting spectrally dependent losses before (pre-shaping) or during the amplification process (intracavity) with greater attenuation at the peak of the gain profile compared to the remaining spectrum. Both solutions have their advantages and disadvantages and are accordingly used in the various amplifiers.

The intracavity modulation leads to an energy loss which has to be compensated by increased pump intensity. This is not advisable in the high-energy amplifier case, as the installed pump power is the main investment and the introduced losses reduce the effectively available energy.

Pre-shaping the injection spectrum leads to a low input energy and the ASE is unaffected. This can lead to a higher ASE level for strong spectral shaping. A spectral attenuation element placed inside the amplifier affects the injection spectrum as well as the ASE per round-trip equally. In principle, it is possible to use a pre-shaped spectrum as well. However, the manipulation during the amplification is preferred, as the ASE is attenuated as well. The intracavity shaping is important for especially high-gain amplifiers ( $G > 10^4$ ), like a regenerative amplifier. Equation (5.3) can be modified for regenerative as well as multipass amplifiers to

$$\tilde{I}_{out}(\lambda) = \tilde{I}_{in}(\lambda) \mathcal{T}_{sha}(\lambda)^k \mathcal{T}_{amp}(\lambda)^k G_0(\lambda)^k, \quad (5.4)$$

where  $k$  is the number of round trips,  $G_0(\lambda)$  spectral gain per round trip and  $\mathcal{T}_{sha}$  is the spectral transmission for one round trip.

Starting from this point, we will concentrate on two different principle methods. The desired spectral response can be introduced either by a passive or an active control element.

A technique using passive elements, especially for Ti<sup>3+</sup>:sapphire-based CPA systems, was introduced by C. Barty et al. [181]. As passive elements, very thin etalon's (3 μm and 5 μm), a prism pair, with a mask in the spatial dispersion region after the second prism and a single-plate quartz birefringent filter were tested [181]. The best result was found with the etalon leading to a broadening factor of about 3. Thus a resulting pulse duration of 18 fs was achieved [182] instead of 26 fs without shaping [183]. Additionally, a spectral attenuation can also be done with a well-designed spectral mirror transmission [184, 185].

The active gain control can also be realized with an acousto-optic crystal or a spatial light modulator placed in the Fourier plane of a zero dispersion stretcher. The second solution is rather complex to implement into a regenerative amplifier. For this reason, the best solution is the acousto-optic device, which can be easily implemented inside the

amplifier. In Ti<sup>3+</sup>:sapphire-based CPA systems the active gain control was introduced by T. Oksenhendler et al. [186] with an obtained pulse duration of 18 fs. This is a comparable result to the passively optimized laser performance. The main drawback of this device is the large dispersion of the tellurium dioxide (TeO<sub>2</sub>) crystal used in the acousto-optic device.

In the following discussion a single-plate quartz birefringent filter for passive shaping and an acousto-optic programmable gain control filter (AOPGCF) using TeO<sub>2</sub> as an active shaping element are compared. Both methods have their pros and cons as given in the following list:

<b>Passive Gain Control</b>	<b>Active Gain Control (TeO<sub>2</sub>)</b>
<ul style="list-style-type: none"> <li>+ large beam diameter possible</li> <li>+ Brewster's angle and normal incidence possible</li> <li>- spectral modulation is limited to a typically sinusoidal shape (arbitrary function not possible)</li> <li>- manual adjustment needed</li> <li>- fixed bandwidth</li> <li>- needed design change for a new gain material</li> </ul>	<ul style="list-style-type: none"> <li>+ spectral resolution of 0.5 nm</li> <li>+ spectral modulation can have an arbitrary shape</li> <li>+ automatic optimization loop</li> <li>- low LIDT (30 mJ/cm<sup>2</sup>, 1 ns)</li> <li>- maximum beam diameter smaller than 2 mm</li> <li>- large single pass dispersion, 25 mm of TeO<sub>2</sub> leads to: <math>GDD = 9258 \text{ fs}^2</math>, <math>TOD = 6351 \text{ fs}^3</math>, <math>FOD = 1283 \text{ fs}^4</math></li> <li>- only Brewster's angle operation possible (AR coating difficult)</li> </ul>

In order to estimate the necessary gain control capacity, it is of utmost importance to characterize the spectral response of the individual optical components in the whole amplification chain. This is the main point of interest for the next section.

### 5.2.3.1 Spectral Response of the Regenerative Amplifier

An amplifier consists of different optical elements (e.g. mirrors, waveplates, Pockels cell), which exhibit a different spectral behavior. The reflectivity (e.g.  $R \geq 99.9\%$ ) of the cavity mirrors can be manufactured very broad and flat over the required spectral range (e.g. 1000 nm to 1070 nm). Therefore their influence on the spectral response of the resonator is neglected. One critical point is the short wave pass filter (SPF), also called dichroic mirror, to separate the pump and laser radiation. A typical specification is  $HR(0^\circ, 1020\text{-}1200 \text{ nm}) > 99.9\% + R(0^\circ, 808\text{-}980 \text{ nm}) < 99.9\%$ . The difference is that in the cavity the mirror is tilted and thus the spectral edges are shifted towards shorter wavelengths by about 5 nm at an AoI of 10° compared to normal incidence. To avoid that, a resonator with a non-collinear pumping geometry has to be built. In this case, the pump and laser beams are angularly separated.

The most critical components are the polarization optics such as the thin film polarizer (TFP), quarter-wave plate (QWP), Pockels cell (PC), etc. The difficulty is to determine the spectral dependence on both states of polarization. The schematic setup to investigate the polarization depending spectral or temporal response of an element is presented in Figure 5.14. Different types of sources are possible, for example a broadband ultrafast fiber

Source	- broadband ultrafast fiber laser	HWP	half-wave plate
	- tunable cw laser diode	Pol	polarizer
	- tunable ns-laser	LT	spherical lens telescope
Detector	- photodiode	L	spherical lens
	- optical spectrum analyzer		
	- CCD camera		

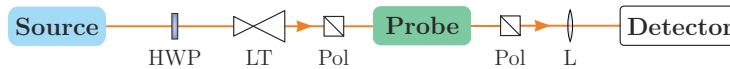


**Figure 5.14:** Schematic setup of the polarization depending measurements with different source and detectors. The probe is placed between two polarizers (parallel or perpendicular).

laser generating a supercontinuum with a spectral bandwidth up to 180 nm.

To measure the spectral response accurately, an optical spectrum analyzer (OSA) is the best choice in this case. This device has a high spectral resolution down to 20 pm and a high dynamic range of up to 50 dB. The used polarizers *colorPol*<sup>®</sup> (IR 1100 BC) are manufactured by CODIXX and are specified to have a high contrast of better than  $10^5$  from 900 nm to 1200 nm. A typical value is  $>10^6$  from 1000 nm to 1100 nm. This is essential to get results with a high dynamic range in the measurement setup.

The TFPs under test are designed to show low modulation within the specified spectral range, but due to fabrication tolerances the spectral characteristics may differ. The reflectivity as a function of the wavelength of two fabricated TFPs are shown in Figure 5.15. The data are provided with kind permission of *LAYERTEC*<sup>®</sup>. Typically, the TFP has to be used with s-polarization as the transmitted p-polarized light exhibits spectral modulations, as shown in Figure 5.15. The spectral characteristics were verified, with the setup in Figure 5.14 and a good agreement was found. However, in the case of the best polarization contrast in a single pass, the transmitted beam has to be used, as the p-polarized light extinction is superior to the reflected case. This can be used in a pulse picking unit or similar, where polarization contrast is especially important.

In the amplifiers and in the transport line, waveplates are needed to adjust the state of polarization of the laser beam. These components have a spectral transmission behavior

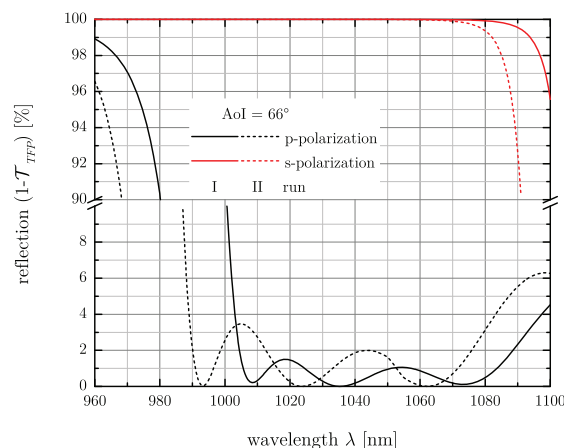


**Figure 5.15:** Polarization depending spectral reflection of two produced thin film polarizer from different coating runs, which are distinguished by solid and dashed line. The data are provided with kind permission of *LAYERTEC*<sup>®</sup>.

dependence. The retardation of the waveplate phase  $\Gamma_{QWP/HWP}$  is a function of the wavelength. The transmission between two polarizers is not constant for a given spectral range and depends on the waveplate order  $\tilde{m}$  as well. In the case of two parallel polarizers, the transmission and phase retardation for a quarter/half-wave plate is given as

$$\mathcal{T}_{QWP/HWP} = 1 - \sin^2(2\xi) \sin^2\left(\frac{\Gamma_{QWP/HWP}}{2}\right) \quad (5.5)$$

$$\Gamma_{QWP/HWP} = \frac{2\pi d}{\lambda} (n_e(\lambda) - n_o(\lambda)) \quad (5.6)$$

$$\Gamma_{QWP} = \frac{\pi}{2} (2\tilde{m} + 1) \quad (5.7)$$

$$\Gamma_{HWP} = \pi (2\tilde{m} + 1) \quad , \quad (5.8)$$

where  $\xi$  is the rotation angle of the waveplate,  $d$  is the thickness of the plate, depending on the waveplate order  $\tilde{m}$  such as the center wavelength  $\lambda$ , and  $n_o$  and  $n_e$  are the ordinary and extraordinary refractive indices [187]. In general, the transmission between perpendicular polarizers is derived to

$$\mathcal{T} = \sin^2(2\xi) \sin^2\left(\frac{\Gamma}{2}\right) \quad . \quad (5.9)$$

The theoretical transmission for zero-, first- and second-order HWPs is given in Figure 5.16(a) over 70 nm and the center wavelength  $\lambda_c$  at 1035 nm. A QWP in a double-pass configuration exhibits the same behavior. The transmission drops close to the center wavelength. The best solution is a true zero-order waveplate, i.e. which is made from a single plate of crystalline quartz. However, they are very thin, thus the handling is delicate.

Other solutions are air spaced or cemented waveplates, which consist of two multiple order quartz waveplates with their effective retardation difference to be  $\lambda/2$  or  $\lambda/4$ . In

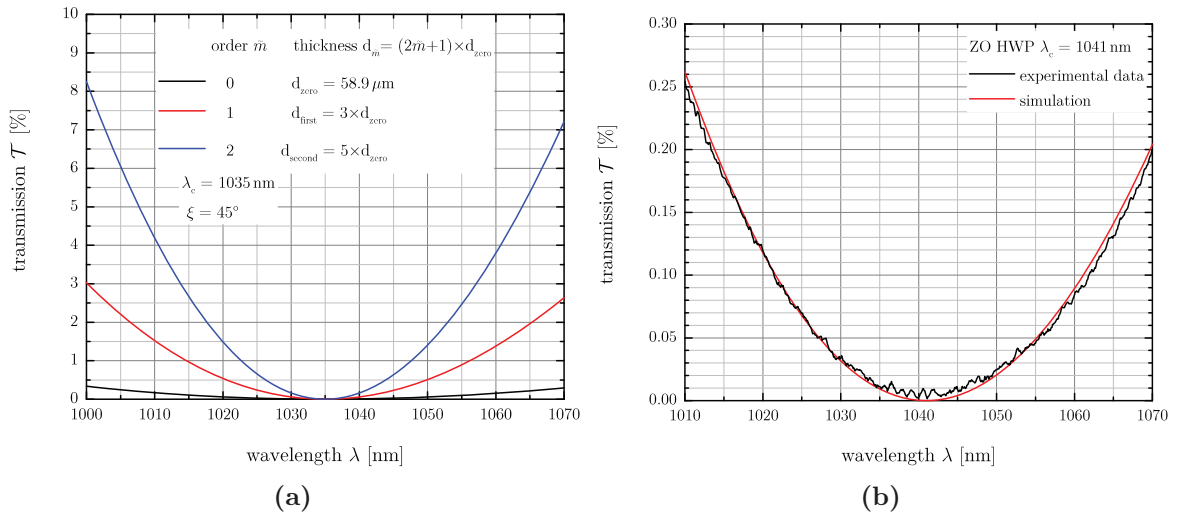


**Figure 5.16:** (a) the theoretical transmission for zero-, first- and second-order HWPs at a rotation angle of  $\xi = 45^\circ$  and a center wavelength of 1035 nm. (b) the measured transmission of a ZO HWP with a specified  $\lambda_c$  of 1035 nm.

any case, the specified center wavelength has to be checked carefully due to manufacturing variations/tolerances.

The spectral transmission was determined using the setup in Figure 5.14 with a broadband source and an OSA. Figure 5.16(b) shows the result of a zero-order HWP (air spaced) and the predicted transmission at a center wavelength of 1041 nm. The specification of  $\lambda_c$  was 1035 nm. Nevertheless, the experimental result indicates a zero-order waveplate ( $\tilde{m} = 0$ ). This is of utmost importance as it exhibits a minimum retardation (thus the loss) over the whole spectral range.

The last component is the Pockels cell, which can be interpreted as a voltage-controlled waveplate. The Pockels electro-optic effect generates additional birefringence in the optical medium (typical materials are  $\beta$ -barium borate (BBO) or KD\*P) by applying an electric field. It is a linear effect in term of phase shift versus voltage. Two types of Pockels cell are generally used. The first is the transversal and the other is the longitudinal Pockels cell. In the following discussions, longitudinal PCs are used.

The optical axis is in the direction of the laser beam. The polarization is rotated to  $90^\circ$ , if the phase shift corresponds to  $\pi$ . This is the half-wave voltage  $U_\pi$  and the quarter-wave voltage  $U_{\pi/2}$  is needed to realize a QWP. The half-wave voltage for KD\*P is derived to

$$U_\pi = \frac{\lambda}{2} \cdot \frac{1}{n_o^3 r_{63}} \quad , \quad (5.10)$$

where  $r_{63}$  is the electro-optic coefficient<sup>a</sup> and  $n_o$  is the refractive index of the ordinary ray [188]. The quarter-wave voltage is half as much of  $U_\pi$ . Please note that all given equations are for DC voltage. Pockels cells are typically operated in pulsed mode. This requires approximately 10 % to 20 % higher voltages compared to the DC due to transition effects.

The phase retardation of the Pockels cell  $\Gamma_{PC}$  is comparable with a waveplate and is given by

$$\Gamma_{PC} = \frac{2\pi}{\lambda} \Delta n d \quad (5.11)$$

$$\Delta n = r_{63} n_o^3 E \quad (5.12)$$

$$\Gamma_{PC} = \frac{2\pi}{\lambda} r_{63} n_o^3 U \quad , \quad (5.13)$$

where  $U$  is the applied voltage. The transmission between parallel polarizers as a function of the applied voltage is derived to

$$\mathcal{T}_{PC} = 1 - \sin^2 \left( \frac{\Gamma_{PC}}{2} \right) \quad (5.14)$$

$$\mathcal{T}_{PC} = 1 - \sin^2 \left( \frac{\pi U}{2 U_\pi} \right) \quad (5.15)$$

---

a Sometimes called Pockels coefficient in order to distinguish for the Kerr effect.

by using Equations (5.10) and (5.13). This Equation does not show the spectral dependence of the PC at a given voltage. Therefore Equation (5.15) is transformed to

$$\mathcal{T}_{PC}(\lambda) = 1 - \sin^2\left(\frac{\pi U_\pi(\lambda_c)}{2 U_\pi(\lambda)}\right), \quad (5.16)$$

where  $U_\pi(\lambda_c)$  is the half-wave voltage at the chosen center wavelength  $\lambda_c$ . The expected transmission of a Pockels cell as a function of the wavelength is shown in Figure 5.17(a). The half-wave voltage was chosen at 1035 nm and the transmission of a zero-order waveplate is given as a comparison. It can be seen that the PC has almost the same transmission and the small residual difference can be explained with the different index of refraction.

An experimental verification was performed with a narrowband tunable nanosecond laser and a photodiode, as depicted in Figure 5.14. The wavelength was changed from 1027 nm to 1047 nm and the result is given in Figure 5.17(b). The experiment matches the estimated transmission to a good degree. The transmission is affected by the drift of the voltage and the low thermal load.

A Pockels cell has two different contrast ratios. The first is called intrinsic contrast ratio *ICR* and the second one is called voltage contrast ratio *VCR*. The *ICR* arises between two perpendicular polarizers, when no voltage is applied to the PC. It is sensitive to the angular alignment of the PC. The intrinsic contrast ratio  $ICR(\lambda)$  depends directly on the wavelength  $\lambda$  and is derived to

$$ICR(\lambda) = ICR(\lambda_c) \left(\frac{\lambda}{\lambda_c}\right)^2, \quad (5.17)$$

where  $ICR(\lambda_c)$  is the intrinsic contrast ratio at the center/measurement wavelength.

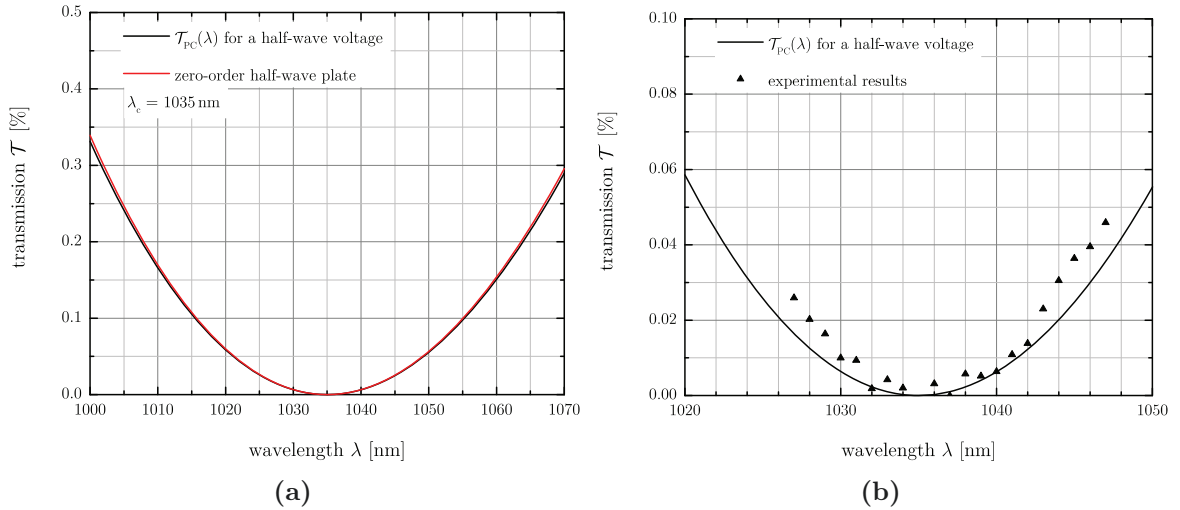


**Figure 5.17:** (a) the theoretical transmission of a PC between two parallel polarizers at  $U_\pi$  for  $\lambda_c = 1035$  nm and a ZO HWP as a comparison. (b) measured transmission of a PC at half-wave voltage and the predicted trend.



On the other hand, the voltage contrast ratio of the PC  $VCR(\lambda)$  between perpendicular polarizers can be written as

$$VCR(\lambda) = \frac{VCR(\lambda_c) \left(\frac{\lambda}{\lambda_c}\right)^2}{VCR(\lambda_c) \left(\frac{\lambda}{\lambda_c}\right)^2 \sin^2 \frac{\Gamma_{PC}}{2} + 1}, \quad (5.18)$$

where  $VCR(\lambda_c)$  is the maximum achievable voltage contrast ratio for a fixed half-wave voltage at the chosen center wavelength  $\lambda_c$ . Here, the contrast drops with the change of the phase retardation  $\Gamma_{PC}$ . Due to this the  $VCR$  decreases very fast by means of a wavelength variation. Figure 5.18 shows the  $VCR$  as a function of the wavelength for two different maximum extinction ratios of  $10^4$  and  $10^3$  at  $\lambda_c$  of 1035 nm. As a comparison the  $ICR$  is presented as well. Out of Figure 5.18 one can clearly recognize that the  $VCR$  depends on the wavelength as well as the maximum contrast. In both peak extinction ratio cases, the voltage contrast ratio is almost the same at the edges of the bandwidth, which means the reduction is much stronger for the  $10^4$  peak  $VCR$ .

As a conclusion, it can be clearly seen that the  $ICR$  of a PC is almost independent from the wavelength, while the  $VCR$  exhibit a strong dependence. Thus, the best contrast can be achieved without applying any voltage. Therefore, the pulse picking unit has to be used in such a way, that the pulse is selected, if the PC is switched on and off. This is essential to get a high temporal intensity contrast (TIC). If the PC angular adjustment is not precise enough, it has a significant impact on the TIC. A more detail investigation is performed in Section 5.3. Furthermore, a non-perfectly well adjusted half-wave voltage as well as a  $VCR$  shift due to thermal load has only a minor influence on the picked pulses (single transmission). For this purpose, all isolation stages in the PENELOPE laser system based on PCs are used in that particular way.

In the regenerative amplifier case the influence of the Pockels cell with an applied voltage cannot be eliminated as the PC switches the quality of the resonator. Additionally, the PC couples the laser pulses in and out. The goal for future development is to design the

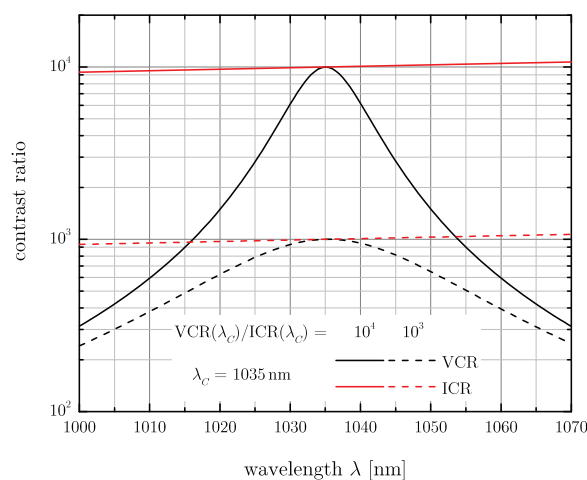


**Figure 5.18:**  $VCR$  and  $ICR$  as a function of the wavelength and for two different maximum extinction ratios.



regenerative amplifier, in such a way that the PC is switched off during amplification. This should reduce the influence of the PC on the spectral transmission of the amplifier.

The influence of most resonator components are investigated. However, there are some points to look into more detail like the resonator without SPF. In the case of the polarization elements, it is possible to eliminate the waveplates based on crystal quartz plates by using reflective waveplates [189–191].

### 5.2.3.2 Passive Gain Control

As was mentioned before in Section 5.2.3, a single-plate quartz birefringent filter (QBF) that acts as a passive gain control element is used for spectral attenuation inside the regenerative amplifier or before a multipass amplifier.

The transmission of the QBF is similar to a waveplate (see Equation (5.5)) in the case of a high order  $\tilde{m}$ . A solution of the birefringent filter can be found in [192] and shows that the spectral modulation is affected by three different factors. The thickness  $d$  adjusts the modulation bandwidth, the rotation angle  $\xi$  around the optical axis influences the modulation depth and the tilt angle  $\zeta$  tunes the peak wavelength of the modulation. This provides the possibility to optimize the spectral attenuation for a given gain material.

Several thicknesses are available to find the best result in the amplifier stages. Figure 5.19(a) shows the experimental results for a 2.55 mm and 5.08 mm thick QBF between two polarizers at  $\xi = 45^\circ$  and  $\zeta = 0^\circ$ . The thickness was calculated to an ideal thickness of 2.69 mm and 5.35 mm using the transmission spectrum. The difference between the experiment and theory can be explained with the optical axis of the crystalline quartz being not perpendicular to the front face. However, the spectral attenuation is still measurable, but an exact prediction using the relation [192], cannot be made. Therefore, the spectral transmission of the 2.55 mm was measured for different tilt angles. The results are given in Figure 5.19(b). The shift of the peak wavelength is clearly visible and the crystalline quartz plates can be used to shape the spectrum of the amplifiers.

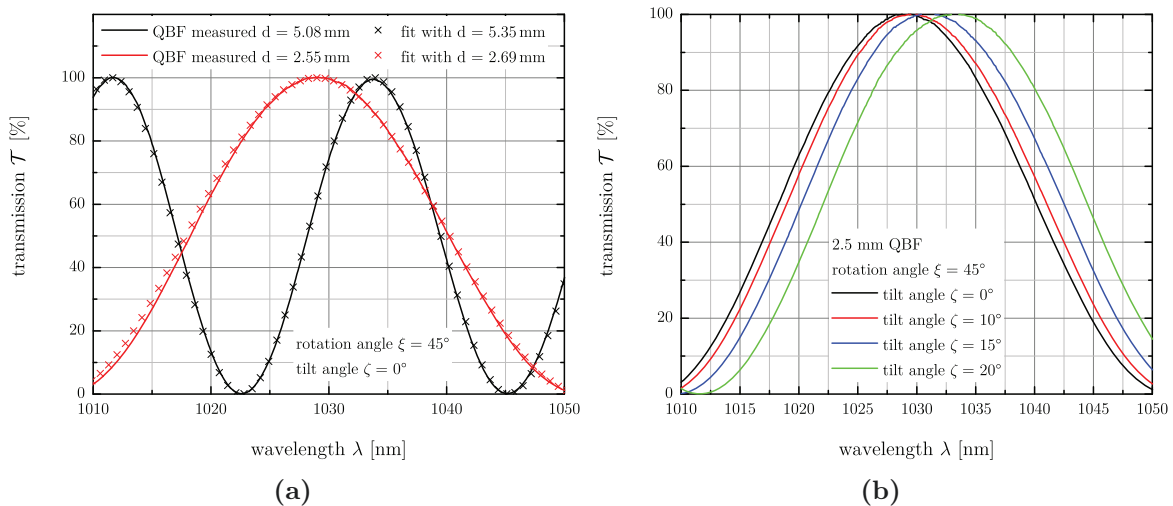


**Figure 5.19:** Spectral transmission of two different QBF at a rotation angle  $\xi = 45^\circ$ . (a) QBFs with a thickness of 2.55 mm and 5.08 mm between two polarizers at a tilt angle of  $\zeta = 0^\circ$ . (b) 2.55 mm QBF at four different tilt angles.

At first, the influence on the output spectrum of a cavity-dumped regenerative amplifier was investigated. Therefore the QBF is implemented into the resonator, as given in Figure 5.20. The crystal is set up in a double pass configuration. This results in twice the retardation, basically doubling its effective thickness.

The best results are obtained with the 2.55 mm thick QBF. The broadest cavity-dumped output spectrum is presented in Figure 5.21 and the initial spectrum is given as comparison. The additional losses were compensated by increasing the pump power to reach the same output energy of about 0.8 mJ. The bandwidth by using the passive gain control is 22 nm at FWHM. The value for the initial spectrum is in the range of 5 nm. The enhancement factor is about 4.4 to the initial spectral bandwidth, which is comparable with the passive gain control results in  $\text{Ti}^{3+}$ :sapphire regenerative amplifiers [181, 182].

The next step is to place the regenerative amplifier with the passive gain control in the CPA system and optimize the angles of QBF in order to obtain the best output spectrum. The pulses out of the stretcher are injected into the amplifier yielding an output energy of more than 300  $\mu\text{J}$ . Figure 5.22 shows the injected as well as the amplified spectrum. As a comparison, this setup is used in cavity-dumping mode and its output spectrum shows a significant difference compared to its optimized case (see Figure 5.21). The red part (i.e. longer wavelength) of this newly cavity dumped spectrum shows a stronger attenuation. This is due to the fact, that the oscillator input spectrum is red-shifted (center wavelength at 1036 nm) to the gain peak (1032 nm) and shows an almost Gaussian shaped compared to the otherwise ideally flattop case of the pure cavity dumping operation. Furthermore, the spectrum above 1045 nm cannot be transferred through the regenerative amplifier. Obviously one has to optimize each individual case, whether the setup should be used as a regenerative amplifier or in the cavity-dumping mode.

The same result was obtained in the cavity-dumped mode of the regenerative amplifier, as shown in Figure 5.21. The reason for the missing spectral part could also be the amplification spectrum, which has a plateau from 1040 nm to 1048 nm, as shown in Figure 4.12(c) on page 90. Therefore, the spectral attenuation has to have an arbitrary distribution. One option to generate such a desired distribution, is to use an active gain control as discussed

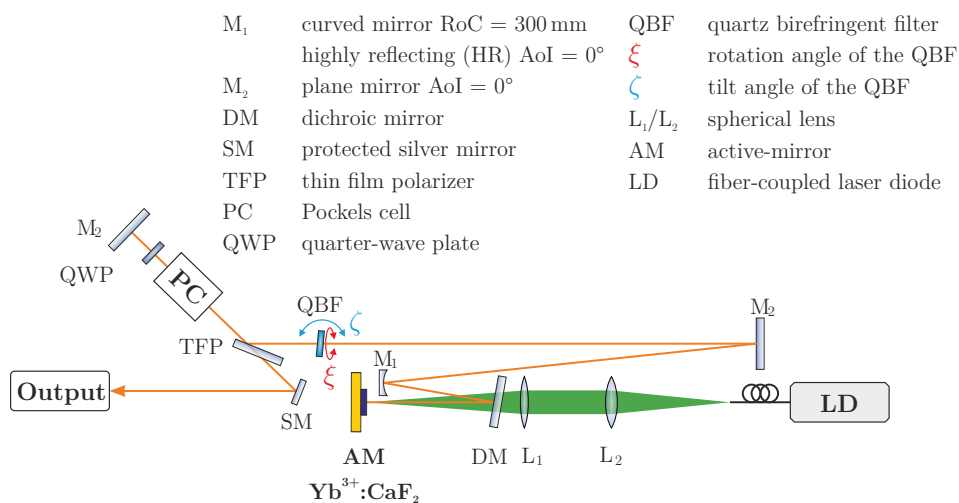


**Figure 5.20:** Schematic setup of a cavity-dumped laser resonator with passive gain control, which is realized by using a QBF.

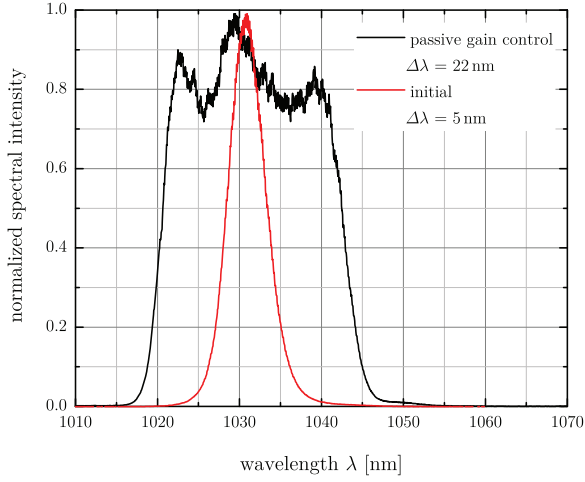


**Figure 5.21:** Output spectrum of the cavity-dumped resonator by using a 2.5 mm thick QBF as a passive gain control element and the initial spectrum without any modulation.

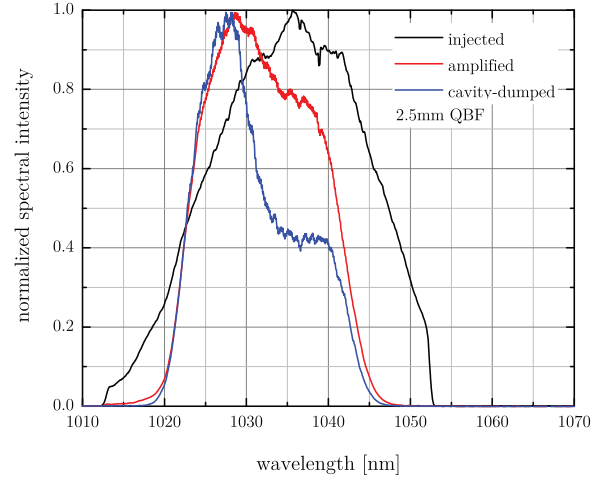
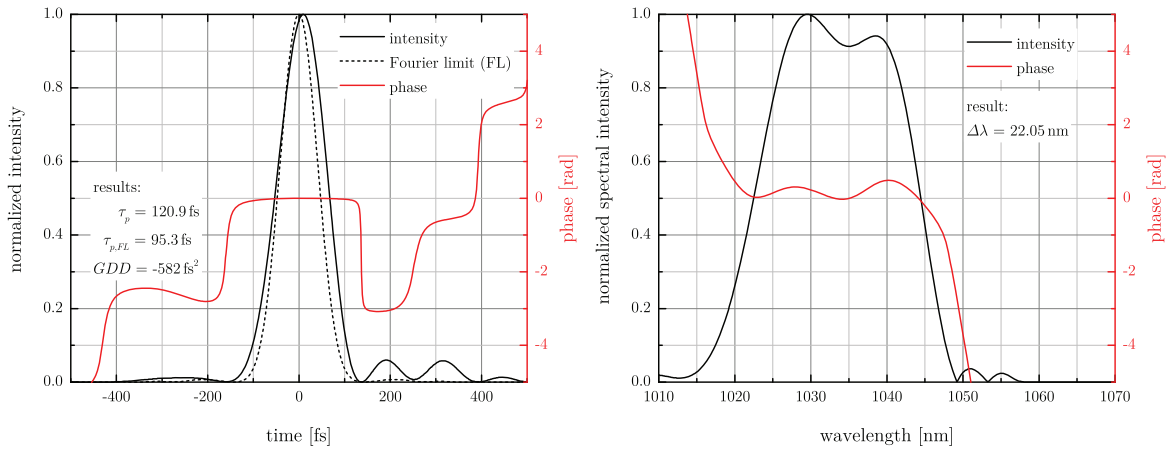


**Figure 5.22:** Output spectrum of the regenerative amplifier with passive gain control. The injected, the amplified and the cavity-dumped spectrum is given. The rotation and tilt angle of the 2.5 mm thick QBF was optimized for the amplified spectrum.

in the next section. The main drawback of the QBF is the inadequate degree of freedom for the spectral attenuation distribution.

The amplified laser pulses are compressed and sent to the diagnostics. The result of a *SPIDER* measurement is shown in Figure 5.23. A pulse duration of 120.9 fs was achieved, which leads to a 1.67 times higher intensity compared to the initial result (193.3 fs) without gain control, as shown in Figure 5.13. The residual phase is low and can be compensated with a *DAZZLER*<sup>TM</sup>.



(a) Calculated temporal intensity and phase of the laser pulse as well as the Fourier limit.

(b) Measured spectral intensity and phase of the laser pulse.

**Figure 5.23:** *SPIDER* measurement of the laser pulse obtained in a Yb<sup>3+</sup>:CaF<sub>2</sub> regenerative amplifier with passive gain control.

One way to overcome the manipulation limit of QBFs is to use two or more of them in the same regenerative amplifier. This enables a higher degree of freedom for spectral attenuation. First preliminary experiments are performed using two QBFs in series with a thickness of 2.5 mm. The setup was the same as in Figure 5.20. The regenerative amplifier is used in the cavity-dumped operation mode. The second quartz plate is placed close to the first one. Both filters are optimized to get a broadened output spectrum. The cavity losses are compensated by adjusting the laser diode driving current. Figure 5.24 shows the best result obtained with two gain control elements and the spectrum using one QBF from Figure 5.21. The spectral bandwidth at FWHM is 4 nm wider compared to one QBF. As this is a preliminary result it indicates a way to get pulse durations in the sub-100 fs range. The modulation of the spectrum is stronger in the case of two QBFs compared to only one.

In the future, more detailed investigations of the different impact factors on the spectral response of the resonator have to be performed. Using a passive gain control, the enhancement indicates a promising solution to support ultrashort laser pulses significantly below 150 fs up to the Joule-level and beyond.

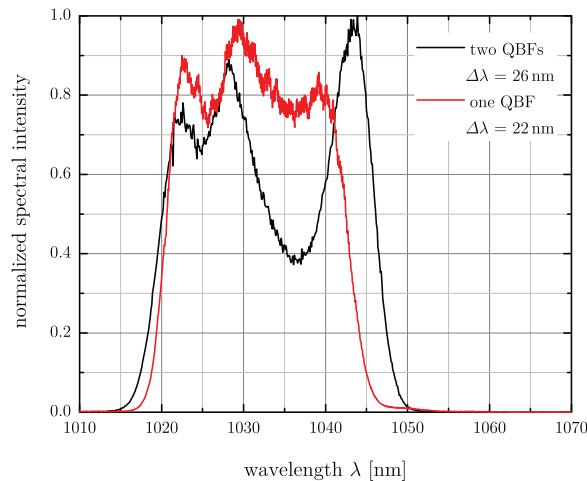


**Figure 5.24:** Output spectrum of the cavity-dumped resonator by using two 2.5 mm thick QBFs as passive gain control elements and the spectrum obtained with one passive gain control element.

### 5.2.3.3 Active Gain Control

As mentioned earlier the active gain shaping is realized with an acousto-optic programmable gain control filter (AOPGCF). It relies on a Brewster cut collinear filter controlling the regenerative amplifier losses. The unwanted spectral components are deflected out of the beam path [193, 194]. The strength of the spectral deflection loss can be adjusted by the radio frequency power applied to the piezo-electric transducer bonded to the crystal.

The schematic experimental setup is presented in Figure 5.25. As the crystal is at Brewster's angle, the resonator has to be adapted accordingly. The difficulty lies in the p-polarization operation (Brewster's angle) while TFPs reflect the s-polarization in our case. For this purpose, the AOPGCF is placed in between two TFPs and rotated by 90° around the optical axis to omit the otherwise needed half-wave plate. Furthermore, no additional changes are done to the regenerative amplifier.

The optical signals are controlled by radio frequency signals in the range of tens of MHz. The desired spectral shape is given to the corresponding software via a data file. A software performs a direct optimization feedback loop. The RF-power is optimized to get a broad spectrum. However, the pump intensity has to be increased due to the insertion losses.

The broadest obtained spectrum in the cavity-dumped mode is shown in Figure 5.26. As comparison, the unshaped and passive shaped spectrum is given. The spectral bandwidth is 28 nm at FWHM being 6 nm more compared to the result in the case of the passive gain control. The increase occurs mainly at the longer wavelength part of the spectrum. The falling edge exhibits a red shift of about 10 nm. However, the falling edge on the blue spectral part is also shifted slightly towards longer wavelengths. The spectral width at the 10% level is almost 30 nm.

The loaded loss spectrum for the AOPGCF is presented in Figure 5.27 as well as the spectral gain distribution at an inversion level of 20% at 300 K taken from Figure 4.12(c) on page 90. It can be clearly seen that the attenuation is similar to the inverse of the

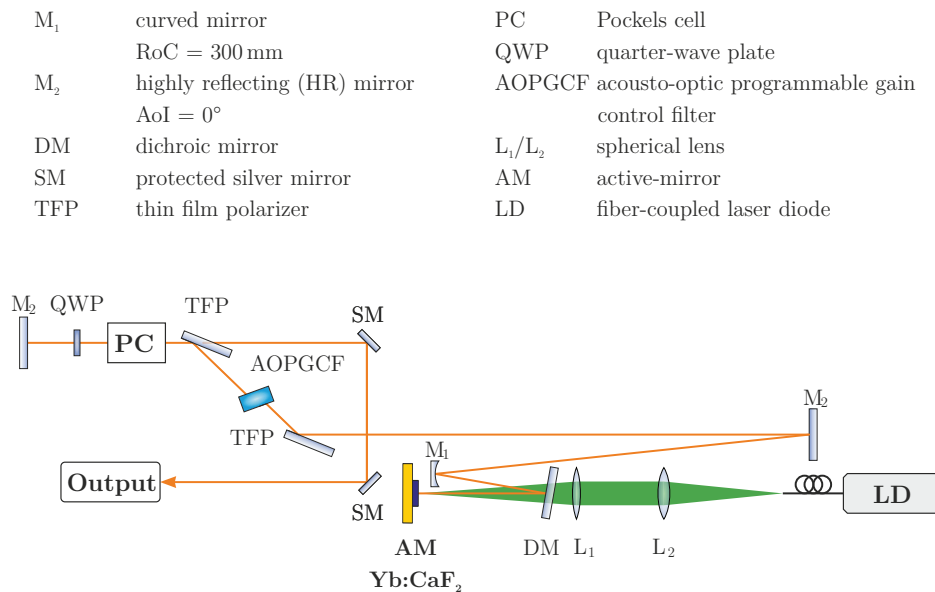


**Figure 5.25:** Schematic experimental setup of a cavity-dumped laser resonator with active gain control, which is realized by using an AOPGCF.

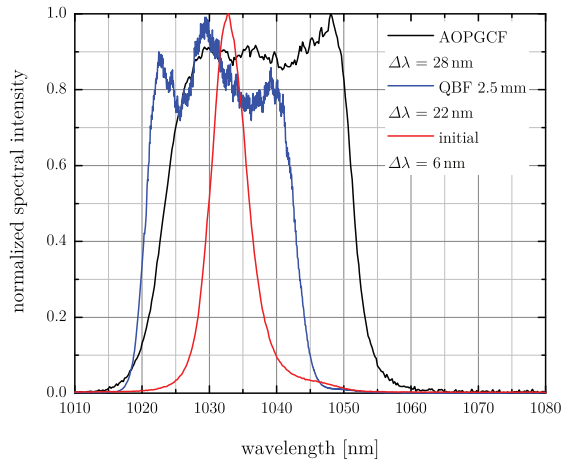


**Figure 5.26:** Cavity-dumped spectrum obtained with an AOPGCF. As comparison the unshaped and passive shaped spectrum is given.

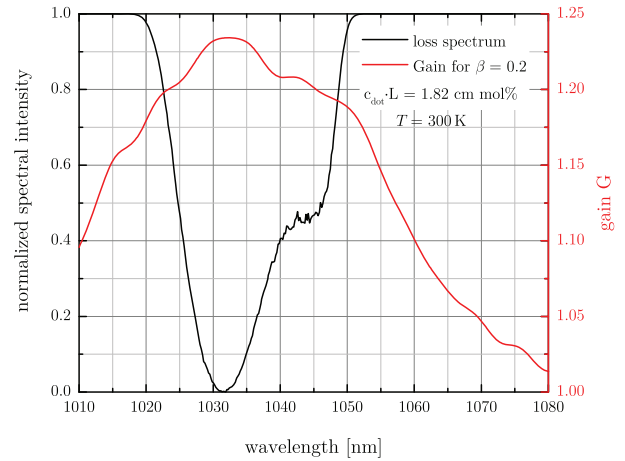


**Figure 5.27:** The loaded loss spectrum for the AOPGCF is given and the spectral gain  $G$  distribution at an inversion level of 20% at 300 K, taken from Figure 4.12(c) on Page 90.

gain spectrum, suggesting that the maximum bandwidth for this setup was obtained. The arbitrary attenuation functions give the possibility to optimize to any laser material gain cross section. The major drawback of this solution is the limited output energy due to the low damage threshold ( $30 \text{ mJ/cm}^2$  with 1 ns pulses).

The spectral width, obtained with the active gain control, is sufficient enough to support sub-100 fs laser pulses.

## 5.2.4 Bandwidth Scaling of the Large Amplifiers

As noted in Section 5.2.3 the spectral manipulation for the multipass amplifiers has to be done in advance. The spectral shaping for MPA I (see Figure 3.2 on page 35) can be performed within the regenerative amplifier. Therefore the output spectrum is not flat but shows a dip at the peak gain wavelength. For the other multipass amplifiers this can be realized using a passive shaping unit (e.g. a single-plate quartz birefringent filter) before each of the amplifiers. What has to be kept in mind is that behind MPA III energy loss cannot be accepted, due to the needed input energy for the final amplifier stage. For this purpose, the better way is to compensate the gain narrowing for both amplifiers in advance. This means a total gain of about 100 for the last two amplifiers has to be taken into account.

In order to study this case, a small scale experiment with MPA II and the regenerative amplifier with passive gain control was carried out. MPA I was selected for several reasons. At first, a large number of amplification passes is possible, which leads to a gain of more than 100. The second reason is the relatively easy setup compared to the complex MPA I, as shown in Figure 3.15 on page 49. Furthermore, spectral shaping for MPA I is required in any case.

The schematic principle of the experiment is presented in Figure 5.28. In these experiments a single crystalline  $\text{Yb}^{3+}:\text{CaF}_2$  active-mirror is used with a diameter of 25 mm, a thickness of 5 mm and an ytterbium concentration of 3 mol %. An FA collimated laser diode stack with 8 bars is used as pump source in a double pass configuration, as shown in principle in

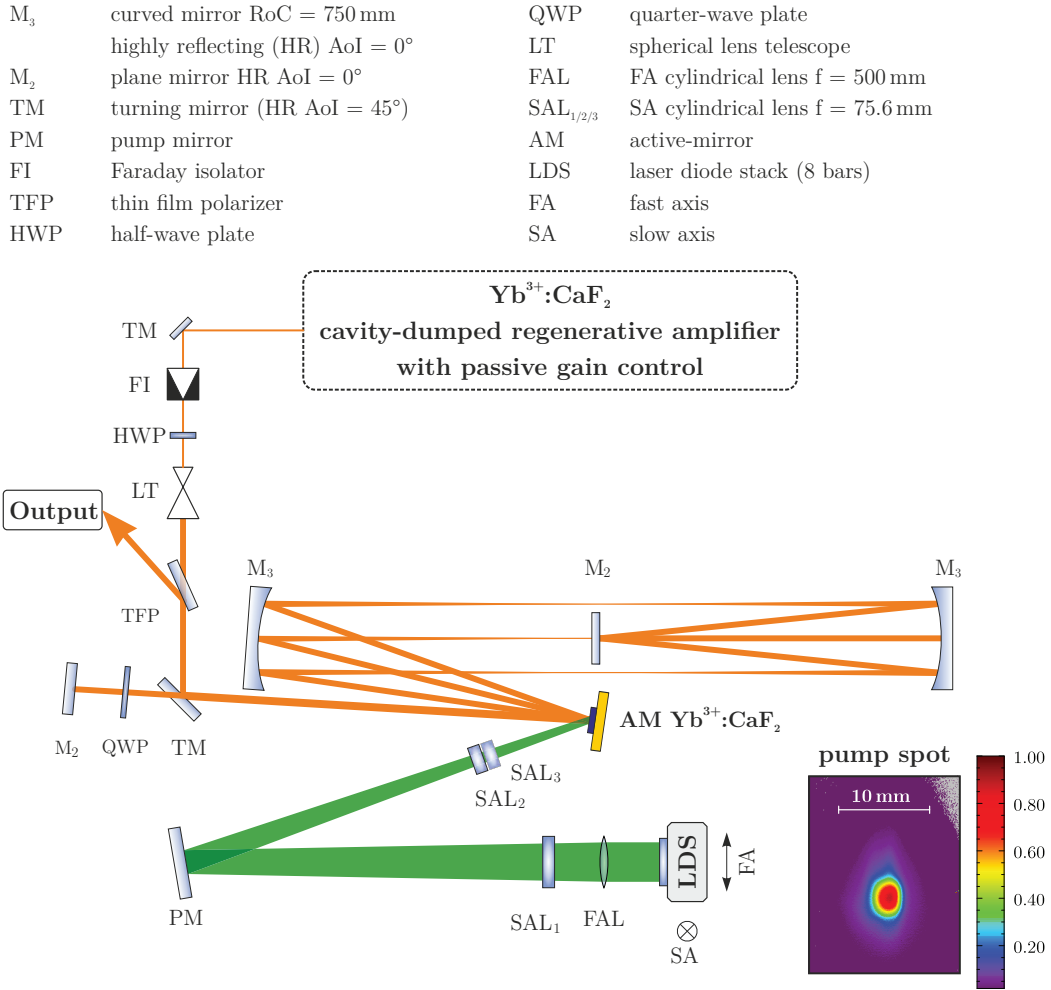


**Figure 5.28:** Schematic experimental setup of the MPA I injected by the cavity-dumped regenerative amplifier (see Figure 5.20) to study the amplifier dynamic in different cases. The resulting pump spot is given on the bottom right.

Figure 5.28. The pump and extraction beam is separated using angular multiplexing. The laser diode stack was not homogenized with an MLA.

The pump beam is shaped with a cylindrical lens telescope. Therefore, the FA is focused with a cylindrical lens FAL onto the crystal to use the far field distribution. This lens has a focal length of 500 mm to realize a large spot size in the FA direction due to the small divergence angle. Additionally, the gain material is slightly out of focus and the AoI on the disk is selected to get a symmetric spot size, as shown in Figure 5.28. With an SA divergence significantly larger than for the FA, a shorter focal length is needed. Consequently, a solution to satisfy both, SA and FA, has to be found. This is realized in such a way that the cylindrical lens SAL<sub>1</sub> is used as a single imaging lens generating the image onto SAL<sub>2/3</sub>. SAL<sub>2</sub> and SAL<sub>3</sub> project the far field of the SA onto the gain media. The focal length has to be short enough to get a small spot size, due to the large divergence angle of the SA ( $\theta_{SA,St} \approx 10^\circ$ ). The pump spot is given in Figure 5.28 (see insert) and has a size of about  $2.2 \times 3 \text{ mm}^2$  (at FWHM). The peak pump intensity at the maximum laser diode driving current  $I_{LD,max} = 250 \text{ A}$  is  $17.7 \text{ kW/cm}^2$  without any transmission losses.



The spatial distribution is smooth but has a Gaussian-like shape in contrast to the almost flat top of pump spot of MPA III (see Figure 3.34 on page 72). The pump duration for all experiments was 2.5 ms and the maximum laser diode driving current  $\mathcal{I}_{LD_{max}}$  was 250 A. The repetition rate was limited to 1 Hz in order to prevent thermally induced losses as well as mechanical damage of the disk.

The output of the regenerative amplifier was isolated using a Faraday isolator and the beam size was magnified with a spherical lens telescope to match the pump spot. A QBF inside the regenerative amplifier was used to get a narrow ( $\Delta\lambda = 1$  nm) or a broad ( $\Delta\lambda > 20$  nm) output spectrum. This allows to compare the amplification dynamic for both cases. In the case of a narrow spectrum, a larger total gain is estimated. For this reason, the center wavelength was selected to match the peak gain at 1031 nm.

The multipass cavity was set up with two concave mirrors with a RoC = 750 mm and 8 extraction passes. The schematic setup is shown in Figure 5.28. The number of passes could be doubled using polarization multiplexing, as described in Section 3.2.2 on page 48.

The obtained result with the described setup are given in Figure 5.29. First of all, a low input energy was used to get an almost unsaturated gain for the narrow bandwidth spectrum in both extraction cases. Figure 5.29(a) shows the gain as a function of the laser diode driving current. In the case of high driving current the gain starts to saturate for 8 and 16 extraction passes, where one extraction pass is defined as the path between entering and exiting the gain medium including internal reflection. The input energy was chosen to get the same output energy at  $\mathcal{I}_{LD_{max}}$ . The maximum total gain was 335 for 16 and 20 for 8 extraction passes at 250 A, resulting in a single pass gain of 1.44 and 1.45. The 16 passes are needed to get the required total gain of more than 100. Therefore all other experiments are performed with polarization multiplexing.

Figure 5.29(b) shows the gain for the narrow and broad spectrum, respectively. The maximum total gain for the broad spectrum is 255, which is  $\sim 76\%$  of the narrow wavelength case. Thus, the single pass gain is reduced to 1.41. The input energy was 10  $\mu$ J in both cases. This relatively high gain is a promising result for the multipass amplifiers.

The amplifier is designed to provide an output energy of about 100 mJ. The maximum input energy of 850  $\mu$ J was used to test the amplifier dynamics for the broadband case. The output energy as a function of the laser diode driving current is shown in Figure 5.29(c). The obtained output energy was 113 mJ, which leads to a total gain of 133. Close to 230 A a gain saturation due to thermal roll over as well as a degeneration of the pump spot is found. The pump spot degradation arises as the SA divergence angle depends of the laser diode driving current.

At this point, the spectral dynamics are investigated and presented in Figure 5.29(d). The input spectrum as well as the output for  $\mathcal{I}_{LD}$  of 50 A, 130 A, 170 A and 250 A is shown. The variation of  $\mathcal{I}_{LD}$  stands for different inversion levels. In the case of 50 A, the blue part of the spectrum is attenuated due to a gain below 1. If the current is increased, the spectrum below 1032 nm is amplified more than the other parts. At 130 A the peak of the spectrum is clearly visible and highlighted up to 250 A. The bandwidth is reduced to 10 nm compared to the injected 20 nm.

Nevertheless, the edges of the spectrum are identifiable and the output can be flattened using a pre-shaped input. This satisfies the expectations and it can be assumed that the final amplifier stages achieve their planned parameters. The first broadband extraction



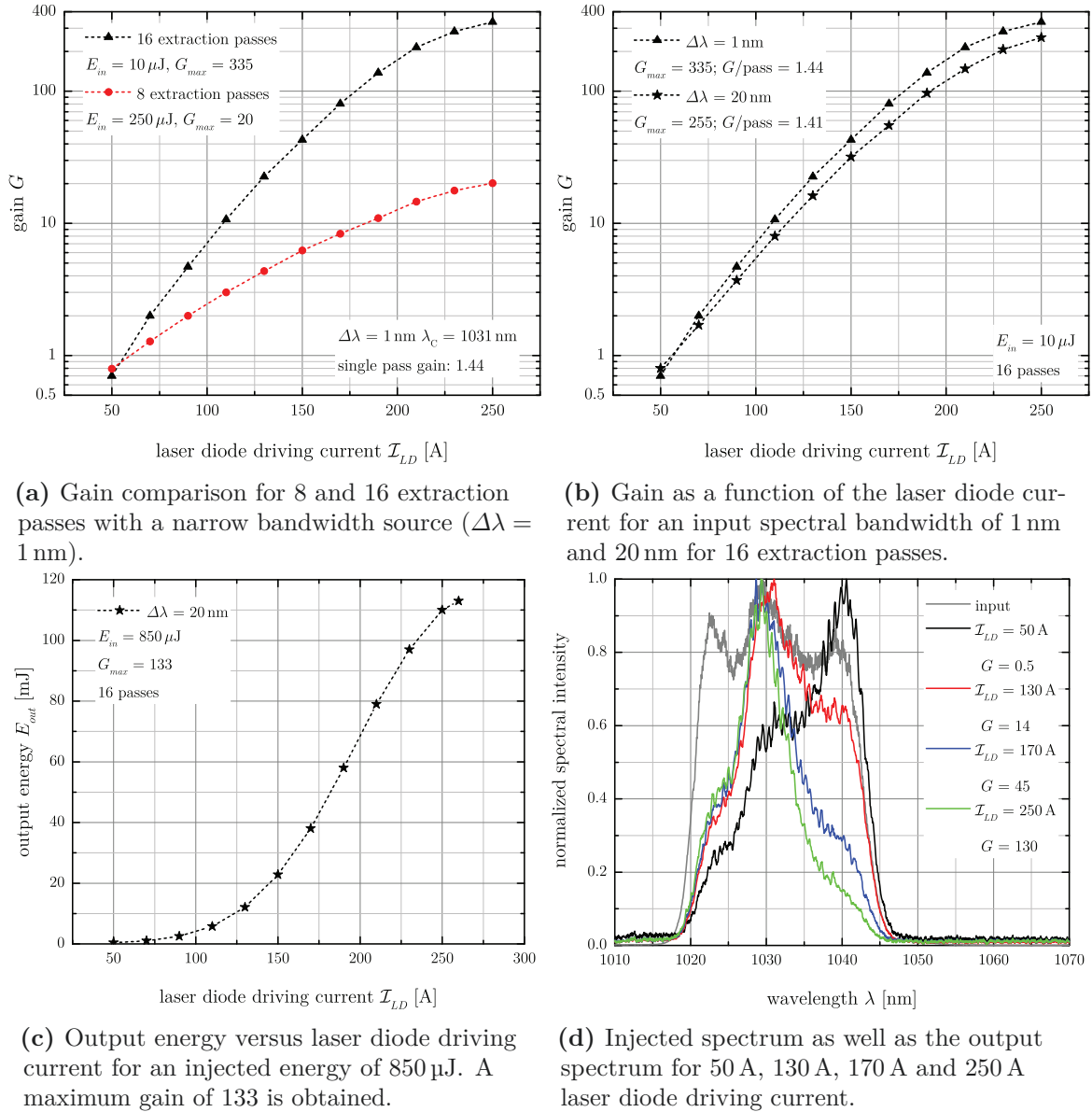


**Figure 5.29:** Experimental results for the MPA I.

campaign with the MPA III was performed and the results are presented in Chapter 6 on Page 131

To verify this result, a numerical model is used to simulate the output spectrum of MPA I. The model based on the theory given in Sections 2.2.1 and 2.2.2. All simulation input parameters are given in Figure 5.30. The experimental and the simulated output spectrum are presented in Figure 5.30. The difficulty for calculation of pump absorption is that the spot is not homogenized and the model holds only for a one-dimensional case. For this reason, the pump intensity was set to  $12 \text{ kW/cm}^2$ , which is an estimated average value. A satisfying agreement is found between both spectra.

Furthermore, the model can be used to estimate the needed pre-shaping spectra for MPA III and IV. The advantage of these amplifiers is the homogenized pump spot, which leads to a constant intensity over the pumped area. The numerical model is taken to

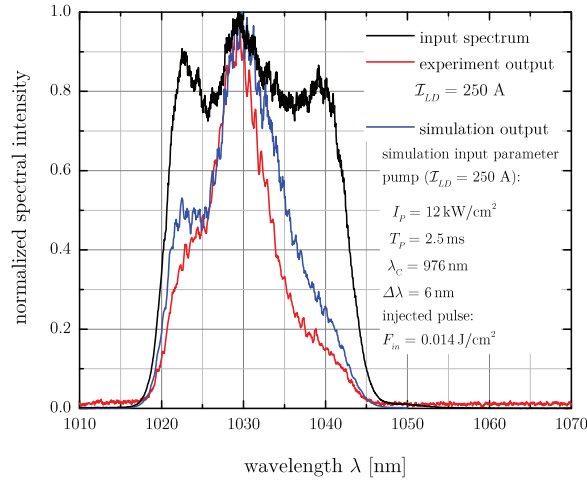


**Figure 5.30:** Comparison of the simulated output spectrum of the MPA I at  $I_{LD_{max}}$  with the measured spectrum. The input spectrum for the simulation and experiment is given as well. The input parameters for the simulation are listed.

give a rough estimation of the MPA III predicted performance operating at 300 K (room temperature). The amplifier has to show a total gain of more than 100 and a bandwidth of more than 20 nm.

Table 5.1 shows the input and output parameter of the simulation. The amplifier fulfills the design parameters and achieved a maximum gain of 268. The high output fluence can be decreased by a shorter pump duration. The predicted optical-to-optical efficiency of 11.1% is very high for an  $\text{Yb}^{3+}:\text{CaF}_2$  amplifier. Figure 5.31 shows the simulated output spectrum as well as the pre-shaped input. The spectral shape is characterized by a fifth-order

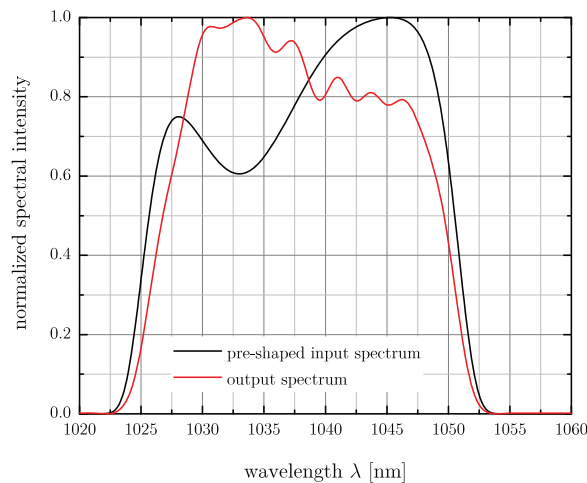


**Figure 5.31:** Numerical result of the output spectrum of MPA III and the pre-shaped input spectrum.

Super-Gaussian distribution with a bandwidth of 25 nm.

The spectral manipulation is assumed with a Gaussian shape. The center wavelength  $\lambda_c$ , the modulation width  $\Delta\lambda_{mod}$  and depth are optimized to get a smooth and flat shaped output spectrum. The used pre-shaped input spectrum is sufficient enough to preserve the spectral bandwidth, as shown in Figure 5.31. The obtained spectrum has a similar

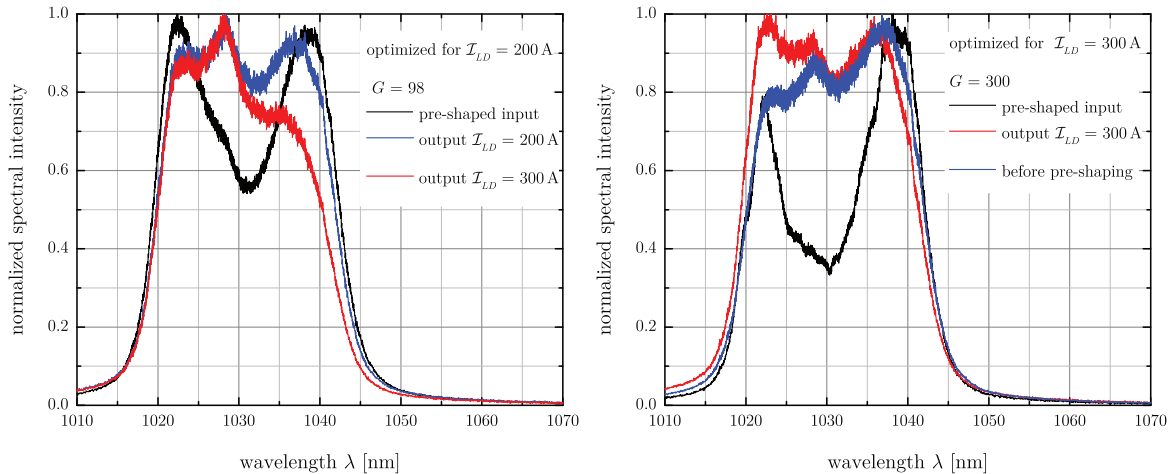
input parameter	
pump	
center wavelength	977 nm
bandwidth (FWHM)	6 nm
intensity	20 kW/cm <sup>2</sup>
pump duration	2.4 ms
injected laser puls	
center wavelength	1038 nm
bandwidth (FWHM)	25 nm
fluence	0.02 J/cm <sup>2</sup>
amplitude modulation	
center wavelength	1033 nm
bandwidth (FWHM)	10 nm
depth	40 %
output parameter	
gain	268
fluence	5.4 J/cm <sup>2</sup>
optical-to-optical efficiency	11.1 %

**Table 5.1:** The input and output parameters for the numerical model.

bandwidth and shape compared to the active gain control result in Figure 5.26. This indicates that the numerical result can be achieved with MPA III. The modulations in the output spectrum result from the measurement noise of the cross sections (see Figure 4.12 on page 90) and should not be visible in the real amplified signal. The output spectrum is smoothed using an FFT filter. As it was mentioned before, MPA III can operate at lower temperatures resulting in a higher gain. This has a positive impact on the amplifier performance.

A similar numerical result can be obtained for the last amplifier stage. In that case, the pre-shaping can be reduced to preserve the bandwidth. This was presented in [81].

An experimental verification of the pre-shaping possibility is needed to point out the capability of this solution to counteract the gain narrowing effect during amplification. For this purpose, a multipass amplifier similar to the presented setup in Figure 5.28 is used. The goal is to get a comparable performance of both amplifiers. The pre-shaping is realized with a 5 mm QBF, which is placed before the Faraday isolator, where the input polarizer of the FI in combination with the QBF is used to shape the spectrum. Figure 5.32 shows the experimental results of two different gain levels for which the spectral manipulation is optimized. In Figure 5.32(a) the output spectrum is optimized for a gain close to 100. The needed pre-shaped input spectrum is given as comparison. While for this gain the spectral bandwidth is preserved, a significant narrowing occurs if the gain is further increased to 300,



(a) Input spectrum optimized for  $G = 98$  as well as the output spectrum for a gain of 100 and 300.

(b) Input spectrum optimized for  $G = 300$  and the unshaped input spectrum.

**Figure 5.32:** Output spectrum of MPA I with a pre-shaped input spectrum for two different gain levels.

as shown in Figure 5.32(a). In this case, pre-shaping has to be adapted to the higher gain level. The result of the optimization is given in Figure 5.32(b). Additionally, the original spectrum before the QBF is given in Figure 5.32(b). This is the same for both cases only the strength of the spectral attenuation is adjusted.

The potential of this technique to obtain a broad spectrum is clearly visible and should open a promising path to amplify laser pulse up to the 100 J-level with  $\text{Yb}^{3+}:\text{CaF}_2$  of pulse durations below 150 fs. Further experiments have to be performed using MPA III to test this approach on a 10 J-level.

Future development has to be done to improve the performance of the MPA I. The number of extraction passes can be increased to 12 and 24 using polarization multiplexing, respectively. Additionally, the unabsorbed pump radiation could be collimated and imaged onto the gain material resulting in a four pass pump configuration with a higher inversion level. By applying all these changes the output energy can be increased. To reduce the fluence on the crystal and the optical components, beam size and the pump spot size have to be increased to support higher energies.

Furthermore, a stack with reduced pitch and increased bar number can be implemented. The pump energy is enhanced while the emitting area is the same. For this reason, the imaging system does not need any adjustment.

## 5.3 Temporal Intensity Contrast

The TIC is defined as the ratio between the pre- or postpulse intensity  $I(t)$  at the time  $t$  before ( $t < 0$ ) or after ( $t > 0$ ) the arrival of the main pulse at  $t = 0$ , where it reaches the peak intensity  $I(t = 0)$ . Prepulses on nanosecond (ns) and picosecond (ps) timescales as well as background generated by amplified spontaneous emission (ASE) in the laser amplifiers need to be as low as possible.

The expected elements and sources influencing the TIC, are given in the following list:

- plane-parallel optical components,
  - the active-mirror
  - waveplates
  - windows
  - the QBF
- ASE of the regenerative amplifier and
- leakage of the non-picked oscillator pulse due to angular misalignment of the Pockels cell (PC) or low intensity contrast ratio  $ICR$  of the PC.

To investigate the current status of the regenerative amplifier a third-order autocorrelation measurement with a *SEQUOIA* is performed. As comparison, an optical spectrum analyzer (OSA) with a resolution of 20 pm is used to analyze the cavity-dumped output spectrum. The measured spectrum is Fourier transformed to the time domain, which should in principle give the same results as the *SEQUOIA* measurement. This gives the possibility to investigate the performance of the regenerative amplifier without a complete CPA laser system.

The drawback of the FFT is the limited temporal resolution, a dynamic range of only 3 to 4 orders of magnitude and a time window of about 100 ps in our case. Additionally, pre- and postpulses cannot be distinguished as the Fourier transformation is without any phase information. However, the time window is sufficient enough to get information about the impact of typical optical elements. For a full range measurement and the highest dynamic range the best choice is the third-order autocorrelation.

A regenerative amplifier with a passive gain control was used for this experiment, as described in Section 5.2.3.2. The experimental setup is shown in Figure 5.20 and the amplifier is placed in the CPA system, as shown in Figure 5.9. The  $\text{Yb}^{3+}:\text{CaF}_2$  crystal is plane-parallel and has a thickness of about 2.5 mm.

At first, the spectrum is obtained using an OSA, as shown in Figure 5.33(a). The inset represents a spectral range of 1 nm and the modulation due to the plane-parallel active-mirror is clearly visible. The Fourier transformation of the spectrum is given in Figure 5.33(b). The pre- or postpulses originate from the gain medium at 22.9 ps, as well as the higher orders, are clearly visible. Furthermore, a pulse at 11.7 ps can be observed, which is not identified at this point.

Secondly, a measurement with the *SEQUOIA* was performed over the full scanning range from  $-520$  ps to 130 ps and the result is shown in Figure 5.34. The pre- and postpulses related to the active-mirror are clearly visible. The ASE background can be determined to be at  $10^{-9}$  compared to the main pulse. The measurement limit is investigated by blocking

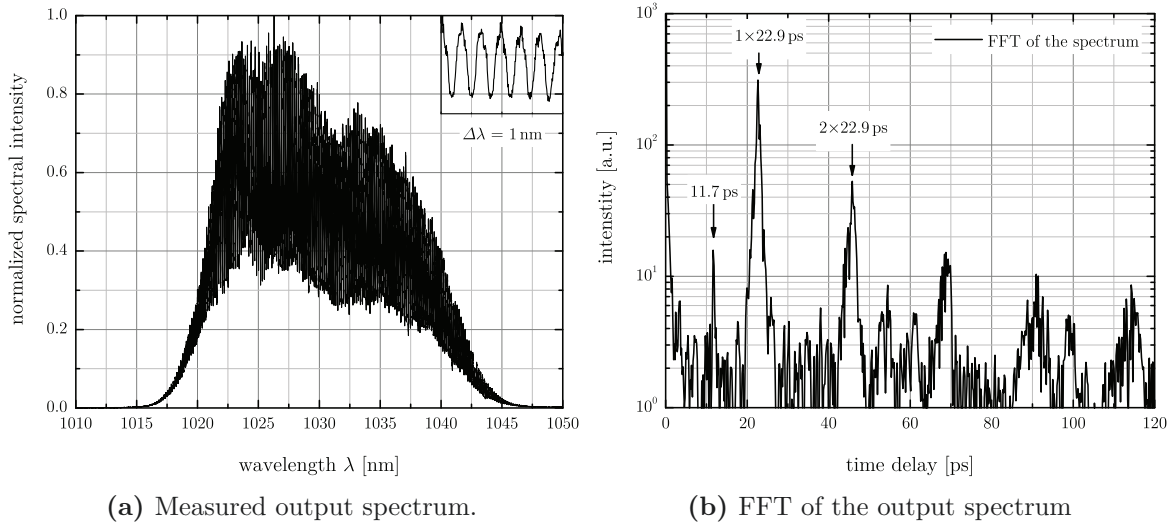


**Figure 5.33:** The output spectrum of the regenerative amplifier and their Fourier transformation.

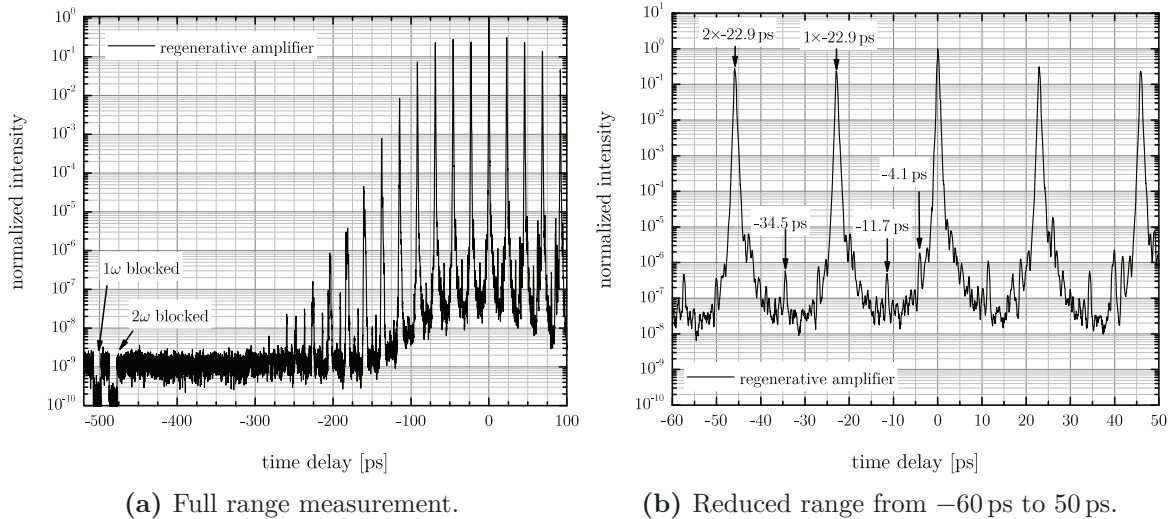


**Figure 5.34:** Temporal intensity contrast of the regenerative amplifier with passive gain control. The active-mirror is plane-parallel.

the fundamental and second harmonic beam during the measurement. It can be seen that the measurement limit is at  $10^{-10}$ . The ASE contrast is at an expected level compared to other  $\text{Yb}^{3+}$ -doped systems (e.g. POLARIS) without any kind of contrast enhancement technique. The TIC is better compared to the PHELIX laser system [73], where the ASE level was at  $10^{-6}$  before any contrast improvement was implemented. Nevertheless, all prepulses have to be identified and canceled out.

For a more detailed view, the TIC is plotted from  $-60$  ps to  $50$  ps in Figure 5.34(b). The prepulses caused by the gain medium are the dominant part, but also some additional pulses can be found. A few of them are marked with their respective delay. Further investigations have to be done to find their origin.

The active-mirror has to be wedged to eliminate the large amount of unwanted pre- and postpulses. A wedged gain material is placed inside a regenerative amplifier (test setup)

to determine the performance. The used sample has a thickness of  $2.0 \pm 0.1$  mm, which will result in a time delay of about  $19.2 \pm 1.0$  ps. The wedge was specified to  $1^\circ$ , but the produced sample has only a wedge of less than  $0.2^\circ$ . For this reason, the reflection of the front face cannot be completely canceled out, as the active-mirror is placed in the focal plane of the curved mirror. The front face reflection has a spatial displacement after the curved mirror. This means that the two beams are separated in the collimated branch of the resonator. An iris can be put into the regenerative amplifier to attenuate the reflection. The iris is closed as long as the output energy is not affected.

The regenerative amplifier is used in the cavity-dumped operation mode and the output spectrum is analyzed with the OSA. Figure 5.35 shows the result of the Fourier transformation for both cases. If we compare Figure 5.35 with Figure 5.33(b), the difference is considerably large. The pulses due to the active-mirror are visible in both cases, but for the closed iris a strong reduction can be measured. Additionally, the higher orders are completely canceled out.

Furthermore, other transmission elements can be identified, for instance the first-order half-wave plate with a thickness of  $174 \mu\text{m}$ . The other pulses are at different positions compared to non wedge case (see Figure 5.33(b)) due to a slight difference in the setup and the necessary realignment of the regenerative amplifier.

The plane-parallel active-mirror in the CPA regenerative amplifier is replaced by the wedged one. Afterwards the amplifier was realigned and almost the same performance is obtained. Additionally, an iris is placed inside the regenerative amplifier as for the test amplifier. The amplified pulses are compressed and sent to the third-order autocorrelation device. Figure 5.36 show the full scanning range measurement result of the wedged active-mirror. The main difference is that the pre- and postpulses due to the active-mirror are nearly canceled out in comparison to Figure 5.34(a). Only two prepulses are visible and marked in Figure 5.36.

Furthermore, other prepulses and their respective time delays are given. The individual sources of the remaining pulses are out of the scope of this work. The ASE background

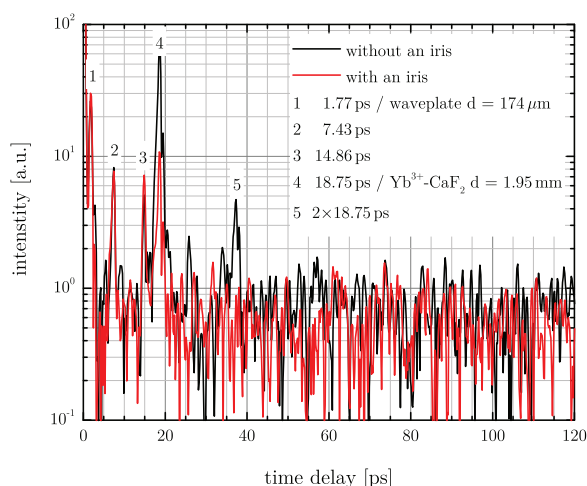


**Figure 5.35:** Fourier transformation of the cavity-dumped output spectrum of a regenerative amplifier with a wedged active-mirror.

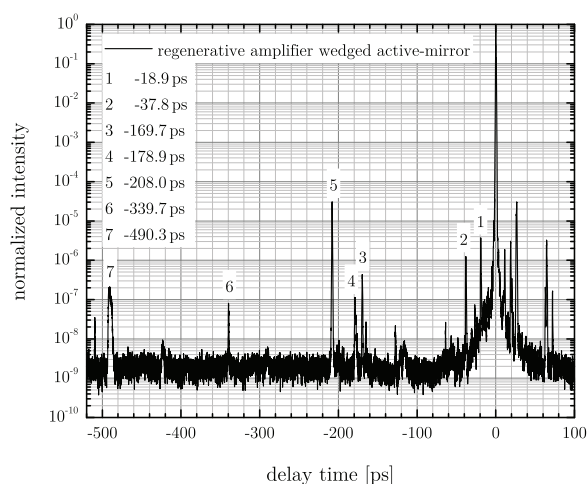


**Figure 5.36:** Temporal intensity contrast of the regenerative amplifier with a wedged active-mirror.



is not affected by the change of the gain material as expected. The background level is obtained after 40 ps. The influence of the pulse compression on the temporal intensity contrast has to be investigated in the future to get the best performance of the PENELOPE laser system.

As it was mentioned before in Section 5.2.3.1 about the pulse picking unit containing a Pockels cell, the extinction of the non-picked pulses has to be as good as possible to achieve a satisfying TIC. To identify the leakage of the oscillator pulses, the angular alignment of the PC is detuned. The regenerative amplifier with the wedged active-mirror is used to investigate the pulse picking contrast. Figure 5.37 shows the result of the angular misalignment of the PC and the optimized pulse picking contrast as comparison. The prepulses at 29.3 ps, 11.7 ps, -37.9 ps and -41.9 ps are related to the pulse picking contrast. Furthermore, the background level is below  $10^{-6}$  until 5 ps before the main pulse arrives.

It can be clearly seen that in the case of an optimized angular alignment of the PC the intrinsic contrast ratio  $ICR$  is not sufficient enough to attenuate the oscillator pulses. The specified  $ICR$  of the used Impact 8 (GOOCH & HOUSEGO) PC is  $1.5 \times 10^3$ . This can be increased, using a QX1020 (GOOCH & HOUSEGO), which has a specified  $ICR$  up to  $10^4$  at a wavelength of 633 nm. That value is almost 2.6 times higher at 1030 nm. If this is not enough, the pulse picking unit has to consist of two pulse picking units in series.

These first results of the TIC of the PENELOPE amplifier chain are very promising to generate high-intensity laser pulses with high temporal intensity contrast, which allows to perform laser-matter interaction experiments. In the future, the prepulses have to be identified and canceled out. For example the waveplates can be replaced using mirrors with zero or a defined phase shift [190, 191]. Furthermore, the background contrast of the PENELOPE laser system can be improved by inserting contrast enhancement stages, like an OPA stage or a double CPA system with an XPW filter (see Figure 3.4 on page 36).

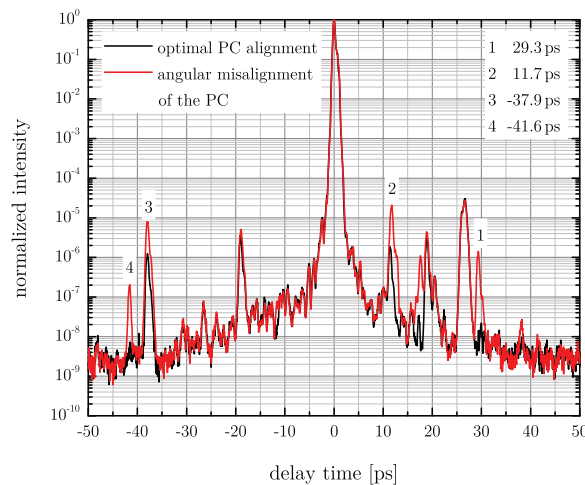


**Figure 5.37:** TIC for an optimal PC alignment and an angular misalignment of the PC.

## 5.4 Conclusion

This chapter deals with amplifier experiments based on  $\text{Yb}^{3+}:\text{CaF}_2$  in the active-mirror configuration as gain material for the PENELOPE laser system. The CW laser performance emphasizes a good potential of the gain medium with a high optical-to-optical efficiency of more than 40 %.

The regenerative amplifier was tested in the cavity-dumped mode as well as for laser pulse amplification. An amplified bandwidth of 8 nm results in pulse duration of only 193.3 fs. The main impact factor on the pulse duration is gain narrowing reducing the bandwidth of the stretched laser pulses by a factor of about 4.

Two ways to perform a spectral manipulation are a passive gain control using an quartz birefringent filter (QBF) and an active gain control with an acousto-optic programmable gain control filter. A thorough analysis of the spectral response of the amplifier showed plane-parallel optical elements as the most critical parts, especially waveplates and Pockels cells.

The passive gain control with a QBF increase the spectral bandwidth by a factor of 3 to 4, which is comparable to  $\text{Ti}^{3+}:\text{sapphire}$  based amplifiers. A pulse duration of 120.9 fs was achieved, which results in a 1.67 times higher intensity as for the initial result. In order to further increase the passive spectral shaping capacity a higher amount of adjustment parameters is necessary. One option would be to use several QBFs in series. A first principle experiment with two QBF yielded 26 nm of spectral bandwidth, being 4 nm more compared to one gain control element. A careful adjustment is necessary to avoid unwanted spectral modulations and opens the option for an improved pre-shaped spectrum for the following amplification.

The active gain control was performed with an acousto-optic crystal based on  $\text{TeO}_2$ . This gives the possibility to apply an arbitrary spectral attenuation shape, which leads to an increased spectral bandwidth of 28 nm. Additionally, a flat top like distribution was obtained compared to the QBF. Table 5.2 summarizes the results without and with the discussed gain control options.

output	initial	passive gain control		active gain control
		one QBF	two QBF	AOPGCF
$\Delta\lambda_{CD}$ [nm]	7	22	26	28
$\Delta\lambda_{CPA}$ [nm]	8	22	-	-
$\tau_p$ [fs]	193.3	120.9	(105)	(100)

**Table 5.2:** Experimental result without and with gain control. The spectral bandwidth at FWHM for the cavity-dumped experiments  $\Delta\lambda_{CD}$  and the CPA experiments  $\Delta\lambda_{CPA}$  are given as well as the obtained pulse duration  $\tau_p$ . The pulse duration in brackets is the Fourier transform-limit of the output spectrum obtained in the cavity-dumped operation mode.

Simulation and experimental results show that the gain narrowing out of the amplification at MPA III and IV can be compensated with the available pre-shaping capability. A bandwidth of 22 nm is preserved supporting 150 fs long pulses at the end of the amplification chain. This shows the scalability of this technique for the high-energy amplifiers of the laser system.

The second thoroughly discussed subject is the temporal intensity contrast of high energy laser pulses, which is one of the most important parameters for laser-matter interaction. Plane-parallel optical elements cause pre- and postpulses and especially the active-mirror concept leads to a large number of prepulses on the picosecond time scale.

Almost all prepulses are suppressed by wedging the gain material. The ASE background level of the regenerative amplifier is  $10^{-9}$  at 40 ps before the main pulse arrives, which is comparable to other high-energy laser systems without any kind of contrast enhancement technique. Remaining parasitic pulses not related to the used regenerative amplifier setup have to be identified for further laser performance optimization.

## CHAPTER 6

---

# Conclusion and Outlook

---

## Conclusion

This thesis is integrated in the framework of the PENELOPE project at the Helmholtz-Zentrum Dresden-Rossendorf. The main focus of the thesis lies on three essential components of an ultrashort, high-energy, diode-pumped solid state laser amplifier. For the PENELOPE laser system the gain medium  $\text{Yb}^{3+}:\text{CaF}_2$  was chosen as the key component. One of the most important features of this particular material is the combination of its good thermal properties, the low refractive index and the large emission bandwidth, all three being crucial to support high-energy, ultrashort laser pulses. The second part is the required optical pump source to deliver the necessary energy for the laser pulses. The last section is the bandwidth conservation of the laser, which is limited by the gain narrowing effect. To overcome and understand this limitation, a detailed investigation was performed. The major results are the scientific parts of this thesis. Furthermore, the amplifier architecture as well as the temporal intensity contrast (TIC) are investigated.

As calcium fluoride is a common material for photolithography applications and readily available in large size and quantity, a good optical quality even for rare-earth doped samples is feasible and opens a new path to a future generation of diode-pumped, high-energy amplifiers. Recent years showed a steady increase of the optical quality for trivalent ytterbium-doped  $\text{CaF}_2$ , as it was shown in Section 4.2, leading to a drastic increase of available output fluence from  $0.2\text{ J/cm}^2$  to  $4\text{ J/cm}^2$ . This is mainly due to the strong reduction of small-angle grain boundaries (SAGB) which disturb the beam after several amplification passes. To identify these defects a sensitive method is crucial. Therefore, the described method in Section 4.2 could be used, but for high quality crystals the resolution is limited. Furthermore, an interferometric measurement with a commercial device is possible. Near field imaging after 12 or 24 passes at the second to last amplification stage can be used to analyze the optical quality. The advantage of the interferometer is a quantitative evaluation of refractive index inhomogeneity such as SAGB. Currently, doped crystals of high optical quality are available up to 120 mm in diameter, enabling the construction of amplifiers supporting several hundreds of joule.

The analysis of the spectroscopic properties in Section 4.3 predict that  $\text{Yb}^{3+}:\text{CaF}_2$  matches the requirements for ultrashort laser pulse amplification and direct diode pumping. The best pump wavelength is close to the zero phonon line at 976 nm. Its advantage compared to the pump bands at 940 nm is that the absorption is more than twice as strong and the saturation intensity is significantly reduced. Therefore the achievable inversion level is higher at pumping close to 976 nm compared to the 940 nm case.

A gain cross section bandwidth of up to 50 nm is accessible for inversion levels of 10 % to 20 %. Cryogenic temperatures can additionally be used to improve the amplification performance due to increased emission cross sections, as well as lower ground state absorption in the laser wavelength range. However, one should note, that the temperature has to stay above  $\sim 200$  K, as the gain cross section becomes structured for significantly lower temperatures.

The second basic element of a laser system is the pump source and was investigated in Section 3.3. Costs of laser diodes have been continuously decreasing over the recent years, which makes DPSSLs attractive to scale up to the PW-level. Additionally, the performance of the laser diode stacks are enhanced at the same time. The central figure of merit is the brightness, including all of its important parameters (e.g. power, emitting area, etc.). As it was shown in Section 4.3.1 to achieve a reasonable gain in the case of  $\text{Yb}^{3+}:\text{CaF}_2$  pump intensity above  $15 \text{ kW/cm}^2$  are needed. Therefore, a high brightness is essential to design suitable pump source for PENELOPE. The whole system should be designed in such a way, that the brightness is conserved as best as possible. In order to do so, a fully image-relayed setup is the only option.

The basic concept is to pump evenly from both sides in a double pass configuration in order to efficiently use the available pump power. A combination of such a setup and the use of a global beam homogenization is a novel approach in the field of diode-pumped laser amplifiers. For a multipass amplifier pump source, all parts were successfully demonstrated and the scalability of that approach was shown in Section 3.3.3. A flat top pump beam with a peak-to-valley of less than 10 % was achieved. Additionally, the beam shaping in the near field as well as the far field fulfilled the amplifier constraints. Particularly the sharp edges in the far field are of utmost importance due to the angular multiplexing of both pump beams.

The proven design can be scaled up to meet the demand for the final amplifier stage. Therefore, two times eight pump modules corresponding to a total peak power of 1.2 MW in two beams have to be combined, homogenized and imaged onto the gain medium. A careful design of all pump sections is essential to realize the pump source of the last amplifier.

The third major component is to generate a sufficiently large bandwidth supporting ultrashort laser pulses even up to the last amplifier stages. One of the main goals was to counteract the gain narrowing effect, which is the limiting factor for spectral bandwidth and depends on the amplification factor. The amplifiers can be split into two groups. The first one has a large gain with a moderate output energy, like a regenerative amplifier (so-called High-Gain Broadband Amplifier (HGBA)). The other group includes the high-energy multipass amplifiers with a low total gain (so-called High-Energy Power Amplifier (HEPA)). As the limiting effect is gain narrowing, different approaches to circumvent this issue by spectral manipulation were investigated in Section 5.2.3. An active gain control using an acousto-optic programmable gain control filter, as well as a passive alternative were thoroughly discussed.

Both techniques can be implemented within the scope of a regenerative amplifier, where most of the gain spectrum shaping occurs. The bandwidth was increased by a factor of 4 to 5 in both cases. The passive spectral attenuation was used in a CPA system, and a pulse duration of 121 fs was obtained. This is a major enhancement by a factor of almost 2 compared to the initial situation before the start of the thesis. For further enhancement of the passive spectral shaping capacity additional adjustment parameters are necessary. One possible way is to use several quartz birefringent filter (QBF) in series instead of a

---

single one. First experimental implementation of two QBF achieves a spectral bandwidth of 26 nm, which is an increase of 4 nm compared to one gain control element.

The active gain control based on a  $\text{TeO}_2$  crystal gives the possibility to use an arbitrary spectral shape, which leads up to 28 nm of bandwidth, large enough to achieve pulse durations down to 100 fs. The adjustable spectral shape gives also the possibility to adapt this device easily to any other laser material.

The spectral attenuation can also be implemented at later amplifier stages (i.e. within or before), like MPA III. The best option to generate a large output spectrum is to pre-shape the input spectrum of the multipass amplifier. This was tested using the passive gain control element and the capability for this technique was demonstrated in Section 5.2.4. The input spectrum ( $>20$  nm) was entirely transferred through the first multipass amplifier stage (MPA I) of the PENELOPE laser system at a gain of up to 300. This proof-of-principle experiment shows the scalability of the PENELOPE amplifier configuration based on  $\text{Yb}^{3+}:\text{CaF}_2$ . For this reason, the gain narrowing out of MPA III and IV can be compensated with the available pre-shaping outcome. Furthermore, the predicted output spectrum of the last amplifier stages with 20 nm was experimentally proven. The experimental results were cross checked with a simulation and a good agreement was found.

The achieved spectrum is comparable to the regenerative case, which should lead to a pulse duration of about 120 fs. As a consequence of this, the main goal to generate laser pulses with a peak power of 1 PW with 150 fs using  $\text{Yb}^{3+}:\text{CaF}_2$  is feasible.

Future work will be dedicated to optimize the demonstrated approaches for the regenerative amplifiers down to the sub-100 fs range and energies up to several mJ. Such a source can be used as a part of the front-end for further amplification in the PENELOPE amplifier chain.

Numerical simulations, validated with experimental results, show that a spectral bandwidth of up to 25 nm is feasible after amplification to the 100 J-level. The generation of such high-energetic, ultrashort pulses will be the central scope of further development of the PENELOPE laser system.

Finally, the temporal intensity contrast (TIC) of the CPA chain including the regenerative amplifier was investigated in Section 5.3. All plane-parallel optical elements result in pre- and postpulses. This issue is addressed by, for example a wedge on the gain medium. The improvement was demonstrated using a wedged active-mirror in the regenerative amplifier. Almost all prepulses due to plane-parallel gain material are suppressed. The residual discrete prepulses have to be identified and removed in the future. The ASE background level of the regenerative amplifier is  $10^{-9}$  at 40 ps before the main pulse starts, which is comparable to other laser systems. This value can be addressed by using contrast enhancement techniques (e.g. XPW), which should be implemented at future upgrades of the laser system.

A further challenge is the architecture of the main amplifiers boosting the energy to the desired level while preserving the quality of the laser pulse. All amplifiers and telescopes are based on relay imaging, as it was presented in Section 3.2.1. For the PENELOPE laser system an imaging system consisting of spherical mirrors was conceived. Some main advantages of this choice are the achromatic behavior, less dispersion, lower B-integral, as well as the absence of the radial group delay. The inherent astigmatism of this setup is compensated by folding the beam into two perpendicular planes. In combination with large F-numbers this provides satisfactory results.



## Outlook

At the current status of the PENELOPE system the activation of MPA III has started and a first experimental campaign is done. First, a continuous wave laser beam was used to analyze the near and far field after the amplifier as well as the small-signal gain (SSG) evolution during the pump duration.

The setup of the MPA III was described in Section 3.2.2 and shown in Figure 3.15(b) on Page 49. For the wavefront study, the gain material was replaced by fused silica disks with a high optical quality to measure only the amplifier performance on its own. Therefore, the optical quality of the gain material is neglected. The Strehl ratio was calculated to  $\sim 0.7$  (out of the wavefront) after 12 passes, which was lower compared to the ideal case (see Figure 3.16 on Page 50). The reason for this is the wavefront error of each optic in the setup (especially the retro mirrors), which was not taken into account for the simulation. But nevertheless, it will be improved by inserting a deformable mirror at the entrance of the amplifier and the Strehl ratio should increase to better than 0.9.

Both final amplifiers can be simulated with MPA III. Therefore, the number of passes is doubled to  $2 \times 12$  using polarization multiplexing. The near field of the output beam was measured for the fused silica disks as well as for the  $\text{Yb}^{3+}:\text{CaF}_2$  disks with a doping concentration of 1.9 at% each. The beam profiles are shown in Figure 6.1. The SAGB are visible in the image, but they are relatively weak due to the fact that the laser beam is 24 times relay imaged onto the laser crystals.

The amplifier was pumped with up to 130 kW for up to 4 ms. The near field of one pump beam at the image plane (IP) and 30 mm out of plane are shown in Figure 6.2. The beam exhibits a smooth and homogeneous distribution in both cases. At 30 mm out of plane the edges of the profile vanish out. The second pump arm gives similar results. The SSG at 1030 nm for 2.5 ms and 4 ms pump duration is presented in Figure 6.3. The maximum gain at room temperature is 150 and 940, respectively. The amplifier is designed to operate at

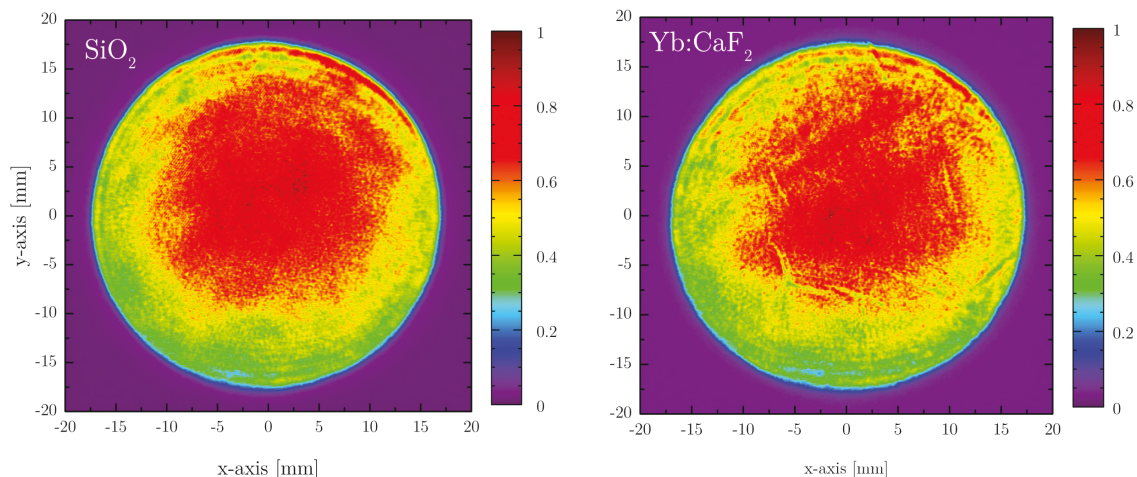


**Figure 6.1:** Near field image of the MPA III output after 24 passes with fused silica disks (on the left hand side) and  $\text{Yb}^{3+}:\text{CaF}_2$  disks (on the right hand side) with a doping concentration of 1.9 at%, respectively.



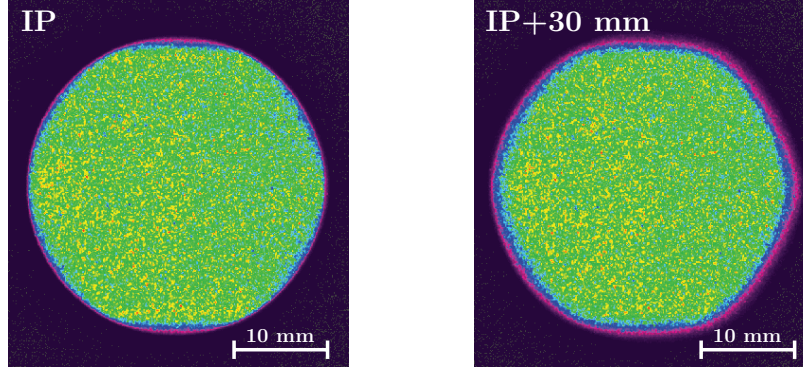


**Figure 6.2:** The near field of one pump beam at the image plane and 30 mm out of plane.

lower temperatures in the range from 200 K to 250 K, which will lead to a higher gain due to lower absorption as well as higher emission cross section (see Figure 4.8 on Page 86).

For the first energetic performance, MPA III in the  $2 \times 12$  configuration was injected with RA I and MPA I providing cavity-dumped 6 ns long pulses. Quartz birefringent filters (QBFs) were implemented inside the regenerative amplifier and between both amplifiers to manipulate the spectral bandwidth of the injected laser pulses in MPA III. The spectral bandwidth at FWHM were adjusted to 0.7 nm, 5 nm and 16 nm, presented in Figure 6.4. These different spectra give the opportunity to test the gain evolution due to a larger amplification spectrum and to investigate the gain narrowing of both main amplifiers. The output energy as a function of the injected energy is shown in Figure 6.5. An energy of more than 10 J was achieved for all cases and up to 12 J for the narrow spectrum. The gain was reduced from 800 to 430 for the bandwidth of 0.7 nm and 16 nm, respectively. The gain of the narrow spectrum is comparable with the time-resolved SSG measurement, which indicates that the pump profile is smooth and flat as well as the gain saturation is low. The output spectra of MPA III for all cases are shown in Figure 6.6 and up to 5 nm bandwidth no gain narrowing is observed. For the broadest input spectrum the spectral bandwidth at FWHM was reduced to 8.7 nm. But the width at the 10 % level is still 20 nm wide, which

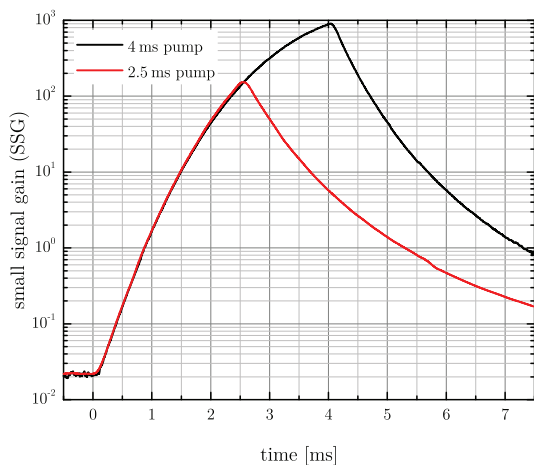


**Figure 6.3:** Small signal gain of MPA III with  $2 \times 12$  passes.

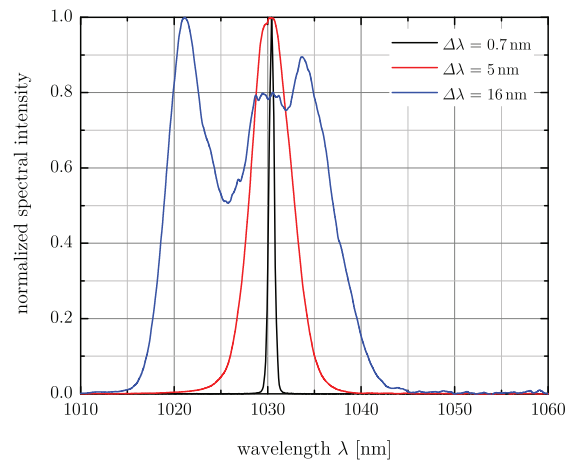


**Figure 6.4:** Input spectra for energetic performance measurement of MPA III.

means that this spectrum is large enough to support transform-limited ultrashort laser pulses below 150 fs.

In the near future, MPA III will operate with 12 passes and therefore the injected energy has to be increased to the joule-level by using MPA II for seeding. A similar output of MPA III is estimated with an injected energy of 600 mJ, when no gain saturation is exhibited for the first 12 passes. Afterwards, the amplifier extraction efficiency can be increased on the basis of temperatures below 250 K by reducing the pump duration. Additionally, the broad band performance of MPA III can be improved to achieve the bandwidth goal of about 20 nm at FWHM, as it was predicted by the experimental proof with MPA I. This will lead to a slight reduction of the gain, which can be easily compensated with the gain reserve of the front-end.

Finally, the amplifier chain will be embedded in between the stretcher and compressor to generate femtosecond pulses below 150 fs with energies of up to 10 J. This will be a major milestone for the PENELOPE project.

The current performance of the amplifier chain is very promising to achieve the target parameters of the PENELOPE project. All sections including target area for the laser-plasma experiments are going to be set up and connected for a first experimental campaign.

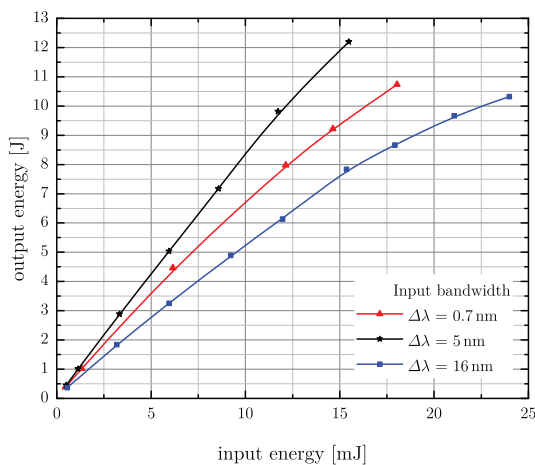


**Figure 6.5:** Output energy as a function of the injected energy.

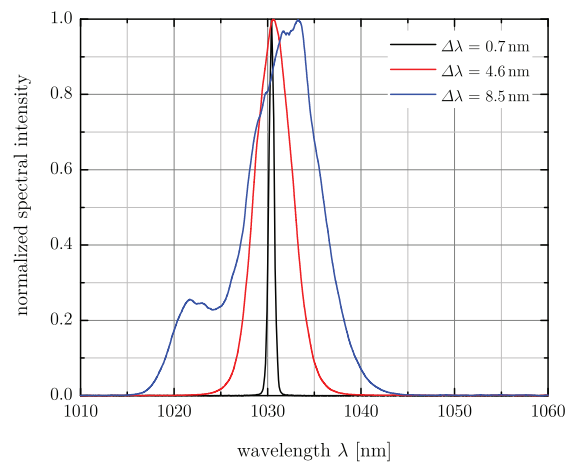


**Figure 6.6:** Output spectra of MPA III at maximum energy.

---

# Bibliography

---

1. BARTY, C. P. J.: *The Explosion of Intense Laser Activities Around the World and Related PW Activities at LLNL*, 10th DOE Laser Safety Workshop, (2014) (cit. on pp. 1, 31, 32).
2. LEEMANS, W., B. NAGLER, A. GONSALVES, C. TOTH, K. NAKAMURA, C. GEDDES, E. ESAREY, C. SCHROEDER, S. HOOKER: GeV electron beams from a centimetre-scale accelerator. *Nature physics* **2**: 696–699 (2006) (cit. on p. 1).
3. JOCHMANN, A., A. IRMAN, U. LEHNERT, J. COUPERUS, M. KUNTZSCH, S. TROTSENKO, A. WAGNER, A. DEBUS, H.-P. SCHLENVOIGT, U. HELBIG, S. BOCK, K. LEDINGHAM, T. COWAN, R. SAUERBREY, U. SCHRAMM: Operation of a picosecond narrow-bandwidth Laser–Thomson-backscattering X-ray source. *Nuclear Instruments and Methods in Physics Research Section B: Beam Interactions with Materials and Atoms* **309**: 214–217 (2013) (cit. on p. 1).
4. JOCHMANN, A. *et al.*: High Resolution Energy–Angle Correlation Measurement of Hard X Rays from Laser–Thomson Backscattering. *Phys. Rev. Lett.* **111**: 114803 (2013) (cit. on p. 1).
5. WAGNER, F., O. DEPERT, C. BRABETZ, P. FIALA, A. KLEINSCHMIDT, P. POTH, V. A. SCHANZ, A. TEBARTZ, B. ZIELBAUER, M. ROTH, T. STÖHLKER, V. BAGNOUD: Maximum Proton Energy above 85 MeV from the Relativistic Interaction of Laser Pulses with Micrometer Thick CH<sub>2</sub> Targets. *Phys. Rev. Lett.* **116**: 205002 (2016) (cit. on p. 1).
6. SCHRAMM, U. *et al.*: ‘First Results with the Novel Peta-Watt Laser Acceleration Facility in Dresden’, 8<sup>th</sup> International Particle Accelerator Conference IPAC17, pp. 48–52, paper MOZB1 (2017) (cit. on p. 1).
7. KLUGE, T., T. COWAN, A. DEBUS, U. SCHRAMM, K. ZEIL, M. BUSSMANN: Electron Temperature Scaling in Laser Interaction with Solids. *Phys. Rev. Lett.* **107**: 205003 (2011) (cit. on pp. 1, 2).
8. HORNUNG, M., H. LIEBETRAU, A. SEIDEL, S. KEPPLER, A. KESSLER, J. KÖRNER, M. HELLWING, F. SCHORCHT, D. KLÖPFEL, A. K. ARUNACHALAM, G. A. BECKER, A. SÄVERT, J. POLZ, J. HEIN, M. C. KALUZA: The all–diode–pumped laser system POLARIS – an experimentalist’s tool generating ultra–high contrast pulses with high energy. *High Power Laser Science and Engineering* **2** (2014) (cit. on p. 2).

9. KALUZA, M., J. SCHREIBER, M. I. K. SANTALA, G. D. TSAKIRIS, K. EIDMANN, J. MEYER-TER-VEHN, K. J. WITTE: Influence of the Laser Prepulse on Proton Acceleration in Thin-Foil Experiments. *Phys. Rev. Lett.* **93**: 045003 (2004) (cit. on p. 3).
10. MANGLES, S. P. D., A. G. R. THOMAS, M. C. KALUZA, O. LUNDH, F. LINDAU, A. PERSSON, Z. NAJMUDIN, C.-G. WAHLSTRÖM, C. D. MURPHY, C. KAMPERIDIS, K. L. LANCASTER, E. DIVALL, K. KRUSHELNICK: Effect of laser contrast ratio on electron beam stability in laser wakefield acceleration experiments. *Plasma Physics and Controlled Fusion* **48**: B83 (2006) (cit. on p. 3).
11. STRICKLAND, D., G. MOUROU: Compression of amplified chirped optical pulses. *Optics Communications* **56**: 219–221 (1985) (cit. on pp. 5, 14, 31).
12. EICHLER, J., H. EICHLER: *Laser* (Springer Berlin Heidelberg, [2007]) (cit. on p. 6).
13. KELLER, U.: *Laser Physics and Applications, 2.1 Ultrafast solid-state lasers*, ed. by G. HERZIGER H. Weber, R. P. (Springer Berlin Heidelberg, [2007]), Vol. 11 (cit. on pp. 7, 25, 26, 28).
14. MORGNER, U., F. X. KÄRTNER, S. H. CHO, Y. CHEN, H. A. HAUS, J. G. FUJIMOTO, E. P. IPPEN, V. SCHEUER, G. ANGELOW, T. TSCHUDI: Sub-two-cycle pulses from a Kerr-lens mode-locked Ti:sapphire laser. *Opt. Lett.* **24**: 411–413 (1999) (cit. on p. 7).
15. JACKSON, J., K. MÜLLER: *Klassische Elektrodynamik* (de Gruyter, [2002]) (cit. on p. 7).
16. DIELS, J., W. RUDOLPH, P. LIAO, P. KELLEY: *Ultrashort Laser Pulse Phenomena* (Elsevier Science, [2006]) (cit. on pp. 7, 8, 10, 11, 13, 25, 26, 28).
17. WALMSLEY, I., L. WAXER, C. DORRER: The role of dispersion in ultrafast optics. *Review of Scientific Instruments* **72**: 1–29 (2001) (cit. on p. 11).
18. MCMULLEN, J. D.: Chirped-pulse compression in strongly dispersive media. *J. Opt. Soc. Am.* **67**: 1575–1578 (1977) (cit. on p. 12).
19. SZIPÖCS, R., C. SPIELMANN, F. KRAUSZ, K. FERENCZ: Chirped multilayer coatings for broadband dispersion control in femtosecond lasers. *Opt. Lett.* **19**: 201–203 (1994) (cit. on p. 12).
20. TREACY, E.: Optical pulse compression with diffraction gratings. *Quantum Electronics, IEEE Journal of* **5**: 454–458 (1969) (cit. on pp. 13, 51).
21. MARTINEZ, O.: 3000 times grating compressor with positive group velocity dispersion: Application to fiber compensation in 1.3–1.6  $\mu\text{m}$  region. *Quantum Electronics, IEEE Journal of* **23**: 59–64 (1987) (cit. on p. 14).
22. PESSOT, M., P. MAINE, G. MOUROU: 1000 times expansion/compression of optical pulses for chirped pulse amplification. *Optics Communications* **62**: 419–421 (1987) (cit. on p. 14).
23. TOURNOIS, P.: Acousto-optic programmable dispersive filter for adaptive compensation of group delay time dispersion in laser systems. *Optics Communications* **140**: 245–249 (1997) (cit. on p. 15).

24. KANE, S., J. SQUIER: Grism-pair stretcher–compressor system for simultaneous second- and third-order dispersion compensation in chirped-pulse amplification. *J. Opt. Soc. Am. B* **14**: 661–665 (1997) (cit. on p. 15).
25. FORGET, N., V. CROZATIER, P. TOURNOIS: Transmission Bragg-grating gratings for pulse compression. English, *Applied Physics B* **109**: 121–125 (2012) (cit. on p. 15).
26. BESPALOV, V., V. TALANOV: Filamentary structure of light beams in nonlinear liquids. *JETP Lett* **3**: 307 (1966) (cit. on p. 16).
27. SIEGMAN, A.: *Lasers* (University Science Books, [1986]) (cit. on pp. 16, 19, 84, 98, 164).
28. BOYD, R.: *Nonlinear Optics* (Elsevier Science, [2013]) (cit. on p. 16).
29. SUYDAM, B.: Self-focusing of very powerful laser beams II. *Quantum Electronics, IEEE Journal of* **10**: 837–843 (1974) (cit. on p. 16).
30. KOECHNER, W.: *Solid-State Laser Engineering* (Springer New York, [2007]) (cit. on pp. 16, 37, 84, 85).
31. SPENCE, D. E., P. N. KEAN, W. SIBBETT: 60-fsec pulse generation from a self-mode-locked Ti:sapphire laser. *Opt. Lett.* **16**: 42–44 (1991) (cit. on p. 16).
32. BRABEC, T., C. SPIELMANN, P. F. CURLEY, F. KRAUSZ: Kerr lens mode locking. *Opt. Lett.* **17**: 1292–1294 (1992) (cit. on p. 16).
33. OF ENERGY, U. S. D., L. L. N. LABORATORY: *Laser Program Annual Report* (Lawrence Livermore National Laboratory., [1974]) (cit. on p. 17).
34. DIDENKO, N. V., A. V. KONYASHCHENKO, A. P. LUTSENKO, S. Y. TENYAKOV: Contrast degradation in a chirped-pulse amplifier due to generation of prepulses by postpulses. *Opt. Express* **16**: 3178–3190 (2008) (cit. on p. 17).
35. KALASHNIKOV, M., A. ANDREEV, H. SCHÖNNAGEL: ‘Limits of the temporal contrast for CPA lasers with beams of high aperture’, Ultrafast Nonlinear Optics 2009, pp. 750104–750104 (2009) (cit. on p. 17).
36. BOURDET, G. L.: Comparison of pulse amplification performances in longitudinally pumped Ytterbium doped materials. *Optics Communications* **200**: 331–342 (2001) (cit. on p. 17).
37. BEACH, R.: Optimization of quasi–three level end-pumped Q–switched lasers. *Quantum Electronics, IEEE Journal of* **31**: 1606–1613 (1995) (cit. on p. 17).
38. MONCORGÉ, R.: English, *Spectroscopic Properties of Rare Earths in Optical Materials*, ed. by HULL, R., J. PARISI, J. OSGOOD R.M., H. WARLIMONT, G. LIU, B. JACQUIER (Springer Berlin Heidelberg, [2005]), Vol. 83: pp. 320–378 (cit. on p. 17).
39. SIEBOLD, M., personal communication, (2017) (cit. on p. 17).
40. ALBACH, D., PhD thesis, Ecole Polytechnique Paris Tech, 2010 (cit. on pp. 21–23, 41, 78, 79).
41. ALBACH, D., J.-C. CHANTELOUP, G. le. TOUZÉ: Influence of ASE on the gain distribution in large size, high gain Yb<sup>3+</sup>:YAG slabs. *Opt. Express* **17**: 3792–3801 (2009) (cit. on p. 22).



42. RULLIERE, C.: *Femtosecond Laser Pulses: Principles and Experiments* (Springer, [2005]) (cit. on pp. 25–28).
43. BLOUNT, E. I., J. R. KLAUDER: Recovery of Laser Intensity from Correlation Data. *Journal of Applied Physics* **40**: 2874–2875 (1969) (cit. on p. 27).
44. LUAN, S., M. H. R. HUTCHINSON, R. A. SMITH, F. ZHOU: High dynamic range third-order correlation measurement of picosecond laser pulse shapes. *Measurement Science and Technology* **4**: 1426 (1993) (cit. on p. 27).
45. GALLMANN, L., D. H. SUTTER, N. MATUSCHEK, G. STEINMEYER, U. KELLER, C. IACONIS, I. A. WALMSLEY: Characterization of sub-6-fs optical pulses with spectral phase interferometry for direct electric-field reconstruction. *Opt. Lett.* **24**: 1314–1316 (1999) (cit. on p. 28).
46. DORRER, C., B. de BEAUVOIR, C. L. BLANC, S. RANC, J.-P. ROUSSEAU, P. ROUSSEAU, J.-P. CHAMBARET, F. SALIN: Single-shot real-time characterization of chirped-pulse amplification systems by spectral phase interferometry for direct electric-field reconstruction. *Opt. Lett.* **24**: 1644–1646 (1999) (cit. on p. 28).
47. DORRER, C., N. BELABAS, J.-P. LIKFORMAN, M. JOFFRE: Spectral resolution and sampling issues in Fourier-transform spectral interferometry. *J. Opt. Soc. Am. B* **17**: 1795–1802 (2000) (cit. on p. 28).
48. OKSENHENDLER, T., S. COUDREAU, N. FORGET, V. CROZATIER, S. GRABIELLE, R. HERZOG, O. GOBERT, D. KAPLAN: Self-referenced spectral interferometry. English, *Applied Physics B* **99**: 7–12 (2010) (cit. on p. 28).
49. MINKOVSKI, N., G. I. PETROV, S. M. SALTIEL, O. ALBERT, J. ETCHEPARE: Nonlinear polarization rotation and orthogonal polarization generation experienced in a single-beam configuration. *J. Opt. Soc. Am. B* **21**: 1659–1664 (2004) (cit. on p. 28).
50. JULLIEN, A., O. ALBERT, G. CHÉRIAUX, J. ETCHEPARE, S. KOURTEV, N. MINKOVSKI, S. M. SALTIEL: Nonlinear polarization rotation of elliptical light in cubic crystals, with application to cross-polarized wave generation. *J. Opt. Soc. Am. B* **22**: 2635–2641 (2005) (cit. on p. 28).
51. LEPETIT, L., G. CHÉRIAUX, M. JOFFRE: Linear techniques of phase measurement by femtosecond spectral interferometry for applications in spectroscopy. *J. Opt. Soc. Am. B* **12**: 2467–2474 (1995) (cit. on p. 28).
52. OKSENHENDLER, T.: Self-referenced spectral interferometry theory. (2012) (cit. on pp. 29, 104).
53. OKSENHENDLER, T., P. BIZOUARD, O. ALBERT, S. BOCK, U. SCHRAMM: High dynamic, high resolution and wide range single shot temporal pulse contrast measurement. *Opt. Express* **25**: 12588–12600 (2017) (cit. on pp. 29, 104).
54. LAWRENCE LIVERMORE NATIONAL LABORATORY: *Crossing the Petawatt Threshold*, Science & Technology Report, (1996) (cit. on p. 31).
55. BARTY, C. P. J.: *A World Tour of Ultrahigh Intensity Lasers*, [http://www.icuil.org/downloads/ICUIL-World-Map-by-C-P-J-Barty\\_147.pdf](http://www.icuil.org/downloads/ICUIL-World-Map-by-C-P-J-Barty_147.pdf), () (cit. on p. 31).

- 
56. BARTY, C. P. J.: *ICUIL world map*, <http://www.icuil.org/events-a-activities/laser-labs.html>, () (cit. on p. 31).
  57. BAYRAMIAN, A., P. ARMSTRONG, E. AULT, R. BEACH, C. BIBEAU, J. CAIRD, R. CAMPBELL, B. CHAI, J. DAWSON, C. EBBERS, *et al.*: The Mercury Project: A high average power, gas-cooled laser for inertial fusion energy development. *Fusion Science and Technology* **52**: 383–387 (2007) (cit. on p. 33).
  58. BAYRAMIAN, A. *et al.*: High average power petawatt laser pumped by the mercury laser for fusion materials engineering. *Fusion Science and Technology* **56**: 295–300 (2009) (cit. on p. 33).
  59. BAYRAMIAN, A. J. *et al.*: ‘Design of a 10 Hz Femto–Petawatt Laser Pumped by the Mercury Laser Facility’, *Advanced Solid-State Photonics*, p. MC1 (2008) (cit. on p. 33).
  60. LAWRENCE LIVERMORE NATIONAL LABORATORY: *Lighting a New Era of Scientific Discovery* (cit. on p. 33).
  61. HORNING, M., H. LIEBETRAU, S. KEPPLER, A. KESSLER, M. HELLWING, F. SCHORCHT, G. A. BECKER, M. REUTER, J. POLZ, J. KÖRNER, J. HEIN, M. C. KALUZA: 54 J pulses with 18 nm bandwidth from a diode-pumped chirped-pulse amplification laser system. *Opt. Lett.* **41**: 5413–5416 (2016) (cit. on p. 33).
  62. MAJOR, Z., S. A. TRUSHIN, I. AHMAD, M. SIEBOLD, C. WANDT, S. KLINGEBIEL, T.-J. WANG, J. A. FÜLÖP, A. HENIG, S. KRUBER, *et al.*: Basic concepts and current status of the petawatt field synthesizer—a new approach to ultrahigh field generation. *Laser Rev* **37**: 431 (2009) (cit. on p. 33).
  63. WANDT, C., S. KLINGEBIEL, S. KEPPLER, M. HORNING, M. LOESER, M. SIEBOLD, C. SKROBOL, A. KESSEL, S. A. TRUSHIN, Z. MAJOR, J. HEIN, M. C. KALUZA, F. KRAUSZ, S. KARSCH: Development of a Joule-class Yb:YAG amplifier and its implementation in a CPA system generating 1 TW pulses. *Laser & Photonics Reviews* **8**: 875–881 (2014) (cit. on pp. 33, 49).
  64. MASON, P. D., M. FITTON, A. LINTERN, S. BANERJEE, K. ERTEL, T. DAVENNE, J. HILL, S. P. BLAKE, P. J. PHILLIPS, T. J. BUTCHER, J. M. SMITH, M. D. VIDO, R. J. S. GREENHALGH, C. HERNANDEZ-GOMEZ, J. L. COLLIER: Scalable design for a high energy cryogenic gas cooled diode pumped laser amplifier. *Appl. Opt.* **54**: 4227–4238 (2015) (cit. on pp. 33, 38).
  65. MASON, P., M. DIVOKÝ, K. ERTEL, J. PILAŘ, T. BUTCHER, M. HANUŠ, S. BANERJEE, J. PHILLIPS, J. SMITH, M. D. VIDO, A. LUCIANETTI, C. HERNANDEZ-GOMEZ, C. EDWARDS, T. MOCEK, J. COLLIER: Kilowatt average power 100 J-level diode pumped solid state laser. *Optica* **4**: 438–439 (2017) (cit. on p. 33).
  66. ERTEL, K., S. BANERJEE, P. D. MASON, P. J. PHILLIPS, M. SIEBOLD, C. HERNANDEZ-GOMEZ, J. C. COLLIER: Optimising the efficiency of pulsed diode pumped Yb:YAG laser amplifiers for ns pulse generation. *Opt. Express* **19**: 26610–26626 (2011) (cit. on pp. 33, 38).
-



67. DIVOKY, M. *et al.*: Overview of the HiLASE project: high average power pulsed DPSSL systems for research and industry. *High Power Laser Science and Engineering* **2** (2014) (cit. on p. 33).
68. SAWICKA, M., M. DIVOKY, J. NOVAK, A. LUCIANETTI, B. RUS, T. MOCEK: Modeling of amplified spontaneous emission, heat deposition, and energy extraction in cryogenically cooled multislabs Yb<sup>3+</sup>:YAG laser amplifier for the HiLASE Project. *J. Opt. Soc. Am. B* **29**: 1270–1276 (2012) (cit. on pp. 34, 38).
69. PILAR, J., O. SLEZAK, P. SIKOCINSKI, M. DIVOKY, M. SAWICKA, S. BONORA, A. LUCIANETTI, T. MOCEK, H. JELINKOVA: Design and optimization of an adaptive optics system for a high-average-power multi-slab laser (HiLASE). *Appl. Opt.* **53**: 3255–3261 (2014) (cit. on p. 34).
70. GONÇALVÈS-NOVO, T., D. ALBACH, B. VINCENT, M. ARZAKANTSYAN, J.-C. CHANTELOUP: 14 J / 2 Hz Yb<sup>3+</sup>:YAG diode pumped solid state laser chain. *Opt. Express* **21**: 855–866 (2013) (cit. on pp. 34, 83, 87, 97).
71. KAWANAKA, J., N. MIYANAGA, T. KAWASHIMA, K. TSUBAKIMOTO, Y. FUJIMOTO, H. KUBOMURA, S. MATSUOKA, T. IKEGAWA, Y. SUZUKI, N. TSUCHIYA, *et al.*: ‘New concept for laser fusion energy driver by using cryogenically-cooled Yb: YAG ceramic’, *Journal of Physics: Conference Series*, Vol. 112, p. 032058 (2008) (cit. on p. 34).
72. DIVOKY, M., S. TOKITA, S. HWANG, T. KAWASHIMA, H. KAN, A. LUCIANETTI, T. MOCEK, J. KAWANAKA: 1-J operation of monolithic composite ceramics with Yb:YAG thin layers: multi-TRAM at 10-Hz repetition rate and prospects for 100-Hz operation. *Opt. Lett.* **40**: 855–858 (2015) (cit. on p. 34).
73. WAGNER, F., C. JOÃO, J. FILS, T. GOTTSCHALL, J. HEIN, J. KÖRNER, J. LIMPERT, M. ROTH, T. STÖHLKER, V. BAGNOUD: Temporal contrast control at the PHELIX petawatt laser facility by means of tunable sub-picosecond optical parametric amplification. *Applied Physics B* **116**: 429–435 (2014) (cit. on pp. 35, 36, 126).
74. LIEBETRAU, H., M. HORNING, A. SEIDEL, M. HELLWING, A. KESSLER, S. KEPPLER, F. SCHORCHT, J. HEIN, M. C. KALUZA: Ultra-high contrast frontend for high peak power fs-lasers at 1030 nm. *Opt. Express* **22**: 24776–24786 (2014) (cit. on p. 35).
75. JULLIEN, A., O. ALBERT, F. BURGY, G. HAMONIAUX, J.-P. ROUSSEAU, J.-P. CHAMBARET, F. AUGÉ-ROCHEREAU, G. CHÉRIAUX, J. ETCHEPARE, N. MINKOVSKI, S. M. SALTIEL: 10<sup>-10</sup> temporal contrast for femtosecond ultraintense lasers by cross-polarized wave generation. *Opt. Lett.* **30**: 920–922 (2005) (cit. on p. 35).
76. DORRER, C., I. A. BEGISHEV, A. V. OKISHEV, J. D. ZUEGEL: High-contrast optical-parametric amplifier as a front end of high-power laser systems. *Opt. Lett.* **32**: 2143–2145 (2007) (cit. on pp. 35, 36).
77. BAGNOUD, V., I. A. BEGISHEV, M. J. GUARDALBEN, J. PUTH, J. D. ZUEGEL: 5 Hz 250 mJ optical parametric chirped-pulse amplifier at 1053 nm. *Opt. Lett.* **30**: 1843–1845 (2005) (cit. on p. 36).

- 
78. GAUL, E. W. *et al.*: Demonstration of a 1.1 petawatt laser based on a hybrid optical parametric chirped pulse amplification/mixed Nd:glass amplifier. *Appl. Opt.* **49**: 1676–1681 (2010) (cit. on pp. 36, 106).
  79. EMMETT, J., W. KRUPKE, W. SOOY: *Potential of high-average-power solid state lasers* (cit. on p. 38).
  80. LABORATORY, L. L. N., U. S. D. of ENERGY: *Laser Program Annual Report* (Lawrence Livermore National Laboratory., [1986]) (cit. on p. 38).
  81. SIEBOLD, M., F. ROESER, M. LOESER, D. ALBACH, U. SCHRAMM: ‘PE<sub>n</sub>ELOPE: a high peak–power diode–pumped laser system for laser–plasma experiments’, *Proc. SPIE*, Vol. 8780, pp. 878005–878014 (2013) (cit. on pp. 38, 51–53, 62, 87, 123).
  82. BAYRAMIAN, A. *et al.*: ‘The Mercury Project: A kW Scale Yb:S–FAP Laser for Inertial Fusion Energy and Target Experiments’, *Advanced Solid-State Photonics*, WD4 (2007) (cit. on p. 38).
  83. BANERJEE, S., K. ERTEL, P. D. MASON, P. J. PHILLIPS, M. SIEBOLD, M. LOESER, C. HERNANDEZ-GOMEZ, J. L. COLLIER: High–efficiency 10 J diode pumped cryogenic gas cooled Yb:YAG multislabs amplifier. *Opt. Lett.* **37**: 2175–2177 (2012) (cit. on pp. 38, 83).
  84. SUTTON, S. B., G. F. ALBRECHT: ‘Thermal management in inertial fusion energy slab amplifiers’, *Solid State Lasers for Application to Inertial Confinement Fusion (ICF)*, pp. 272–281 (1995) (cit. on p. 39).
  85. ALBRECHT, G. F., H. F. ROBEY, A. C. ERLANDSON: Optical properties of turbulent channel flow. *Appl. Opt.* **29**: 3079–3087 (1990) (cit. on p. 39).
  86. TINKER, F., K. XIN: ‘Correlation of mid-spatial features to image performance in aspheric mirrors’, *Material Technologies and Applications to Optics, Structures, Components, and Sub-Systems*, Vol. 8837, 88370N–88370N (2013) (cit. on pp. 40, 43).
  87. AUERBACH, J. M., V. P. KARPENKO: Serrated–aperture apodizers for high–energy laser systems. *Appl. Opt.* **33**: 3179–3183 (1994) (cit. on pp. 40, 41).
  88. TRENHOLME, J.: *Apodizers Record of Invention 1978* (cit. on p. 40).
  89. BOR, Z.: Distortion of Femtosecond Laser Pulses in Lenses and Lens Systems. *Journal of Modern Optics* **35**: 1907–1918 (1988) (cit. on p. 42).
  90. HEUCK, H.-M., P. NEUMAYER, T. KÜHL, U. WITTRICK: Chromatic aberration in petawatt-class lasers. English, *Applied Physics B* **84**: 421–428 (2006) (cit. on p. 42).
  91. BORN, M., E. WOLF: *Principles of optics: electromagnetic theory of propagation, interference and diffraction of light* (Cambridge university press, [1999]) (cit. on pp. 43, 57).
  92. MAHAJAN, V. N.: Strehl ratio for primary aberrations in terms of their aberration variance. *J. Opt. Soc. Am.* **73**: 860–861 (1983) (cit. on p. 43).
  93. DRIGGERS, R. G.: *Encyclopedia of Optical Engineering: Las-Pho, pages 1025-2048* (CRC press, [2003]), Vol. 2 (cit. on p. 43).

94. KUMKAR, M.: *Laser amplifying system*, US Patent 6,765,947, (2004) (cit. on p. 47).
95. SIEBOLD, M., M. LOESER, F. ROESER, M. SELTMANN, G. HARZENDORF, I. TSYBIN, S. LINKE, S. BANERJEE, P. D. MASON, P. J. PHILLIPS, K. ERTEL, J. C. COLLIER, U. SCHRAMM: High-energy, ceramic-disk Yb:LuAG laser amplifier. *Opt. Express* **20**: 21992–22000 (2012) (cit. on pp. 48, 95).
96. SIEBOLD, M., M. LOESER, G. HARZENDORF, H. NEHRING, I. TSYBIN, F. ROESER, D. ALBACH, U. SCHRAMM: High-energy diode-pumped D<sub>2</sub>O-cooled multislabs Yb:YAG and Yb:QX-glass lasers. *Opt. Lett.* **39**: 3611–3614 (2014) (cit. on pp. 48, 173).
97. METZGER, T., PhD thesis, Technische Universität Berlin, Fakultät V – Verkehrs- und Maschinensysteme, 2009 (cit. on p. 49).
98. ALBACH, D., personal communication, (2017) (cit. on p. 50).
99. HARZENDORF, G., personal communication, (2017) (cit. on p. 52).
100. CHERIAUX, G., B. WALKER, L. F. DIMAURO, P. ROUSSEAU, F. SALIN, J. P. CHAMBARET: Aberration-free stretcher design for ultrashort-pulse amplification. *Opt. Lett.* **21**: 414–416 (1996) (cit. on p. 52).
101. ÖFFNER, A., 3748015 (1971) (cit. on p. 52).
102. KEPPLER, S., M. HORNUNG, R. BÖDEFELD, A. SÄVERT, H. LIEBETRAU, J. HEIN, M. C. KALUZA: Full characterization of the amplified spontaneous emission from a diode-pumped high-power laser system. *Opt. Express* **22**: 11228–11235 (2014) (cit. on p. 53).
103. KROEMER, H.: A proposed class of hetero-junction injection lasers. *Proceedings of the IEEE* **51**: 1782–1783 (1963) (cit. on p. 54).
104. KROEMER, H.: Quasi-electric fields and band offsets: teaching electrons new tricks. *International Journal of Modern Physics B* **16**: 677–697 (2002) (cit. on p. 54).
105. ALFEROV, Z. I.: Nobel Lecture: The double heterostructure concept and its applications in physics, electronics, and technology. *Reviews of modern physics* **73**: 767 (2001) (cit. on p. 54).
106. ALFEROV, Z.: Double heterostructure lasers: early days and future perspectives. *IEEE Journal of Selected Topics in Quantum Electronics* **6**: 832–840 (2000) (cit. on p. 54).
107. DINGLE, R., W. WIEGMANN, C. H. HENRY: Quantum States of Confined Carriers in Very Thin Al<sub>x</sub>Ga<sub>1-x</sub>As-GaAs-Al<sub>x</sub>Ga<sub>1-x</sub>As Heterostructures. *Phys. Rev. Lett.* **33**: 827–830 (1974) (cit. on p. 54).
108. PIETRZAK, A., R. HUELSEWEDE, M. ZORN, O. HIRSEKORN, J. SEBASTIAN, J. MEUSEL, V. BLUEMEL, P. HENNIG: ‘New highly efficient laser bars and laser arrays for 8xx-10xx nm pumping applications’, Proc. SPIE, Vol. 8965, 89650T–89650T (2014) (cit. on p. 57).
109. CRUMP, P. *et al.*: ‘Progress in high-energy-class diode laser pump sources’, Proc. SPIE 9348, High-Power Diode Laser Technology and Applications XIII, Vol. 9348, 93480U–93480U (2015) (cit. on p. 57).

- 
110. BACHMANN, F., P. LOOSEN, R. POPRAWA: *High power diode lasers: technology and applications* (Springer New York, [2007]), Vol. 128 (cit. on pp. 60, 61).
  111. *OpticStudio 15 SP1 Help Files*, Zemax, LLC (cit. on p. 64).
  112. KÖHLER, A.: Gedanken zu einem neuen Beleuchtungsverfahren für mikrographische Zwecke. *Zeitschrift für wissenschaftliche Mikroskopie* **10**: 433–440 (1893) (cit. on p. 65).
  113. DICKEY, F. M., T. E. LIZOTTE, S. C. HOLSWADE, D. L. SHEALY: *Laser beam shaping applications* (CRC Press, [2005]) (cit. on p. 65).
  114. BESOLD, B., N. LINDLEIN: Fractional Talbot effect for periodic microlens arrays. *Optical Engineering* **36**: 1099–1105 (1997) (cit. on p. 66).
  115. SIEBOLD, M., J. HEIN, M. HORNING, S. PODLESKA, M. KALUZA, S. BOCK, R. SAUERBREY: Diode-pumped lasers for ultra-high peak power. *Applied Physics B* **90**: 431–437 (2008) (cit. on pp. 78, 79).
  116. KRUPKE, W. F., M. D. SHINN, J. E. MARION, J. A. CAIRD, S. E. STOKOWSKI: Spectroscopic, optical, and thermomechanical properties of neodymium- and chromium-doped gadolinium scandium gallium garnet. *J. Opt. Soc. Am. B* **3**: 102–114 (1986) (cit. on p. 78).
  117. MARION, J.: Strengthened solid state laser materials. *Applied Physics Letters* **47**: 694–696 (1985) (cit. on p. 78).
  118. STOLZ, C. J., D. RISTAU, M. TUROWSKI, H. BLASCHKE: ‘Thin film femtosecond laser damage competition’, Vol. 7504, 75040S–75040S (2009) (cit. on p. 78).
  119. NIEMZ, M. H.: Threshold dependence of laser-induced optical breakdown on pulse duration. *Applied Physics Letters* **66**: 1181–1183 (1995) (cit. on p. 79).
  120. *Lasers and laser-related equipment: test methods for laser-induced damage threshold*, Norm, ISO 21254-1:2011-07, (2011) (cit. on p. 79).
  121. LIDARIS, <http://lidaris.com/glossary-2/>, () (cit. on p. 79).
  122. STOLZ, C. J., M. D. THOMAS, A. J. GRIFFIN: ‘BDS thin film damage competition’, Vol. 7132, pp. 71320C–71320C (2008) (cit. on p. 79).
  123. STOLZ, C. J., J. RUNKEL: ‘Brewster Angle Polarizing Beamsplitter Laser Damage Competition: P polarization’, Vol. 8530, pp. 85300M–85300M (2012) (cit. on p. 79).
  124. STOLZ, C. J., J. RUNKEL: ‘Brewster angle thin film polarizing beamsplitter laser damage competition: “S” polarization’, Vol. 8885, pp. 888509–888509 (2013) (cit. on p. 79).
  125. *Optics and photonics - Preparation of drawings for optical elements and systems - Part 5: Surface form tolerances*, Norm, ISO 10110-5, (2015) (cit. on p. 79).
  126. *MIL-PRF-13830B*, Norm, (1997) (cit. on p. 79).
  127. PETIT, V., J. DOUALAN, P. CAMY, V. MÓNARD, R. MONCORGÉ: CW and tunable laser operation of Yb<sup>3+</sup> doped CaF<sub>2</sub>. *Applied Physics B* **78**: 681–684 (2004) (cit. on p. 80).

128. SIEBOLD, M., S. BOCK, U. SCHRAMM, B. XU, J. DOUALAN, P. CAMY, R. MONCORGÉ: Yb:CaF<sub>2</sub> – a new old laser crystal. *Applied Physics B* **97**: 327–338 (2009) (cit. on pp. 80, 85, 93).
129. LOESER, M., F. RÖSER, A. REICHELT, M. SIEBOLD, S. GRIMM, D. LITZKENDORF, A. SCHWUCHOW, J. KIRCHHOF, U. SCHRAMM: Broadband, diode pumped Yb:SiO<sub>2</sub> multicomponent glass laser. *Opt. Lett.* **37**: 4029–4031 (2012) (cit. on pp. 83, 92, 93, 168, 169, 173).
130. RÖSER, F., M. LOESER, D. ALBACH, M. SIEBOLD, S. GRIMM, D. BRAND, A. SCHWUCHOW, A. LANGNER, G. SCHÖTZ, D. SCHÖNFELD, U. SCHRAMM: Broadband, diode pumped Yb-doped fused silica laser. *Opt. Mater. Express* **5**: 704–711 (2015) (cit. on pp. 83, 92, 168, 174, 175).
131. IKESUE, A., Y. L. AUNG: Ceramic laser materials. *Nat Photon* **2**: 721–727 (2008) (cit. on p. 83).
132. SANGHERA, J., W. KIM, G. VILLALOBOS, B. SHAW, C. BAKER, J. FRANTZ, B. SADOWSKI, I. AGGARWAL: Ceramic laser materials: Past and present. *Optical Materials* **35**: 693–699 (2013) (cit. on p. 83).
133. IKESUE, A., Y. L. AUNG, T. TAIRA, T. KAMIMURA, K. YOSHIDA, G. L. MESSING: PROGRESS IN CERAMIC LASERS. *Annual Review of Materials Research* **36**: 397–429 (2006) (cit. on p. 83).
134. LYBERIS, A., G. PATRIARCHE, P. GREDIN, D. VIVIEN, M. MORTIER: Origin of light scattering in ytterbium doped calcium fluoride transparent ceramic for high power lasers. *Journal of the European Ceramic Society* **31**: 1619–1630 (2011) (cit. on p. 83).
135. ABALLEA, P., A. SUGANUMA, F. DRUON, J. HOSTALRICH, P. GEORGES, P. GREDIN, M. MORTIER: Laser performance of diode-pumped Yb:CaF<sub>2</sub> optical ceramics synthesized using an energy-efficient process. *Optica* **2**: 288–291 (2015) (cit. on p. 83).
136. LUCIANETTI, A., M. SAWICKA, O. SLEZAK, M. DIVOKY, J. PILAR, V. JAMBUNATHAN, S. BONORA, R. ANTIPENKOV, T. MOCEK: Design of a kJ-class HiLASE laser as a driver for inertial fusion energy. *High Power Laser Science and Engineering* **2**: 10 (2014) (cit. on pp. 83, 87).
137. ALBACH, D., J.-C. CHANTELOUP: Large size crystalline vs. co-sintered ceramic Yb<sup>3+</sup>:YAG disk performance in diode pumped amplifiers. *Opt. Express* **23**: 570–579 (2015) (cit. on p. 83).
138. KOERNER, J., C. VORHOLT, H. LIEBETRAU, M. KAHLE, D. KLOEPFEL, R. SEIFERT, J. HEIN, M. C. KALUZA: Measurement of temperature-dependent absorption and emission spectra of Yb:YAG, Yb:LuAG, and Yb:CaF<sub>2</sub> between 20 °C and 200 °C and predictions on their influence on laser performance. *J. Opt. Soc. Am. B* **29**: 2493–2502 (2012) (cit. on pp. 84–86).
139. <http://www.chem.agilent.com/en-US/products-services/Instruments-Systems/Molecular-Spectroscopy/Cary-5000-UV-Vis-NIR/Pages/default.aspx>, () (cit. on p. 84).
140. MCCUMBER, D. E.: Einstein Relations Connecting Broadband Emission and Absorption Spectra. *Phys. Rev.* **136**: A954–A957 (1964) (cit. on p. 84).



- 
141. PAYNE, S., L. CHASE, L. K. SMITH, W. L. KWAY, W. F. KRUPKE: Infrared cross-section measurements for crystals doped with  $\text{Er}^{3+}$ ,  $\text{Tm}^{3+}$ , and  $\text{Ho}^{3+}$ . *Quantum Electronics, IEEE Journal of* **28**: 2619–2630 (1992) (cit. on p. 85).
  142. KÜHN, H., K. PETERMANN, G. HUBER: Correction of reabsorption artifacts in fluorescence spectra by the pinhole method. *Opt. Lett.* **35**: 1524–1526 (2010) (cit. on p. 85).
  143. DRUON, F., S. RICAUD, D. N. PAPADOPOULOS, A. PELLEGRINA, P. CAMY, J. L. DOUALAN, R. MONCORGÉ, A. COURJAUD, E. MOTTAY, P. GEORGES: On  $\text{Yb}:\text{CaF}_2$  and  $\text{Yb}:\text{SrF}_2$ : review of spectroscopic and thermal properties and their impact on femtosecond and high power laser performance [Invited]. *Opt. Mater. Express* **1**: 489–502 (2011) (cit. on pp. 85, 91).
  144. KÖRNER, J., V. JAMBUNATHAN, J. HEIN, R. SEIFERT, M. LOESER, M. SIEBOLD, U. SCHRAMM, P. SIKOCINSKI, A. LUCIANETTI, T. MOCEK, M. KALUZA: Spectroscopic characterization of  $\text{Yb}^{3+}$ -doped laser materials at cryogenic temperatures. *Applied Physics B* **116**: 75–81 (2014) (cit. on pp. 85, 86).
  145. PETIT, V., P. CAMY, J.-L. DOUALAN, X. PORTIER, R. MONCORGÉ: Spectroscopy of  $\text{Yb}^{3+}:\text{CaF}_2$ : From isolated centers to clusters. *Phys. Rev. B* **78**: 085131 (2008) (cit. on p. 86).
  146. ITO, M., C. GOUTAUDIER, Y. GUYOT, K. LEBBOU, T. FUKUDA, G. BOULON: Crystal growth,  $\text{Yb}^{3+}$  spectroscopy, concentration quenching analysis and potentiality of laser emission in  $\text{Ca}_{1-X}\text{Yb}_X\text{F}_{2+X}$ . *Journal of Physics: Condensed Matter* **16**: 1501 (2004) (cit. on p. 86).
  147. LACROIX, B., C. GENEVOIS, J. L. DOUALAN, G. BRASSE, A. BRAUD, P. RUTERANA, P. CAMY, E. TALBOT, R. MONCORGÉ, J. MARGERIE: Direct imaging of rare-earth ion clusters in  $\text{Yb}:\text{CaF}_2$ . *Phys. Rev. B* **90**: 125124 (2014) (cit. on p. 86).
  148. STEF, M., A. PRUNA, N. PECINGINA-GARJOABA, I. NICOARA: Influence of Various Impurities on the Optical Properties of  $\text{YbF}_3$ -Doped  $\text{CaF}_2$  Crystals. *ACTA PHYSICA POLONICA SERIES A* **112**: 1007 (2007) (cit. on p. 91).
  149. SHCHEULIN, A., A. ANGERVAKS, T. SEMENOVA, L. KORYAKINA, M. PETROVA, P. FEDOROV, V. REITEROV, E. GARIBIN, A. RYSKIN: Additive colouring of  $\text{CaF}_2:\text{Yb}$  crystals: determination of  $\text{Yb}^{2+}$  concentration in  $\text{CaF}_2:\text{Yb}$  crystals and ceramics. *Applied Physics B* **111**: 551–557 (2013) (cit. on p. 91).
  150. SU, L., J. XU, H. LI, L. WEN, W. YANG, Z. ZHAO, J. SI, Y. DONG, G. ZHOU: Crystal growth and spectroscopic characterization of Yb-doped and Yb, Na-codoped  $\text{CaF}_2$  laser crystals by TGT. *Journal of crystal growth* **277**: 264–268 (2005) (cit. on p. 91).
  151. KUZNETSOV, S., P. FEDOROV: Morphological stability of solid-liquid interface during melt crystallization of  $\text{M}_{1-x}\text{R}_x\text{F}_{2+x}$  solid solutions. *Inorganic Materials* **44**: 1434–1458 (2008) (cit. on p. 91).
-

152. ANGERVAKS, A., A. SHCHEULIN, A. RYSKIN, E. GARIBIN, M. KRUTOV, P. GUSEV, A. DEMIDENKO, S. KUZNETSOV, E. CHERNOVA, P. FEDOROV: Di- and trivalent ytterbium distributions along a melt-grown  $\text{CaF}_2$  crystal. *Inorganic Materials* **50**: 733–737 (2014) (cit. on p. 91).
153. DRUON, F., F. BALEMBOIS, P. GEORGES: New Materials for Short-Pulse Amplifiers. *Photonics Journal, IEEE* **3**: 268–273 (2011) (cit. on p. 92).
154. KUHN, S., M. TIEGEL, A. HERRMANN, J. KÖRNER, R. SEIFERT, F. YUE, D. KLÖPFEL, J. HEIN, M. C. KALUZA, C. RÜSSEL: Effect of hydroxyl concentration on  $\text{Yb}^{3+}$  luminescence properties in a peraluminous lithium-alumino-silicate glass. *Opt. Mater. Express* **5**: 430–440 (2015) (cit. on pp. 92, 168).
155. HÖNNINGER, C., R. PASCHOTTA, M. GRAF, F. MORIER-GENOUD, G. ZHANG, M. MOSER, S. BISWAL, J. NEES, A. BRAUN, G. MOUROU, I. JOHANNSEN, A. GIESEN, W. SEEBER, U. KELLER: Ultrafast ytterbium-doped bulk lasers and laser amplifiers. *Applied Physics B* **69**: 3–17 (1999) (cit. on pp. 92, 168, 172).
156. PETIT, J., P. GOLDNER, B. VIANA: Laser emission with low quantum defect in  $\text{Yb}:\text{CaGdAlO}_4$ . *Opt. Lett.* **30**: 1345–1347 (2005) (cit. on pp. 92, 93, 170).
157. HASSE, K., T. CALMANO, B. DEPPE, C. LIEBALD, C. KRÄNKEL: Efficient  $\text{Yb}^{3+}:\text{CaGdAlO}_4$  bulk and femtosecond-laser-written waveguide lasers. *Opt. Lett.* **40**: 3552–3555 (2015) (cit. on pp. 93, 170).
158. BOUDEILE, J., F. DRUON, M. HANNA, P. GEORGES, Y. ZAOUTER, E. CORMIER, J. PETIT, P. GOLDNER, B. VIANA: Continuous-wave and femtosecond laser operation of  $\text{Yb}:\text{CaGdAlO}_4$  under high-power diode pumping. *Opt. Lett.* **32**: 1962–1964 (2007) (cit. on p. 93).
159. LI, D., X. XU, H. ZHU, X. CHEN, W. D. TAN, J. ZHANG, D. TANG, J. MA, F. WU, C. XIA, J. XU: Characterization of laser crystal  $\text{Yb}:\text{CaYAlO}_4$ . *J. Opt. Soc. Am. B* **28**: 1650–1654 (2011) (cit. on pp. 93, 170, 171).
160. TIEGEL, M., A. HERRMANN, S. KUHN, C. RÜSSEL, J. KÖRNER, D. KLÖPFEL, R. SEIFERT, J. HEIN, M. C. KALUZA: Fluorescence and thermal stress properties of  $\text{Yb}^{3+}$ -doped alumino silicate glasses for ultra high peak power laser applications. *Laser Physics Letters* **11**: 115811 (2014) (cit. on p. 93).
161. KARRAS, C., D. LITZKENDORF, S. GRIMM, K. SCHUSTER, W. PAA, H. STAFAST: Nonlinear refractive index study on  $\text{SiO}_2\text{-Al}_2\text{O}_3\text{-La}_2\text{O}_3$  glasses. *Opt. Mater. Express* **4**: 2066–2077 (2014) (cit. on p. 93).
162. PASCHOTTA, R., J. NILSSON, A. TROPPER, D. HANNA: Ytterbium-doped fiber amplifiers. *Quantum Electronics, IEEE Journal of* **33**: 1049–1056 (1997) (cit. on pp. 93, 168, 169).
163. BUCARO, J. A., H. D. DARDY: High-temperature Brillouin scattering in fused quartz. *Journal of Applied Physics* **45**: 5324–5329 (1974) (cit. on p. 93).
164. KIGRE, INC: QX LASER GLASSES - Kigre, Inc. [www.kigre.com/files/qxdata.pdf](http://www.kigre.com/files/qxdata.pdf), () (cit. on p. 93).



- 
165. GIESEN, A., H. HÜGEL, A. VOSS, K. WITTIG, U. BRAUCH, H. OPOWER: Scalable concept for diode-pumped high-power solid-state lasers. *Applied Physics B* **58**: 365–372 (1994) (cit. on p. 95).
  166. GIESEN, A., J. SPEISER: Fifteen Years of Work on Thin-Disk Lasers: Results and Scaling Laws. *Selected Topics in Quantum Electronics, IEEE Journal of* **13**: 598–609 (2007) (cit. on p. 95).
  167. KILLI, A., C. STOLZENBURG, I. ZAWISCHA, D. SUTTER, J. KLEINBAUER, S. SCHAD, R. BROCKMANN, S. WEILER, J. NEUHAUS, S. KALFHUES, E. MEHNER, D. BAUER, H. SCHLUETER, C. SCHMITZ: ‘The broad applicability of the disk laser principle: from CW to ps’, Proc. SPIE, Vol. 7193, 71931T–71931T (2009) (cit. on p. 95).
  168. PAPADOPOULOS, D. N., A. PELLEGRINA, L. P. RAMIREZ, P. GEORGES, F. éric DRUON: Broadband high-energy diode-pumped Yb:KYW multipass amplifier. *Opt. Lett.* **36**: 3816–3818 (2011) (cit. on p. 95).
  169. REAGAN, B. A., K. A. WERNING, A. H. CURTIS, F. J. FURCH, B. M. LUTHER, D. PATEL, C. S. MENONI, J. J. ROCCA: Demonstration of a 100&#xA0;Hz repetition rate gain-saturated diode-pumped table-top soft x-ray laser. *Opt. Lett.* **37**: 3624–3626 (2012) (cit. on p. 95).
  170. CHRIS MYATT, N. T., K. L. DESSAU: *OPTICAL FABRICATION: Optical contacting grows more robust*, Laser Focus World, (2006) (cit. on p. 96).
  171. GRABIELLE, S., A. MOULET, N. FORGET, V. CROZATIER, S. COUDREAU, R. HERZOG, T. OKSENHENDLER, C. CORNAGGIA, O. GOBERT: Self-referenced spectral interferometry cross-checked with SPIDER on sub-15 fs pulses. *Nuclear Instruments and Methods in Physics Research Section A: Accelerators, Spectrometers, Detectors and Associated Equipment* **653**: 121–125 (2011) (cit. on p. 104).
  172. ROSS, I. N., M. TRENTELMAN, C. N. DANSON: Optimization of a chirped-pulse amplification Nd:glass laser. *Appl. Opt.* **36**: 9348–9358 (1997) (cit. on p. 105).
  173. POUYSEGUR, J., M. DELAIGUE, C. HÖNNINGER, Y. ZAOUTER, P. GEORGES, F. DRUON, E. MOTTAY: Numerical and Experimental Analysis of Nonlinear Regenerative Amplifiers Overcoming the Gain Bandwidth Limitation. *Selected Topics in Quantum Electronics, IEEE Journal of* **21**: 212–219 (2015) (cit. on p. 105).
  174. POUYSEGUR, J., M. DELAIGUE, Y. ZAOUTER, C. HÖNNINGER, E. MOTTAY, A. JAFFRÈS, P. LOISEAU, B. VIANA, P. GEORGES, F. DRUON: Sub-100-fs Yb:CALGO nonlinear regenerative amplifier. *Opt. Lett.* **38**: 5180–5183 (2013) (cit. on pp. 105, 170).
  175. PATTERSON, F. G., M. D. PERRY: Design and performance of a multiterawatt, subpicosecond neodymium:glass laser. *J. Opt. Soc. Am. B* **8**: 2384–2391 (1991) (cit. on p. 106).
  176. SQUIER, J., S. COE, K. CLAY, G. MOUROU, D. HARTER: An alexandrite pumped Nd:glass regenerative amplifier for chirped pulse amplification. *Optics Communications* **92**: 73–78 (1992) (cit. on p. 106).

177. BUENTING, U., H. SAYINC, D. WANDT, U. MORGNER, D. KRACHT: Regenerative thin disk amplifier with combined gain spectra producing 500  $\mu$ J sub 200 fs pulses. *Opt. Express* **17**: 8046–8050 (2009) (cit. on p. 106).
178. KIM, G. H., J. H. YANG, D. S. LEE, A. V. KULIK, E. G. SALL', S. A. CHIZHOV, U. KANG, V. E. YASHIN: Femtosecond laser based on Yb:KYW crystals with suppression of spectral narrowing in a regenerative amplifier by spectral profiling of the pulse. *J. Opt. Technol.* **80**: 142–147 (2013) (cit. on p. 106).
179. GUICHARD, F., M. HANNA, L. LOMBARD, Y. ZAOUTER, C. HÖNNINGER, F. MORIN, F. DRUON, E. MOTTAY, P. GEORGES: Two-channel pulse synthesis to overcome gain narrowing in femtosecond fiber amplifiers. *Opt. Lett.* **38**: 5430–5433 (2013) (cit. on p. 106).
180. STOKOWSKI, S. E., R. SAROYAN, M. J. WEBER: *Nd-doped laser glass spectroscopic and physical properties* (Lawrence Livermore National Laboratory, University of California Livermore, CA, [1981]) (cit. on p. 106).
181. BARTY, C., G. KORN, F. RAKSI, A.-C. TIEN, K. WILSON, V. YAKOVLEV, C. ROSE-PETRUCK, J. SQUIER, K. YAMAKAWA: Regenerative pulse shaping and amplification of ultrabroadband optical pulses. *Optics letters* **21**: 219–221 (1996) (cit. on pp. 106, 114).
182. BARTY, C. P. J., T. GUO, C. L. BLANC, F. RAKSI, C. ROSE-PETRUCK, J. SQUIER, K. R. WILSON, V. V. YAKOVLEV, K. YAMAKAWA: Generation of 18-fs, multiterawatt pulses by regenerative pulse shaping and chirped-pulse amplification. *Opt. Lett.* **21**: 668–670 (1996) (cit. on pp. 106, 114).
183. ZHOU, J., C.-P. HUANG, M. M. MURNANE, H. C. KAPTEYN: Amplification of 26-fs, 2-TW pulses near the gain-narrowing limit in Ti:sapphire. *Opt. Lett.* **20**: 64–66 (1995) (cit. on p. 106).
184. TAKADA, H., M. KAKEHATA, K. TORIZUKA: Broadband Regenerative Amplifier Using a Gain-Narrowing Compensator with Multiple Dielectric Layers. *Japanese Journal of Applied Physics* **43**: L1485 (2004) (cit. on p. 106).
185. GIAMBRUNO, F., A. FRENEAUX, G. CHÉRIAUX: Spectral mirror for ultra-short, high peak power, multi-PW Ti:sapphire lasers. English, *Applied Physics B* **111**: 161–164 (2013) (cit. on p. 106).
186. OKSENHENDLER, T., D. KAPLAN, P. TOURNOIS, G. GREETHAM, F. ESTABLE: Intracavity acousto-optic programmable gain control for ultra-wide-band regenerative amplifiers. English, *Applied Physics B* **83**: 491–494 (2006) (cit. on p. 107).
187. GHOSH, G.: Dispersion-equation coefficients for the refractive index and birefringence of calcite and quartz crystals. *Optics Communications* **163**: 95–102 (1999) (cit. on p. 109).
188. DMITRIEV, V., G. GURZADYAN, D. NIKOGOSYAN: *Handbook of Nonlinear Optical Crystals* (Springer Berlin Heidelberg, [2013]) (cit. on p. 110).
189. AURAND, B., S. KUSCHEL, C. RÖDEL, M. HEYER, F. WUNDERLICH, O. J. ÄCKEL, M. C. KALUZA, G. G. PAULUS, T. KÜHL: Creating circularly polarized light with a phase-shifting mirror. *Opt. Express* **19**: 17151–17157 (2011) (cit. on p. 113).

- 
190. AURAND, B., C. RÖDEL, H. ZHAO, S. KUSCHEL, M. WÜNSCHE, O. JÄCKEL, M. HEYER, F. WUNDERLICH, M. C. KALUZA, G. G. PAULUS, T. KUEHL: Note: A large aperture four-mirror reflective wave-plate for high-intensity short-pulse laser experiments. *Review of Scientific Instruments* **83** (2012) (cit. on pp. 113, 128).
  191. KEPPLER, S., M. HORNING, R. BÖDEFELD, M. KAHLE, J. HEIN, M. C. KALUZA: All-reflective, highly accurate polarization rotator for high-power short-pulse laser systems. *Opt. Express* **20**: 20742–20747 (2012) (cit. on pp. 113, 128).
  192. PREUSS, D. R., J. L. GOLE: Three-stage birefringent filter tuning smoothly over the visible region: theoretical treatment and experimental design. *Appl. Opt.* **19**: 702–710 (1980) (cit. on p. 113).
  193. OPTO-ELECTRONIC, A.: *Do you know Acousto-optics?* (Cit. on p. 117).
  194. KORPEL, A.: *Acousto-Optics, Second Edition* (Taylor & Francis, [1996]) (cit. on p. 117).
  195. PETIT, V., P. CAMY, J.-L. DOUALAN, X. PORTIER, R. MONCORGÉ: Spectroscopy of  $\text{Yb}^{3+}:\text{CaF}_2$ : From isolated centers to clusters. *Physical Review B* **78**: 085131 (2008) (cit. on p. 163).
  196. HEIN, J., S. PODLESKA, M. SIEBOLD, M. HELLWING, R. BÖDEFELD, R. SAUER-BREY, D. EHRT, W. WINTZER: Diode-pumped chirped pulse amplification to the joule level. *Applied Physics B* **79**: 419–422 (2004) (cit. on p. 168).
  197. EHRT, D., T. TÖPFER: ‘Preparation, structure and properties of  $\text{Yb}^{3+}$  FP laser glass’, Proc. SPIE, Vol. 4102, pp. 95–105 (2000) (cit. on p. 168).
  198. KOPONEN, J. J., M. J. SÖDERLUND, H. J. HOFFMAN, S. K. T. TAMMELA: Measuring photodarkening from single-mode ytterbium doped silica fibers. *Opt. Express* **14**: 11539–11544 (2006) (cit. on p. 169).
  199. MANEK-HÖNNINGER, I., J. BOULLET, T. CARDINAL, F. GUILLEN, S. ERMENEUX, M. PODGORSKI, R. B. DOUA, F. SALIN: Photodarkening and photobleaching of an ytterbium-doped silica double-clad LMA fiber. *Opt. Express* **15**: 1606–1611 (2007) (cit. on p. 169).
  200. ENGHOLM, M., P. JELGER, F. LAURELL, L. NORIN: Improved photodarkening resistivity in ytterbium-doped fiber lasers by cerium codoping. *Opt. Lett.* **34**: 1285–1287 (2009) (cit. on p. 169).
  201. PIRZIO, F., S. D. D. D. CAFISO, M. KEMNITZER, A. GUANDALINI, F. KIENLE, S. VERONESI, M. TONELLI, J. A. der AU, A. AGNESI: Sub-50-fs widely tunable  $\text{Yb}:\text{CaYAlO}_4$  laser pumped by 400-mW single-mode fiber-coupled laser diode. *Opt. Express* **23**: 9790–9795 (2015) (cit. on p. 170).
  202. SÉVILLANO, P., P. GEORGES, F. DRUON, D. DESCAMPS, E. CORMIER: 32-fs Kerr-lens mode-locked  $\text{Yb}:\text{CaGdAlO}_4$  oscillator optically pumped by a bright fiber laser. *Opt. Lett.* **39**: 6001–6004 (2014) (cit. on p. 170).
  203. AGNESI, A., A. GREBORIO, F. PIRZIO, G. REALI, J. A. der AU, A. GUANDALINI: 40-fs  $\text{Yb}^{3+}:\text{CaGdAlO}_4$  laser pumped by a single-mode 350-mW laser diode. *Opt. Express* **20**: 10077–10082 (2012) (cit. on p. 170).

204. CARACCILO, E., M. KEMNITZER, A. GUANDALINI, F. PIRZIO, J. A. der AU, A. AGNESI: 28-W, 217 fs solid-state Yb:CaIGdO<sub>4</sub> regenerative amplifiers. *Opt. Lett.* **38**: 4131–4133 (2013) (cit. on p. 170).
205. CALENDRON, A.-L.: Dual-crystal Yb:CALGO high power laser and regenerative amplifier. *Opt. Express* **21**: 26174–26181 (2013) (cit. on p. 170).
206. LI, D., X. XU, Y. CHENG, S. CHENG, D. ZHOU, F. WU, C. XIA, J. XU, J. ZHANG: Crystal growth and spectroscopic properties of Yb: CaYAlO<sub>4</sub> single crystal. *Journal of Crystal Growth* **312**: 2117–2121 (2010) (cit. on p. 170).
207. HÖNNINGER, C., F. MORIER-GENOUD, M. MOSER, U. KELLER, L. R. BROVELLI, C. HARDER: Efficient and tunable diode-pumped femtosecond Yb:glass lasers. *Opt. Lett.* **23**: 126–128 (1998) (cit. on p. 172).
208. LIU, H., S. BISWAL, J. PAYE, J. NEES, G. MOUROU, C. HÖNNINGER, U. KELLER: Directly diode-pumped millijoule subpicosecond Yb:glass regenerative amplifier. *Opt. Lett.* **24**: 917–919 (1999) (cit. on p. 172).
209. BISWAL, S., PhD thesis, The University of Michigan, 1999 (cit. on p. 172).
210. RÖSER, F., M. LOESER, M. SIEBOLD, D. ALBACH, S. GRIMM, A. LANGNER, G. SCHÖTZ, U. SCHRAMM: ‘Regenerative amplification in Yb<sup>3+</sup>-doped fused silica’, 2015 European Conference on Lasers and Electro-Optics - European Quantum Electronics Conference, CA\_P\_21 (2015) (cit. on p. 175).

---

# List of Figures

---

1.1	The maximum proton energy as a function of the laser peak power. . . . .	2
2.1	Schematic drawing of the CPA scheme. . . . .	6
2.2	Time dependent laser intensity. . . . .	7
2.3	Principle optical setup of a Treacy compressor in a double-pass configuration.	13
2.4	Illustration of a relay imaging Stretcher setup (a) zero dispersion, (b) positive dispersion and (c) negative dispersion. . . . .	14
2.5	Energy flow in a solid state laser amplifier. . . . .	23
2.6	Experimental setups for second-order autocorrelation. . . . .	26
2.7	Schematic setup of a third-order autocorrelation. . . . .	27
2.8	Schematic of the <i>SPIDER</i> apparatus. . . . .	28
2.9	Schematic of the <i>WIZZLER</i> apparatus. . . . .	29
3.1	ICUIL world map of ultrahigh intensity laser capabilities of 2009 and today.	32
3.2	The layout of the PENELOPE laser system. . . . .	35
3.3	Projected lab infrastructure. . . . .	36
3.4	PENELOPE laser system alternative layout . . . . .	36
3.5	Cooling schemata and He-gas cooled multi-slab laser head. . . . .	37
3.6	Galilean and Keplerian telescope. . . . .	39
3.7	Relay imaging telescope and a spatial filter. . . . .	39
3.8	(a) Serrated aperture of the PENELOPE laser. (b) the unfiltered and filtered beam in the IP. . . . .	41
3.9	Comparison of the hard and soft apodized beam after 2.5 m propagation; (a) profile lines and (b) images. . . . .	42
3.10	Influence of the AoI on the spherical mirror to the optical quality of a reflective telescope. . . . .	44
3.11	Influence of the magnification factor on the ratio of the AoI on the first mirror $\alpha_1$ and second mirror $\alpha_2$ as well as the rms wavefront error $\bar{\Phi}_{rms}$ is shown. . . . .	45
3.12	Scaling of the F-number $F^\#$ by changing the beam diameter $D$ to have a constant rms wavefront error. . . . .	45
3.13	Top and side view of the two mirror based relay imaging amplifier setup. . . . .	48
3.14	Top view of the two mirror based relay imaging amplifier setup with doubled pass configuration via polarization coupling. . . . .	48
3.15	Simplified (a) and experimental setup (b) of MPA III. . . . .	49

---

3.16	Result of the wavefront with Zemax <sup>TM</sup> analysis of the MPA III. . . . .	50
3.17	Ray tracing plot as well as the mechanical layout of the compressor. . . . .	52
3.18	Ray tracing plot as well as the mechanical layout of the stretcher. . . . .	52
3.19	Temporal performance of the stretcher and compressor for a 100 fs Gaussian pulse (FWHM) in logarithmic scale. . . . .	53
3.20	Schematic representation of the temporal intensity contrast of an ultrashort high-energy laser. . . . .	53
3.21	Solid angle. . . . .	55
3.22	Overview on laser diodes. . . . .	56
3.23	Principle measurement setup of the laser diode parameters. . . . .	59
3.24	Laser diode stack performance. . . . .	60
3.25	76 kW pump module consisting of 32 stack for design A and 16 for B and a typical near field profile. . . . .	62
3.26	Fast axis divergence is given for the pump modules. . . . .	63
3.27	Imaging homogenizer. . . . .	65
3.28	Principle setup of the homogenization and the two side pumped multi-slab amplifier. . . . .	67
3.29	The top and side view of both cylindrical lens telescopes are given, where the SA is in the top and the FA in the side view. . . . .	69
3.30	Opto-mechanical layout of the MPA III pump source. . . . .	70
3.31	Technical drawing of the used MLA. . . . .	70
3.32	Beam shaping of the hexagonal flattop pump spot with a hard aperture. . . . .	71
3.33	Experimental and simulated near and far field of one PM in the combination plane. . . . .	71
3.34	he homogenized beam profile and the associated far field distribution for both cases (experiment and simulation). . . . .	72
3.35	Vertical profile line of the measured and simulated beam spot. . . . .	72
3.36	Contour plot of the height profile of a part of the real produced lens array. . . . .	73
3.37	The vertical profile line of the transition zone . . . . .	73
4.1	Bandwidth (x-axis) and saturation intensity (y-axis) for several host materials, doped with Nd, Yb or transition metals. . . . .	79
4.2	Thermal shock parameter $R_S$ as a function of the thermal conductivity $\kappa$ . . . . .	79
4.3	Shadowgraph technique. . . . .	81
4.4	Volume damage of a 25 mm long and 2.2 mol% doped calcium fluoride. . . . .	81
4.5	Near field beam profiles for an eight pass relay imaging multipass cavity. . . . .	81
4.6	FFT analysis of multipass near field images. . . . .	82
4.7	Transmission between crossed polarizers of 3 mm thick $\text{Yb}^{3+}:\text{CaF}_2$ with 2.0 mol % doping concentration. . . . .	83
4.8	Absorption and emission cross section of $\text{Yb}^{3+}$ -doped $\text{CaF}_2$ at different temperatures. . . . .	86
4.9	The doping length $L \times c'_{dop}$ for 90 % pump intensity absorption for $\lambda_c$ from 920 nm to 940 nm at 300 K and 200 K. . . . .	88
4.10	The doping length $L \times c'_{dop}$ for 90 % pump intensity absorption for $\lambda_c$ from 970 nm to 985 nm at 300 K and 200 K. . . . .	88
4.11	Steady state inversion at 300 K and 200 K. . . . .	89

---



---

4.12	The gain cross section as a function of the wavelength. . . . .	90
4.13	Absorption coefficient of calcium fluoride with and without divalent ytterbium. . . . .	91
5.1	Direct and indirect cooling of a active-mirror. . . . .	96
5.2	Bonded crystals. . . . .	97
5.3	Beam profiles after eight passes in a multipass cavity. . . . .	97
5.4	Experimental setup for the cw-operation mode. . . . .	98
5.5	Polarization analysis and cw-operation results of $\text{Yb}^{3+}:\text{CaF}_2$ . . . . .	99
5.6	Schematic setup of a cavity-dumped laser resonator. . . . .	100
5.7	Cavity-dumping results. . . . .	101
5.8	Cavity-dumping output spectrum. . . . .	101
5.9	Experimental setup of the CPA laser system. . . . .	102
5.10	Intensity autocorrelation trace of the oscillator. . . . .	102
5.11	Spectrum of the oscillator and stretcher output. . . . .	103
5.12	Theoretical diffraction efficiency of gratings. . . . .	104
5.13	Pulse duration measurement. . . . .	104
5.14	Schematic setup of the polarization depending measurements. . . . .	108
5.15	Polarization depending spectral reflection of a TFP. . . . .	108
5.16	Spectral transmission of different half-wave plates. . . . .	109
5.17	Transmission of a Pockels cell at the $U_\pi$ . . . . .	111
5.18	$VCR$ and $ICR$ as a function of the wavelength. . . . .	112
5.19	Spectral transmission of two different QBF. . . . .	113
5.20	Schematic setup of a cavity-dumped laser resonator with passive gain control. . . . .	114
5.21	Output spectrum passive gain control. . . . .	115
5.22	Output spectrum of the regenerative amplifier with passive gain control. . . . .	115
5.23	Pulse duration measurement. . . . .	115
5.24	Output spectrum passive gain control with two QBFs. . . . .	116
5.25	Schematic setup of a cavity-dumped laser resonator with active gain control. . . . .	117
5.26	Cavity-dumped spectrum obtained with an AOPGCF. . . . .	118
5.27	AOPGCF loss spectrum. . . . .	118
5.28	Schematic experimental setup of the MPA I. . . . .	119
5.29	Experimental results for the MPA I. . . . .	121
5.30	Simulated output spectrum MPA I. . . . .	122
5.31	Numerical result of the output spectrum of MPA III. . . . .	122
5.32	Output spectrum of MPA I with a pre-shaped input spectrum for two different gain levels. . . . .	124
5.33	The output spectrum of the regenerative amplifier and their Fourier transformation. . . . .	126
5.34	TIC of the regenerative amplifier with a plane-parallel active-mirror. . . . .	126
5.35	FFT of the output spectrum achieved with a wedged active-mirror. . . . .	127
5.36	TIC of the regenerative amplifier with a wedged active-mirror. . . . .	127
5.37	TIC for an optimal PC alignment and an angular misalignment of the PC. . . . .	128
6.1	Near field image of the MPA III output after 24 passes. . . . .	134
6.2	The near field of one pump beam from MPA III. . . . .	135
6.3	SSG of MPA III. . . . .	135

---



6.4	Input spectra of MPA III. . . . .	135
6.5	Energetic performance of MPA III. . . . .	136
6.6	Output spectra of MPA III. . . . .	136
A.1	Term schemata of $\text{Yb}^{3+}:\text{CaF}_2$ . . . . .	163
A.2	Beam path for a direct imaging. . . . .	164
A.3	Beam path of a relay imaging. . . . .	166
A.4	Influence of $\text{Yb}^{2+}$ concentration on cw operation. . . . .	167
A.5	Influence of $\text{Yb}^{2+}$ concentration on cavity-dumping operation. . . . .	167
A.6	Emission and absorption cross section of Yb-doped fused silica and SAL glass. . . . .	169
A.7	Output power as a function of time for $\text{Yb}^{3+}:\text{SiO}_2$ . . . . .	169
A.10	Cavity-dumping output spectrum. . . . .	172
A.11	SSG for different inversion levels in $\text{Yb}^{3+}:\text{QX}$ glass. . . . .	172
A.12	Output spectrum of the $\text{Yb}^{3+}:\text{QX}$ glass regenerative amplifier without and with passive gain control. . . . .	173
A.13	Pulse duration measurement. . . . .	174
A.14	Cavity-dumping output spectrum. . . . .	174
A.15	Cavity-dumping output spectrum. . . . .	175
A.16	Pulse duration measurement. . . . .	176

---

# List of Tables

---

2.1	The mathematical description of three different pulse shapes in the time and frequency domain. . . . .	11
3.1	List of the planned vacuum telescopes. . . . .	46
3.2	Compressor design parameters. . . . .	51
3.3	Definition for cone and pyramid shaped solid angle $\Omega$ . . . . .	55
3.4	Comparison of three different stacks from three suppliers with the old (300 W bar <sup>-1</sup> ) and new (500 W bar <sup>-1</sup> ) bars. . . . .	57
3.5	Statistical analysis of the performance of the two stack design. . . . .	60
3.6	Comparison of both PM concepts in terms of brightness conservation. . . . .	64
3.7	Example of the Zemax <sup>TM</sup> source parameters and the resulting angular distribution. . . . .	64
3.8	Component list of the crossed cylindrical lens system with the given dimensions and tolerances. . . . .	68
4.1	Properties of selected laser materials. . . . .	93
5.1	The input and output parameters for the numerical model. . . . .	123
5.2	Experimental result without and with gain control. . . . .	129



---

# Acronyms

---

Notation	Description
<i>SPIDER</i>	Phase Interferometry for Direct Electric-field Reconstruction
PENELOPE	Petawatt, Energy-Efficient Laser for Optical Plasma Experiments
AM	active mirror
AoI	angle of incidence
AOPGCF	acousto-optic programmable gain control filter
ASE	amplified spontaneous emission
BBO	$\beta$ -barium borate
CADB <sup>®</sup>	Chemically Activated Direct Bonding Process
CEO	carrier-envelope phase
CPA	chirped pulse amplification
CTE	coefficient of thermal expansion
CW	continuous wave
DiPOLE	Diode Pumped Optical Laser for Experiments
DM	dichroic mirror
Draco	Dresden laser acceleration source
ELBE	Electron Linac for beams with high Brilliance and low Emittance
ELI	Extreme Light Infrastructure
F-L	Füchtbauer-Ladenburg
FA	fast axis
FAC	fast axis collimation
FI	Faraday isolator

---

<b>Notation</b>	<b>Description</b>
FOD	fourth-order dispersion
FOM	figure of merit
FP	Fourier/focal plane
FR	Faraday rotator
FWHM	full width at half maximum
GD	group delay
GDD	group delay dispersion
GENBU	Generation of ENergetic Beam Ultimate
HEC-DPSSL	High-Energy-Class Diode-Pumped Solid-State Lasers
HEPA	High-Energy Power Amplifier
HGBA	High-Gain Broadband Amplifier
HWP	half-wave plate
HZDR	Helmholtz-Zentrum Dresden-Rossendorf
iAC	interferometric autocorrelation
IAD	ion assisted deposition
IBS	ion beam sputtering
ICUIL	International Committee on Ultrahigh Intensity Lasers
IFE	inertial fusion energy
IP	image plane
KD*P	deuterated potassium dihydrogen phosphate
L	spherical lens
LD	fiber coupled laser diode
LIDT	laser induced damaged threshold
LT	spherical lens telescope
M	mirror
MLA	microlens array
MLD	multilayer dielectric

Notation	Description
NA	numerical aperture
OAP	off-axis parabola
OC	output coupler
OPCPA	optical parametric chirp pulse amplification
OSA	optical spectrum analyzer
P-V	peak-to-valley
PC	Pockels cell
PFS	Petawatt Field Synthesizer
PM	pump module
Pol	polarizer
PSF	point spread function
QBF	quartz birefringent filter
QCW	quasi continuous wave
QWP	quarter-wave plate
RGD	radial group delay
rms	root mean square
RoC	radius of curvature
SA	slow axis
SAGB	small-angle grain boundaries
sapphire	$\text{Al}_2\text{O}_3$
SM	silver mirror
SPF	short wave pass filter
SPM	self-phase modulation
SRSI	Self-Referenced Spectral Interferometry
SSG	small-signal gain
TBP	time bandwidth product
$\text{TeO}_2$	tellurium dioxide

Notation	Description
TFP	thin film polarizer
TIC	temporal intensity contrast
TM	turning mirror
TOD	third-order dispersion
uOPA	ultrafast optical parametric amplifier
VSF	vacuum spatial filter
XPW	cross polarized wave generation
YAG	yttrium aluminum garnet $Y_3Al_5O_{12}$
Yb <sup>3+</sup> :CALGO	Yb <sup>3+</sup> :CaGdAlO <sub>4</sub>
Yb <sup>3+</sup> :CALYO	Yb <sup>3+</sup> :CaYdAlO <sub>4</sub>
ZPL	zero phonon line



## APPENDIX A

# Appendix

### A.1 The Term Schema of the Quasi-Three-Level System $\text{Yb}^{3+}:\text{CaF}_2$

Figure A.1 shows the term schema of trivalent ytterbium ions in the calcium fluoride crystal ( $\text{Yb}^{3+}:\text{CaF}_2$ ). This is a quasi-three-level laser system, which is somewhere in between a three-level and four-level system. The lower laser level is thermally close to the ground level (lower pump level). Therefore, it is considerably populated by the Boltzmann-distribution. This results in absorption at the laser wavelength range at room temperature.

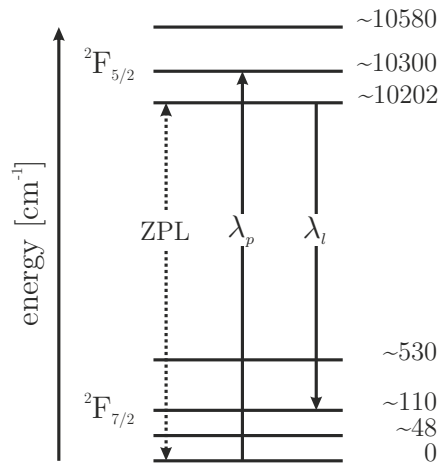


**Figure A.1:** Term schema of  $\text{Yb}^{3+}:\text{CaF}_2$  and the stark splitting of the lower  $^2F_{7/2}$  and the upper  $^2F_{5/2}$  energy levels [195]. ZPL: zero phonon line;  $\lambda_p$ : pump wavelength;  $\lambda_l$ : laser wavelength.

## A.2 Single Lens Imaging versus Relay Imaging

All calculations are done by using the matrix formalism, which is described in more detail in [27]. The matrix  $M_{prop}$  for a propagation length  $l$  is

$$M_{prop} = \begin{pmatrix} 1 & l \\ 0 & 1 \end{pmatrix} \quad (\text{A.1})$$

and for a lens  $M_{lens}$  with a focal length  $f$  is

$$M_{lens} = \begin{pmatrix} 1 & 0 \\ -1/f & 1 \end{pmatrix} . \quad (\text{A.2})$$

### Single lens imaging

A 1:1 imaging can be realized with a single lens. If the object distance is two times the focal length, the image distance is also two times the focal length. This can be called single lens imaging. The principle setup is shown in Figure A.2, where a point source is imaged with a magnification of 1. The problems (e.g. increasing beam divergence) with the direct imaging can be seen, when the beam evolution is investigated by using a ray tracing software like Zemax<sup>TM</sup>. An increasing lens diameter (i.e. larger F-number) is needed in a sequence of several single lens imaging systems to transport the power or to capture all rays of the point source.

To calculate the beam diameter in the image plane by using the paraxial approximation, the input diameter  $D_1$  and divergence  $\Theta_1$  is needed. The starting vector for the matrix formalism is derived to

$$\begin{pmatrix} D_1 \\ \Theta_1 \end{pmatrix} . \quad (\text{A.3})$$

The minimum size of the lens can be calculated to

$$\begin{pmatrix} D_L \\ \Theta_L \end{pmatrix} = \begin{pmatrix} 1 & 2f \\ 0 & 1 \end{pmatrix} \begin{pmatrix} D_1 \\ \Theta_1 \end{pmatrix} = \begin{pmatrix} 2f\Theta_1 + D_1 \\ \Theta_1 \end{pmatrix} , \quad (\text{A.4})$$

where the distance is two times of the focal length. The beam diameter on the lens is  $2f\Theta_1 + D_1$ .

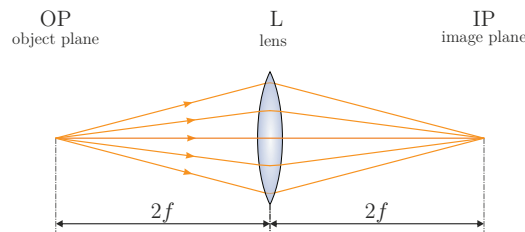


**Figure A.2:** Beam path for a direct imaging with a single lens L of a point source. The magnification factor is one.

The system matrix  $M_{DI}$  in the image plane of the telescope is derived to

$$M_{DI} = \begin{pmatrix} 1 & 2f \\ 0 & 1 \end{pmatrix} \begin{pmatrix} 1 & 0 \\ -1/f & 1 \end{pmatrix} \begin{pmatrix} 1 & 2f \\ 0 & 1 \end{pmatrix} = \begin{pmatrix} -1 & 0 \\ -1/f & -1 \end{pmatrix} . \quad (\text{A.5})$$

The vector in the image plane results to

$$\begin{pmatrix} D_2 \\ \Theta_2 \end{pmatrix} = \begin{pmatrix} -1 & 0 \\ -1/f & -1 \end{pmatrix} \begin{pmatrix} D_1 \\ \Theta_1 \end{pmatrix} = - \begin{pmatrix} D_1 \\ \Theta_1 + D_1/f \end{pmatrix} , \quad (\text{A.6})$$

where  $D_2$  is the output beam diameter and  $\Theta_2$  is the output divergence. The output and input beam diameter is the same as it is expected for an 1:1 imaging. The negative algebraic sign stands for an inverted image. A magnification of the beam diameter is not possible in the case of the direct imaging. The crucial fact is, that the output divergence is increased with the term  $D_1/f$ , which is the inverse of the F-number  $F^\#$ . Thus the beam parameter product is not preserved and increases more for smaller F-numbers.

### Relay Imaging

The relay imaging is also called telecentric imaging. A Keplerian telescope is taken for comparison. The system consists of two converging lenses and the principle setup is shown in Figure A.3. Here, the object and image plane are placed at the front focal length of the first lens  $f_1$  and the back focal length of the second lens  $f_2$ , respectively. The distance between the two lens is the sum of the focal length. Consequently, the system matrix  $M_{RI}$  is derived to

$$\begin{aligned} M_{RI} &= \begin{pmatrix} 1 & f_2 \\ 0 & 1 \end{pmatrix} \begin{pmatrix} 1 & 0 \\ -1/f_2 & 1 \end{pmatrix} \begin{pmatrix} 1 & f_1 + f_2 \\ 0 & 1 \end{pmatrix} \begin{pmatrix} 1 & 0 \\ -1/f_1 & 1 \end{pmatrix} \begin{pmatrix} 1 & f_1 \\ 0 & 1 \end{pmatrix} , \\ &= - \begin{pmatrix} f_2/f_1 & 0 \\ 0 & f_1/f_2 \end{pmatrix} , \end{aligned} \quad (\text{A.7})$$

which the negative algebraic sign stands for an inverted image. If the focal lengths are the same, a unit matrix is found. The term  $f_2/f_1$  represents the magnification factor  $m$ , as it is given in Equation (3.2). The beam vector in the image plane is derived to

$$\begin{aligned} \begin{pmatrix} D_2 \\ \Theta_2 \end{pmatrix} &= \begin{pmatrix} f_2/f_1 & 0 \\ 0 & f_1/f_2 \end{pmatrix} \begin{pmatrix} D_1 \\ \Theta_1 \end{pmatrix} \\ &= - \begin{pmatrix} D_1 m \\ \Theta_1/m \end{pmatrix} . \end{aligned} \quad (\text{A.8})$$

The result is that the beam parameter product is preserved in a *4f optical system*.

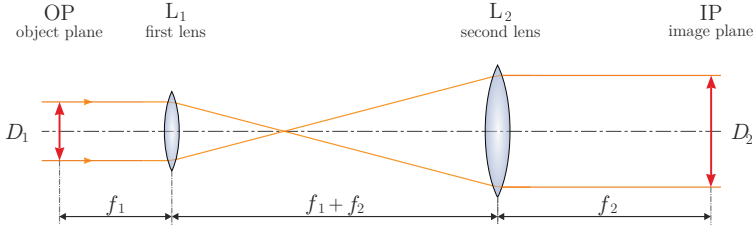


**Figure A.3:** Beam path of a relay imaging with two lenses  $L_1$  and  $L_2$  between the object and the image plane.

## A.3 Influence of Yb<sup>2+</sup>-ions on the Laser Performance

Due to the unknown influence of the divalent ytterbium ions (Yb<sup>2+</sup>) on the laser performance, two different experiments were performed. At first the CW laser performance is obtained to clarify the influence of the laser threshold  $P_{thres}$  as such as the slope efficiency  $\eta_{slope}$ . The laser resonator is comparable to the present setup in Figure 5.4 (b) on page 98 without pump recovery. In Figure A.4 a comparison of two different samples is done. One of them has Yb<sup>2+</sup>-ions and the other is Yb<sup>2+</sup>-ion free. Due to the unequal doping concentration of the samples the absorbed pump power  $P_{abs}$  was obtained for a better comparison. The slope efficiency and laser threshold are determined by a linear regression of the measurement and is given in Figure A.4. No significant difference between both samples is observable. As  $P_{thres}$  is also influenced by the optical quality, the alignment of the resonator and the contamination of the laser mirrors (e.g. dust), which can explain the weak difference, play an important role. The effective  $\eta_{slope}$  is almost the same for each sample and no evidence of a clear difference is visible. A degradation was not observable over 15 min at maximum pump power. For this reason there is no measurable effect of the Yb<sup>2+</sup> content on the continuous wave laser operation. A detailed study can be done with more equal samples on the base of optical quality and doping concentration.

In addition, a cavity-dumping operation of the resonator was arranged by inserting a Pockels cell. Thereby it is possible to test nanosecond amplification and damage issues. More detailed information about the setup can be found in Section 5.2.2 on page 99. In this experiment the gain material was pumped at a 10 Hz repetition rate. Figure A.5 shows the needed pump peak power  $P_{peak}$  at a given pump duration  $\tau_p$  to obtain 230  $\mu$ J. This was done to increase the inversion for short pump durations and to see some degradation effects, but no influence is observable. Due to the cavity length, a pulse duration of 6 ns was obtained.

Furthermore the damage threshold was not reduced with Yb<sup>2+</sup> inside the crystal. A detailed investigation can be done to have a closer look on the inversion level, but at the present state no hint for this is given by the proof of principle experiments.

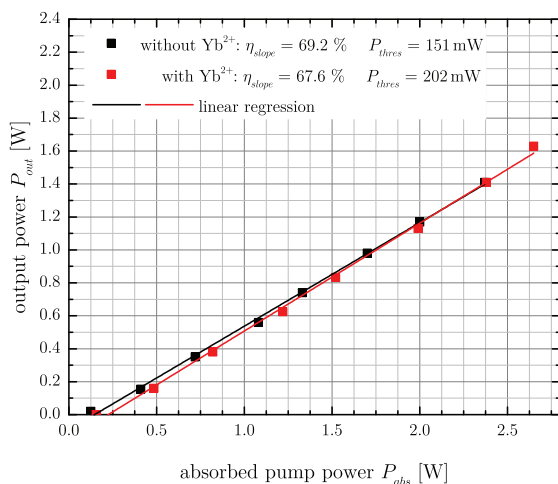


**Figure A.4:** The output power is given as a function of the absorbed pump power.

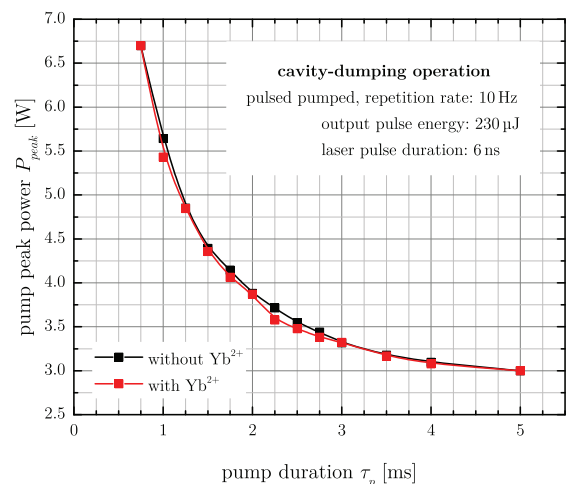


**Figure A.5:** Pump peak power is given as a function of pump duration to obtain a constant output energy for both samples.

## A.4 Alternative Yb<sup>3+</sup>-doped Gain Materials

A wide range of broadband Yb<sup>3+</sup>-doped gain materials were arising in the last years. Mostly crystals were in the focus due to their good thermal mechanical properties, which is important for high-average-power ultrashort lasers. Here, material processing needs ultrashort laser pulses with high pulse energies at a high repetition rate.

In the front-end of a high-energy laser chain the repetition rate is not an issue. For this purpose a very large emission cross section is required to get a sufficiently large bandwidth out of the front-end as a seed for the high-energy amplifiers. For this reason the gain material is not only linked to crystals, also glasses are possible. Typically, ytterbium doped glasses have a smooth emission spectrum compared to crystals. But for the high-energy amplifiers the thermal properties are not as good as needed. A short discussion of potential candidates follows.

### A.4.1 Spectroscopic Properties

#### A.4.1.1 Laser Glasses

Glasses are well-known for high-energy ultrashort pulse lasers like POLARIS [196], where an Yb<sup>3+</sup>-doped fluoride phosphate glass is used. The availability is one of the major problems. Optical quality issues, like bubbles and inclusions, are an issue as well [197].

For this reason, new alumino-silicate glasses are under development, containing lithium oxide (LiAS) [154] or aluminum oxide (SAL) [129]. Pure fused silica can be an attractive candidate as well [130]. The multicomponent glasses are available with high doping concentrations. However, such high concentrations lead to a reduction of the upper-state lifetime [129]. Large apertures are possible due to well established production techniques (e.g. direct glass melting).

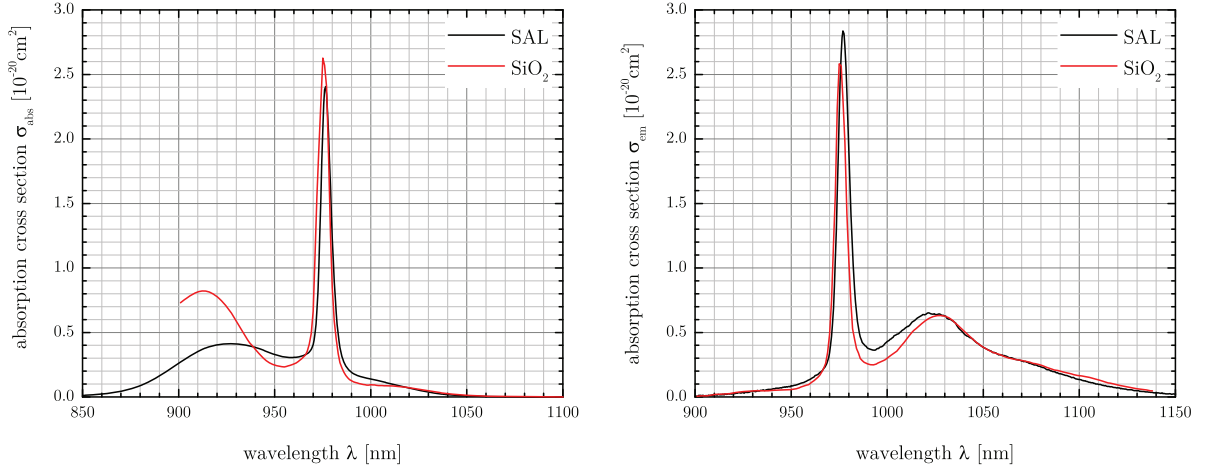
Besides these new materials, some other well-known glasses like pure phosphate glass (QX-glass) are available [155]. However, a detailed look into the properties is only done for the multicomponent glass, as well as the pure fused silica because previous experiment were performed with them and are given in Appendix A.4.2.1.

Figure A.6 depicts the cross sections for Yb<sup>3+</sup>-doped fused silica [162] and SAL glass [129]. Both exhibit a broad emission needed for ultrashort pulse lasers and amplifiers. In comparison to CaF<sub>2</sub> the nonlinear refractive index is higher (see Table 4.1), leading to a higher sensitivity to nonlinear effects.

Nevertheless these are promising candidates for high-energy lasers. For lower doping concentrations the upper-state lifetime of the SAL glass is in a good compliance with the doped fused silica ( $\tau_f = 0.8$  ms) [162].

In contrast to the phosphate glass (QX), as well as fluoride phosphate (FP) glasses, glass transition temperature of the SAL is nearly doubled, thus the thermal shock resistance and the thermal stability are improved.

Photodarkening in glasses, a well-known effect in fiber lasers, can occur. For this reason, pure fused silica is strongly affected and all experiments were done with untreated fused silica. In Figure A.7 the output power as a function of time for different pump powers is shown.  $P_{out}$  decreases much faster over time, if the pump power is increased. This indicates



(a) Absorption cross section of pure fused silica in red and SAL glass in black.

(b) Emission cross section of pure fused silica in red and SAL glass in black.

**Figure A.6:** Emission and absorption cross section of Yb<sup>3+</sup>-doped fused silica and SAL glass, according to [129, 162].

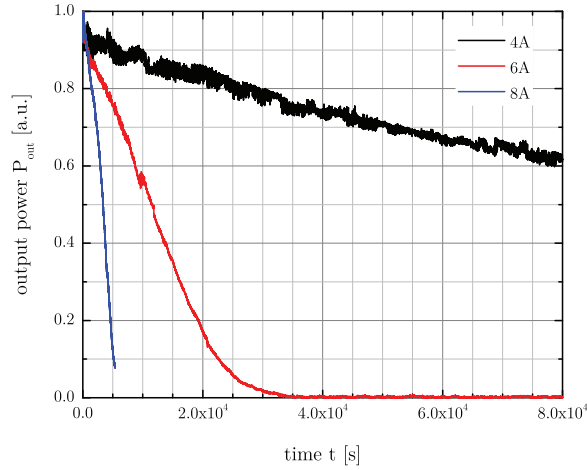


**Figure A.7:** Output power as a function of time for Yb<sup>3+</sup>:SiO<sub>2</sub>.

an impact of photodarkening. The loss growth rate depends on the density of excited ions (inversion level  $\beta$ ) [198].

Irradiated samples exhibit dark channels in the material. These are readily identifiable and stable over a long time.

Although it has been shown that it can be reversed, for example by irradiation with UV light [199]. To lower this effect, additional materials are added to the glass melt like cerium (CE) [200]. Other parasitic effects like color centers and quenching can also arise and have to be taken into account.



### A.4.1.2 CALGO and CALYO

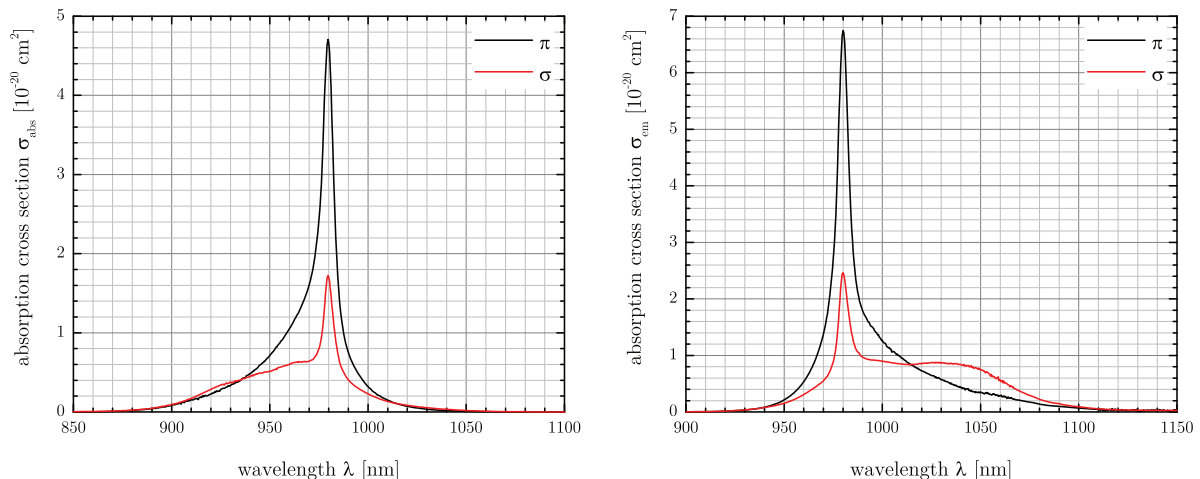
Interesting candidates are  $\text{Yb}^{3+}$ :CALGO and  $\text{Yb}^{3+}$ :CALYO. Both crystals are a member of the isostructural family with the general formula  $\text{ABCO}_4$ , where A denotes Ca, B is Gd or Y and C is Al. The difference between these two crystals is the ionic radii of  $\text{Gd}^{3+}$  and  $\text{Y}^{3+}$ . In the literature it can be found, that  $\text{Yb}^{3+}$ :CALYO is easier to grow [201]. However,  $\text{Yb}^{3+}$ :CALGO is the most investigated crystal starting from 2005 [156].

Femtosecond oscillators with pulses as short as 32 fs [202] were demonstrated with Kerr-lens mode-locking or 40 fs with SEAM mode-locking [203]. Regenerative amplifiers with output powers of 28 W at 217 fs [204] or pulse energies up to several mJ [205] and pulse durations the sub-100 fs pulse duration in a nonlinear regenerative amplifier [174] are developed so far.

Figure A.8 shows the absorption and emission cross section of  $\text{Yb}^{3+}$ :CALGO for parallel ( $\pi$ ) and perpendicular ( $\sigma$ ) polarization to the c-axis [157]. An absorption peak is close to 980 nm matching reasonably well to the other gain materials, such as  $\text{Yb}^{3+}$ : $\text{CaF}_2$ . The broadest emission cross section is observable for the  $\sigma$ -polarization, but an absorption maximum is found for the  $\pi$ -polarization.

In contrast to  $\text{Yb}^{3+}$ :CALGO,  $\text{Yb}^{3+}$ :CALYO was investigated in 2010 [206]. In the beginning it was known as  $\text{Yb}^{3+}$ :CYA. Until now pulse durations of about 43 fs were demonstrated with a Kerr-lens mode-locked oscillator [201]. A detailed polarized spectral analysis was done by D. Li et al. [159]. The cross section, presented in Figure A.9, is provided with kind permission by Li.

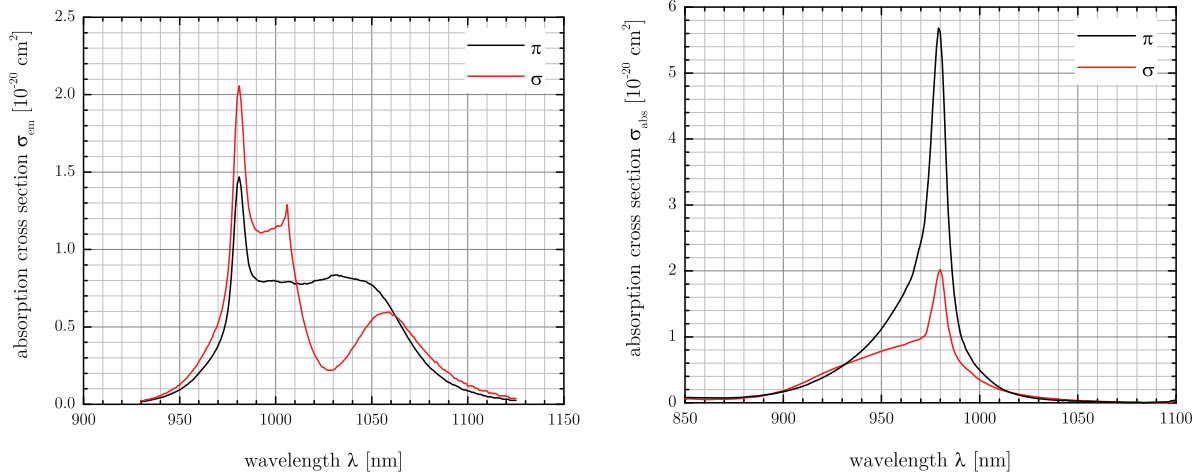
The behavior is very similar to  $\text{Yb}^{3+}$ :CALGO for  $\sigma$ -polarization, but a local minimum around 1025 nm is found for  $\pi$ . This can be used to counteract gain narrowing effects. The largest apertures are at the moment in the 10 mm range, which can be used for amplifiers with output energies up to 100 mJ.



(a) Absorption cross section of  $\text{Yb}^{3+}$ :CALGO for  $\pi$  (black line) and  $\sigma$  (red line) polarization to the c-axis.

(b) Emission cross section of  $\text{Yb}^{3+}$ :CALGO for  $\pi$  (black line) and  $\sigma$  (red line) polarization to the c-axis.

**Figure A.8:** Absorption and emission cross section of  $\text{Yb}^{3+}$ :CALGO for parallel ( $\pi$ ) and perpendicular ( $\sigma$ ) polarization to the c-axis, according to K. Hasse et al. [157]



(a) Absorption cross section of Yb<sup>3+</sup>:CALYO for  $\pi$  (black line) and  $\sigma$  (red line) polarization to the c-axis.

(b) Emission cross section of Yb<sup>3+</sup>:CALYO for  $\pi$  (black line) and  $\sigma$  (red line) polarization to the c-axis.

**Figure A.9:** Absorption and emission cross section of Yb<sup>3+</sup>:CALGO for parallel ( $\pi$ ) and perpendicular ( $\sigma$ ) polarization to the c-axis. Data are plotted according to [159].

Both material are promising candidates for ultrashort laser pulse amplification below 100 fs. However, at the moment there are only a few experiments performed and the crystal quality has yet to be improved for multipass amplifiers. First CW and regenerative amplifier experiments were performed, see Appendix A.4.2.2.

## A.4.2 Amplifier Experiments with Alternative Gain Materials

In Appendix A.4.1 numerous gain materials and their spectral properties are presented. These materials are compared in Table 4.1 with CaF<sub>2</sub>, which is the standard gain material in the PENELOPE project. The crystal based materials can only be produced is small size. This is the reason that they are not suitable for the large scale amplifiers. Another factor is the birefringent properties of the most broadband materials like Yb<sup>3+</sup>-doped CALGO and CALYO.

The CW laser performance of the materials is investigated and compared as well as the output spectrum in a cavity-dumped regenerative amplifier. The experimental setups are the same as given in Figures 5.5, 5.6 and 5.9. Furthermore, first CPA experiments are performed on a preliminary scale. This results are very promising and have to be improved in the future.

### A.4.2.1 Laser Glasses

The following section describes the results of the experiments for three different glasses. The silicate glasses are new materials, which were developed in the last years as gain materials for high-energy lasers.

## Phosphate Glass (QX)

The phosphate glass is a well-known material. It has been investigated more than one decade and is also used in  $\text{Nd}^{3+}$ -doped flash lamp pumped lasers. The glass samples were produced by Kigre Inc. The fluorescence lifetime is about 2 ms, more details can be found in Table 4.1.

In contrast to the other materials it has a very high nonlinear index of refraction ( $n_2$ ). For this reason, it is less suitable to use in high-energy laser amplifiers compared to  $\text{CaF}_2$ .

Until now, the material was used in femtosecond oscillator that achieved pulses as short as 58 fs [207]. Regenerative amplifiers with an output energy up to 1 mJ were obtained with a pulse duration of 200 fs [208]. Due to the broad emission cross section it is attractive for ultrashort laser pulse amplification. The maximum achieved energy was up to 150 mJ in an all  $\text{Yb}^{3+}$ :glass based CPA system, which was presented by Biswal [209]. The spectral bandwidth was 9 nm, which results in a pulse duration of 350 fs after the compressor. The TBP is 0.856, which leads to non-perfect compressed pulse. The spectral phase of the pulses was not measured.

At first, the output spectrum in a cavity-dumped regenerative amplifier was investigated. The experimental setup was presented in Figure 5.6 on page 100. The used glass sample had a thickness of 3 mm and a doping concentration of 15 wt%. All measurements were done in pulsed mode due to the bad thermal properties of the glass. At high average power, a rollover was observed and the material can be damaged.

The output spectrum for different laser diode driving currents is shown in Figure A.10. The energy was kept constant by changing the round-trip time of the amplified signal. In comparison to  $\text{Yb}:\text{CaF}_2$  (see Figure 5.8 on page 101) the center wavelength is shifted towards shorter wavelengths more clearly (blue-shifted), by increasing the laser diode driving current. A maximum displacement of 7.5 nm is observed at a laser diode driving current change of 3 A. This can be explained by the small-signal gain (SSG), which is shown in Figure A.11 according to [155]. If higher excitation levels are obtained by increasing the pump intensity, the small-signal gain peak exhibit a shift to shorter wavelengths.

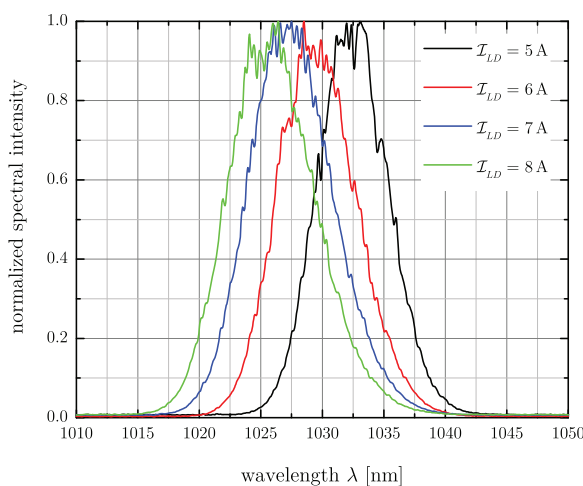


**Figure A.10:** Cavity-dumped output spectrum at different laser diode driving currents for  $\text{Yb}^{3+}$ :QX glass.

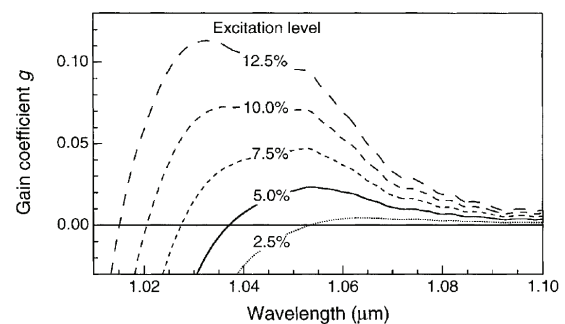


**Figure A.11:** SSG for different inversion levels in  $\text{Yb}^{3+}$ :QX glass, according to [155].

The amplifier was placed inside the CPA chain, as described in Section 5.2.2. Furthermore, a passive gain control was performed as it was investigated in Section 5.2.3.2. Figure A.12 shows the injected as well as the amplified spectrum with and without passive gain control. The gain narrowing is clearly visible. The initial spectrum is narrowed down by the spectral response of the resonator, as shown in Figure A.10. The bandwidth is increased with the passive gain control by a factor of about 2.

The amplified pulse is compressed and analyzed with the *SPIDER* device. The result is given in Figure A.13. The pulse has bandwidth of 15.2 nm and a duration of 151.9 fs such as a Fourier limit of 106.8 fs. The spectral phase is not flat and shows residual higher order phase terms, which can be compensated with a *DAZZLER*<sup>TM</sup>.

In addition, first high-energy experiments has been done in a multi-slab laser setup [96]. The slabs were heavy-water (D<sub>2</sub>O) cooled and nanosecond laser pulse amplification with a narrow line width are performed. A maximum pulse energy of 1 J was demonstrated at 1 Hz repetition rate, thus showing the feasibility and scalability of directly water-cooled, diode-pumped, high-energy lasers.

### Alumino-Silicate glass

The Yb<sup>3+</sup>-doped glass samples investigated here were developed at the Institute of Photonic Technology, Jena. The SAL glass, which was used in CW experiments, consisted of 70 mol % SiO<sub>2</sub>, 20 mol % Al<sub>2</sub>O<sub>3</sub>, 9.1 mol % La<sub>2</sub>O<sub>3</sub>, and a doping level of 0.9 mol % Yb<sub>2</sub>O<sub>3</sub>. It had a thickness of 3.4 mm and was polished in laser quality, but not anti-reflection coated.

The laser performance obtained with three different output couplers (OCs) are shown in [129]. The best slope efficiency of 51 % was reached with a 1.6 % OC with a maximum optical-to-optical efficiency of 42 %. Furthermore, the tuning range was determined by inserting a Brewster prism inside the cavity. The material exhibited a broad tunability of 80 nm. The sample shows depolarization losses, which make them not usable in a regenerative amplifier. To solve the problem an additional heat treatment can be done to remove the stress inside the material.

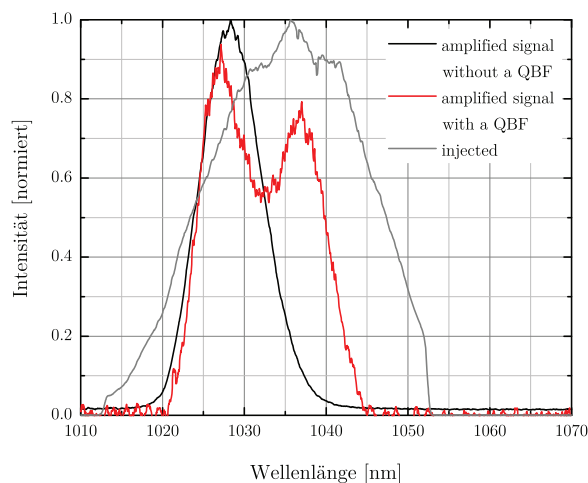
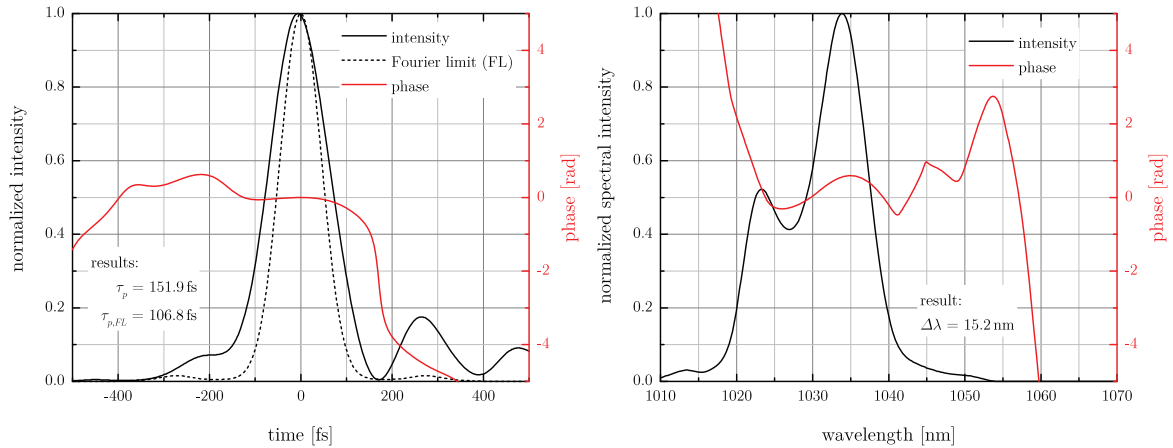


**Figure A.12:** Output spectrum of the Yb<sup>3+</sup>:QX glass regenerative amplifier without and with passive gain control. The injected spectrum is given as a comparison.



(a) Calculated temporal intensity and phase of the laser pulse as well as the Fourier limit. (b) Measured spectral intensity and phase of the laser pulse.

**Figure A.13:** *SPIDER* measurement of the laser pulse obtained with passive gain control.

The optical quality of the multicomponent glass was improved over the last years. New samples do not have this high intrinsic stress birefringence and can be used for laser amplifier experiments. The glass mixture is slightly changed compared to the sample in the CW experiment. As a preliminary result the output spectrum of a cavity-dumped regenerative amplifier is shown in Figure A.14. A spectral bandwidth of 7 nm was obtained and a maximum output energy of 260  $\mu\text{J}$ .

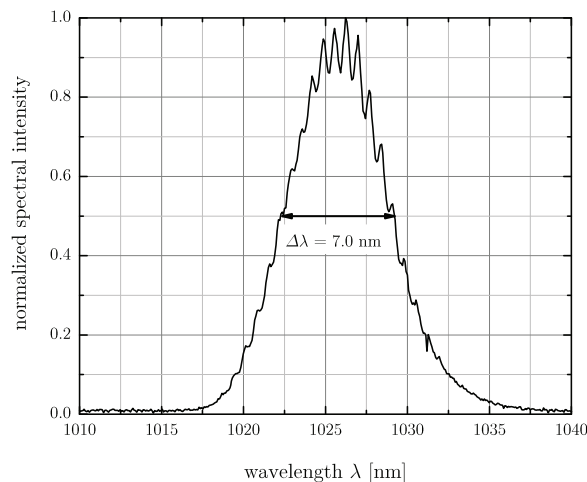


**Figure A.14:** Output spectrum of a cavity-dumped  $\text{Yb}^{3+}:\text{SAL}$  glass regenerative amplifier.

### Fused Silica glass

The doped fused silica samples were developed by Heraeus Quarzglas GmbH & Co. KG, Hanau together with the Institute of Photonic Technology, Jena. The rod was sintered from nano particles, which makes it possible to generate large volumes and to overcome the typically size limitation of the other techniques. Additionally, the material is homogenized with further fabrication steps to smooth the refractive index distribution. The variation of  $n$  is in the 10 ppm range inside the clear aperture [130].

Similar CW experiments were done and the results are comparable with the SAL glass. The complete study is presented in [130]. First regenerative amplifier experiment were performed and shown in Figure A.15, according to [210]. The used sample has a thickness of 5 mm and is uncoated. This is the reason for the spectral modulations in the 7.3 nm (FWHM) wide spectrum. The regenerative amplifier exhibits a maximum output energy of 340  $\mu$ J. Further investigations has to be done in terms of broadband laser amplification and so on. Therefore the material has to be anti-reflection coated to avoid the spectral modulations.

Nevertheless, these are promising results and further amplification experiments have to be performed.

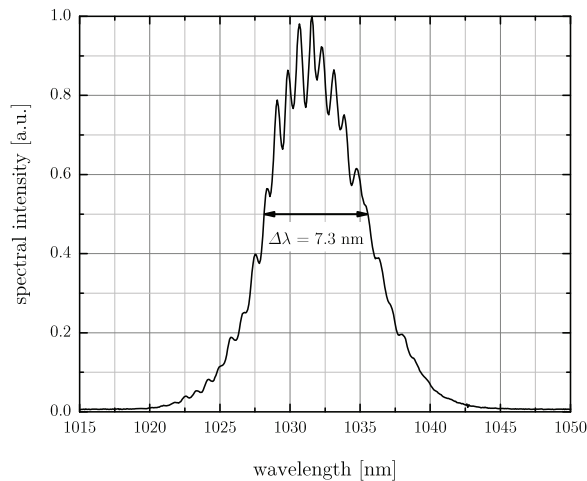


**Figure A.15:** Output spectrum of a cavity-dumped Yb<sup>3+</sup>:SiO<sub>2</sub> glass regenerative amplifier, according to [210].

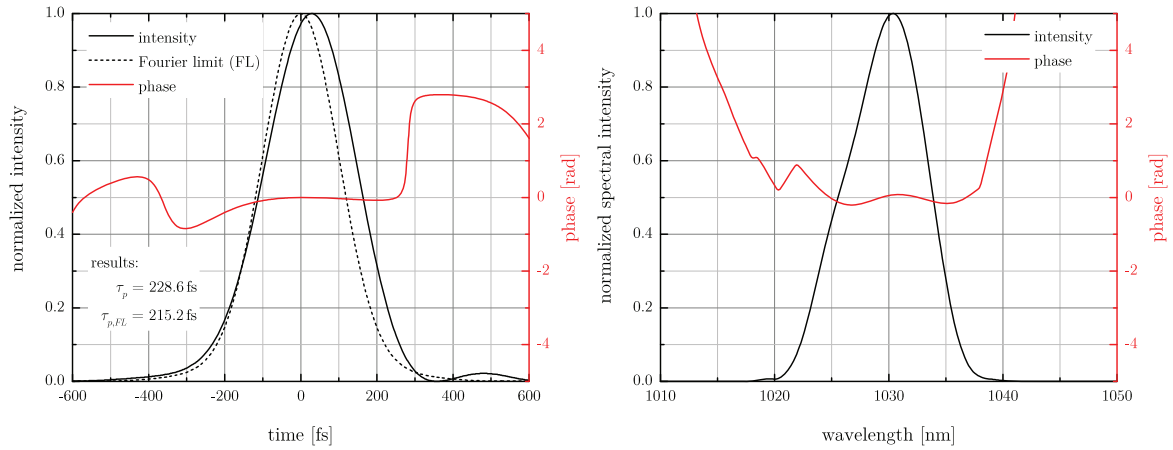
#### A.4.2.2 CALGO

The laser material properties are presented in Table 4.1 on Page 93 and the spectroscopic characteristics are very promising for ultrashort laser amplification.

The used Yb<sup>3+</sup>:CALGO sample had a thickness of 1 mm and a doping concentration of 2 mol%. As a result of the birefringent behavior, it was not possible to perform a spectral modulation with passive gain control. Therefore, the resonator has to be adapted with an additional polarizer.

The SSG is low, which results in a large number of amplification round-trips. The reason for this can be a low optical quality. Another indication is the limited output energy of the cavity-dumped regenerative amplifier. To adjust the best polarization a half waveplate (HWP) was inserted between the gain medium and the polarizer. The regenerative amplifier is placed between the stretcher and compressor of the CPA system.

Figure A.16 shows the CPA results detected with the *SPIDER*.



(a) Calculated temporal intensity and phase of the laser pulse as well as the Fourier limit. (b) Measured spectral intensity and phase of the laser pulse.

**Figure A.16:** *SPIDER* measurement of the laser pulse obtained in a  $\text{Yb}^{3+}$ :CALGO regenerative amplifier.

The pulse duration of 228.8 fs is obtained with a spectral bandwidth of 8.55 nm. The spectral phase is not flat, which leads to a non-transform limited pulse duration. The pulse duration is comparable to the results in the literature.

In further experiments a passive gain control can be implemented, using a second polarizer. Furthermore, a comparison with the  $\text{Yb}^{3+}$ -doped CALYO is possible.



---

# Publications

---

## Scientific publications

1. SIEBOLD, M., **M. Loeser**, U. SCHRAMM, J. KOERNER, M. WOLF, M. HELLWING, J. HEIN, K. ERTEL: High-efficiency, room-temperature nanosecond Yb:YAG laser. *Opt. Express* **17**: 19887–19893 (2009).
2. WALBAUM, T., M. LÖSER, P. GROSS, C. FALLNICH: Mechanisms in passive synchronization of erbium fiber lasers. English, *Applied Physics B* **102**: 743–750 (2011).
3. BANERJEE, S., K. ERTEL, P. D. MASON, P. J. PHILLIPS, M. SIEBOLD, **M. Loeser**, C. HERNANDEZ-GOMEZ, J. L. COLLIER: High-efficiency 10 J diode pumped cryogenic gas cooled Yb:YAG multislabs amplifier. *Opt. Lett.* **37**: 2175–2177 (2012).
4. **Loeser, M.**, F. RÖSER, A. REICHELT, M. SIEBOLD, S. GRIMM, D. LITZKENDORF, A. SCHWUCHOW, J. KIRCHHOF, U. SCHRAMM: Broadband, diode pumped Yb:SiO<sub>2</sub> multicomponent glass laser. *Opt. Lett.* **37**: 4029–4031 (2012).
5. SIEBOLD, M., **M. Loeser**, F. ROESER, M. SELTMANN, G. HARZENDORF, I. TSYBIN, S. LINKE, S. BANERJEE, P. D. MASON, P. J. PHILLIPS, K. ERTEL, J. C. COLLIER, U. SCHRAMM: High-energy, ceramic-disk Yb:LuAG laser amplifier. *Opt. Express* **20**: 21992–22000 (2012).
6. BANERJEE, S., J. KOERNER, M. SIEBOLD, Q. YANG, K. ERTEL, P. D. MASON, P. J. PHILLIPS, **M. Loeser**, H. ZHANG, S. LU, J. HEIN, U. SCHRAMM, M. C. KALUZA, J. L. COLLIER: Temperature dependent emission and absorption cross section of Yb<sup>3+</sup> doped yttrium lanthanum oxide (YLO) ceramic and its application in diode pumped amplifier. *Opt. Express* **21**: A726–A734 (2013).
7. KÖRNER, J., J. HEIN, H. LIEBETRAU, R. SEIFERT, D. KLÖPFEL, M. KAHLE, **M. Loeser**, M. SIEBOLD, U. SCHRAMM, M. C. KALUZA: Efficient burst mode amplifier for ultra-short pulses based on cryogenically cooled Yb<sup>3+</sup>:CaF<sub>2</sub>. *Opt. Express* **21**: 29006–29012 (2013).
8. KÖRNER, J., V. JAMBUNATHAN, J. HEIN, R. SEIFERT, **M. Loeser**, M. SIEBOLD, U. SCHRAMM, P. SIKOCINSKI, A. LUCIANETTI, T. MOCEK, M. KALUZA: Spectroscopic characterization of Yb<sup>3+</sup>-doped laser materials at cryogenic temperatures. *Applied Physics B* **116**: 75–81 (2014).

9. NAUMANN, L., M. SIEBOLD, M. KASPAR, B. KÄMPFER, R. KOTTE, A. L. GARCIA, **M. Loeser**, U. SCHRAMM, J. WÜSTENFELD: Precision measurement of timing RPC gas mixtures with laser–beam induced electrons. *Journal of Instrumentation* **9**: C10009 (2014).
10. SIEBOLD, M., **M. Loeser**, G. HARZENDORF, H. NEHRING, I. TSYBIN, F. ROESER, D. ALBACH, U. SCHRAMM: High–energy diode-pumped D<sub>2</sub>O–cooled multislabs Yb:YAG and Yb:QX–glass lasers. *Opt. Lett.* **39**: 3611–3614 (2014).
11. WANDT, C., S. KLINGEBIEL, S. KEPPLER, M. HORNING, **M. Loeser**, M. SIEBOLD, C. SKROBOL, A. KESSEL, S. A. TRUSHIN, Z. MAJOR, J. HEIN, M. C. KALUZA, F. KRAUSZ, S. KARSCH: Development of a Joule–class Yb:YAG amplifier and its implementation in a CPA system generating 1 TW pulses. *Laser & Photonics Reviews* **8**: 875–881 (2014).
12. BERGMANN, F., M. SIEBOLD, **M. Loeser**, F. RÖSER, D. ALBACH, U. SCHRAMM: MHz Repetition Rate Yb:YAG and Yb:CaF<sub>2</sub> Regenerative Picosecond Laser Amplifiers with a BBO Pockels Cell. *Applied Sciences* **5**: 761–769 (2015).
13. D. WINTERS *et al.*: Laser cooling of relativistic heavy–ion beams for FAIR. *Physica Scripta* **2015**: 014048 (2015).
14. RÖSER, F., **M. Loeser**, D. ALBACH, M. SIEBOLD, S. GRIMM, D. BRAND, A. SCHWUCHOW, A. LANGNER, G. SCHÖTZ, D. SCHÖNFELD, U. SCHRAMM: Broadband, diode pumped Yb-doped fused silica laser. *Opt. Mater. Express* **5**: 704–711 (2015).
15. WANG, H. B. *et al.*: Progress of laser cooling of 12 C<sup>3+</sup> ions at the CSRe. *Journal of Physics: Conference Series* **635**: 022080 (2015).
16. SIEBOLD, M., **M. Loeser**, F. RÖSER, D. ALBACH, M. BUSSMANN, S. ECKHARDT, A. F. LASAGNI, R. SAUERBREY, U. SCHRAMM: High energy Yb:YAG active mirror laser system for transform limited pulses bridging the picosecond gap. *Laser & Photonics Reviews* **10**: 673–680 (2016).
17. WEN, W. *et al.*: Recent progress on laser cooling of relativistic Lithium-like <sup>12</sup>C<sup>3+</sup> ion beams at heavy ion storage ring CSRe. *Scientia Sinica Physica, Mechanica & Astronomica*: – (2016).

---

## Submissions to international conferences

1. SIEBOLD, M., **M. Loeser**, J. KOERNER, M. WOLF, J. HEIN, C. WANDT, S. KLINGEBIEL, S. KARSCH, U. SCHRAMM: ‘Efficiency, Energy, and Power Scaling of Diode-Pumped, Short-Pulse Laser Amplifiers Using Yb-Doped Gain Media’, Lasers, Sources and Related Photonic Devices, AWB19 (2010).
2. KOERNER, J., J. HEIN, H. LIEBETRAU, M. KAHLE, M. LENSKI, **M. Loeser**, M. SIEBOLD: ‘Temperature resolved measurements of absorption and emission cross sections for various Yb<sup>3+</sup>-doped gain media from 100 K to room temperature’, Lasers and Electro-Optics Europe (CLEO EUROPE/EQEC), 2011 Conference on and 12th European Quantum Electronics Conference, pp. 1–1 (2011).
3. KOERNER, J., J. HEIN, H. LIEBETRAU, M. KAHLE, **M. Loeser**, M. SIEBOLD: ‘Cryogenic-cooled Yb:YAG amplifier for ns-pulses obtaining high optical efficiencies’, Lasers and Electro-Optics Europe (CLEO EUROPE/EQEC), 2011 Conference on and 12th European Quantum Electronics Conference, pp. 1–1 (2011).
4. KÖRNER, J., J. HEIN, M. KAHLE, H. LIEBETRAU, M. KALUZA, M. SIEBOLD, **M. Loeser**: ‘High-efficiency cryogenic-cooled diode-pumped amplifier with relay imaging for nanosecond pulses’, Proc. SPIE, Vol. 8080, pp. 80800D–6 (2011).
5. KÖRNER, J., J. HEIN, M. KAHLE, H. LIEBETRAU, M. LENSKI, M. KALUZA, **M. Loeser**, M. SIEBOLD: ‘Temperature dependent measurement of absorption and emission cross sections for various Yb<sup>3+</sup> doped laser materials’, Proc. SPIE, Vol. 8080, pp. 808003–808007 (2011).
6. **Loeser, M.**, F. ROESER, A. REICHELT, F. KROLL, M. SIEBOLD, U. SCHRAMM, S. GRIMM, J. KIRCHHOF, D. LITZKENDORF: ‘Broadband, diode-pumped Yb:SiO<sub>2</sub> multicomponent glass laser’, Advances in Optical Materials, AMB16 (2011).
7. **Loeser, M.**, M. SIEBOLD, F. KROLL, F. ROESER, J. KOERNER, J. HEIN, U. SCHRAMM: ‘Analysis of a high-energy, diode-pumped Yb:CaF<sub>2</sub> disk laser’, Advances in Optical Materials, ATuB13 (2011).
8. SIEBOLD, M., **M. Loeser**, F. ROESER, F. KROLL, J. KORNER, J. HEIN, U. SCHRAMM: ‘High-energy, diode-pumped Yb:CaF<sub>2</sub> disk-laser’, Lasers and Electro-Optics Europe (CLEO EUROPE/EQEC), 2011 Conference on and 12th European Quantum Electronics Conference, pp. 1–1 (2011).
9. **Loeser, M.**, M. SIEBOLD, F. ROESER, U. SCHRAMM: ‘High energy CPA-free picosecond Yb:YAG amplifier’, Lasers, Sources, and Related Photonic Devices, AM4A.16 (2012).
10. SIEBOLD, M., **M. Loeser**, F. ROESER, R. UECKER, J. KOERNER, J. HEIN, M. HORNUNG, M. KALUZA, U. SCHRAMM: ‘High-energy Laser Amplifiers using Ultra-broad Emitting Yb-doped Materials’, Lasers, Sources, and Related Photonic Devices, IW5D.1 (2012).

11. KÖRNER, J., J. HEIN, H. LIEBETRAU, R. SEIFERT, D. KLÖPFEL, M. KAHLE, M. **Loeser**, M. SIEBOLD, U. SCHRAMM, M. C. KALUZA: ‘Highly efficient all diode pumped burst mode laser system for ultra–short pulses’, Advanced Solid-State Lasers Congress, ATu3A.63 (2013).
12. SIEBOLD, M., M. **Loeser**, D. ALBACH, F. ROESER, S. BANERJEE, U. SCHRAMM: ‘Diode–pumped Yb:LuAG and Yb:YAG disk laser amplifiers with high pulse energies’, Lasers and Electro-Optics Europe (CLEO EUROPE/IQEC), 2013 Conference on and International Quantum Electronics Conference, pp. 1–1 (2013).
13. SIEBOLD, M., F. ROESER, M. **Loeser**, D. ALBACH, U. SCHRAMM: ‘PEnELOPE: a high peak–power diode-pumped laser system for laser–plasma experiments’, Proc. SPIE, Vol. 8780, pp. 878005–878014 (2013).
14. ROESER, F., M. LÖSER, D. ALBACH, M. SIEBOLD, U. SCHRAMM, S. GRIMM, D. BRAND, A. LANGNER, G. SCHÖTZ: ‘Broadband, diode-pumped Yb–doped fused bulk silica laser’, Advanced Solid State Lasers, AM2A.2 (2014).
15. SIEBOLD, M., M. LÖSER, F. ROESER, D. ALBACH, U. SCHRAMM: ‘High–energy diode-pumped D<sub>2</sub>O–cooled multislabs Yb:YAG and Yb:QX–glass lasers’, Advanced Solid State Lasers, AF1A.3 (2014).
16. ALBACH, D., M. SIEBOLD, M. **Loeser**, F. ROESER, U. SCHRAMM: ‘Development update on the PENELOPE laser system’, The 4<sup>th</sup> Advanced Lasers and Photon Sources (2015).
17. ECKHARDT, S., L. MÜLLER-MESKAMP, M. **Loeser**, M. SIEBOLD, A. F. LASAGNI: ‘Fabrication of highly efficient transparent metal thin film electrodes using Direct Laser Interference Patterning’, Proc. SPIE, Vol. 9351, pp. 935116–935116 (2015).
18. RÖSER, F., M. **Loeser**, M. SIEBOLD, D. ALBACH, S. GRIMM, A. LANGNER, G. SCHÖTZ, U. SCHRAMM: ‘Regenerative amplification in Yb<sup>3+</sup>-doped fused silica’, 2015 European Conference on Lasers and Electro-Optics - European Quantum Electronics Conference, CA\_P\_21 (2015).
19. ALBACH, D., M. SIEBOLD, M. **Loeser**, F. ROESER, P. EISELT, U. SCHRAMM: ‘PENELOPE laser system update–on the way to first light’, The 5<sup>th</sup> Advanced Lasers and Photon Sources (2016).
20. ALBACH, D., M. SIEBOLD, M. **Loeser**, F. ROESER, U. SCHRAMM: ‘PENELOPE–a high energy 150 fs diode–pumped laser system’, 7<sup>th</sup> International Conference on Ultrahigh Intensity Lasers (ICUIL), Invited (2016).
21. DEBUS, A., K. STEINIGER, D. ALBACH, M. **Loeser**, R. PAUSCH, F. ROESER, U. SCHRAMM, M. SIEBOLD, M. BUSSMANN: ‘Scaling EUV and X–ray Thomson Sources to Optical Free–Electron Laser Operation with Traveling–Wave Thomson Scattering’, Advanced Accelerator Conference 2016 (2016).
22. REHWALD, M. *et al.*: ‘High–contrast laser–proton acceleration from condensed hydrogen jet and ultra–thin foils’, 34<sup>th</sup> European Conference on Laser Interaction with Matter (2016).

23. STEINIGER, K., D. ALBACH, A. DEBUS, **M. Loeser**, R. PAUSCH, F. ROESER, U. SCHRAMM, M. SIEBOLD, M. BUSSMANN: ‘Scaling EUV and X-ray Thomson Sources to Optical Free-Electron Laser Operation with Traveling-Wave Thomson-Scattering’, The 15<sup>th</sup> International Conference on X-Ray Lasers (2016).
24. ZEIL, K. *et al.*: ‘High-contrast laser-proton acceleration from condensed hydrogen jet’, Advanced Accelerator Conference 2016 (2016).
25. ALBACH, D., M. SIEBOLD, **M. Loeser**, C. BERNERT, U. SCHRAMM: ‘PENELOPE – amplifier benchmarks and 10 J performance’, The 6<sup>th</sup> Advanced Lasers and Photon Sources, Invited (2017).
26. SCHRAMM, U. *et al.*: ‘First Results with the Novel Peta-Watt Laser Acceleration Facility in Dresden’, 8<sup>th</sup> International Particle Accelerator Conference IPAC17, pp. 48–52, paper MOZB1 (2017).

## Patent

1. THORALD, B., M. SIEBOLD, **M. Loeser**: German, Patent, EP3023832 A1 (2016).



---

# Danksagung

---

Auf diesem Weg bedanke ich mich bei allen, die zum Gelingen der Arbeit beigetragen haben! Ein solches Ziel kann nicht allein erreicht werden und für die aufgebrachte Unterstützung in den letzten Jahren bin ich sehr dankbar.

An allererster Stelle möchte ich mich beim wissenschaftlichen Direktor des Helmholtz-Zentrum Dresden-Rossendorf Herrn Prof. Dr. R. Sauerbrey bedanken, der mir die Möglichkeit gegeben hat, in der Abteilung Laser-Teilchenbeschleunigung, meine Arbeit im Bereich der Laserentwicklung anfertigen zu dürfen. Ihm ist es zu verdanken, dass dieses interessante Feld nach Dresden gekommen ist.

An zweiter Stelle möchte ich mich bei Herrn Prof. P. Hartmann bedanken, der mich über meine Zeit vom Studium bis zur Doktorarbeit unterstützt hat. Durch seine Vorlesungen während meines Studiums bin ich zur Optik und Laserphysik gekommen. Er hat mir dieses spannende Feld nähergebracht und mich dafür begeistert. Dies hält bis zum heutigen Tag an. Darüber hinaus hat er mich bestärkt eine Promotion anzustreben. Seine Bemühungen zur Ausbildung junger Leute im Bereich der Optik und Laserphysik ist beispielhaft und nützt nicht nur der Hochschule sondern auch vielen Unternehmen. Ich wünsche ihm und seinem Team viel Erfolg mit dem neu eröffneten Fraunhofer-Anwendungszentrum für Optische Messtechnik und Oberflächentechnologien (AZOM).

Ebenfalls ein großer Dank geht an die beiden Institutsdirektoren des Instituts für Strahlenphysik Tom Cowan und Ulrich Schramm. Tom Cowan brachte viel interessante Ideen und Anregungen sowie internationale Kontakte mit ins Institut.

Ulrich Schramm möchte ich hier besonders danken, der mich in seiner Position als Institutsdirektor sowie Abteilungsleiter immer unterstützte und damit beim Gelingen dieser Arbeit einen großen Anteil hat. Seine Tür stand und steht immer offen für Fragen sämtlicher Art. Sein Vertrauen in meine Entscheidungen während des Projektes war mir eine große Hilfe. Dies stellte für mich auch eine Verantwortung dar, die gesetzten Ziele für das PENELOPE Projekt zu unterstützen.

Die Möglichkeit meine Promotion im Rahmen des PENELOPE Projektes zu machen, gibt es vor allem wegen Mathias. Er brachte die Erfahrung von HEC-DPSSL mit nach Dresden sowie zahlreichen Ideen ein besonders effizientes Lasersystem zu realisieren. Damit hatte das Team begonnen. Ihm gilt auch ein großer Dank für die Unterstützung in den letzten Jahren. Von ihm habe ich das Arbeiten mit Lasern gelernt. Des Weiteren haben wir gemeinsam gelernt wie man ein Labor einrichtet (mehrfach). Fabian unterstützte bald das Team. Von ihm habe ich viel über Strecker und Kompressor eines CPA-Systems gelernt. Die gemeinsame Arbeit am Projekt sowie weiteren interessanten Themen hat mir in meiner wissenschaftlichen Entwicklung sehr geholfen.



Als weitere Unterstützung des PENELOPE-Teams kam Daniel zu uns. Er brachte jede Menge Erfahrung auf dem Gebiet der High-Energy Laser aus Frankreich mit. Er war und ist ein wichtiger Anlaufpunkt für Diskussionen komplizierter Fragestellungen. Von ihm habe ich nicht nur viel über Simulationen erfahren, sondern auch zu allgemeinen Dingen des Lebens. Ab und zu war es auch mehr als ich wissen wollte. Vielen Dank für deine Freundschaft und Hilfe während der Entstehung der Doktorarbeit sowie langer Messreihen im Labor.

Die mechanische und konstruktive Unterstützung eine experimentelle Arbeit zu erstellen ist riesig. Das wäre ohne die fantastische Hilfe der Institutswerkstatt wohl kaum möglich gewesen. Deswegen gilt mein Dank dem Werkstattteam um Matthias Langer, Mathias Boeck, Marco Böse, Robert Schönert und Rolf Hensel. Ein großer Dank geht an Gunter, Harald und Simon für manch schwierige Konstruktion und die Geduld auf meine Sonderwünsche einzugehen sowie auch umzusetzen. Christoph danke ich für die Unterstützung bei der Schaltungsentwicklung, das Löten vieler Kabel sowie Stecker und sonstige kleine Hilfen. Für die schnelle und konstruktive Hilfe bei allen administrativen Fragen wie Dienstreisen und Bestellungen danke ich Petra Neumann und Katrin Thiele.

I also want to thank all my colleagues and friends of the HEC-DPSSL community out of Germany. It is a great pleasure to be a member of it. Thanks a lot guys.

Nicht zu vergessen ist auch die Unterstützung durch Industriepartner, die zur Umsetzung eines solchen Projektes benötigt werden. Ein besonderer Dank geht dabei an Stefan Götz, Frank Wunderlich sowie alle Mitarbeiter von Layertec für die Realisierung manch komplizierter und ausgefallener Optik sowie Beschichtung. Frank Zimmermann und Patrick Incorvaia von Liop-Tec gilt ein großer Dank für die Unterstützung mit kundenspezifischer Optomechanik. Danke für die Geduld und die vielen guten Ideen Frank.

Für die geteilten guten und manchmal auch zähen Zeiten - im Labor oder anderswo - möchte ich dem (ehemaligen) Doktoranden-Team mit Karl, Thomas, Alexander, Axel, Josefine und Jurjen danken! Die daraus entstandenen Ausflüge und sonstigen Events haben sehr viel Freude bereitet und sind eine gute Ablenkung vom Alltag gewesen.

Ein besonderer Dank geht an meine Familie und Freunde, die mich immer auf meinem Weg begleitet und unterstützt haben. Meiner Schwester Kristin danke ich für das Korrektur lesen der Arbeit und auch für die schönen Besuche in der Schweiz. Vor allem möchte ich mich bei meinen Eltern Karin und Thomas bedanken. Ihnen gilt mein Dank mich immer in meiner Entwicklung unterstützt zu haben sowie auch die Geduld, dass ich meinen Weg finde. Ab 2011 ist die Hilfe bei der Kinderbetreuung nicht zu vergessen. Dies hat vieles sehr viel leichter gemacht.

Ein ganz großer Dank geht an meine Frau Kristin, sowie meine Kinder Emma und Rosalie. Ohne die Freiheit von meiner Frau meine Leidenschaft für die Wissenschaft ausleben zu dürfen, hätte ich das alles nicht geschafft. Dabei mussten sie auch mal auf mich verzichten. Die Ablenkung und die Freude mit meinen drei Mädels, hat viel Stress auch vergessen lassen. Ich freue mich und bin stolz solch eine Familie zu haben. Dieser berufliche Abschnitt in meinem Leben endet nun und ein neuer beginnt. Aber das Wichtigste ist, dass ich mich immer auf meine gesamte Familie verlassen kann.

Fall du dich hier nicht gefunden hast, bitte ich das zu entschuldigen. Daher danke ich an dieser Stelle all denjenigen, die ich vergessen habe.

---

# Eidesstattliche Erklärung

---

Hiermit versichere ich, Markus Löser, geboren am 08.01.1983 in Pirna, im Rahmen meines Promotionsverfahrens an der Fakultät Mathematik und Naturwissenschaften der Technischen Universität Dresden und an Eides statt, dass

1. ich die Ache ohne unzulässige Hilfe Dritter und ohne Benutzung anderer als der angegebenen Hilfsmittel angefertigt habe; die aus fremden Quellen direkt oder indirekt übernommenen Gedanken sind als solche kenntlich gemacht. Die Arbeit wurde bisher weder im Inland noch im Ausland in gleicher oder ähnlicher Form einer anderen Prüfungsbehörde vorgelegt.
2. ich die vorliegende Arbeit am Helmholtz-Zentrum Dresden-Rossendorf am Institut für Strahlenphysik unter der wissenschaftlichen Betreuung von Prof. Roland Sauerbrey angefertigt habe.
3. mir ist die geltende Promotionsordnung (Stand 23.02.2011, Fakultät Mathematik und Naturwissenschaften der TU Dresden) bekannt ist und ich diese anerkenne.

Dresden, 09.08.2017

Markus Löser







Bautzner Landstr. 400  
01328 Dresden, Germany  
Tel. +49 351 260-3006  
Fax +49 351 260-13006  
m.loeser@hzdr.de  
<http://www.hzdr.de>